INTERFACIAL ELECTROCHEMISTRY OF COPPER AND SPECTRO-ELECTROCHEMICAL CHARACTERIZATION OF OXYGEN REDUCTION REACTION

Kyle Kai-Hung Yu, B.E., M.Sc.

Dissertation Prepared for the Degree of

DOCTOR OF PHILOSOPHY

UNIVERSITY OF NORTH TEXAS

August 2011

APPROVED:

Oliver M. R. Chyan, Major Professor
Michael G. Richmond, Committee Member
Guido Verbeck, Committee Member
Rob Petros, Committee Member
William E. Acree, Chair of the Department of Chemistry
James D. Meernik, Acting Dean of the Toulouse Graduate School

Yu, Kyle Kai-Hung. Interfacial Electrochemistry of Copper and Spectro-Electrochemical Characterization of Oxygen Reduction Reaction. Doctor of Philosophy (Chemistry-Analytical Chemistry), August 2011, 211 pp., 3 tables, 140 figures, 3 schemes, chapter references.

The first part of this dissertation highlights the contents of the electrochemical characterization of Cu and its electroplating on Ru-based substrates. The growth of Ru native oxide does diminish the efficiency of Cu plating on Ru surface. However, the electrochemical formed irreversible Ru hydrate dioxide (RuO_xH_y) shows better coverage of Cu UPD. The conductive Ru oxides are directly plateable liner materials as potential diffusion barriers for the IC fabrication. The part II of this dissertation demonstrates the development of a new rapid corrosion screening methodology for effective characterization Cu bimetallic corrosion in CMP and post-CMP environments. The corrosion inhibitors and antioxidants were studied in this dissertation. In part III, a new SEC methodology was developed to study the ORR catalysts. This novel SEC cell can offer cheap, rapid optical screening results, which helps the efficient development of a better ORR catalyst. Also, the SEC method is capable for identifying the poisoning of electrocatalysts. Our data show that the RuO_xH_y processes several outstanding properties of ORR such as high tolerance of sulfation, high kinetic current limitation and low percentage of hydrogen peroxide.

ACKNOWLEDGEMENTS

I wish to express my gratitude to those who have encouraged and supported me to complete this dissertation.

I greatly appreciate my advisor Dr. Oliver M. R. Chyan for his valuable advice, objective critiques and helpful suggestions. With his apt teaching and guidance, I learned knowledge of know-how and experienced in doing it in both of my academic and personal life. The comments and critiques from my committee members have greatly helped in making this dissertation a better shape. The financial support from the Welch Foundation, the chemistry department, SRC and ATMI is deeply appreciated.

This work owes much to the thoughtful and helpful comments of my comrade-in-arms, Karthik Pillai. With his wise philosophic approach of humorous personality and his endless kindness, I have had a joyful research time for the past six years.

For my wife, Tai-fen, I cannot begin to thank you years of understanding, sacrifice and endless love. I can concentrate on my research to make this dissertation possible. Last, but not least, my parents and parents-in-law receive my deepest gratitude and love for their dedication and the many years of unwavering support and confidence on my education.

Lastly I would like to thank DCC members and our pastor, Peter. With their concern and love, I become a Christian and follow God's providence.

TABLE OF CONTENTS

Page

LIST OF TABLES

Page

LIST OF FIGURES

Page

LIST OF SCHEMES

Page

CHAPTER 1

INTRODUCTION OF INSTRUMENTS

This dissertation is the cumulative effort of my research work done in the Interfacial Electrochemistry and Materials Research Lab (IEMR) at the University of North Texas under the apt supervision and guidance of Dr. Oliver M. R. Chyan. Chapter 1 discusses the instruments and techniques that have been used in this dissertation. Chapters 2 and 3 highlight the contents of the electrochemical characterization of Cu and its electroplating on ruthenium substrates. The second part of my research covers chapter 4 and 5, which is dedicated to the investigation of bimetallic corrosion of Cu and the interaction between Cu and antioxidants or inhibitors. The final section of this dissertation introduces the new method of spectroelectrochemical characterization of oxygen reduction reaction. I conclude with chapter 7 on proposing further explorations and future plans for continuation in this research project.

1.1 Electrochemistry

1.1.1 Fundamentals of Electrochemistry

The science of electrochemistry began with the discovery of electrical charge from the twitching muscle of a frog dissection during an anatomic experiment made at the end of the eighteenth century. A few years later,

Alessandro Volta developed the battery cell. But it was Michael Faraday who greatly enhanced the study of electrochemistry and brought it to the attention of the scientific community in the middle of the nineteenth century [1]. Since then, there have been many applications of electrochemistry introduced into the commercial and domestic use of our daily living. Electrochemistry can be generally defined as the study on the phenomenon of charge and electron transfer. The discipline of electrochemistry covers a wide range of different physical and chemical field which includes coulometry, ion-selective electrodes, photosynthesis, and biochemistry etc. In addition, there are also reports on the many applications in using electroanalytical measurements [2, 3].

1.1.2 The Nature of Electrochemical System [4]

There are some basic and important concepts about electrochemical systems. First, the electrochemical system is usually heterogeneous rather than homogeneous because of the electrode/electrolyte interface. For instance, various electrode reactions take place in a heterogeneous condition involving activities such as hydrogen evolution, copper plating, electrode oxidation and oxygen reduction. The solution of electrolyte can be separated in three parts consisting the double layer, diffusion layer and bulk layer as shown in Figure 1-1. The double layer is located within the interface between the electrode interior and the electrolyte and extending further to the bulk layer. Second, surface reactions near the electrode usually cover several complex kinetic steps which come with

the adsorption or deposition of atoms, intermediate products, migration of atoms, and recombination of atoms. In that manner, the electrochemical systems show a dynamic nature that link with the activity of chemical transportation. Third, the current represents the reaction rate and the potential reflects the energy of electrons. Finally, the potential and current are parameters which are inter-related to each other; as a result, two of them cannot be controlled at the same time.

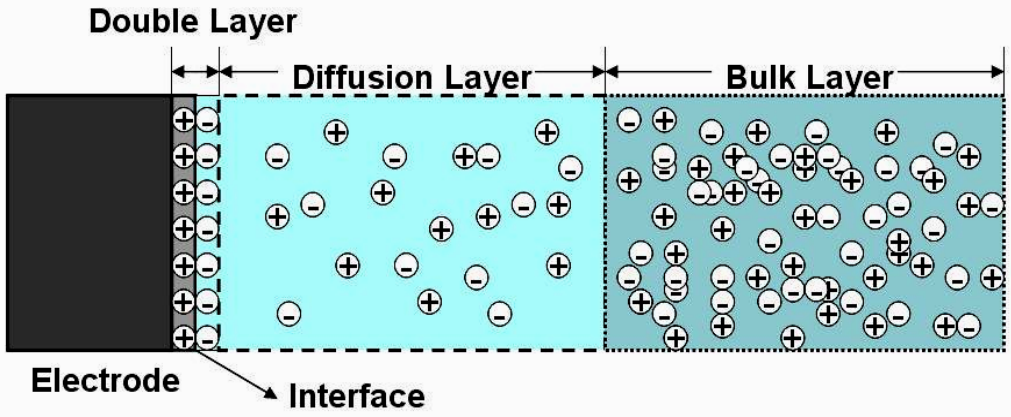

Figure 1-1: Configuration of layers of electrolyte in electrochemical system.

1.1.3 Three Electrode System

Due to the advantage of precise electrode potential control during the measurement, the three-electrode method is the most widely used in electrochemistry. In this system, a reference electrode, working electrode, and counter electrode (secondary or auxiliary electrode) are used. An electrolyte is usually added to ensure satisfactory conductivity for charge transfer between electrodes. The range of the potential window is determined collectively by the

mixture of the solvent, electrolyte and particular working electrode.

1.1.4 Open Circuit Potential (OCP)

Open circuit potential (OCP) measurement is a fundamental property responding to the nature of working electrode in equilibrium with its chemical environments. The OCP value represents the stability of potential of working electrode in different ambients and can reflect the purity and cleanliness of the electrode.

1.1.5 Cyclic Voltammetry (CV)

Cyclic voltammetry (CV) is one kind of potentio-dynamic electrochemical measurement. The redox properties of chemicals in electrolyte or electrochemical reactivity of reactive electrode can be determined from CV. In CV, the potential is measured between the working electrode and the reference electrode and the current is recorded between the working electrode and the counter electrode. The CV experiment provides valuable information by plotting current (i) vs. potential (E). The potential sweeps linearly back and forth with time in a pre-defined range. Take a reversible redox reaction as an example, the anodic forward scan will reach the potential of oxidation which produces the oxidative current peak, and the reverse scan will usually have a similar reduction current peak which has a symmetrical shape of oxidation peak. As a result, not only the potentials of each oxidation and reduction but also the rate of electrochemical

reaction can be obtained. There is an example in Figure 1-2. The redox reaction of $Fe(CN)_6^{3-/4-}$ is represented as two current peaks which have peak current potentials of E_a and E_c.

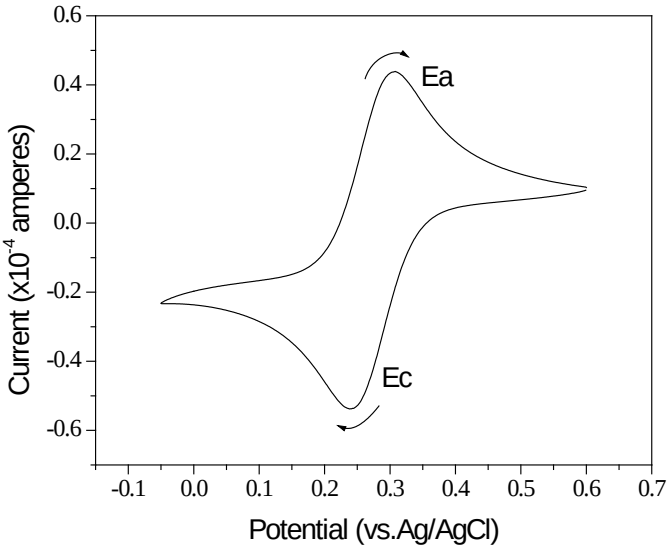

Figure 1-2: CV of redox reaction of Fe ion in 10mM $K_3Fe(CN)_6$/0.5 M K_2SO_4 electrolyte with scan rate 50 mV/s.

1.1.6 Tafel Plot

Tafel plots relate to the tafel equation which concerns the rate of an electrochemical reaction to overpotential (η). Tafel plot is the graph of the logarithm of the current density (i) against the (η). A polarized electrode regularly produces a relationship between current and potential in a region which can be approached by:

$$\eta = \pm B \log (I/I_0)$$

Where η is applied overpotential with respect to the open circuit potential, I is the measured current density, B and I_0 are constants, I_0 is defined as the

equilibrium current density, and B is defined as the tafel slope.

The Tafel plot is generated by starting the polarization at about -200mV from open circuit potential (OCP) and increasing till the potential is +200mV from OCP. In Figure 1-3 (a), it shows that the corrosion current (I_{corr}) can be estimated by crossing extrapolation of cathodic and anodic current curves. The corrosion potential (E_{corr}) is allocated by extrapolation of the pointed tip of the tafel plot curve to the axis of potential V. By characterizing the slope of two cathodic and anodic branches, the tendency of redox reaction can be found as shown in Figure (b). The Tafel plot was used to measure the corrosion potential and corrosion current of Cu interconnects, diffusion barrier materials like Ta or Ru in chemical mechanical planarization (CMP) slurry solution.

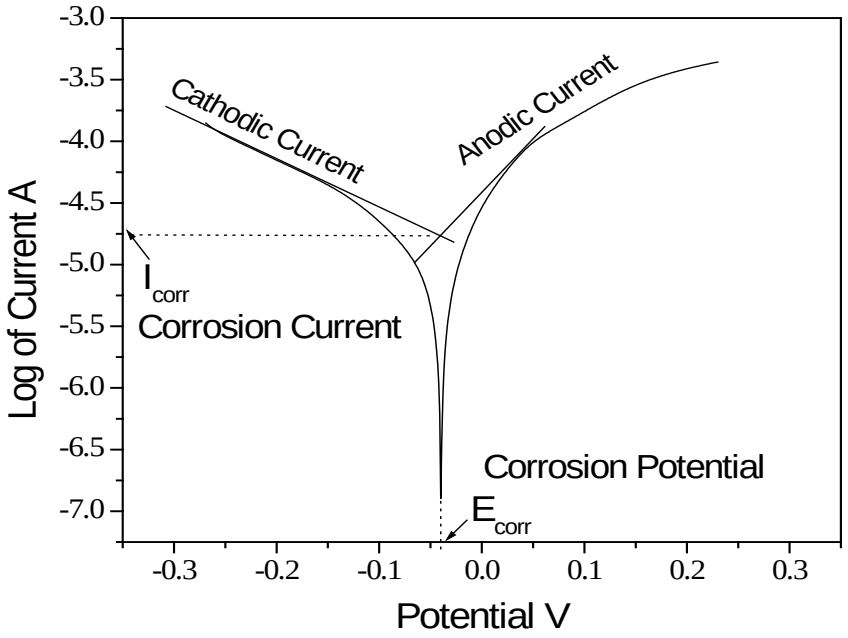

Figure 1-3 (a): A typical Tafel plot of Cu electrode shows E_{corr}, I_{corr}, cathodic curve, and anodic curve.

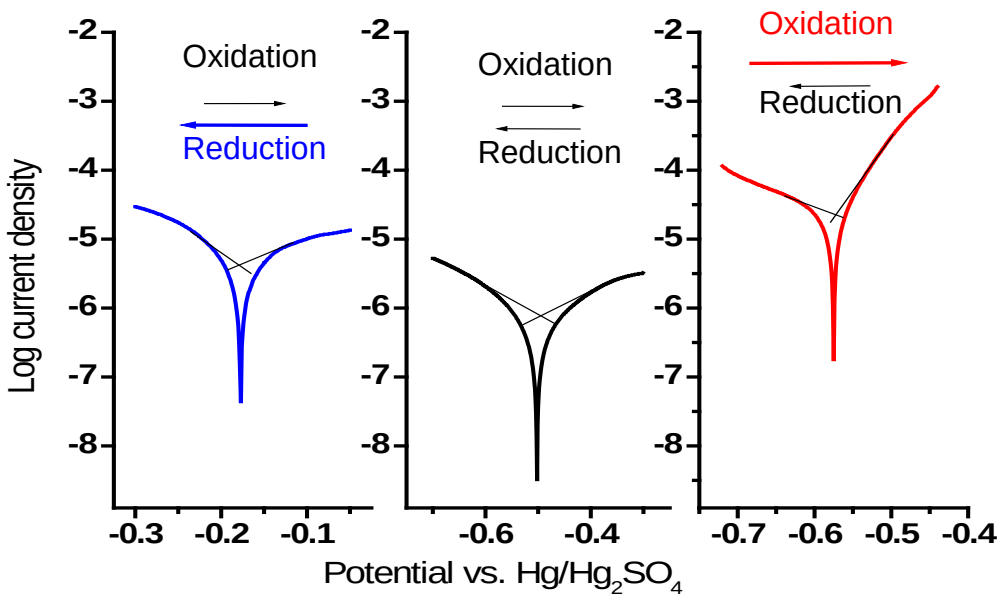

Figure 1-3 (b) Tafel plots of different reaction tendency.

1.1.7 Electrochemical Quartz Crystal Microbalance (EQCM)

The electrochemical quartz crystal microbalance (EQCM) is the analytical technique which combines the electrochemical techniques with the QCM sensor as shown in Figure 1-4. The QCM is a piezoelectric device that is equipped with alpha quartz crystals sandwiched between two metal electrodes which create an electric bias across the quartz crystal as shown in Figure 1-5. With the electric field, the vibrational motion of the crystal at its resonant frequency is sensitive to mass changes on its electrodes. Hence, the EQCM can reveal detailed information about adsorption or desorption process on electrode surface with mass changes during examining redox reactions or chemical processes. The EQCM is capable to measure the minute mass difference in nano-gram range

which allows detecting the monolayer or sub-monolayer films on its electrode [5].

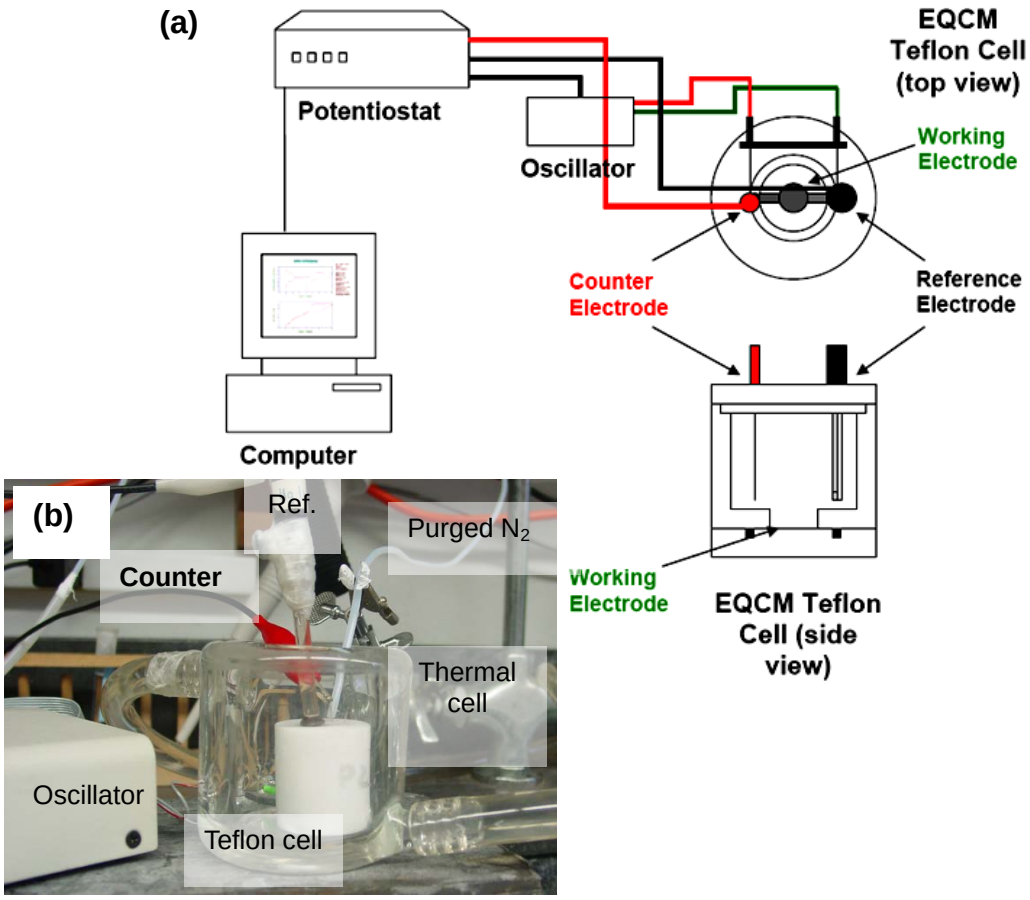

Figure 1-4 (a) the scheme of EQCM system. (b) EQCM set up.

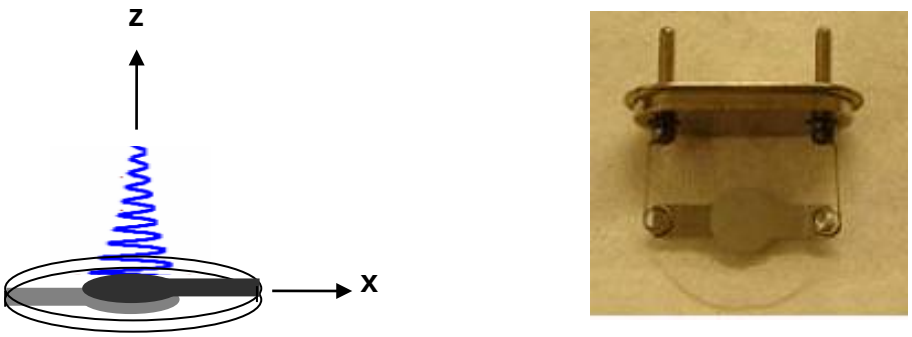

Figure 1-5: Thin quartz crystal sandwiched between two metal electrodes.

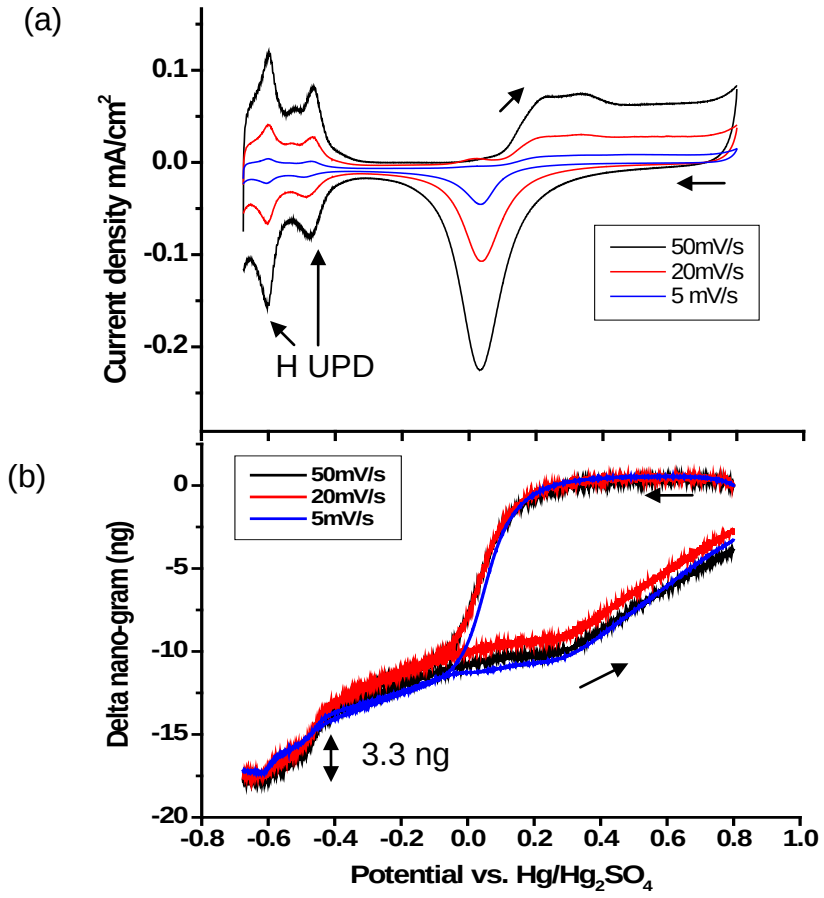

Figure 1-6 The EQCM of Pt electrode (a) CVs of different scan rate in 0.5 M sulfuric acid (b) mass difference corresponds to CVs in (a).

The EQCM has been used in various electrochemical systems involving mass changes on electrodes, including the underpotential deposition (UPD) of metals, mass changes in polymer films during redox processes, synthetic gene delivery system [6] and biosensors [7-9]. In Figure 1-6 shows a typical the EQCM result of CVs with and mass response on Pt electrode in 0.5 M sulfuric acid. The mass difference in hydrogen UPD area (0.205cm^2) is *ca.* 3.3 ng which provides the surface roughness *ca.* 1.39 which means the theoretical exposure area is slightly

larger than calculated geometry area. Also, the hydrogen UPD on Pt surface does not depend on scan rate of potential because the mass spectra overlapped even with different scan rate. The EQCM technique has become increasingly important in the development of integrated circuits (IC) industry as wells as lab-on-a-chip total analytical systems like the growth of Cu UPD on seedless diffusion barriers. Also, the EQCM can be applied into the absorption or desorption of inhibitors in the study of corrosion inhibition under corrosive environments such as chemical mechanical plarnarization (CMP) and post-CMP environments for IC chips fabrications.

1.1.8 Rotating Ring Disk Electrode system (RRDE)

A rotating ring – disk electrode (RRDE) can be used as a double hydrodynamic working electrode in a three electrode system [10]. The working electrode rotates during experiments creating a flux of electrolyte flow to the electrode. The continuous conversion of reactant to product requires the steady supply of reactant to the electrode surface and the removal of product. The RRDE working electrodes are usually used in electrochemical studies when investigating reaction mechanisms related to redox chemistry that involve the transfer of electrons across the interface between a solid and an adjacent solution phase.

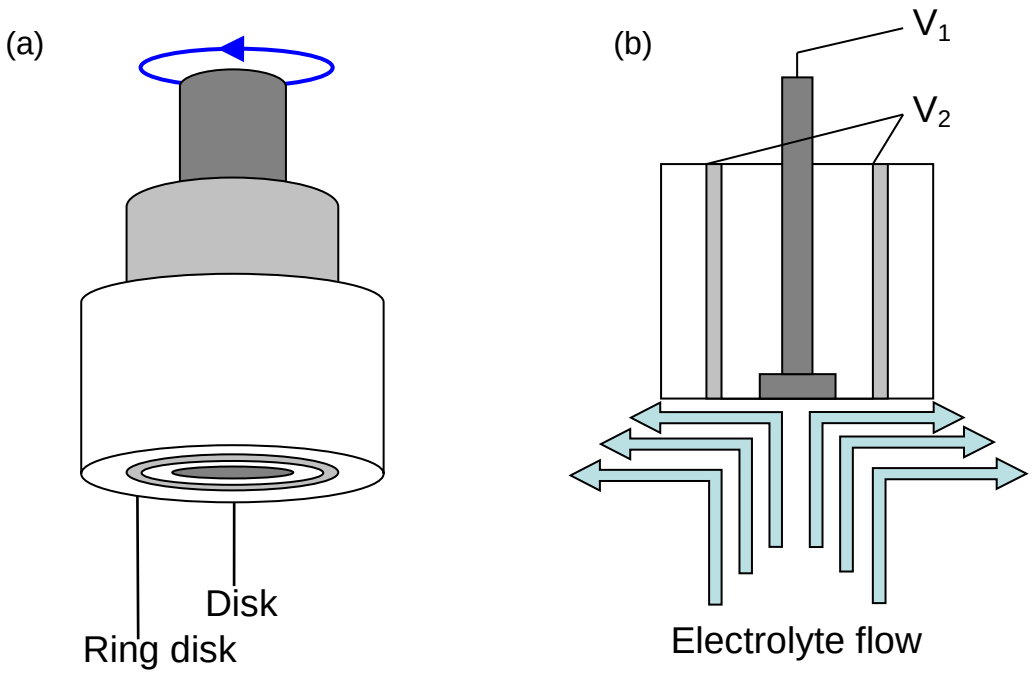

Figure 1-7 (a) the structure of RRDE and (b) the flow pattern of electrolyte while rotating the RRDE.

A rotating ring-disk electrode (RRDE) is encased by an insulating sheath of substantially larger diameter (Figure 1-7a). The structure is rotated about an axis perpendicular to the surface of the disc electrode [10]. In addition, mass transport usually dominates the reaction rate when solutions are diluted. The supply and removal of reactant and product can be affected by three mass transport processes which are diffusion, convection, and migration. A RRDE is a device that creates a flow pattern (Figure 1-7b) where the mass transport of the species is almost completely due to convection [11]. For instance, Figure 1-8 demonstrates the RRDE system in 0.05 M $K_3Fe(CN)_6$ + 0.1 M KCl. The ring electrode was held at 0.33V to re-oxidize the $Fe(CN)_6^{4-}$ which was reduced from

center disk during linear sweep voltammetry (LSV) from 0.4V to -0.1V. Based on the ratio of current between ring and center disk, the collection efficiency, N_{eff}, is different according to different rotating speeds. For instance, the N_{eff} is 15% at 900 rpm, and 25.7% at 100 rpm. The RRDE is used in chapter 6 for the study of oxygen reduction reaction (ORR) by characterizing the cathodic catalysts in proton exchange membrane fuel cell (PEMFC).

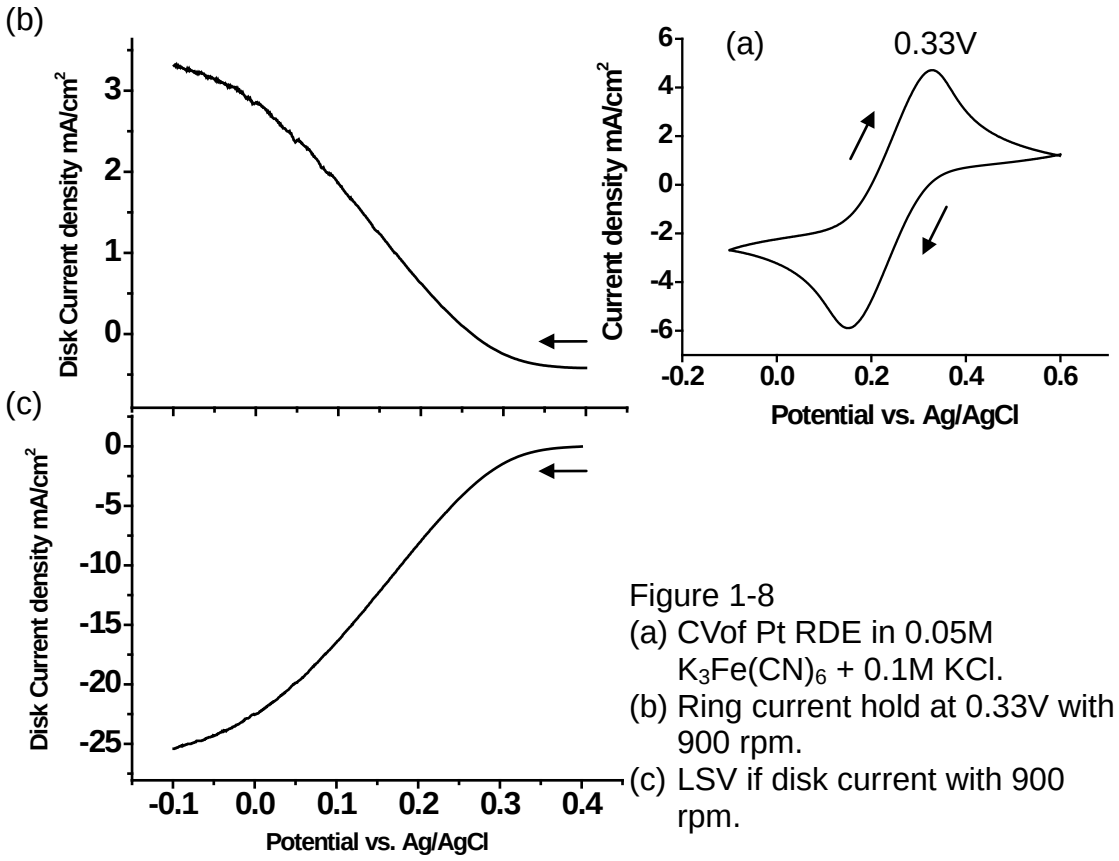

Figure 1-8
(a) CVof Pt RDE in 0.05M $K_3Fe(CN)_6$ + 0.1M KCl.
(b) Ring current hold at 0.33V with 900 rpm.
(c) LSV if disk current with 900 rpm.

1.1.9 Spectroelectrochemistry

Spectroelectrochemical (SEC) method deals with the measurement of spectroscopic transformation activated by electrochemistry. An electrochemical

system investigates the charge transport mechanism at a boundary of two phases, mainly electrolyte/solid interface [12]. On the other hand, spectroscopic methods often focus on bulk optical properties of different materials [13]. In situ methods in electrochemical studies can offer information of the kinetic data on electrode reactions and quantitative information for electrochemical characterization such as complex redox reactions, electron transfer processes, current, charge, and potential.

Currently, two different SEC cells are applied in a conventional UV/Vis spectrometer [14]. One is optically transparent electrochemical (OTE) cell and the other is long optical path thin layer (LOPTL) cell. The OTE cell should have lower absorption coefficient than the absorption of the products being investigated. The LOPTL cell has longer optical path than OTE cell, therefore, electrochemically generated products of the lower absorption coefficients can be measured.

In chapter 6, the SEC method combines the pH indicator with the UV-Visible spectrometer to measure the proton concentration variation that can directly relate to the proton consumption or hydroxide generation caused by oxygen reduction reaction (ORR). Therefore, the ORR causes the pH indicator to change color which represents increasing absorbance in UV-Vis spectra. The enhanced relative absorbance indicates the better ORR catalysts. The operational scheme is shown in Figure 1-9.

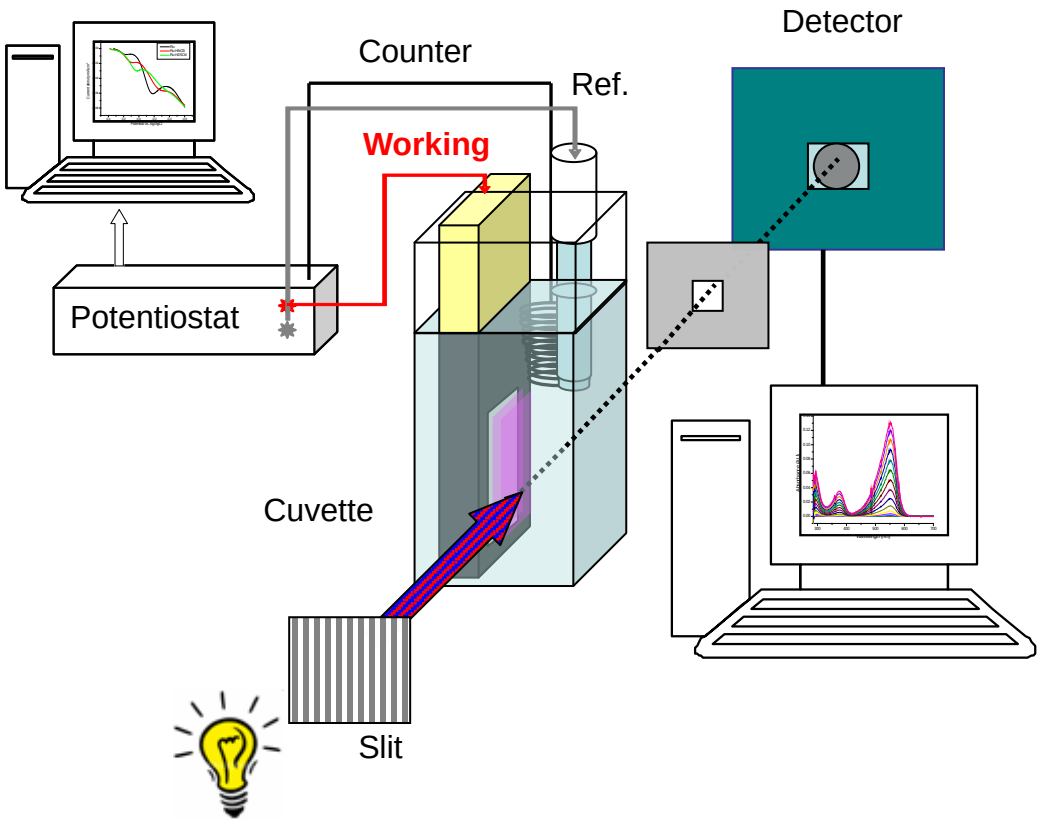

Figure 1-9: Scheme of spectroelectrochemistry.

1.2 Thin Film Deposition

Thin film is a relative term for deposition. The most deposition techniques control layer thickness under micrometer range. The deposition techniques are separated into two broad categories, one is chemical deposition and the other is physical deposition. The chemical depositions are usually conformal film whereas the physical depositions are commonly directional rather than conformal.

1.2.1 Chemical Deposition

Chemical depositions indicate the process is primarily chemical reaction

during the deposition such as electroplating and chemical vapor deposition (CVD). The electroplating is a plating process where metal ions in aqueous are deposited on conductive substrate by an electric field. The electroplating has been done for hundred years, but it is still critical for modern technology.

The CVD requires volatile precursor to react or decompose on the substrate surface. During the chemical deposition, the gas-phase by-products are produced which are removed by gas flow through the reaction chamber. Atomic layer deposition (ALD) is similar to the CVD. But, the ALD is a self-limiting thin film deposition. The precursor reacts with a surface one-at-a-time in a sequential manner. By exposing the precursors to the surface repeatedly, atomic layer control of film growth rate can be obtained as fine as ~0.1 Å (10 pm) per monolayer. Recently, there has been a rapidly growing interest in ALD of materials used in microfabrication processes, especially in integrated circuits (ICs) [15, 16].

1.2.2 Physical Deposition

The physical deposition usually operates under a vacuum environment to assure the particles can travel freely to form a solid layer on a cooler substrate like formation of frost. The varying techniques of PVD are divined by the method of producing the particles from an evaporant or a target. For instance, the magnetron sputtering system uses magnetic field to attract argon plasma to bombard the target, which sputters a cluster of few atoms from the target onto a

substrate. It is a fast deposition technique and also provides a good thickness control. In Figure 1-10, the desk pro dual magnetron sputtering system (Denton Vacuum LLC.) is capable to deposit thin film of multi-layers or alloys. This sputtering system is equipped with a direct current (DC) power and a radio frequency (RF) power magnetron guns. The high radio frequency corresponds to the alternating currents, which allows sputtering of insulating material even in air ambient. Hence, the magnetic field can be generated on insulating target and sputter-deposit insulating materials like Si by using RF power source. The thin film techniques of CVD, ALD, electroplating and PVD are used in this dissertation.

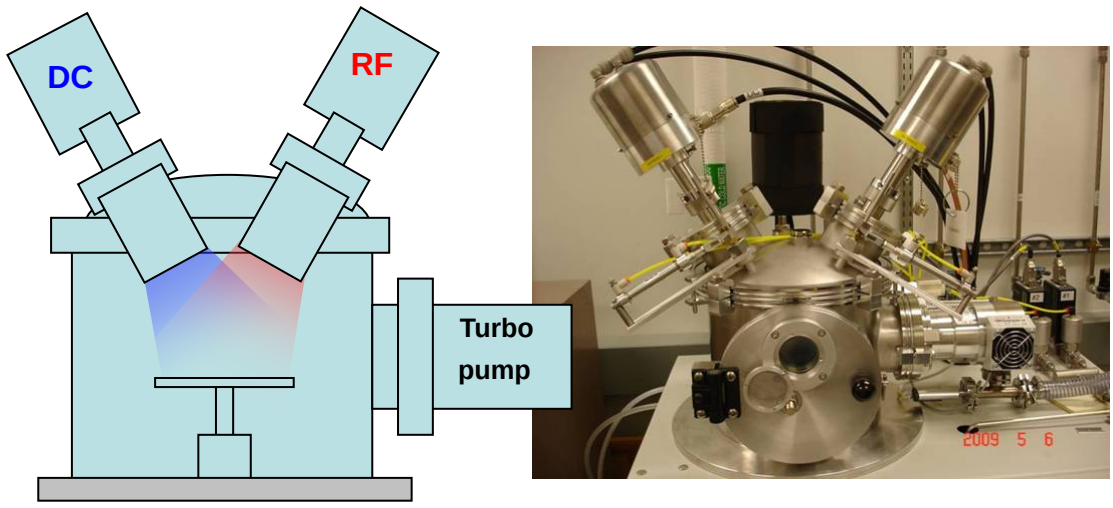

Figure 1-10: Dual magnetron gun sputtering system.

1.3 Surface Analysis Techniques

Surface analysis techniques such as AES (auger electron spectroscopy), XPS (X-ray photoelectron spectroscopy) also known as ESCA (electron

spectroscopy for chemical analysis), are used to characterize the elemental composition, surface chemistry and elemental distribution in concerned region (*ca.* 1 to 10nm). Moreover, the information from a thicker region of the specimen is also capable to be obtained by using depth profiling techniques which aimed a high energy ion (generally between 500 and 5,000 eV) to bombard material off the sample surface and the consequent freshly exposed surface is then analyzed. Techniques are important which can analyze the surface chemical and physical state and clarify it from that of the underlying solid [17]. Some of fundamental techniques are used in this dissertation which will be introduced in the subsequent sections.

1.3.1 X-ray Photoelectron Spectroscopy

X-ray photoelectron spectroscopy (XPS) is a technique which is widely used in the field of surface science [18]. The X-ray photon energy (E = hv) is the product of Planck's constant (h = 6.623 x 10^{-34} joules · second) with the frequency of the X-ray radiation (v). The X-ray photoemission was generated by bombarding a core electron in a target element like Al or Mg. There is photoemission onto the specimen surface if the core electron is able to overcome the binding energy (E_B). Since emitted photoelectrons must travel a relatively long distance to the detector, XPS is under ultra high vacuum (UHV; < 10^{-9} torr) to avoid losing the photoelectron through collisions on its way to the electron energy analyzer. Consequently, the XPS signal counts were collected by the

electron detector. The energy of the photoelectron E_k is related to the atomic and molecular chemical environment where it is emitted. So, XPS can provide qualitative and quantitative information on nearly all elements present on a very top specimen (except H and He) within 7 to 10 nm depth. Photoemission may be viewed such that:

$$E_B = hv - E_k$$

Where E_B is the binding energy of the electron needed to escape the vacuum energy level where the atom cannot exert influence on the electron. E_k is the kinetic energy of the emitted electron [19]. The emitted photoelectrons are channeled through an electrostatic hemispherical electron energy analyzer onto a large area detector that is measured. The hemispherical analyzer establishes an electrostatic field to allow only those electrons of a given pass energy to arrive onto the detector itself [20].

Since the X-ray photon energy (hv) and E_k are known, E_B can be calculated. The binding energy also provides important information about the bonding characteristics of the environment. A chemical shift towards lower binding energy would be seen if a chemical element was to be in an electron-donating environment whereas the higher binding energy would be observed when an element was in oxidation state.

The X-ray photoelectron spectroscopy was accomplished using a PHI 5000Versa Probe™ Scanning XPS as shown in Figure 1-11. A standard Al-K_α X-ray source at 280 watts and electrostatic analysis in constant pass energy mode

of 114.7eV for survey scans and 23.5 eV for detail scans. The Versa Probe scanning XPS provides a highly focused monochromatic X-ray beam, (10μm to 100μm) which can precisely focus on the concerned region even mapping the chemical composition by scanning X-ray beam. A 100V to 5kV differentially pumped Ar ion gun with regulated leak valve is available for specimen cleaning and sputter depth profiling with monolayer resolution. Also, the Ar ion gun is used to neutralize the insulating materials to prevent the electronic field from emitting photoelectron on local area during the X-ray irradiation. In this dissertation, the XPS was utilized in several chapters to characterize metallic copper, Cu(I) oxide and Cu(II) oxide while exposing to different chemical environments.

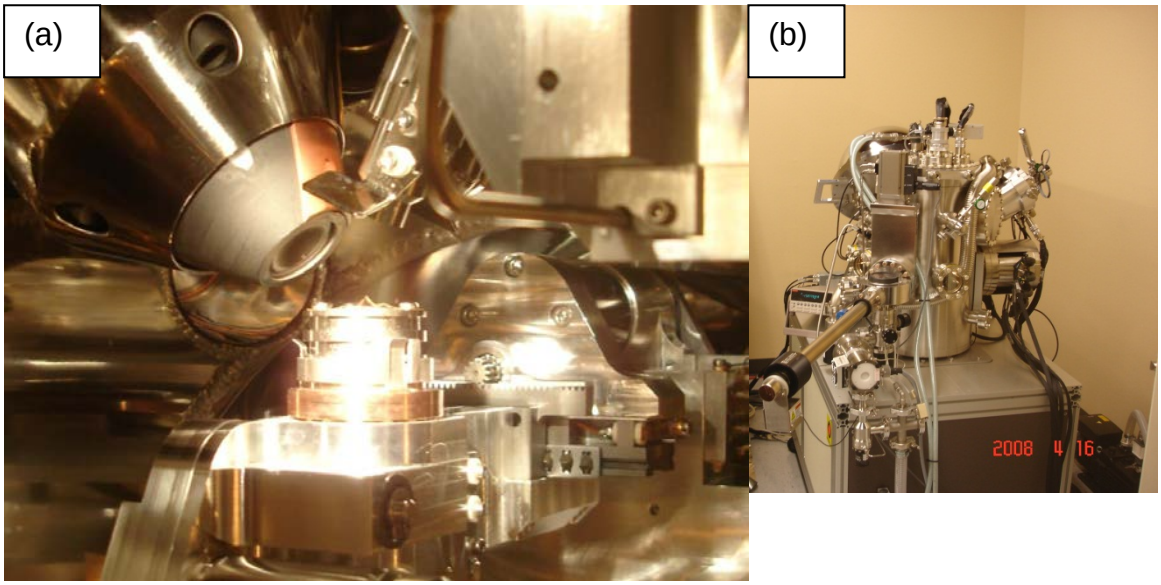

Figure 1-11 (a) XPS chamber in (b) PHI 5000VersaProbe™ Scanning XPS.

1.3.2 X-Ray Diffraction (XRD)

XRD is a valuable technique to obtain information about the

crystallographic structure, chemical composition, and physical properties of materials and thin film. Since W. L. Bragg (1913) was first to show the scattered intensity which leads to diffraction can be equally visualized as if the X-ray were reflecting from the imaginary planes defined by Miller indices. Bragg's law is given:

$$n\lambda = 2d \sin\theta$$

Where n is an integer, λ is the wavelength of incident wave, d is the distance between the planes in atomic lattice, and the θ is the angle between the incident X-ray and the scattering planes.

A thin film has small grain size where scattering planes are gathered with couple of atoms. The thin film diffraction required a low grazing incidence X-ray which allows characterizing the crystallographic structure and preferred orientation of substrate-anchored thin films. In Figure 1-12, the low grazing incident thin film XRD (Rigaku Ultima III high resolution X-ray diffraction) was used to characterize the Ru crystalline structure and its grain size after electrochemical oxidation or thermal oxidation. The tube source was operated using Cu Kα radiation, which emits x-rays with wavelengths of 1.542 Å at 40kV and 30 mA. The scan rate was 4°/min.

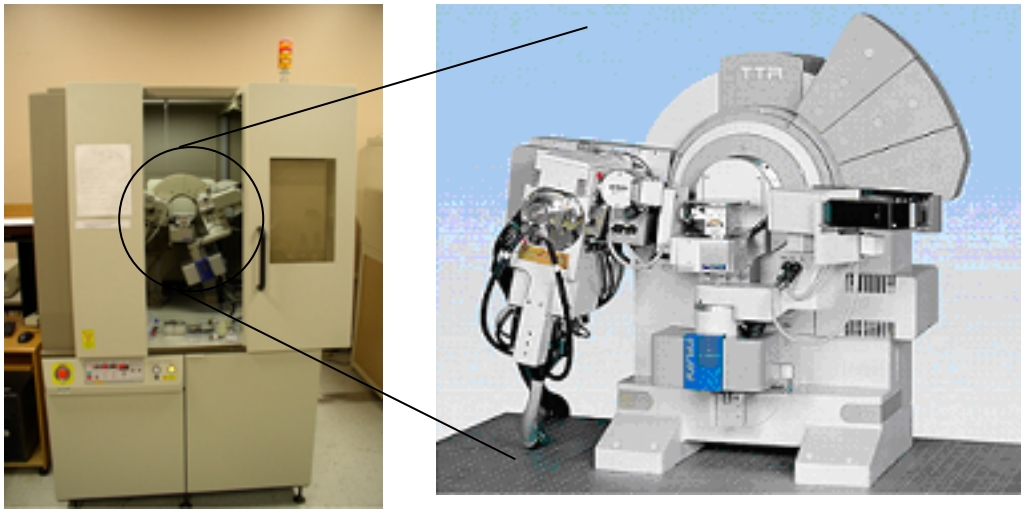

Figure 1-12: the Rigaku Ultima III high resolution X-ray diffraction (XRD)

1.4 Surface Microscope

1.4.1 Atomic Force Microscopy (AFM)

Atomic force microscopy (AFM), a very high-resolution type of scanning probe microscopy, was developed by Binnig, Quate and Gerber in 1986. The AFM is one of the leading tools for 3D-imaging, measuring and manipulating matters at nanoscale which is 1000 times better than the optical diffraction limit. Unlike scanning tunneling microscopy (STM), AFM does not need a conducting sample [23-24]. The surface information is obtained by scanning the surface with a mechanical probe which consists of a cantilever with a sharp needle-like tip at its end. The cantilever is typically made by silicon or silicon nitride with a tip radius of curvature on the order of nanometers. Piezoelectric elements that facilitate tiny but accurate and precise movements on (electronic) command enable the very precise scanning. When the tip is moved close to a sample

surface, forces between the tip and the sample resulted in a deflection of the cantilever according to Hooke's law. It works as a spring to keep the tip against the surface when moving back and forth. Topographic images of sample are produced by mapping the tip movement. A fixed laser beam points on the top of the tip and reflected to a photodiode sensor to measure the movement of the tip. By combining the tip Z direction movement with X and Y movements of piezoelectric stage, the 3-D topographic images of sample are produced. Also, a feed-back regulator responds to the changes of the path by activating a piezoelectric control, which adjusts the height of sample to balance the force between tip and surface to prevent the tip damage during scanning.

AFM imaging modes are divided into contact (also called static) modes and a non-contact (or variety of dynamic) modes where the cantilever is vibrated. From the beginning, AFM was designed as a contact mode. However, it is difficult to obtain a good image for a soft surface or a surface under liquid. Non-contact mode AFM was invented by Martin et al. [25] to solve those problems. In non-contact mode, the AFM tip should vibrate close to the sample surface with low energy. The applied force of tip is in the 0.1 to 1 nano-Newton range, which is significantly lower than the force applied by the contact mode. In Figure 1-13, Nanoscope III Scanning Probe Microscope Multi-Mode® system (Veeco Inc.) is used to provide us surface information of Ru PVD thin film.

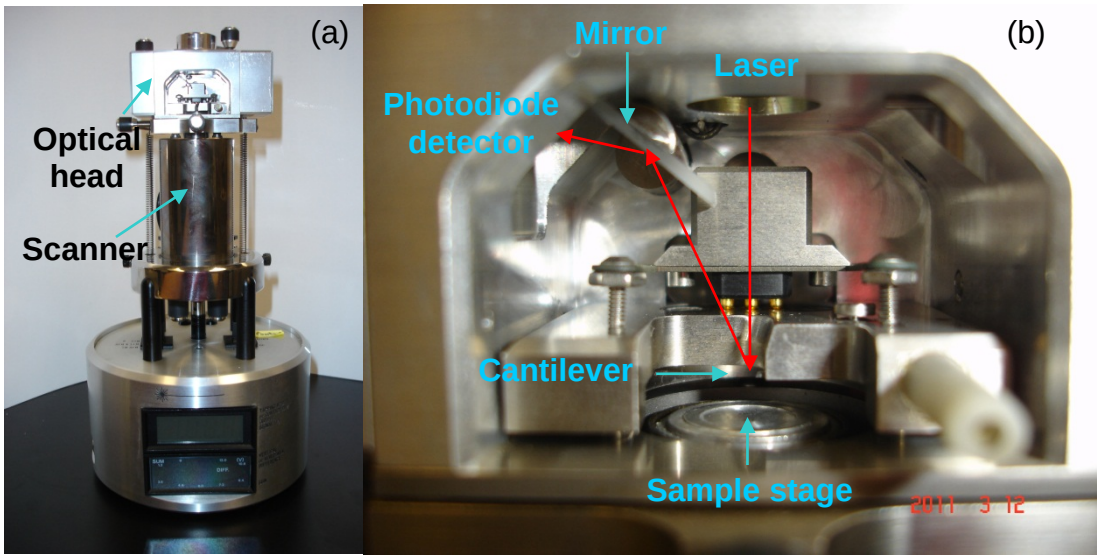

Figure 1-13 (a) Nanoscope III SPM multimode system.
(b) Close view of optical head.

1.4.2 Transmission Electron Microscopy (TEM)

The transmission electron microscope (TEM) operates on the same basic principles as a slide projector which images the structures and objects on the slide and magnifies those onto the viewing screen. But, TEMs use electrons instead of light source. The TEM has better resolution than light microscope because TEM use electrons as “light source” which has lower wavelength (ca. 6 pm with 200 KeV) than the wavelength of light (400-700nm). Therefore, the resolution from TEM is a thousand times better than from light microscope, which means the objects can be obtained in the order of a few angstroms (10^{-10}m). The A fluorescent screen is used as an image device and a detected sensor CCD device is equipped to save the images.

Another associated technique of scanning transmission electron microscopy (STEM) can visualize the atoms with Z-contrast images by high–angle annular

dark-field (HAADF) detector [26]. During the electron scanning, the electrons are allowed to pass through the center of the annular detector to a detector of electron energy loss spectroscopy (EELS). Also, the energy dispersive X-ray (EDX) is produced by refilling electron vacancy of core orbital which is kicked out by probing electron beam. The EELS and EDX are complementary to each other just like IR and Raman spectroscopy. The EELS trends to work best at relatively lower atomic numbers comparing with the EDX [27, 28]. Therefore, the TEM is capable to study small details in the cell or different materials down to near atomic levels in both medical, biological and materials research [29, 30]. In Figure 1-14 (a) shows the TEM instrument (FEI Tecnai G2 F20 S-Twin 200keV field emission scanning transmission electron microscope), and the Figure 1-14 (b) shows TEM image of Pt thin film made by PVD sputter deposition. The techniques of STEM, HRTEM, and EDX were used to characterize the Ru thin film. Also, the selected area diffraction (SAD) of polycrystalline or single crystalline gives spot patterns as shown in Figure 1-15(a). The SAD of nanocrystalline provides ring patterns (Figure 1-15b) which can be used to identify texture or nanocrystalline from amorphous phases.

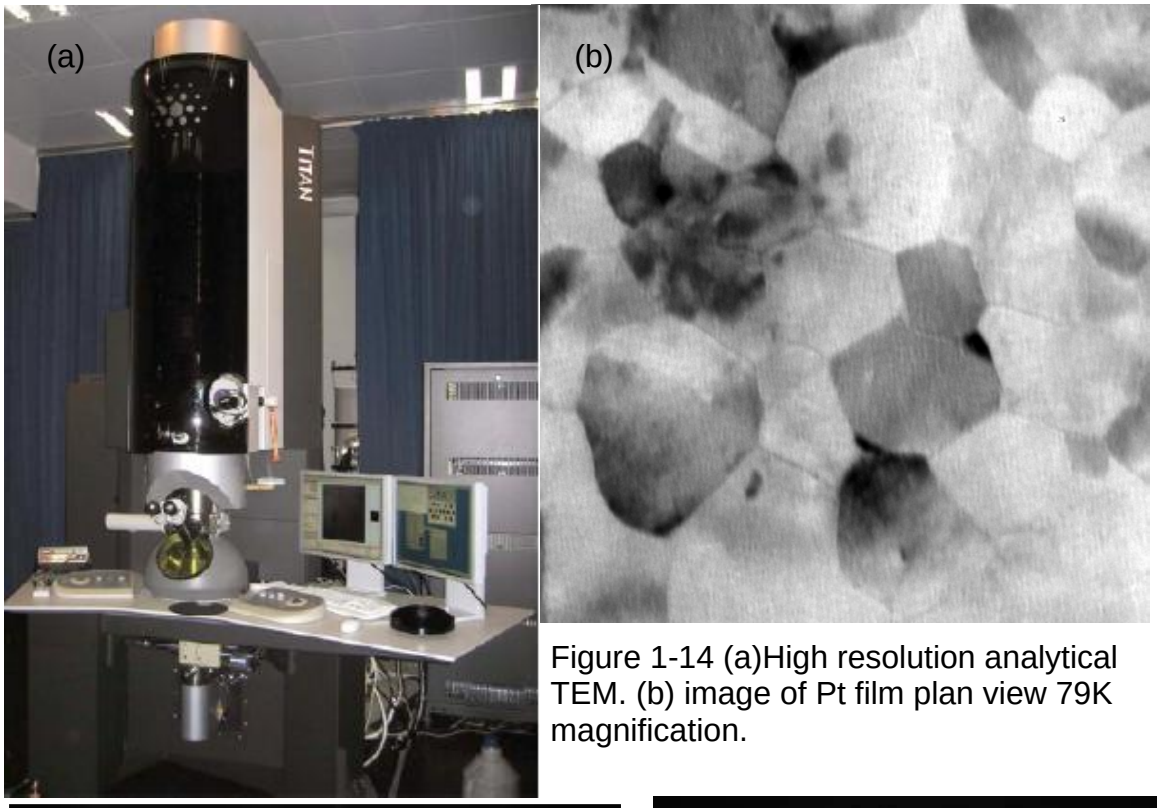

Figure 1-14 (a)High resolution analytical TEM. (b) image of Pt film plan view 79K magnification.

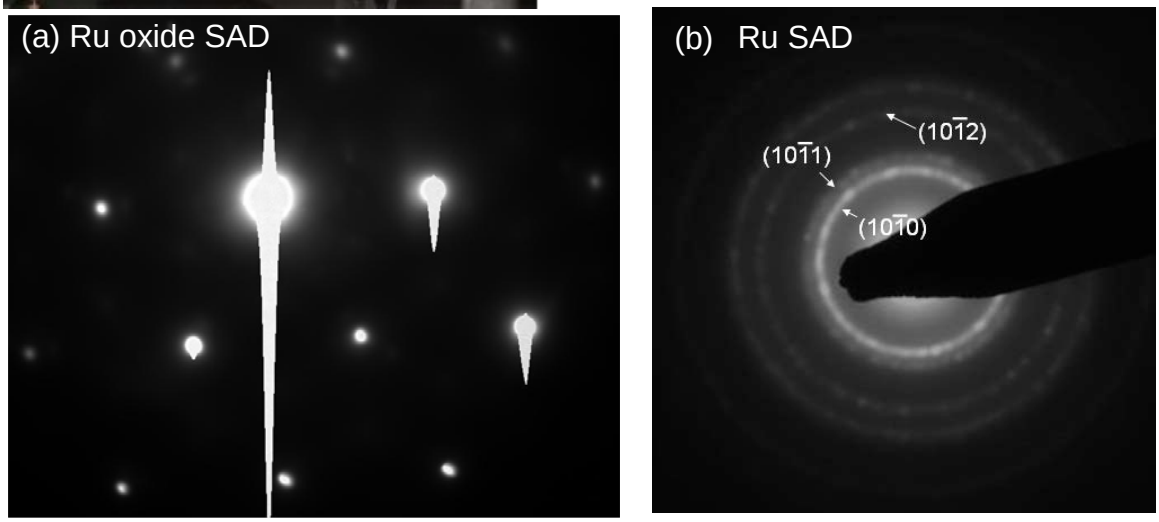

Figure 1-15 (a) SAD pattern of Ru single crystal and (b) SAD pattern of Ru plain view.

1.5 Nuclear Magnetic Resonance (NMR)

Nuclear magnetic resonance is a an invaluable technique that utilizes the

magnetic properties of certain nuclei which includes isotopes that contain an odd number of protons and neutrons such as ^{1}H and ^{13}C. NMR spectra are the most important characterization tool for the organic chemist. The NMR spectroscopy is a very useful analytical method because several types of information can be obtained from an NMR spectrum like using infrared spectroscopy (IR) to identify functional groups. By analysis of a NMR spectrum, it gives information on the number and type of chemical entities in a molecule. However, NMR provides much more chemical structural information than IR.

The NMR spectroscopy can be used to study mixtures of analytes, to understand dynamic effects such as change in temperature and reaction mechanisms. The NMR can be applied to a wide variety of samples, both in the solution and the solid state. In chapter 5, the structure of gallic acid was characterized by ^{1}H and ^{13}C NMR spectra which were recorded by a Varian VXR-500 spectrometer at 500 MHz and 125 MHz, respectively.

1.6 References

1 Rieger, Philip H. *Electrochemistry*; Chapman & Hall: New York, 1994; Chapter 1. p 3.

2. *Laboratory Techniques in Electroanalytical Chemistry,* 2nd ed., rev. and expanded,; Kissinger, Peter T. Ed.; Heineman, William R.Ed.; Marcel Dekker.: New York, 1996; Chapter 2.

3. Skoog; West; Holler; *Fundamentals of analytical chemistry*, Eighth ed.; Thomson: Belmont, 2002; Chapter 1, p 25.
4. Faulkner, Larry R. *Journal of Chemical Education*. **1983,** 60(4), 262.
5. Bard, A. J.; Faulkner, L. R. Electrochemical Methods: fundamentals and applications. 2nd ed, John Wiley and Sons: New York, 2001, pp 725
6. Jiang, M.; Ray, W. W.; Mukherjee, B.; Wang, J. *Electrochem. Comm.* **2004,** 6, 576-582.
7. Marx, K.A., et al. *Biosensors and Bioelectronics* **2001**, 16, 773-782.
8. Tenreiro, A.; Cordas, C. M.; Abrantes, L. M. Portugaliae *Electrochim. Acta* **2003,** 21(4), 361-370.
9. Deakin, M.R.; Buttry, D. A. *Anal. Chem.* **1989,** 61(20), 1147A-1154A
10. Bard, A.J.; Faulkner, L.R. *Electrochemical Methods: Fundamentals and Applications*, 2nd ed.; John Wiley & Sons, New York, 2000
11. J. Nikolic, E. Expósito, J. Iniesta, J. González-García, and V. Montiel, *Journal of Chemical Education*, **2000,** 77(9)
12. W. Forker, *Electrochemische Kinetik, 2. Aufl.* Akademie-Verlag, Berlin, 1989
13. L. Dunsch, Habil.-schr., TU Dresden, Dresden, 1996
14. W. Plieth, G. S. Wilson and C. Gutierrez De La Fe, *Pur & Appl. Chem.*, **1998,** 70, 1395
15. T. Suntola, Handbook of Crystal Growth, Vol. 3, D. T. J. Hurle, Ed.; Chap. 14, *Elsevier Science* B. V., Amsterdam 1994.
16. M. Leskela and M. Ritala, *Thin Solid Films*, **2002,** 409, 138.

17. J.M Walls, *Methods of Surface analysis*, Printed In Great Britain at the University Press, Cambridge, 1989.
18. Jone F. Watts and John Wolstenholme, *An introduction to surface analysis by XPS and AES*; Wiley: New York, 2003.
19. Ebel, M.F., Absolute calibration of an X-Ray photoelectron Spectrometer, *Journal of Electron Spectroscopy and Related Phenomena*, **1976,** 8, 213.
20. Vickerman, J. C. *Surface Analysis - The Principal Techniques*; John Wiley & Sons: New York, 1997.
21. Wagner, C. D.; Riggs, W. M.; Davis, L. E.; Moulder, J. F. *Handbook of X-ray Photoelectron Spectroscopy*; Physical Electronics: Eden Prarie, MN, 1995.
22. Azároff, L. V.; R. Kaplow, N. Kato, R. J. Weiss, A. J. C. Wilson, R. A. Young. *X-ray diffraction*. McGraw-Hill, 1974.
23. Wickramashinghe, H. K. *Sci. Am*., **1989,** 98.
24. Pool, R. *Science*, **1990,** 247, 634.
25. Martin, Y.; Wichramasinghe, H. K. *Appl. Phys. Lett*. **1987**, 50, 1455
26. DE Jesson and SJ Pennycook. *Proc. Roy. Soc. A,* **1995,** 449: 273.
27. Ahn C. C., *Transmission electron energy loss spectrometry in material science and the EELS Atlas*, Wiley, Weinheim, Germany, 2004.
28. R. F. Egerton, *Electron Energy Loss Spectroscopy in the Electron Microscope*, 2nd ed., Plenum, New York, 1996.
29. Ludwig Reimer, *Transmission Electron Microscopy*, Springer-Verlag: New York, 1993.

30. Andreas Rosenauer, *Transmission electron Microscopy of Semiconductor Nanostructures*, Springer: New York, 2002.

PART I

ELECTROCHEMICAL CHARACTERIZATION OF COPPER PLATING ON RUTHENIUM-BASED SUBSTRATES

CHAPTER 2

ELECTRODEPOSITION COPPER ON RUTHENIUM-BASED SUBSTRATES

2.1 Introduction to Cu Interconnects and Diffusion Barriers

In the microelectronic industry, Ta/TaN or TiN/Ti has been the material of choice for copper diffusion barrier [1-4]. Since the adherence of Ta alone is poor on SiO_2 dielectrics, TaN is commonly used as an adhesion layer. Recently, the the dimension of integrated circuit (IC) chip is being shrinked continuously to follow the Moore's law which states that the number of transistors in IC chip will be doubled approximately every eighteenth months [5]. Due to the scaling difficulty in case of Ta/TaN bilayer, extensive research are focused on finding new materials for copper diffusion barrier that can be used with only one layer. In Pt group metals, ruthenium has been studied to be one of the candidates for barrier materials. The properties such as high thermal and chemical stability, high electrical conductivity, high melting point and less solubility of Cu on Ru even at high temperatures makes Ru to be metal of choice for barrier applications. Also, electrochemical Cu underpotential deposition (UPD) on Ru, a phenomenon that demonstrates the strong interfacial binding between Ru and Cu plays a

significant role in Cu plateable diffusion barrier performance [6]. There is an increased interest on exploring Ru for barrier material because recently, an ultra thin Ru was proved to function as barrier layer that can be electroplated with Cu without the need of copper seed layer [7,8]. However, the effect of different treatments on Ru surface as the substrate for Cu deposition becomes increasingly more important. This chapter describes the study of Cu electrodeposition on the various Ru-related surfaces prepared from air exposed Ru surfaces, fresh polished Ru surface, electro-oxidized and reduced Ru surface, hydrogen plasma treated, and forming gas annealed Ru on Cu deposition. The characteristics of Ru surface and its influences on Cu plating were systematically studied.

2.2 Materials Preparation and Experimentation

For electrochemical experiments, Pt sheet is used as the counter electrode and saturated silver/silver chloride as reference electrode (Ag/AgCl 0.197V vs. SHE). All potential values are referred against Ag/AgCl reference electrode in this chapter. The three electrode electrochemical cell set up was connected to one of the 400, 440a and 760b series model electrochemical potentiostats from CHI (CHI instruments). In order to prepare 0.5 M sulfuric acid with 2mM copper sulfate electrolyte solution as plating bath for Cu, high purity (99.999%) copper sulfate pentahydrate was purchased from Aldrich® and all acids like sulfuric acid, nitric acid, perchloric acid, phosphoric acid, and hydrochloric acid were obtained

from Mallinckrodt Baker, Inc. Extra pure research grade hydrogen gas was purchased from AIR LIQUIDE. The purity of hydrogen gas is 99.9995%. The hydrogen gas is used for two purposes; as feeding gas in plasma system and as purging gas to purge the Cu plating bath in electrochemical analysis. Electrochemical reduction or oxidation of Ru electrode is achieved by applying negative or positive potential respectively. Ru electrode surface is reduced by applying cathodic potential at -0.4V in 0.5 M sulfuric acid and also oxidized by applying anodic potential at 1.3V in the same electrolyte. Beside electrochemical treatment, the Ru surface is cleaned by using the HARRICK PLASMA, plasma etcher. Plasma cleaning is a dry process for surface treatment and the surface is activated by plasma treatment with hydrogen gas.

Ruthenium (99.98% pure) was deposited on Ti (99.7% pure) pre-coated Si wafer by using magnetron sputtering physical vapor deposition (PVD) system (Desk Pro Denton Vacuum). Both Ti and Ru coating was deposited by DC power source. The cross sectional images of Ru wafer were obtained by using high-resolution transmission electron microscopy (HR-TEM). HR-TEM and scanning transmission electron microscopy (STEM)-energy dispersive X-ray (EDX) were performed by FEI Tecnai G2 F20 S-Twin 200keV (S/TEM) at Center for Advanced Research and Technology (CART). Atomic force microscopy (AFM) (Veeco® Nanoscope III) provides the 3D-topography of sputtering PVD Ru wafer.

2.3 Ruthenium Native Oxide Growth by Air Exposure

Ruthenium native oxide is formed naturally when exposed to air [9, 10]. The thin layer of native oxide is formed rapidly on a freshly polished Ru electrode surface. Therefore, the difference in Cu deposition on reduced Ru surface and surface with native oxide layer becomes a fundamental issue for Ru as the barrier material. In this study, OCP (open circuit potential) and CV (cyclic voltammogram) experiments are carried out to examine the formation of Ru native oxide

Ru native oxide can be electrochemically reduced by holding the Ru electrode at negative potential [6]. From the amount of charge consumed for the reduction reaction, the native oxide formation on Ru surface can be quantified. In order to maintain a reproducible Ru surface, the Ru electrode was polished once before the first air exposure experiment, then the air-exposed Ru shot was cleaned by electrochemical reduction (hold at -0.4V for 2 minutes) before each new air exposed run. After the air exposure, OCP value of air exposed Ru was measured and CV was recorded starting from OCP to -0.4V. Figure 2-1 shows CV of native oxide formed on Ru surface in sulfuric acid solution. It was observed that the oxide reduction charge is higher for the electrode exposed to air for longer time, which means that the coverage of Ru native oxide increases when the surface is exposed to atmosphere.

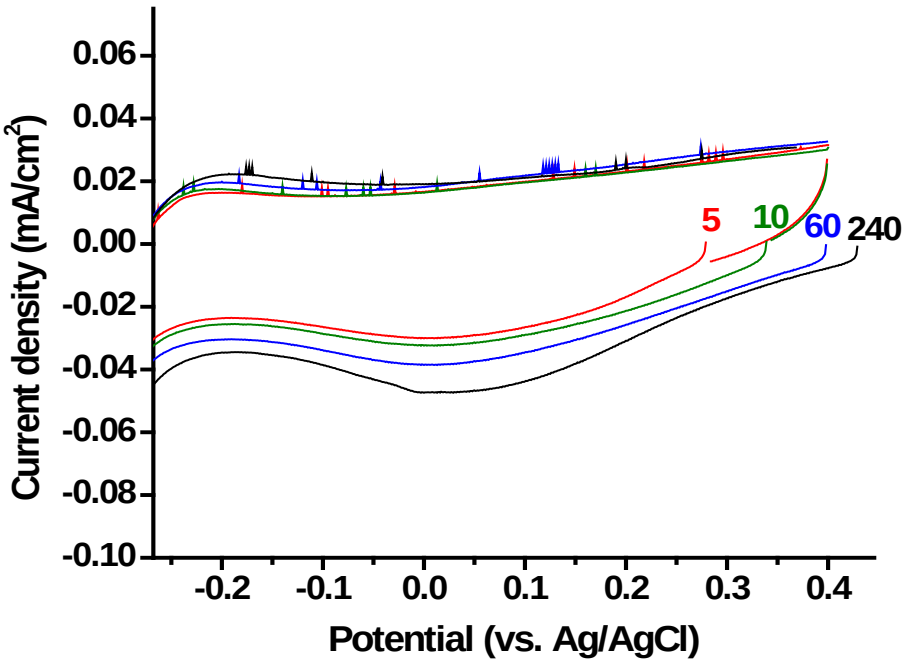

Figure 2-1 CVs of Ru electrode exposed to air for different times (5-240 min) in 0.5M H_2SO_4.

The CHI software has a program that enables to calculate the charge under the reduction or oxidation peak in cyclic voltammogram. Using that program, the charge under each native oxide reduction peak is obtained and plotted as shown in Figure 2-2. Both the oxide reduction charge and the OCP value reveal the state of the Ru surface. The OCP of air exposed, saturated Ru native oxide is found to be higher than that of electrochemically reduced surface. In the other words, the OCP value keeps increasing with the increase in native oxide layer thickness on the Ru surface. Figure 2.2 shows that the growth of native oxide on Ru will reach a saturation point in a time period of 3 hours.

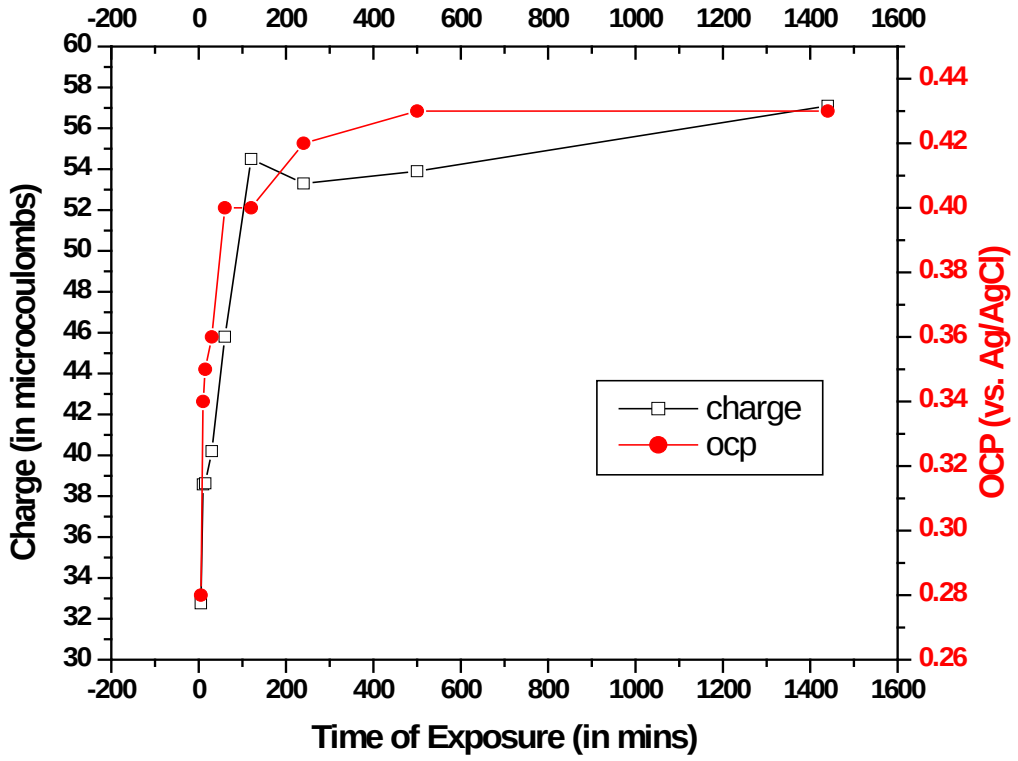

Figure 2-2 Native oxide reduction charge and OCP value vs. time of exposure.

2.4 The Effect of Ru Surface Conditions on Cu Electrodeposition

The effect of Ru surface nature on Cu electrodeposition is explored. The study is crucial since the native oxide will dominate the Ru/Cu interface before plating thin layer of Cu. In the following sections, experiments results are shown from the investigation of Cu underpotential deposition on Ru surfaces exposed to air for different time intervals. Before the experiment, the Ru shot electrode is well polished using fine polishing pad (≤1μm roughness). The smooth Ru surface is very important in order to calculate the correct geometric area of Ru surface. In the CV of Ru in Cu plating solution, the monolayer coverage of Cu on Ru

surface can be calculated from the Cu UPD stripping charge, from the formula given in Eq. 2-1

$$Monolayer\ (ML) = \frac{QN_a}{nFA(1.27x10^{15})} \qquad \text{Eq. 2-1}$$

Where,

Q – Charge of Cu UPD stripping (in coulombs)

N_a – Avogadro number ($6.022X10^{23}$)

n – Number of the electrons for Cu^{2+} reduction = 2

F – Faraday constant (96485 Coulomb/mole)

A – Geometric area (cm^2)

2.4.1 Effect of Ru native Oxide On Cu ECD

Figure 2-3 shows the CV of native oxide covered Ru in 2mM $CuSO_4$/0.5MH_2SO_4 solution. It was clearly observed that the copper UPD striping peak at 0.15V is decreasing when Ru electrode air exposure time is increasing. This is attributed to the fact that the continuous growth of Ru native oxide upon exposure to air results in increased coverage of oxygen atoms on the surface and thereby leaving only a lesser amount of fresh Ru for Cu first layer nucleation. In other words, the binding force between Cu atom and Ru native oxide surface is not as strong as Cu atom and oxide free Ru surface. Hence, the

presence of native oxide layer decreases the efficiency of both bulk and UPD Cu plating on Ru surface.

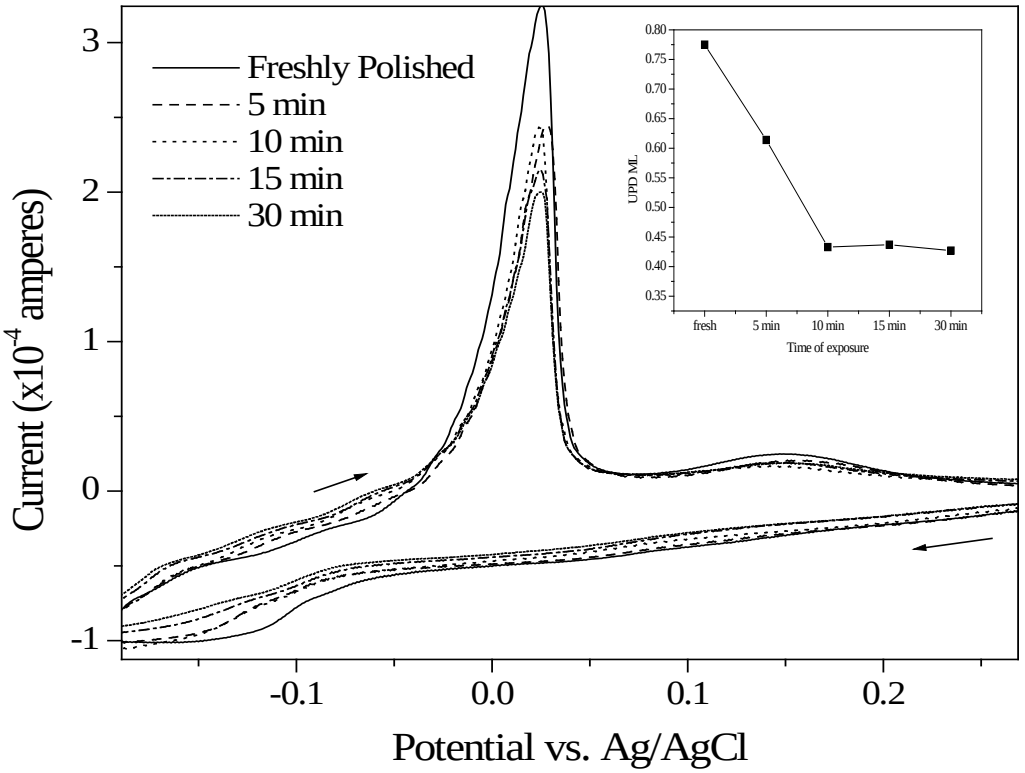

Figure 2-3 Cu electrodeposition on Ru surface in 2mM $CuSO_4$/0.5M H_2SO_4 at a scan rate of 20 mV/s. *Inset:* Cu UPD Monolayer (ML) coverage on Ru exposed to air for different time intervals.

2.4.2 Effect of Ru Electrochemical Oxide on Cu ECD

In the previous section, the Ru native oxide was shown to hinder the Cu deposition. In this section, Cu UPD results were obtained on electrochemically grown Ru oxide and compared to that of air exposed oxide. Ru oxide can be formed electrochemically by applying certain potential to oxidize surface of metal

electrode [11]. It was previously demonstrated that Ru oxide (RuO_xH_y) formed at 1.3V on fresh polished Ru surface are conductive and have strong binding with Cu [6, 12, 13]. Both of these Ru surfaces were found to have Cu UPD. Cu UPD growth was studied on Ru electrochemical oxide that was developed by applying different oxidizing potentials (0.55V, 0.65V, 0.85V, 0.95V, 1.1V, 1.2V and 1.3V vs. Ag/AgCl) for 30 seconds. Ru electrode surface was polished freshly before immersing it in sulfuric acid solution to grow electrochemical oxide. In figure 2-4, anodic bulk Cu stripping peak from first CV cycle from different electrochemical Ru oxide surfaces are shown. Both the peak current and charge associated with Cu bulk stripping decreases when the Ru oxidizing potential increases from 0.55V to 1.10V. However, the bulk striping peak current increases when Ru surface was oxidized over 1.10V.

Cu UPD measurements also show that oxidizing Ru electrode at 1.10V does change its surface nature in such a way to resist the Cu monolayer formation. Figure 2-5 shows the Cu UPD stripping peak obtained from the CV scan of Ru oxide prepared at different applied potentials. It was observed that the Cu monolayer growth decreases for increasing oxidation potential from 0.55 V and reaches a minimum value for 1.1 V oxidized Ru surface. The anodic bulk and UPD stripping peak charges are obtained by integrating area under the peak and plotted against Ru oxidation potentials (inserts in Figure 2.4 and 2.5). The V shape curve in both the Cu bulk and UPD stripping charges shown in the insets point out that the electrochemical Ru oxide formed at around 1.10V is likely a

transition state between reducible and irreducible oxides (RuO_xH_y).

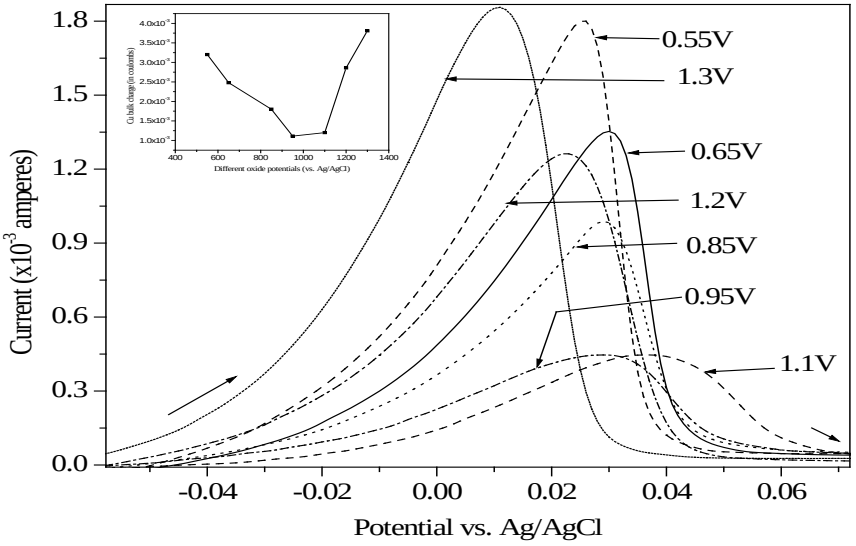

Figure 2-4 Anodic Cu bulk stripping on RuOx/Ru formed at various oxidizing potentials. *Insert*: Cu bulk charge vs. potential of RuOx/Ru. Oxide formed till 1.1 V affects Cu plating efficiency and > 1.2 V greatly improves the Cu plating characteristics.

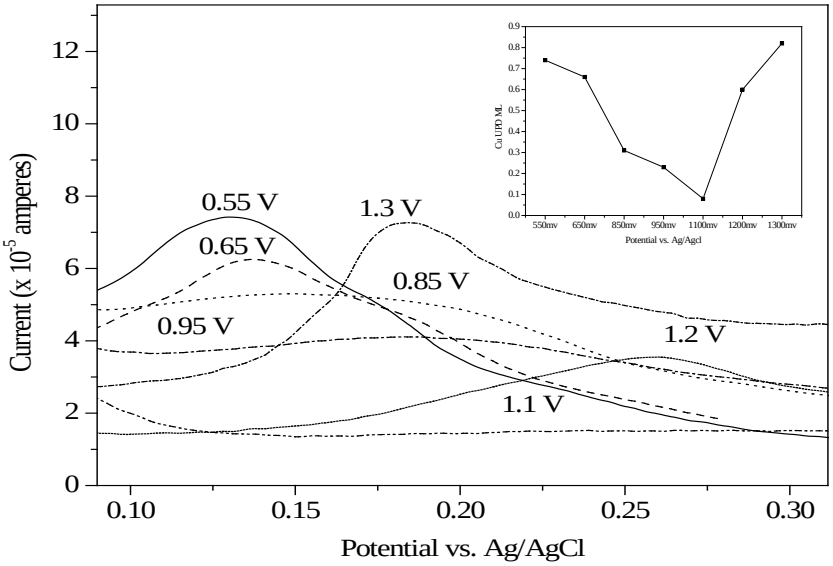

Figure 2-5 Cu UPD on RuO_x/Ru formed at various positive potentials as mentioned in the text. *Insert*: Cu UPD ML on RuO_x/Ru.

The ratio of bulk stripping charge to the bulk reduction charge will give information about Cu plating efficiency. From the bulk stripping charge (*insert*) obtained from Figure 2-4, the Cu plating efficiencies are calculated and found to be decreasing when the oxidized potential increases from freshly polished Ru surface to 0.55V to 1.10V oxidized surface. Furthermore, from the Cu UPD peak charge in Figure 2-5 (*insert*), the calculated monolayer values decrease from 0.75 to less than 0.1 when the oxidized potential increases from 0.55 V to 1.10 V. Comparing with air-exposed Ru oxide, which is saturated with Ru native oxides, its monolayer coverage of Cu UPD doesn't drop as much as it does on Ru electrochemical oxide prepared at potential 1.10 V. So, the oxidation potential at 1.10V can be the transition potential to form reducible to irreducible oxide on Ru surface. Figure 2-6 shows the CVs of progressive oxidation of Ru electrode in 0.5 M sulfuric acid. As the oxidizing potential increases, the oxide formed becomes harder to reduce and it takes more negative potential at the reverse scan to reduce it. When the oxidizing potential reaches higher than 1.10V, the reduction current of the oxide formed at this potential was not present in the reverse potential scan. This oxide formed at higher than 1.10V is irreducible and is labeled as hydrate Ru oxide (RuO_xH_y).

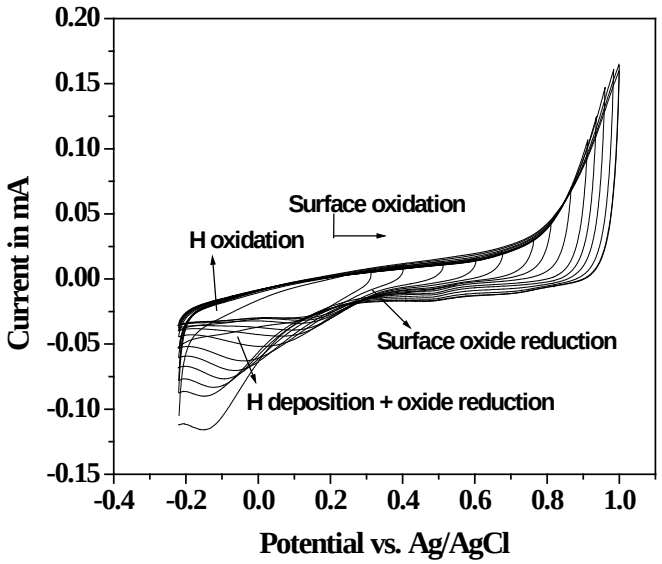

Figure 2-6 CV of progressing oxidation of Ru electrode in 0.5 M H_2SO_4 solution with scan rate 50mV/s.

2.5 The Study of Cu UPD by Using Electrochemical Quartz Crystal Microbalance (EQCM)

The adsorption and deposition of metal atoms on foreign metal substrates represents an interesting area of study because the strong adatom/substrate interfacial bonding can control the growth behavior and the resulting structures, especially as a function of surface coverage like UPD in electrochemistry. EQCM is particularly suited for the study of UPD process, which refers to the electrodeposition of metal monolayer(s) like Cu on a Ru substrate can take place at more positive potentials than that for Cu deposition on Cu substrate. By utilizing the EQCM technique, the surface coverage of Cu UPD can be precisely and reproducibly controlled and the coverage-dependent properties including the

structure of the metallic adlayer and its electronic properties can be explored [14-17].

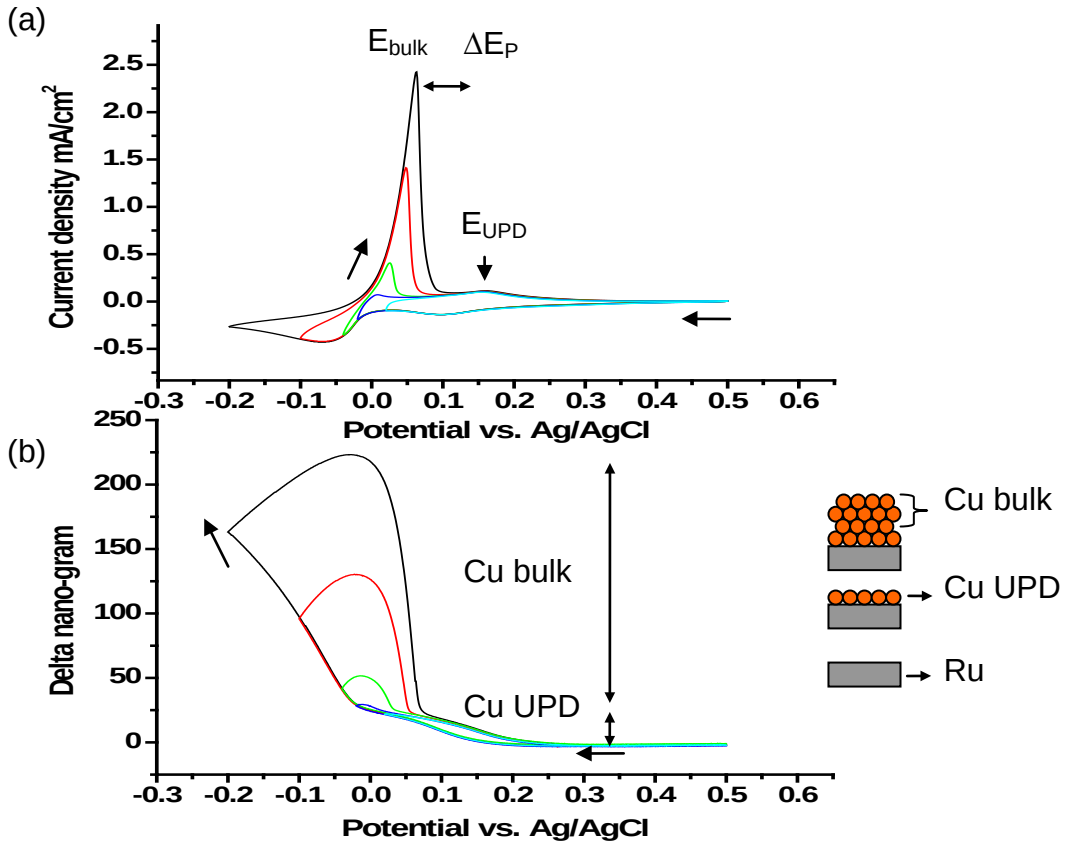

Figure 2-7 (a) Progressive CVs of DC Ru thin film electrode in 2mM $CuSO_4$/0.5M H_2SO_4 scan rate: 10mV/s. (b) the mass difference response to the CVs from Figure 2-7(a).

Figure 2-7a is the EQCM result of Cu UPD on Ru thin film which was sputter-deposited with DC power under 150W and Figure 2-7(b) shows the corresponding mass changes on Ru electrode. The EQCM reveals the insightful details of Cu UPD with mass response during the potential scan. The progressing scanning CVs and the mass response show that the onset potential of Cu UPD and bulk deposition are 0.2V and -0.025V, respectively. From the progressing

CVs in Figure 2-7(a), it was observed that the bulk Cu stripping peaks shifted to more positive potential with thicker Cu deposition. But, both anodic and cathodic E_{UPD} (UPD potential) maintained the same value independent on the thickness of bulk deposition. Therefore, the analysis at ΔE_p in anodic curve may not be suitable due to the shifting of E_{bulk}. The monolayer (ML) coverage of Cu UPD was calculated by two ways. One is to convert the charge into the ML by using integrated Cu UPD stripping peak in CV as shown in Figure 2-8(a). The 0.74 ML is obtained by converting $7.23x10^{-5}$ C.

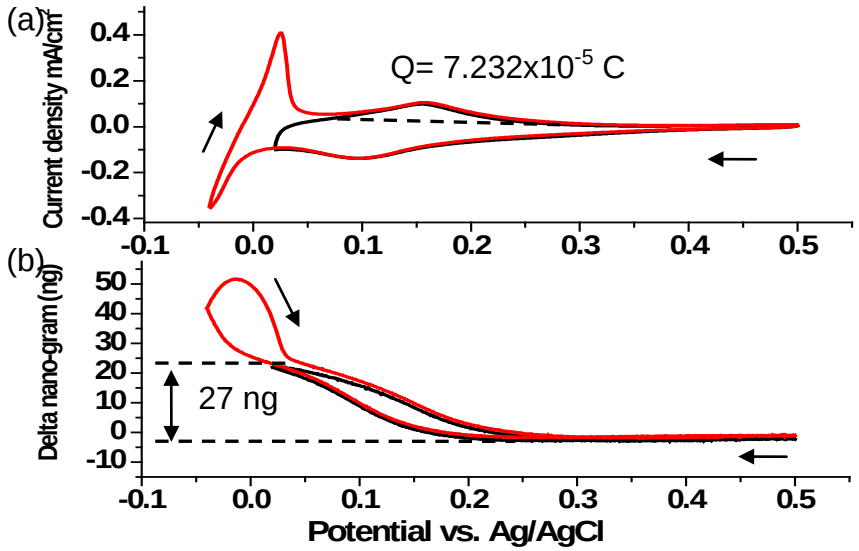

Figure 2-8 (a) CVs of Cu plating on DC Ru in 2mM $CuSO_4$/0.5M H_2SO_4. (b): The mass difference response to the CVs from Figure 2-8(a).

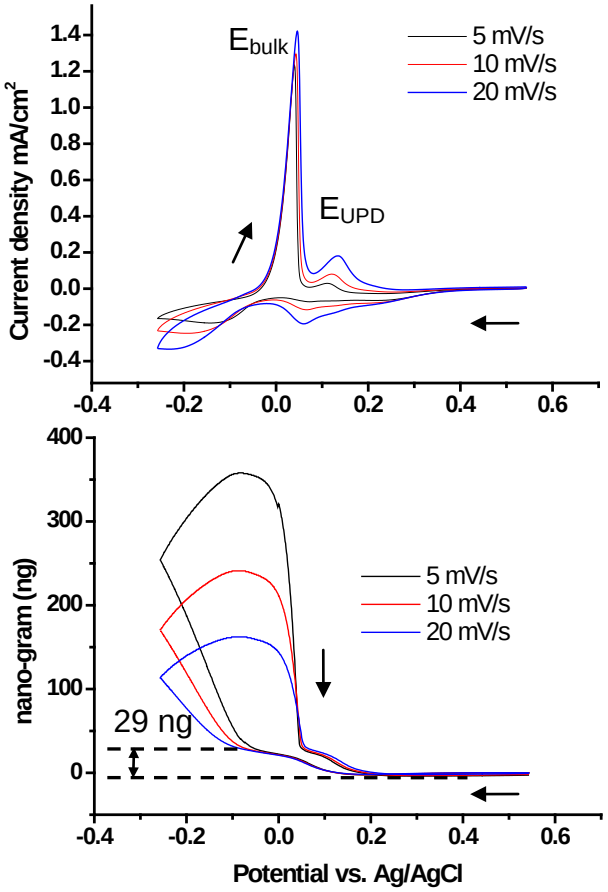

Figure 2-9 (a) Cyclic voltammograms of Cu UPD on RF Ru with different scan rate: 5 mV/s, 10 mV/s, 20 mV/s; (b) corresponding mass response from EQCM.

The alternative way is to calculate ML by using the mass difference from its baseline right before the deposition of bulk Cu as shown in figure 2-7(b). The 27 ng of Cu UPD yields 1.0 ML coverage. The ML coverage derived from the mass data (1.0 ML) is more reliable than that calculated from charge (0.74 ML) because the integrated area of Cu UPD peak was interferenced by the partial overlapping with bulk stripping peak.

Figure 2-9 demonstrates the EQCM result of Cu electroplating on Ru thin

film which was sputter-deposited by RF power under 150W. Figure 2-9(a) shows the CVs with different potential scan rates (5mV/s, 10mV/s and 20mV/s) and Figure 2-9(b) shows that the extent of bulk deposition can be affected by scan rates that determine the scanning duration in negative potential region. Hence, proportionally the bulk Cu was coated thicker when the applied scan rate was slower. However, the similar mass increase for UPD deposition and decrease for UPD stripping during the CVs even with different scanning rates, illustrates that the Cu UPD is thermodynamic controlled up to 20mV/s. The 0.84 ML coverage of Cu UPD was obtained from charge calculation. And 1.1 ML coverage was obtained by converting EQCM mass result. The mass response of Cu UPD in Figure 2-9(b) is similar to that in Figure 2-8(b). But the Cu UPD part show more pronounced peak on RF Ru (figure 2-9a) than DC Ru (figure 2-7a) surface.

The Figure 2-10 shows the morphology difference between RF sputtered Ru and DC sputtered Ru obtained by AFM (*insert*) and XRD spectra. The different sputtering methods affect the grain size of Ru and the coating efficiency. Also, with the same power (150W) under the same sputtering time the DC power sputtering resulted in thickness twice more than RF power. The higher thickness of DC Ru is due to the larger grain size obtained from DC power than RF. In Figure 2-10, the XRD spectra also illustrate the different grain size by relative full width at half maximum (FWHM). The Scherrer's equation is given

$$\tau = \frac{K\lambda}{\beta \cos\theta} \qquad \text{Eq.2-2}$$

Where *K* = 0.9 is the shape factor, λ is the x-ray wavelength (Cu 40keV, K_α: 1.542Å), β is the line broadening at half the maximum intensity (FWHM) in radians, and θ is the Bragg angle; τ is the mean size of the ordered (crystalline) domains.

Based on the Scherrer's equation the particle size, τ, is anti-proportional to the β (FWHM). Therefore, the ratio of particle size between DC Ru and RF Ru is 1.57: 0.8, which is similar to the ratio of AFM result: 2:1.

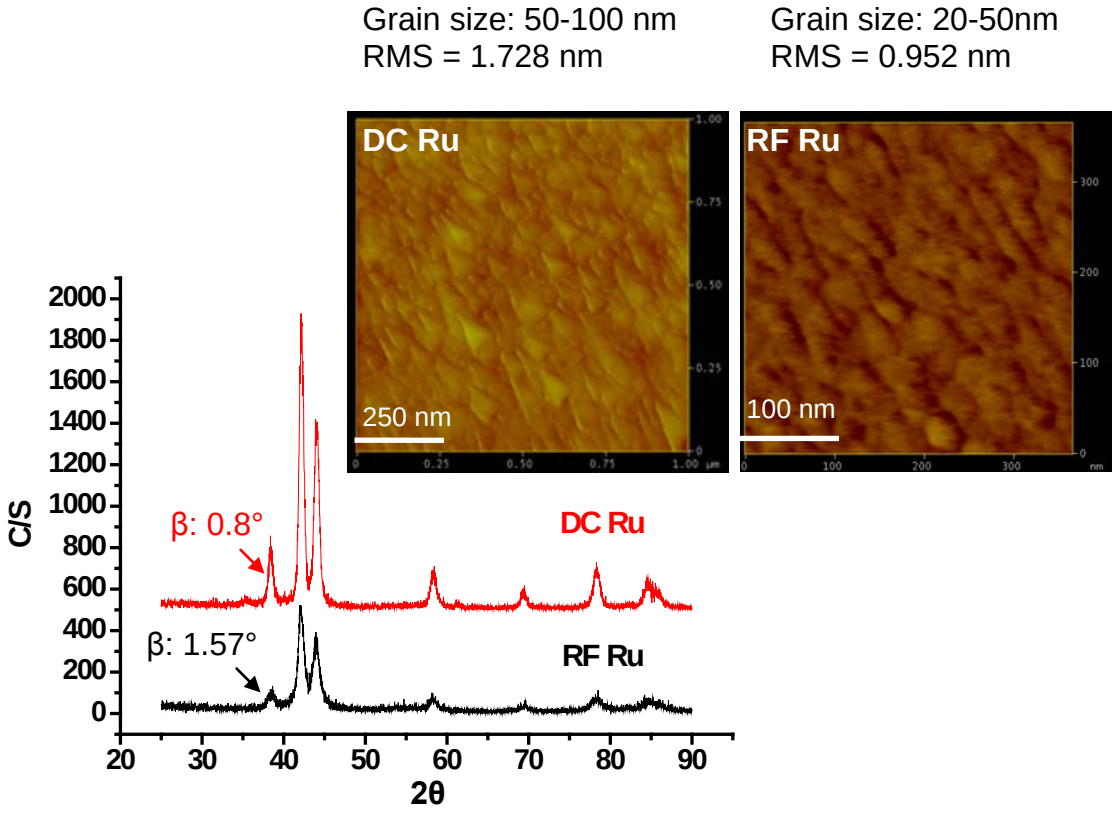

Figure 2-10 XRD spectra of DC Ru and RF Ru thin film. *Insert*: AFM images RF right DC left.

2.6 Effect Cu UPD on RuO_xH_y Formed by Different Acidic Media

Recently, there are increased interests on utilizing electrochemical formed Ru oxide (RuO_xH_y) thin film for various applications. The (RuO_xH_y) not only can be a potential Cu seedless liner material for semiconductor fabrication and memory device [18,19] but also can be a potential catalyst in direct methanol fuel cell (DMFC) as an anode for methanol oxidation [20-22]. In water splitting system the RuO_xH_y also can be a cathodic catalyst due to pronounced hydrogen evolution reaction (HER) in acidic environments. This section discusses the thin film preparation of RuO_xH_y in selected acidic media. The thin film PVD Ru (95 nm) wafer was prepared by sputtering deposition of Ru on Si wafer. RuO_xH_y was made by electrochemically oxidizing the Ru/Si electrode at 1.3V vs. Ag/AgCl for 60 seconds in different acidic media (0.5 M each of sulfuric acid, perchloric acid, nitric acid, phosphoric acid, and hydrochloric acid) as the electrolytes. During the oxidation process vigorous oxygen evolution occurred, and the color of Ru wafer changed from metallic color to brownish after electrochemical oxidation.

2.6.1 Ruthenium Hydride Dioxide (RuO_xH_y) Using Sulfuric Acid

Figure 2-11 shows the CVs of thin film RuO_xH_y made by electrochemical oxidation in 0.5 M sulfuric acid. The CV of Cu electrodeposition is shown in Figure 2-11(a) in 2 mM $CuSO_4$/0.5 M H_2SO_4 with scan rate 50mV/s. The Cu UPD peak is at *ca.* 0.1V vs. Ag/AgCl in cathodic region and the Cu UPD stripping peak is at *ca*. 0.2V anodic region.

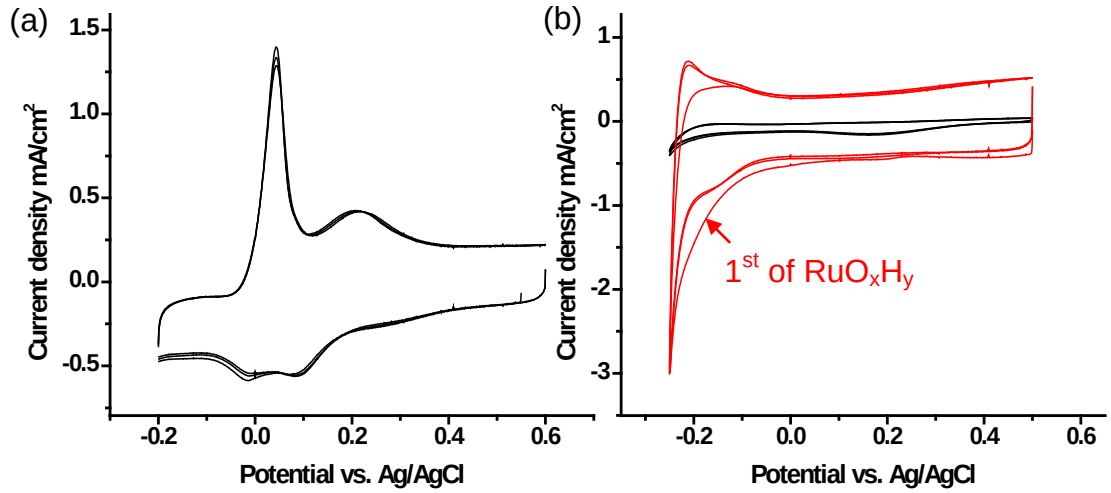

Figure 2-11 RuO_xH_y electrode was electrochemically formed in 0.5 M H_2SO_4. (a) Cu electrodeposition on RuO_xH_y electrode in 2 mM $CuSO_4$/0.5 M H_2SO_4. (b) background of RuO_xH_y (red) and Ru (black) in 0.5 M H_2SO_4.

The figure 2-11(b) demonstrates that the thin film RuO_xH_y grew on the top of PVD Ru, causing the capacitance increase in background CV. Also, not only the higher capacitance on RuO_xH_y is obvious, but also the more pronounced current of hydrogen evolution reaction (HER) on RuO_xH_y is dissimilar to Ru.

2.6.2 Ruthenium Hydride Dioxide (RuO_xH_y) Using Perchloric Acid

Figure 2-12 shows the CVs in Cu UPD solution of thin film RuO_xH_y that was oxidized in 0.5 M $HClO_4$ at 1.3V vs. Ag/AgCl. The deposition of Cu UPD is *ca.* 0.098V on cathodic curve, and stripping peak of Cu UPD is located at 0.212V. From the presence of pronounced hydrogen evolution peak and increased capacitance current, it was confirmed that RuO_xH_y was also formed in perchloric acid. But the coverage of Cu UPD of RuO_xH_y formed in $HClO_4$ was less than

those formed in sulfuric acid, reference to Figure 2-11.

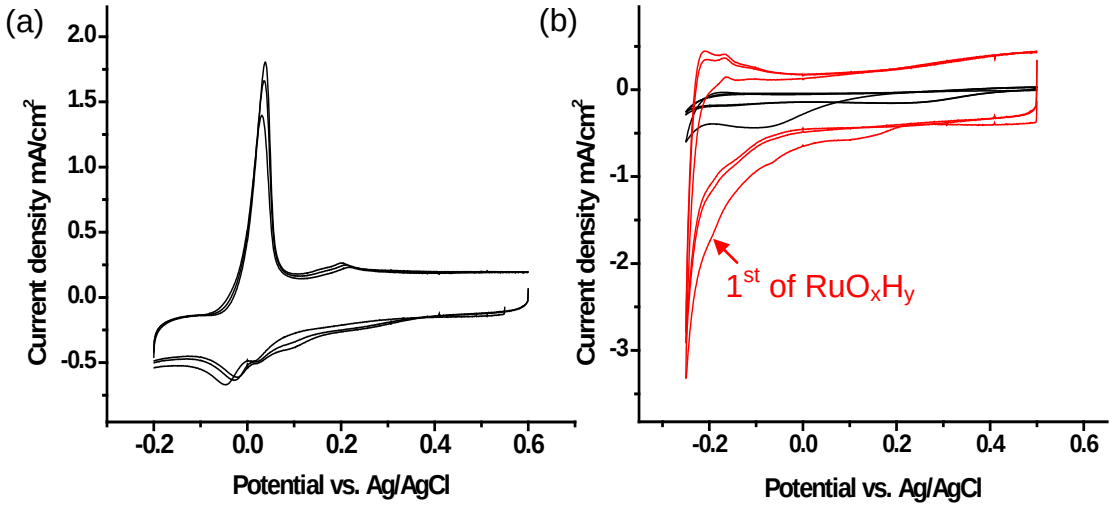

Figure 2-12 RuO_xH_y electrode was electrochemically formed in 0.5 M $HClO_4$. (a) Cu electrodeposition on RuO_xH_y electrode in 2 mM $CuSO_4$/0.5 M H_2SO_4. (b) Background of RuO_xH_y (red) and Ru (black) in 0.5 M $HClO_4$.

2.6.3 Ruthenium Hydride Dioxide (RuO_xH_y) Using Nitric Acid

Figure 2-13 shows the CVs of thin film RuO_xH_y oxidized in 0.5 M HNO_3 at 1.3V vs. Ag/AgCl. Slight Cu UPD observed at 0.037V on cathodic curve, and the stripping peak of Cu UPD is absent in anodic curve. Based on the HER and capacitance, the RuO_xH_y was also formed in nitric acid. But the Cu UPD coverage was not noticeable in RuO_xH_y formed in nitric acid.

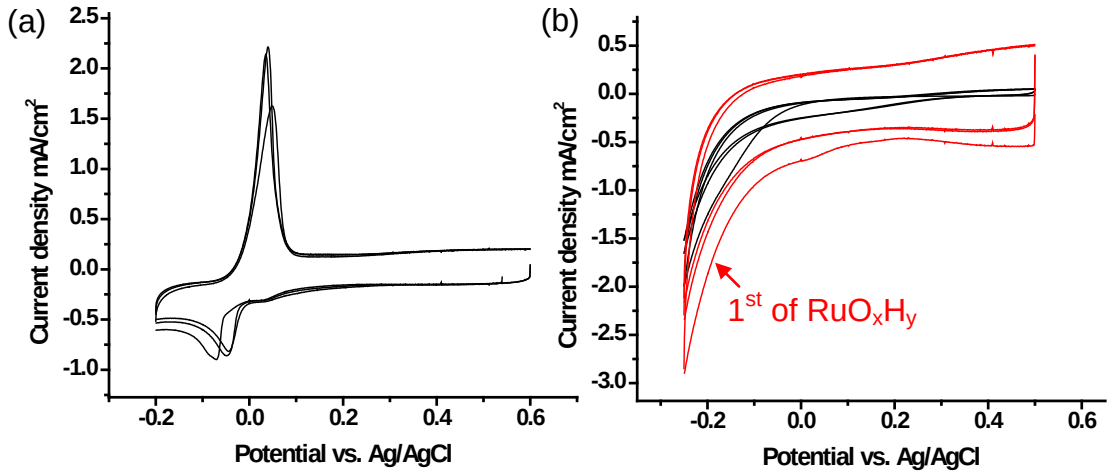

Figure 2-13 RuO_xH_y electrode was electrochemically formed in 0.5 M HNO_3.
(a) Cu electrodeposition on RuO_xH_y in 2 mM $CuSO_4$/0.5 M H_2SO_4.
(b) Background of RuO_xH_y (red) and Ru (black) in 0.5 M HNO_3.

2.6.4 Ruthenium Hydride Dioxide (RuO_xH_y) Using Phosphoric Acid

Figure 2-14 shows the CVs of thin film RuO_xH_y oxidized in 0.5 M H_3PO_4 at 1.3V vs. Ag/AgCl. The deposition of Cu UPD is ca. 0.094V on cathodic curve, and stripping peak of Cu UPD is present at 0.181 V. According to HER and capacitance, the RuO_xH_y was also formed in phosphoric acid. But the coverage of Cu UPD was less than those formed in sulfuric acid.

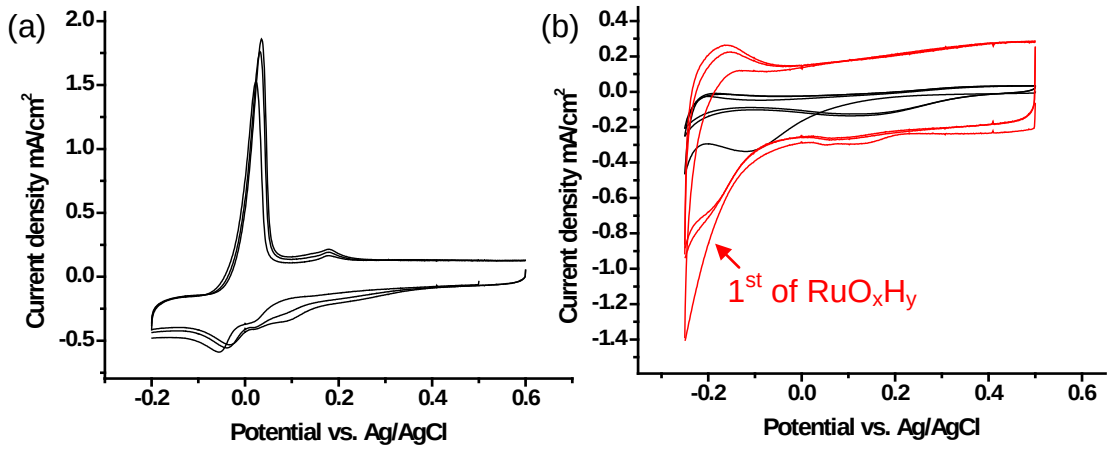

Figure 2-14 RuO_xH_y electrode was electrochemically formed in 0.5 M H_3PO_4.
(a) Cu electrodeposition on RuO_xH_y in 2 mM $CuSO_4$/0.5 M H_2SO_4.
(b) Background of RuO_xH_y (red) and Ru (black) in 0.5 M H_3PO_4.

2.6.5 Ruthenium Hydride Dioxide (RuO_xH_y) Using Hydrochloric Acid

Figure 2-15 shows the CVs of thin film RuO_xH_y oxidized in 0.5 M HCl at 1.3V vs. Ag/AgCl. The deposition of Cu UPD is ca. 0.095V on cathodic curve, and stripping peak of Cu UPD is present at 0.197V. Owing to HER and capacitance, the RuO_xH_y was also formed in hydrochloric acid. But the coverage of Cu UPD was still less than those formed in sulfuric acid.

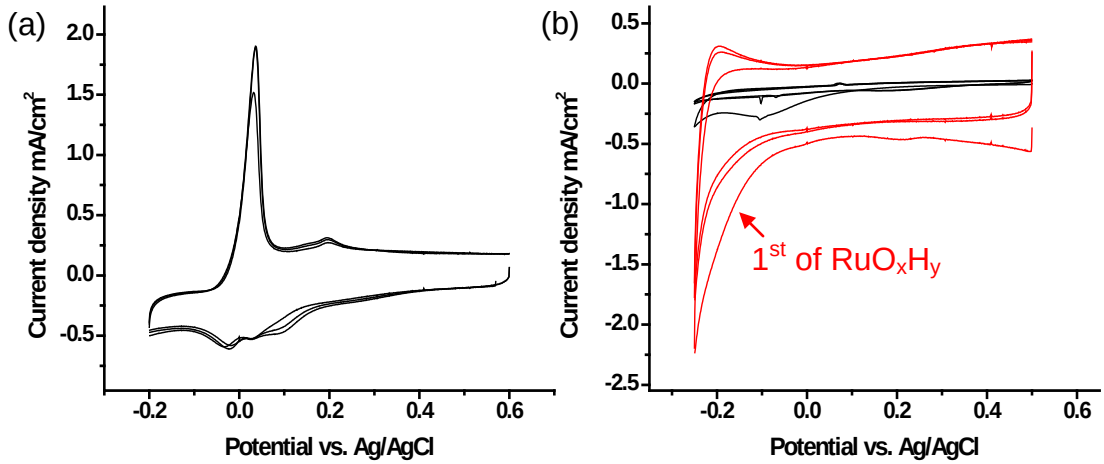

Figure 2-15 RuO_xH_y electrode was electrochemically formed in 0.5 M HCl.
(a) Cu electrodeposition on RuO_xH_y in 2 mM $CuSO_4$/0.5 M H_2SO_4.
(b) Background of RuO_xH_y and Ru in 0.5 M HCl.

2.6.6 Analysis of Cu UPD on Ruthenium Hydride Dioxide (RuO_xH_y)

Figure 2-16 (a) shows the overlapped CVs of Cu UPD on RuO_xH_y which were oxidized in different acidic media. Figure 2-16(b) and (c) show the zoom-in Cu UPD deposition and Cu UPD stripping peaks, respectively. From the results, it was observed that the electrochemical oxidation of Ru in different acidic media resulted in RuO_xH_y formation with different characteristics though the pH of acidic media is the same ca. 0.3. The cathodic and anodic peaks of Cu UPD in Figure 2-16 (b) and (c) illustrate the trend of the favorable Cu UPD: sulfuric acid > hydrochloric acid > perchloric acid > phosphoric acid > nitric acid. Figure 2-17 shows the analysis result from Figure 2-16(b) and (c). Figure 2-17(a) shows the calculated charge and discharge of Cu UPD by integrating the peak area in CVs in figure 2-16(b) and (c). For instance, the Cu UPD stripping charge was obtained

from the anodic peak integration from the potential 0.1V to 0.4V; the Cu UPD cathodic charge was obtained from integrating the cathodic curve between the potential regions 0.05V and 0.2V. The trend of charge calculation in Figure 2-17(a) shows the same trend as expected from the Figure 2-16. The charge can be converted to monolayer (ML) coverage by using eq. 2-1. The peak potentials (E_p) of both cathodic and anodic Cu UPD follow the same trend as that of charge result. The more favorable of Cu UPD means the more interfacial bonding strength between RuO_xH_y surface with Cu atoms because the higher positive peak potential of Cu UPD demonstrates the lower required voltage for ML deposition and higher applied voltage to remove the deposited ML.

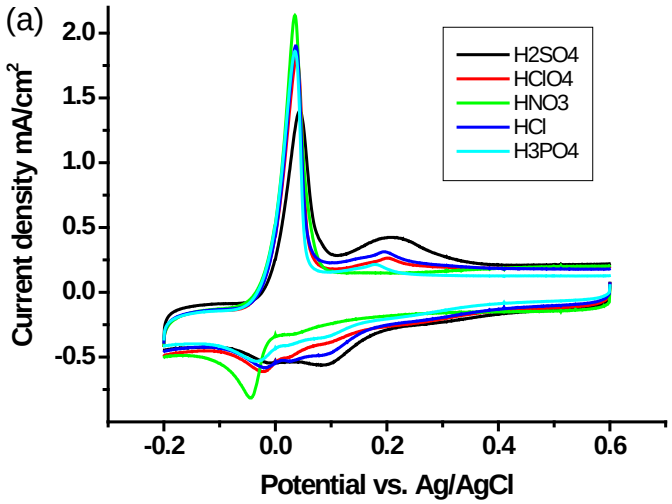

Figure 2-16 (a) Overlapped CVs of RuOxHy made in different acid.

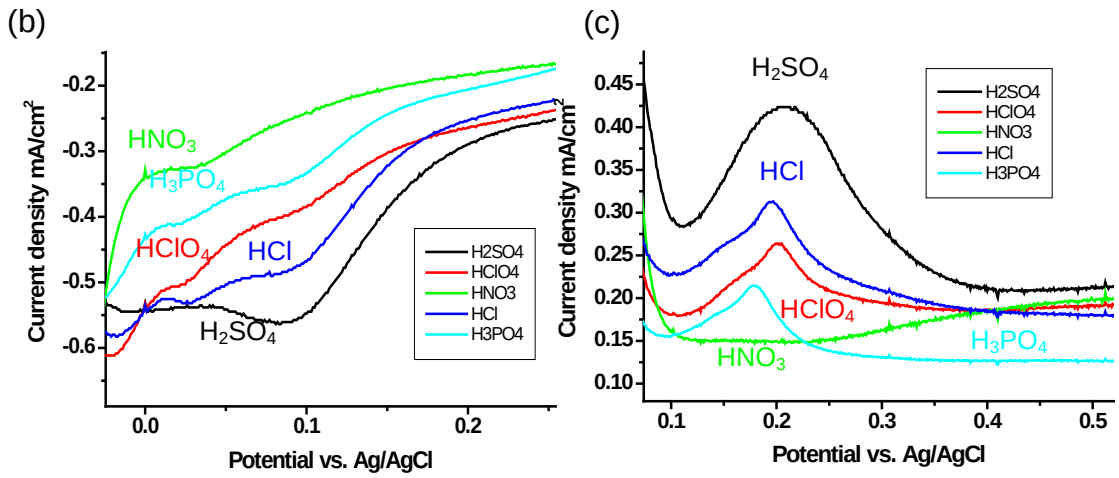

Figure 2-16 (b) Zoom in overlapped CVs in cathodic region of Cu UPD (c) Zoom in overlapped CVs in anodic region of Cu UPD stripping.

The low grazing angle (2°Ω) XRD (Rigaku Ultima III XRD) characterization can provide the lattice and crystalline information especially on thin film analysis. Figure 2-18 shows the XRD patterns of Ru thin film (100 nm, DC sputter deposition) and RuO_xH_y thin films which were made by electrochemically oxidizing Ru in 0.5 M H_2SO_4 or 0.5 M $HClO_4$ as well as the thin film RuO_xH_y for Cu UPD samples. The RuO_xH_y thin film has less Ru signal compared to Ru only sample because the formation of the amorphous RuO_xH_y on the top of Ru surface blocks the Ru signal from inner part of film stack. The RuO_xH_y thin film made in perchloric acid shows less Ru signal than the RuO_xH_y made in sulfuric acid even though the capacitance of those RuO_xH_y surface are similar to each other. It is interesting to investigate with further study. The nature of RuO_xH_y caused much differences on Cu UPD even with similar capacitance property.

(a)

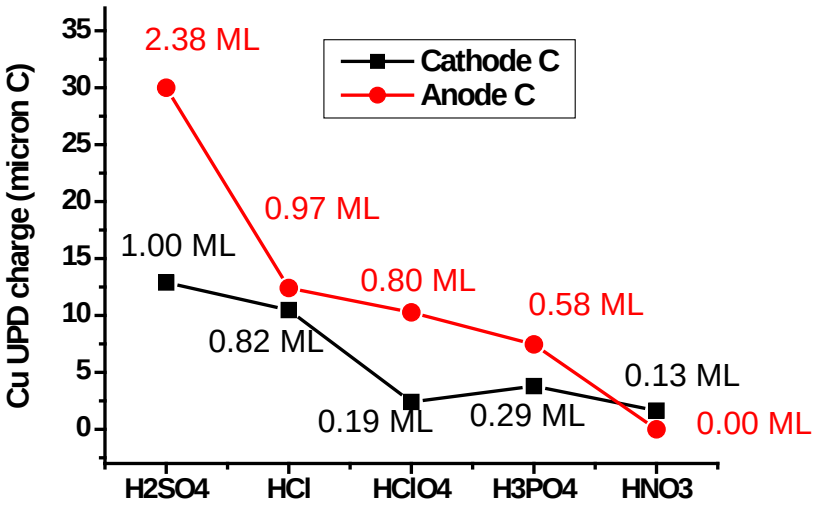

Figure 2-17 (a) Stripping or depositing charge of Cu UPD on RuO_xH_y made by different acidic media.

(b)

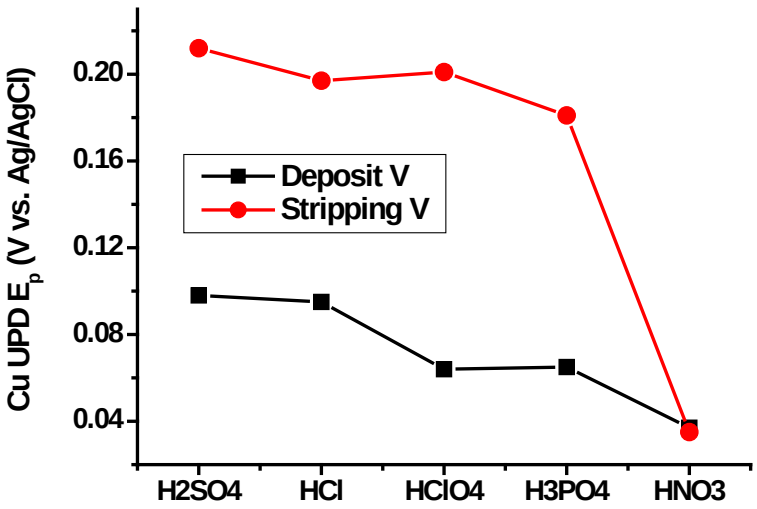

Figure 2-17 (b) Cu UPD stripping peaks and depositing peaks on RuO_xH_y made by different acidic media.

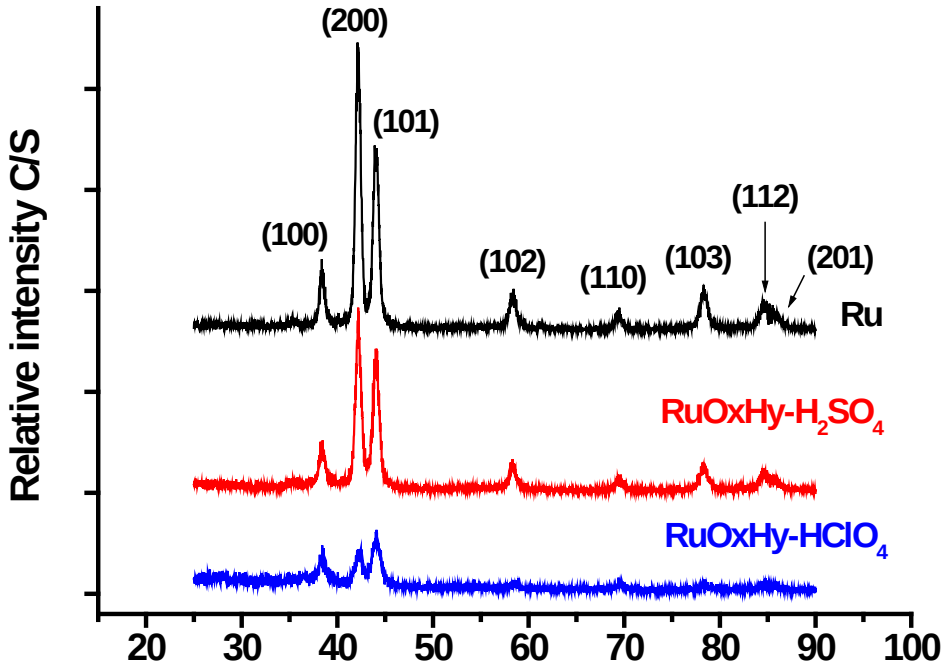

Figure 2-18 XRD of Ru and RuO_xH_y made in H_2SO_4 or $HClO_4$.

2.7 Effect of Cu UPD on Thermally Treated Ru Oxides

Ruthenium dioxide (RuO_2) features a tetragonal rutile structure which is a promising material due to its exceptional properties such as thermal stability [23, 24], low room temperature electrical resistivity, and excellent diffusion barrier properties [25-28]. Both RuO_2 and ruthenium hydrous dioxide (RuO_xH_y) are conducting oxides which can be used in DRAM metal-insulator-metal capacitors. Owing to the requirement of semiconductor fabrication process, the bottom electrode Ru oxides could be more suitable for crystallization anneal in an oxidizing ambient such as the atomic layer deposition process using oxidizing organic precursor.

From previous study, the Cu UPD was observed on Ru Echem oxide (RuO_xH_y) especially prepared in sulfuric acid. It is important to know what the RuO_xH_y will behave after heat treatment at 600°C. Figure 2-19(a) & (b) show the CVs of Ru and RuO_xH_y in Cu plating and background solutions, respectively. Cyclic voltammetric curves were collected from freshly prepared PVD Ru wafer (black line) and RuO_xH_y wafer (red line) in a 2 mM $CuSO_4$/0.5 M H_2SO_4 solution. The potential was scanned from positive end toward negative side then reversed to positive end.

The RuO_xH_y was formed by holding Ru wafer at +1.3V (vs. Ag/AgCl) in 0.5 M H_2SO_4 solution for 60 seconds as discussed in previous section. In Figure 2-19 (a) both anodic and cathodic Cu UPD peaks are present at 0.2V and 0.1V, respectively. The background CVs demonstrate that the RuO_xH_y layer was formed on top of Ru surface owing to the increased capacitance current as shown in Figure 2-19 (b) red line. The ML surface coverage of Cu UPD was *ca.* 0.5 ML on Ru surface and was *ca.* 0.9 ML on RuO_xH_y surface. The Ru and RuO_xH_y thin films were heat treated in annealing chamber at 600°C for 60 minutes in air ambient. The surface of Ru wafer and RuO_xH_y changed to brownish red. After annealing process, both Ru and RuO_xH_y did not show Cu UPD peaks. Also, the capacitance current of RuO_xH_y has reduced to $1/40^{th}$ after annealing as shown in Figure 2-20(b). The CVs of the annealed Ru (green line) and RuO_xH_y (blue line) obtained in sulfuric acid background solution were overlapped in Figure 2-20(a). Figure 2-21 shows charge density vs. potential

curve in Cu electrochemical deposition. It shows that both the thermally treated Ru (green line) and RuO_xH_y (blue line) possessed similar strength of interfacial binding between Cu and thermally oxidized Ru oxide surface even electrochemically pre-formed oxide. The absence of Cu UPD illustrates the interfacial bonding between Cu and the thermal Ru oxide is less than Cu on Ru and RuO_xH_y.

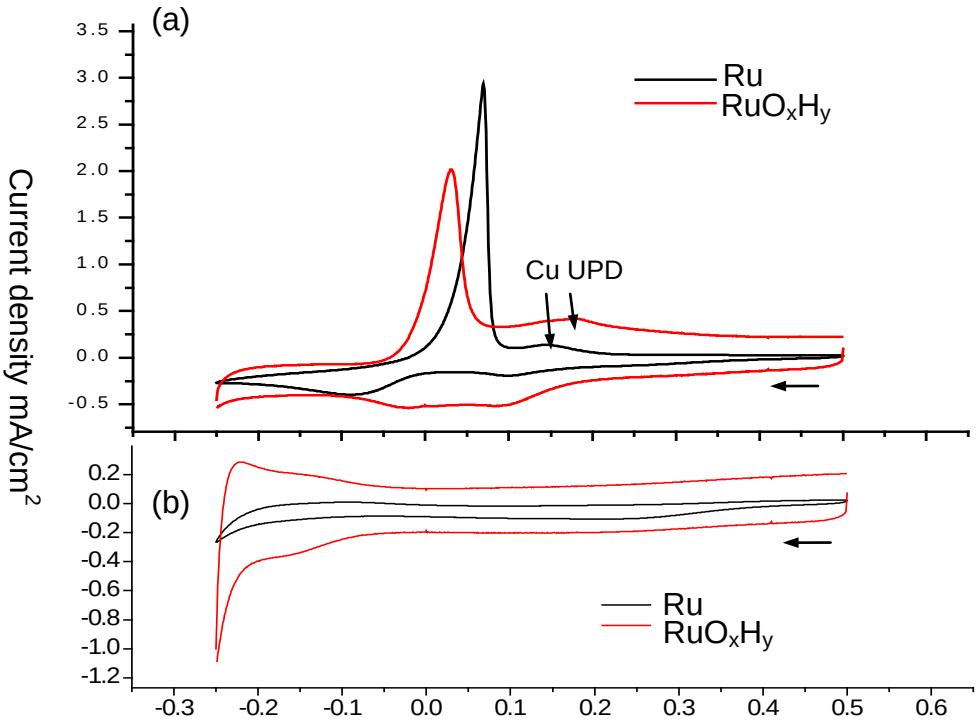

Figure 2-19 (a) CVs collected from a freshly prepared Ru wafer and electrochemical oxidized Ru (RuO_xH_y) immersed in a 2 mM $CuSO_4$/0.5 M H_2SO_4 solution. (b) Background CVs in 0.5 M H_2SO_4 solution scanning rate 20 mV/s.

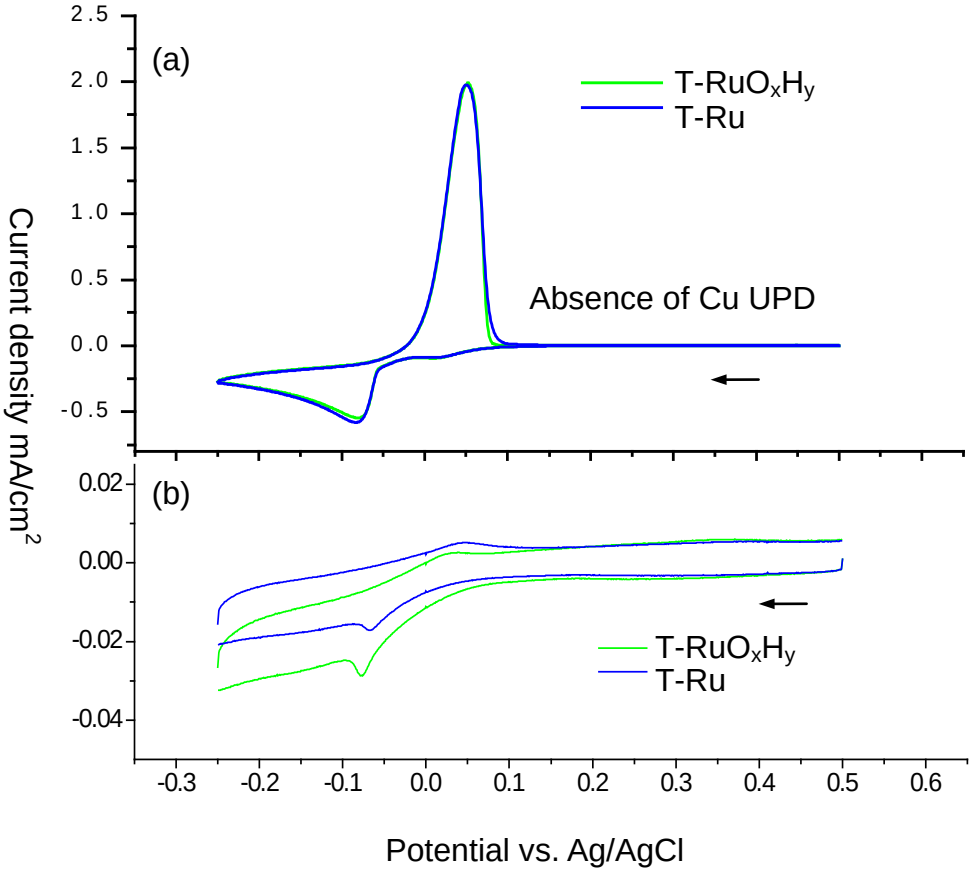

Figure 2-20 (a) CVs collected from a thermal oxidized Ru wafer and thermal oxidized RuO_xH_y immersed in a 2 mM $CuSO_4$/0.5 M H_2SO_4 solution. (b) Background CVs in 0.5 M H_2SO_4 solution scanning rate 20 mV/s.

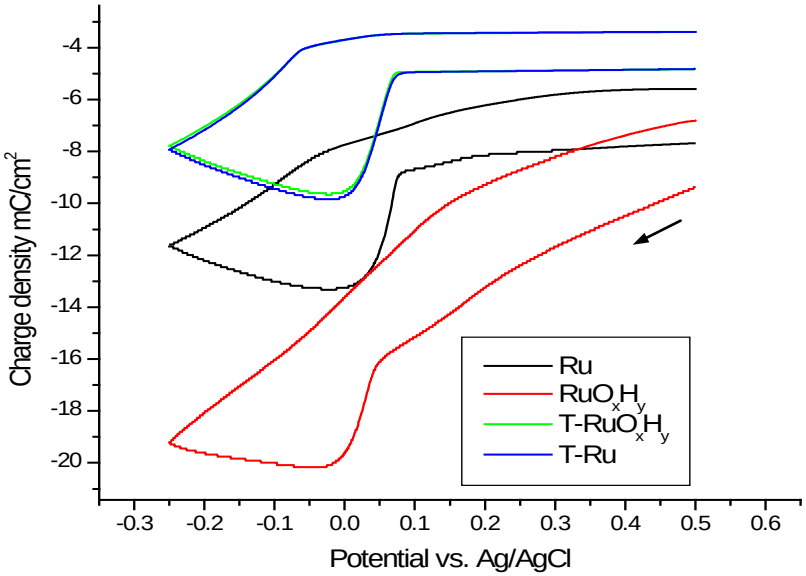

Figure 2-21 charge density vs. applied potential was collected from Figure 2-18(a) and Figure 2-19(a) in 2 mM $CuSO_4$/ 0.5 M H_2SO_4 solution.

The Figure 2-22 shows the XRD results of Ru with different treatments. The black line is DC Ru thin film; the red line is electrochemical oxidized Ru (RuO_xH_y); and the blue line is the thermal treated Ru (RuO_2). The XRD spectrum of RuO_xH_y thin film exhibits the XRD signal of crystalline properties that of Ru thin film, but the thermally treated Ru oxide shows mostly the rutile structure of RuO_2 with only weaker intensity of Ru phase that was present underneath of RuO_2 over layer.

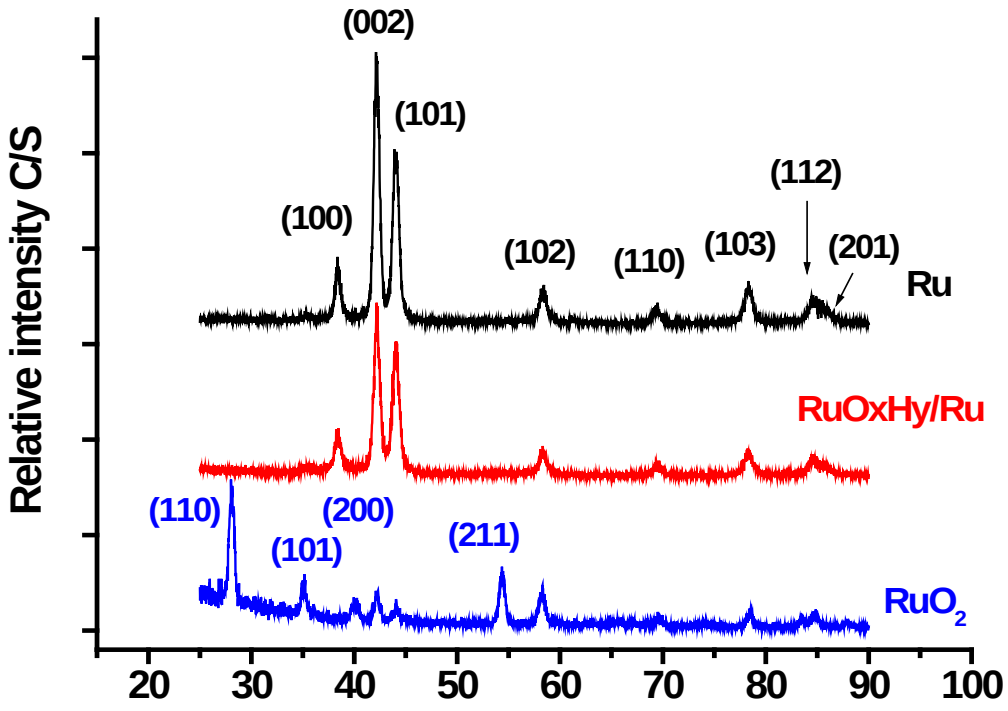

Figure 2-22 XRD result of Ru, RuO_xH_y/Ru and RuO_2/Ru.

2.8 TEM Characterization of Ru and Ru Oxide Films

In order to explore the differences besides electrochemical characterizations, cross-sectional TEM images were obtained to determine the thickness of each layer such as Cu/Ru/Ti/Si, Cu/RuO_xH_y/Ru/Ti/Si before and after the thermal treatments. Before obtaining the cross-sectional TEM images, plain view and selected area diffraction (SAD) pattern of PVD Ru film were obtained to determine the polycrystalline structure (in Figure 2-23 SAD ring pattern) with the topography from AFM (in Figure 2-24) which provides the roughness of Ru wafer (*ca.* 1.7 nm). The AFM image were obtained as references for later cross-

sectional TEM to understand whether the interfacial layer of PVD Ru were damaged by sample preparation or covered with junk.

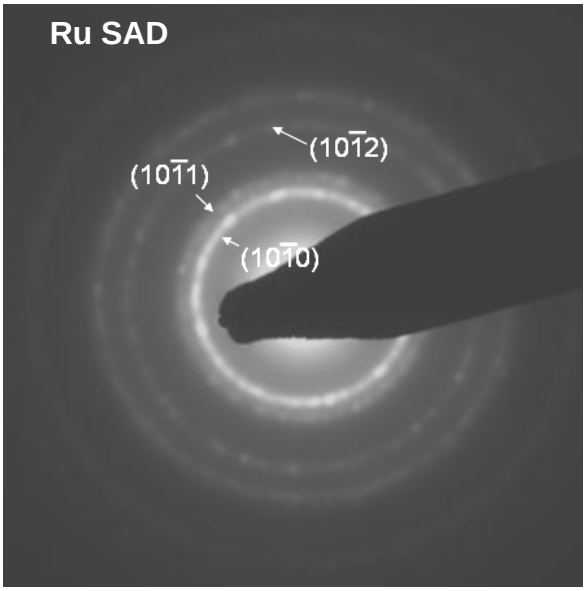

Figure 2-23 Selected aperture diffraction (SAD) of PVD Ru camera length: 122 mm.

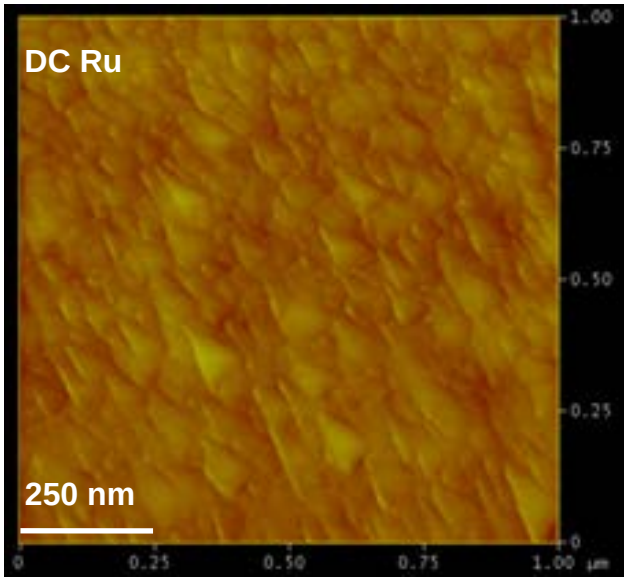

Figure 2-24 Atomic force microscope image of PVD Ru.

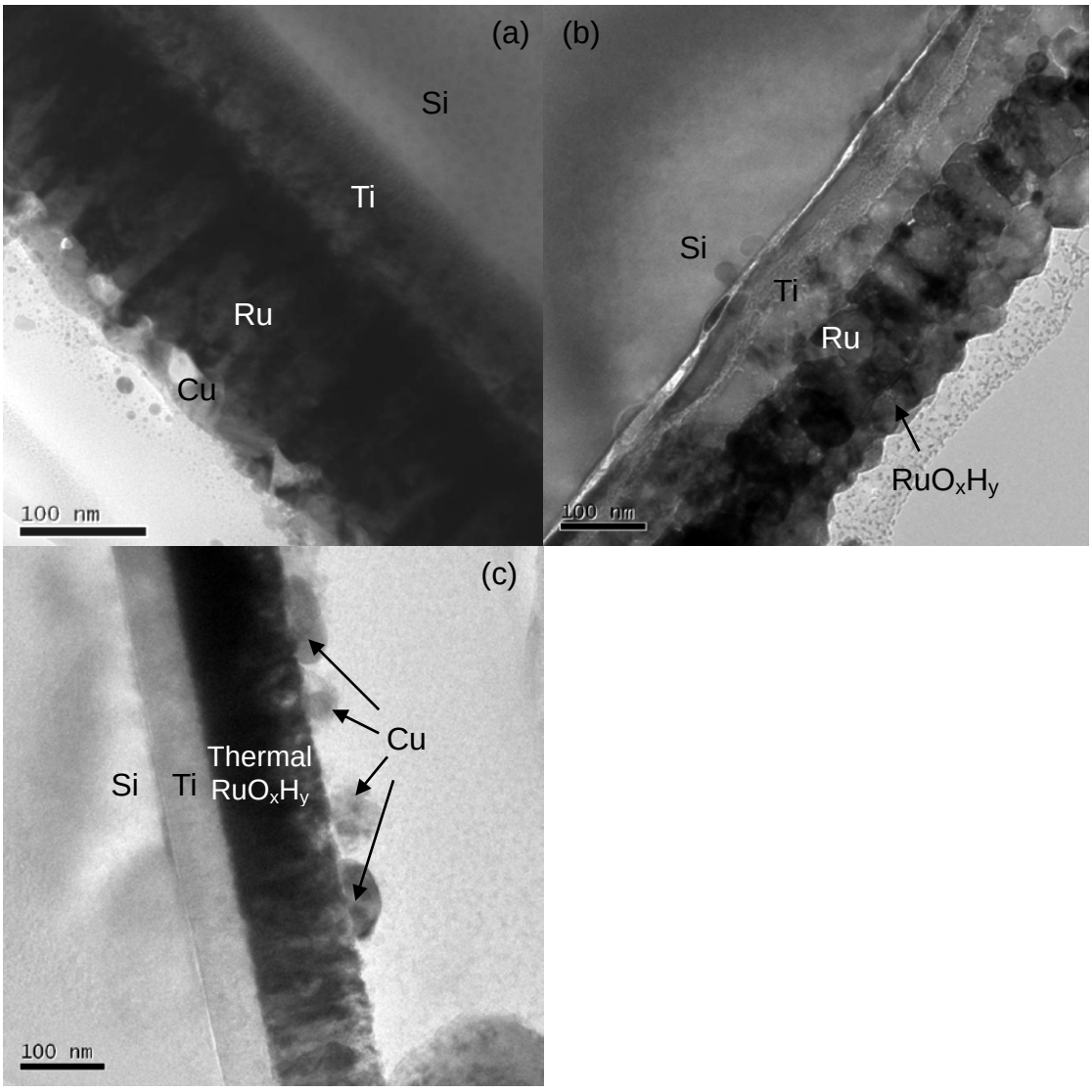

Figure 2-25 Cross section view of ECD Cu on (a) freshly prepared Ru wafer. (b) electrochemically oxidized PVD Ru wafer (Ru/RuO_xH_y). (c) 600°C thermal annealed of an electrochemically oxidized Ru wafer (Ru/RuO_xH_y).

The cross-sectional TEM in Figure 2-25(a) demonstrates that the thickness of Ru layer is *ca*. 120 nm and the grain size is *ca.* 50-100 nm which is in agreement with AFM results. In Figure 2-25(b) the thickness of Ru and RuO_xH_y

is *ca*. 120 nm also; in Figure 2-25(c) the thickness of thermal treated RuO_xH_y is *ca*. 120 nm. From the viewpoint of ECD Cu layer on (a) Ru and (c) thermal annealed of RuO_xH_y, the wettability of Cu is higher on Ru surface than on thermal annealed of RuO_xH_y that results in fewer and discontinued Cu grains on thermal annealed of RuO_xH_y, as shown in Figure 2-25(c). The TEM results support that the interfacial bonding strength is favorable on Ru rather than thermal Ru oxides. The ECD Cu layer was lost on RuO_xH_y substrate during the TEM sample preparation likely due to the soft property of Echem RuO_xH_y layer.

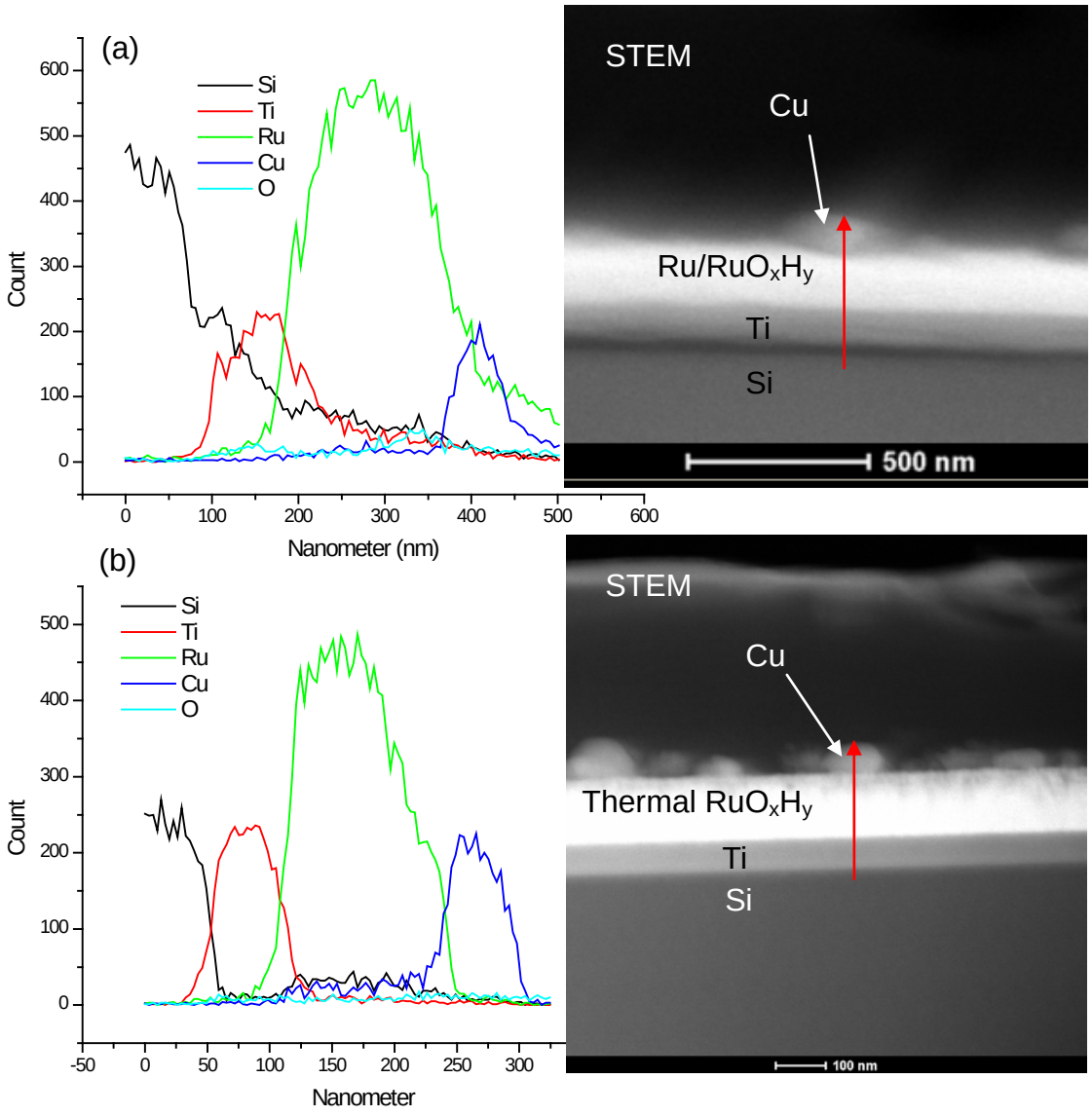

Figure 2-26 STEM-EDX atomic profiling of (a) Cu/RuO_xH_y/Ru/Ti/Si and (b) Cu/thermal annealed RuO_xH_y/Ru/Ti/Si.

2.8.1 Scanning TEM and Energy Dispersive X-ray Analysis

Figure 2-26 depicts the depth profile of the atomic signals of each layer in

Cu/RuO_xH_y/Ru/Ti/Si and Cu/thermal annealed RuO_xH_y/Ru/Ti/Si with respect to EDX probing position (~1 nm probe size). The probing direction is showed by the red arrow in STEM image for both Cu/RuO_xH_y/Ru/Ti/Si and Cu/thermal annealed RuO_xH_y/Ru/Ti/Si. The atomic concentration can be calculated from the measured EDX intensity with an empirical sensitivity factor for each detected element [29].

2.8.2 Select Area Diffraction Pattern Analysis

In order to clarify the crystalline structure of Ru and RuO_xH_y, high resolution (HR) TEM results and micro-diffraction pattern were used to calculate the lattice parameter of Ru grain as shown in figure 2-27(a). The lattice parameters of hexagonal closed packed (HCP) Ru are found by calculating the d spacing from Figure 2-27(b) and converting to lattice parameters a_a = 0.274 nm and a_c = 0.424 nm, which is comparable with the data base of Ru parameters a_a = 0.271 nm and a_c = 0.428 nm [30-32].

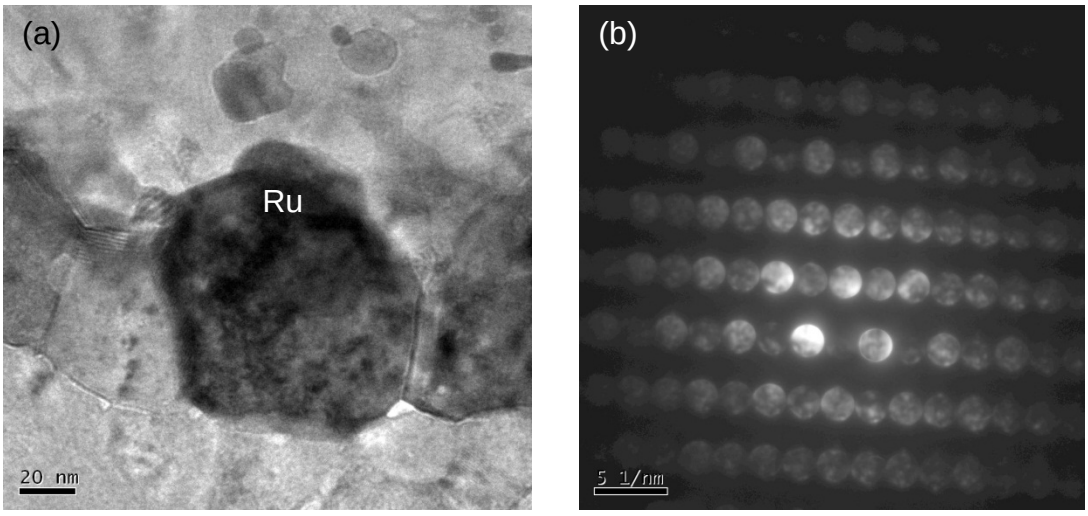

Figure 2-27 (a) HR-TEM image of big Ru grain (b) Micro-diffraction pattern of Ru.

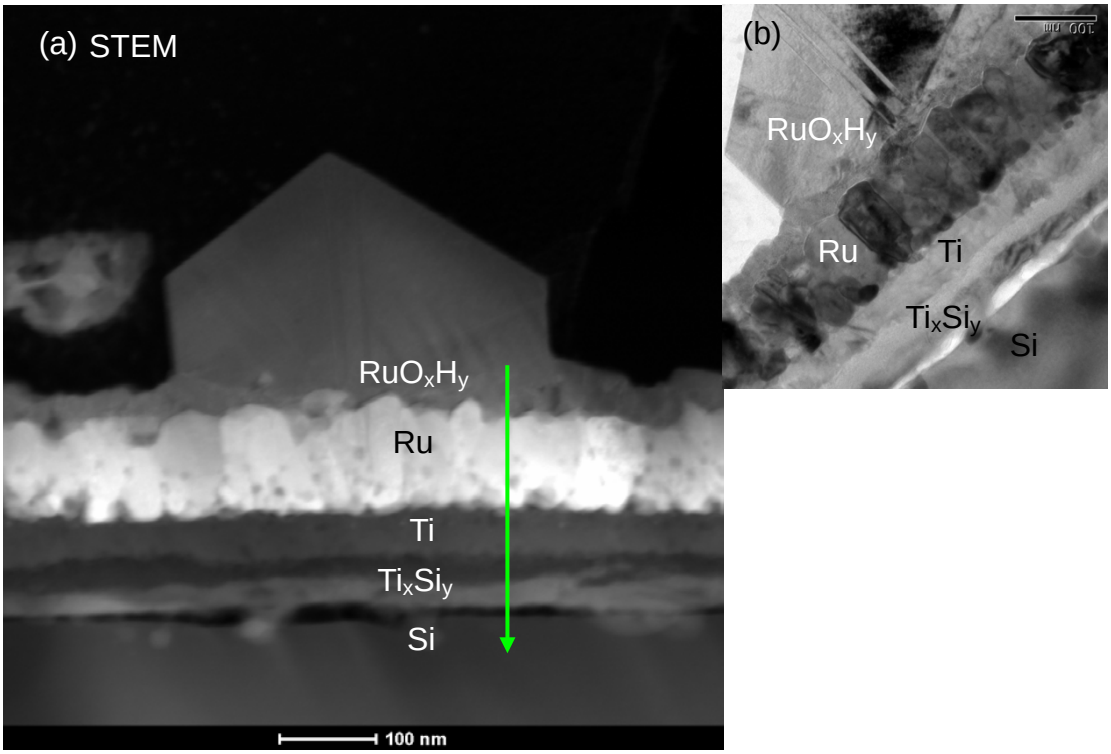

Figure 2-28 Images of RuO_xH_y/Ru/Ti/Si by STEM (a) and TEM (b).

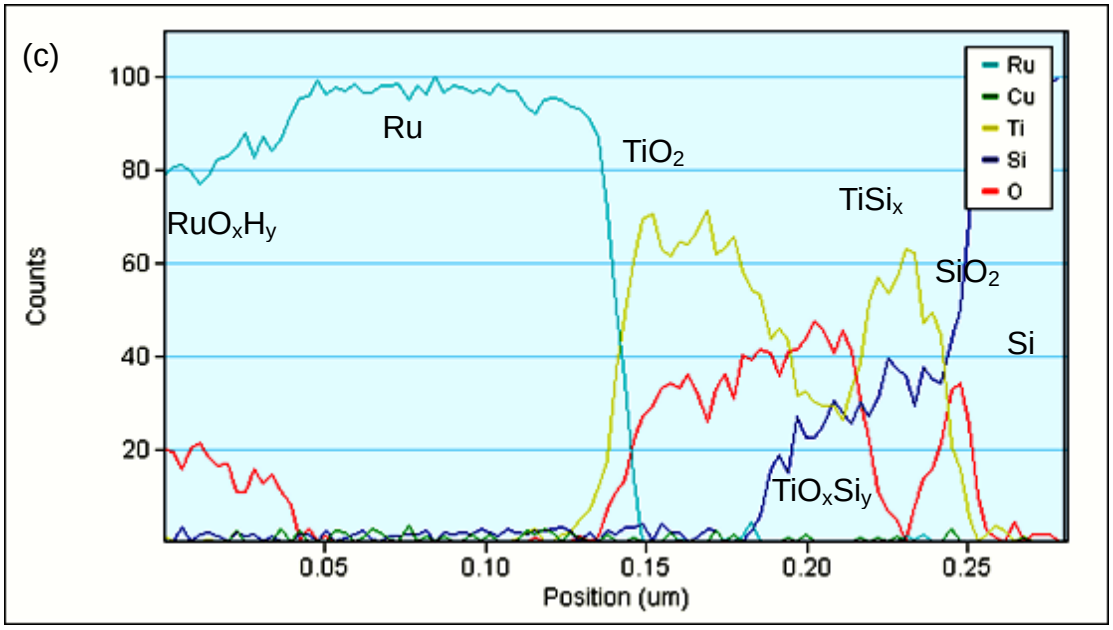

Figure 2-28 (c) STEM-EDX atomic profiling of RuO_xH_y/Ru/Ti/Si from green arrow at STEM image (a).

The Figure 2-28 shows the depth profile of the atomic signals with respect to EDX probing position followed by the green arrow in STEM image for RuO_xH_y/Ru/Ti/Si sample. Figure 2-28(a) and (b) are the images of STEM and TEM, respectively. The contrasts present in STEM image demonstrate the difference in mass of the materials. The heavier the material higher the reflected signal from the sample. Therefore, the Ru layer shows brighter contrast than Ti, and Si layers. The RuO_xH_y layer has darker image compared with underneath Ru and is likely due to the presence of lighter elements i.e. hydrogen and oxygen in Ru hydrous dioxide. The layers of thin film were labeled after characterization by EDX shown in Figure 2-28(c). In Figure 2-29(a) and (b), the images of micro-diffraction pattern and SAD pattern are collected by focusing on the large grain

on RuO_xH_y that is shown in figure 2-28(a) and (b). From the characterization of d spacings, the calculated lattice parameters do not match with either HCP-Ru or RuO_2 rutile crystalline structure. Only FCC crystalline is the possible choice for RuO_xH_y. This large RuO_xH_y crystal located on the top of Ru surface and the more than three grains can be found. This is an interesting preliminary finding. However, more works are need to systematically study the micro-structure of RuO_xH_y phase.

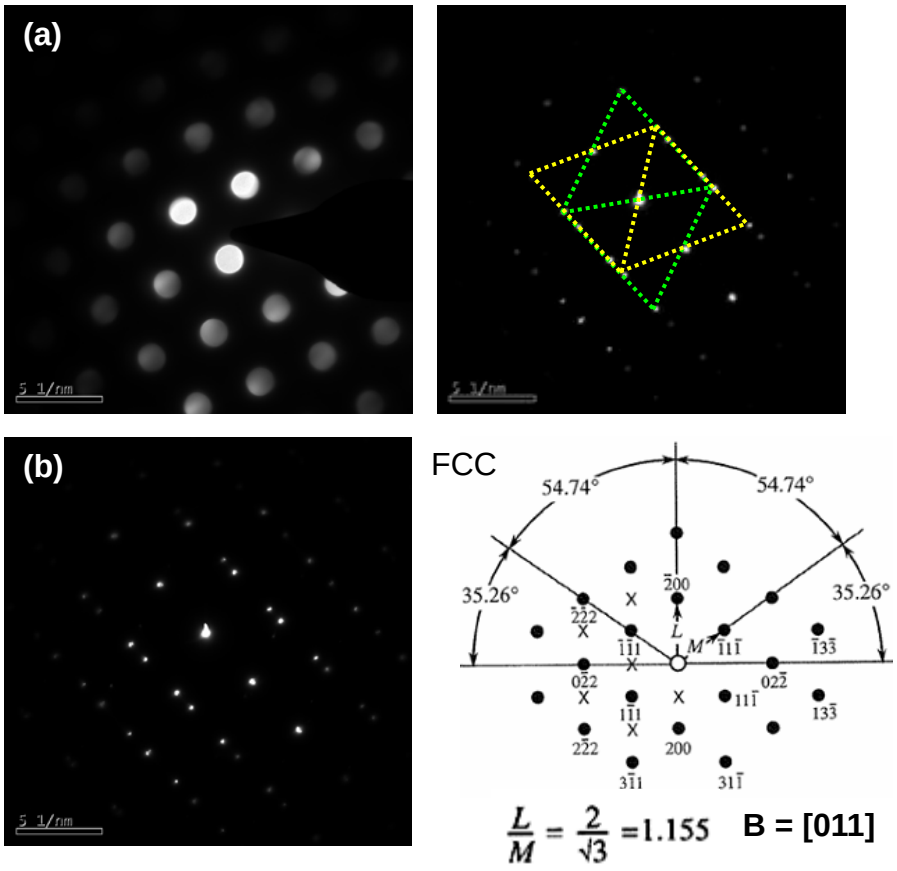

Figure 2-29 (a) Micro-diffraction pattern of RuO_xH_y grain (b) SAD pattern of RuO_xH_y twin-face crystal.

2.9 Summary

Since the increase interests of using Ru as direct plateable liner material, better fundamental understanding of Cu electroplating on Ru various substrates is important. The effect of growing Ru oxides on Cu electroplating is discussed. The growth of Ru native oxide upon air exposure does diminish the efficiency of Cu UPD, ML and bulk plating on Ru surface. Saturated native oxide can be formed in air-exposed ambient after three hours. Second, electrochemical formed oxide can be reversible when applied potential is less than 1.10V, but it changes to irreversible oxide (RuO_xH_y) when applied potential is greater than 1.20V. The EQCM provides accurate mass response during Cu electroplating that supports the ML coverage and the phenomenon of Cu UPD is thermodynamic controlled. The RuO_xH_y formed in sulfuric acid electrolyte shows better Cu UPD than nitric acid or perchloric acid. The TEM result shows that the Ru surface has better wetibility of Cu electroplating than thermal treated Ru surface. The crystalline of RuO_xH_y still needs more data to confirm whether it is amorphous or crystalline.

2.10 References

1. Olowolafe, J. O.; Mogab, C. J.; Gregory, M. Kottke. *J. Appl. Phys.* **1992,** 72(9),
2. Wang, M. T.; Lin, Y. C.; Chen, M. C. *J. Electrochem. Soc.***1998,** 145, 7.
3. Holloway, Karen; Fryer, Peter M. *Appl. Phys. Lett.* **1990,** 57(17), 22.
4. Ono, H.; Nakano, T.; Ohta, T. *Appl. Phys. Lett.* **1994,** 64(12), 21.

5. Schaller, R. R.: *Spectrum, IEEE*. **1997,** 34(6), 52-59.
6. Zhang, Yibin; Huang, Long; Arunagiri, Tiruchirapalli N.; Ojeda, Oscar; Flores, Sarah; Chyan, Oliver; Wallace, Robert M. *Electrochemical and Solid-State Letters.* **2004,** 7(9), C107-C110.
7. Josell, D.; Wheeler, D.; Witt, C.; Moffat, T. P. *Electrochemical and Solid-State Letters*. **2003,** 6(10), C143-145.
8. Chan, R.; Arunagiri, T. N.; Zhang, Y., Chyan, O.; Wallace, R. M.; Kim, M. J.; Hurd, T. Q.
9. Moffat, T. P.; Walker, M.; Chen, P. J.; Bonevich, J. E; Egelhoff, W. F.; Richter, L.; Witt, C.; Aaltonen, T.; Ritala, M.; Leskela, M.; Josell, D.; *J. Electrochem. Soc.* **2006,** 153(1), C37-C50.
10. Liu, J.; Lei, J.; Magtoto, N.; Rudenja, S.; Garza, M.; Kelber, J. A. *J. Electrochem. Soc.* **2005,** 152(2), G115-G121.
11. Yeung, Ho; Chan, H.; Zou, S.; Weaver, M. J.; *J. Phys. Chem. B*. **1999,** 103, 11141-11151.
12. Josell, D.; Bonevich, J. E.; Moffat, T. P.; Aaltonen, T.; Ritala, M.; Lekela, M. *Electrochemical and Solid-State Letters.* **2006,** 9(2), C48-C50.
13. Josell, D.; Witt, C.; Moffat, T. P. *Electrochemical and Solid-State Letters*. **2006,** 9(2), C41-C43.

14 Wunsche, M., *Electrochim. Acta.* **1995,** 5(40), 629-635.

15 Kraznaric, G., *Langmuir* **2001,** 17, 43-4351.

16 Lay et al. *J. Electroanal. Chem*. **2003,** 1, 1-11.

17 Herrero, E.; Buller, L. J.; Abruña, H. D. *Chem. Rev.* **2001,** 101(7), 1897-1930.

18 Matthey, Johnson. *Platinum Metals Review.* **2002,** *46*, 3, 105

19 Ping Mao, Zhigang Zhang, Liyang Pan, Jun Xu, Peiyi Chen, *APPLIED PHYSICS LETTERS.* **2008,** 93, 242102,

20 M. Schaekers, B. Capon, C. Detavernier, and N. Blasco, *ECS Transactions*, **2010,** 33 (2) 135-144

21 Shan Zhu, Suli Wang, Yan Gao, Luhua Jiang, Hai Suna, Gongquan Sun, *International journal of hydrogen energy*. **2010,** 35 11254-11260

22 Rolison DR, Hagans PL, Swider KE, Long JW. *Langmuir* **1999,**15 774e9.

23 Cui X, He Q, Cui F, Zhao J, Li L, Chen H., *Dalton Trans* **2009,** 18: 3395e402.

24 Profeti LPR, Profeti D, Olivi P., *Int. J. Hydrogen Energy*, **2009,** 34:2747e57.

25 R. G. Vadimski, R. P. Frankenthal, and D. E. Thompson, *J. Electrochem. Soc*. **1979,** 126, 2017.

26 Y. Gao, G. Bai, Y. Liang, G. C. Dunham, and S. A. Chambers, *J. Mater. Res*. **1997,** 12, 1844.

27 Y. S. Huang and P. C. Liao, *Sol. Energy Mater. Sol. Cells* **1998,** 55, 179.

28 G. R. Bai, A. Wang, C. M. Foster, and J. Vetrone, Thin Solid Films **1997,** 310, 75.

29 Williams, David B., and C. Barry Carter. *Transmission Electron Microscopy: A Textbook for Materials Science.* 2nd ed., New York: Springer, 2010, 1st ed. New York: Plenum Press, 1996.

30 L. Vitos, A.V. Ruban, H.L. Skriver, J. Kollar, *Surface Science*, **1998,** 411 186–202

31 M.P. Engelhardt, M. Schmid, A. Biedermann, R. Denecke, H.-P. Steinruck, P. Varga, *Surface Science*, **2005,** 578 124–135

32 J. Cerda, F. Soria, *PHYSICAL REVIEW B*, **2000,** 61.

CHAPTER 3

CHARACTERIZATION OF COPPER OXIDES AFTER COPPER ELECTRODEPOSITION AND SURFACE CLEANING PROCESSES

3.1 Introduction to Cuprous Oxide (Cu_2O)

Cuprous oxide is a non-toxic p-type semiconductor material due to the presence of copper vacancies. In 1926, Cu/Cu_2O rectifier was produced by Grondahl [1]. Also, the photovoltaic properties of cuprous oxide have been applied to convert solar radiation into electricity in the early of 20^{th} century [2]. Because of its useful properties, the study of cuprous oxide has been spread out and the different methods of preparation were discovered such as high-temperature and low-temperature thermal oxidation, electro-deposition, anodic oxidation, chemical oxidation and reactive sputtering. In this chapter, the thin film cuprous oxide was prepared by two methods. One is chemical oxidation by dipping the copper into high alkaline condition, and the other one is electro-deposition of cuprous oxide on conductive substrate.

Moreover, the interest on cuprous oxide was increased in semiconductor industry in the late 20^{th} century due to the implementation of copper interconnects in the integrated circuit fabrication process. International Business Machines (IBM), is the first company to find the application of copper as a better interconnect material and in turn they replaced aluminum with Cu on 1997[3].

Though Cu was found to be better choice, the IC fabrication process encountered several challenges during implementation. For example, after the reactive ion etching of interlayer dielectrics, the post plasma etch cleaning chemicals affect the copper surface. Also, the native copper oxide exhibits poor adhesion that generated contact resistance when another conductor is deposited on the oxide covered copper [4]. Copper can form three different oxidation states: Cu^0 metallic copper, Cu^I (cuprous oxide, Cu_2O), and Cu^{II} (Cupric oxide, CuO) upon exposure to air. The native oxide film is composed of mixture of cuprous oxide, cupric oxide, cupric hydroxide: $Cu(OH)_2$ [4]. This chapter deals with the characterization of copper oxides by two different techniques viz. cathodic chronopotentiometry and XPS.

In the dual damascene process sequence, the chemical mechanical polishing (CMP) is utilized to remove excess of copper that results after electroplating step. Subsequently, the post-CMP clean is used to remove the residual organic slurry contamination. Both of the CMP and post-CMP processes are usually done under alkaline condition [5]. Based on the Figure 3-1, the Cu Pourbaix diagram shows regions of passivation and corrosion in alkaline condition. Therefore, it is necessary to study the behavior of cuprous oxide that formed in alkaline solution. Also, the etching rate of Cu in alkaline condition becomes critical in IC fabrication. Hence, in order to study Cu, the different Cu oxides layer need to be prepared. J. A. Switzer et al. have previously reported the electroplated Cu oxides in alkaline condition [6-8]. Electrochemical deposition

is an attractive method for plating uniform thin layer on conductive substrates. The method was applied largely due to its advantages of low cost and high purity. Also, electrochemical deposition can be controlled easily and precisely using potentiostat instrumentation [9]. Various types of Cu oxides can be deposited by electrodeposition method and can be studied to understand their behavior in CMP related environments.

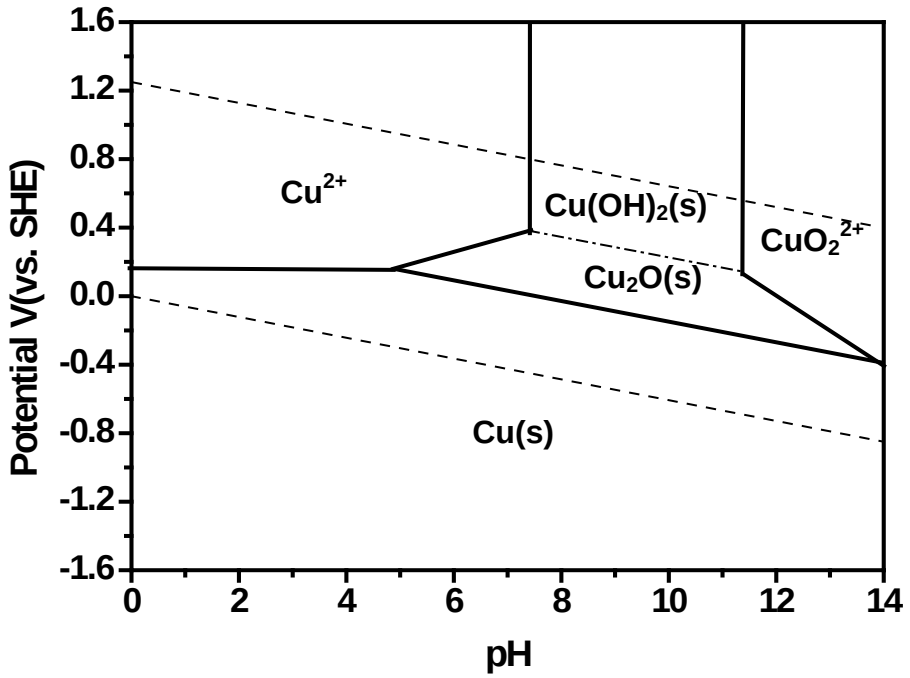

Figure 3-1 Pourbaix diagram of Cu – domains of corrosion, immunity and passivation for copper.

3.2 Experiment

A three electrode system with Ag/AgCl as reference electrode from CHI Inc. was used for electrochemical studies. Cu and Ru electrodes were used as working electrodes. Both Cu and Ru electrode were covered with epoxy resin

and fine polished by 0.5 μm size polishing pad. Platinum foil was used as counter electrode. All electrochemical experiments were performed using 760 mode potentiostat from CH Instrument Inc.

Cu electrode was made from Cu rod that was purchased from ESPI with 99.999% purity. Cu native oxide layer was produced by exposing Cu electrode to air or immersing into 0.1 M $NaHCO_3$ at pH 8.8 for varied periods of time. A ruthenium electrode (99.995%) was used as working electrode on which a thin layer of copper layer *ca.* 100 nm was electrodeposited using 0.05 M $CuSO_4$/0.5 M H_2SO_4 solution. Ru was chosen as the substrate because of its ability to plate Cu directly and its potential usage as Cu diffusion barrier in interconnects fabrication process [10].

The Cu_2O plating solution was prepared by adding 450mL of 5 M NaOH to 90 g of cupric sulfate pentahydrate with 150mL of 85% lactic acid (0.6 M $CuSO_4$ within lactate pH 9). The pH was adjusted to a final value in the 9-12 range with adding additional 5 M NaOH [7]. All chemicals were reagent-grade and purchased from Sigma-Aldrich. The Cu_2O deposition was controlled by potentiostat in Cu_2O plating solution. And then the coated Cu oxide was characterized by cathodic chronopotentiometry in 0.1 M $NaHCO_3$ solution (pH 8.8) with constant current density (0.3mA/cm^2).

3.3 Electrochemical Deposition of Copper on Ru Surface

A thin Cu layer *ca.* 100nm was deposited on Ru electrode by cathodic

deposition in acidic Cu plating solution (0.05 M $CuSO_4$/0.5M H_2SO_4). Figure 3-2 shows that the coated copper layer can be reduced by holding at constant current density (-0.3mA/cm^2) in 0.1 M $NaHCO_3$ solution. From first curve of chronopotentiogram (red line) in Figure 3-2, the surface of freshly copper-deposited on Ru electrode was reduced to metallic copper after 12 seconds followed by the hydrogen evolution. In the second curve, the blue chronopotentiogram demonstrates the oxide free surface after electrochemically reduced the copper surface from the first curve. The reduction current plateau area (-0.5V to -0.6V) of first curve was disappeared after the complete electrochemical reduction pre-treatment.

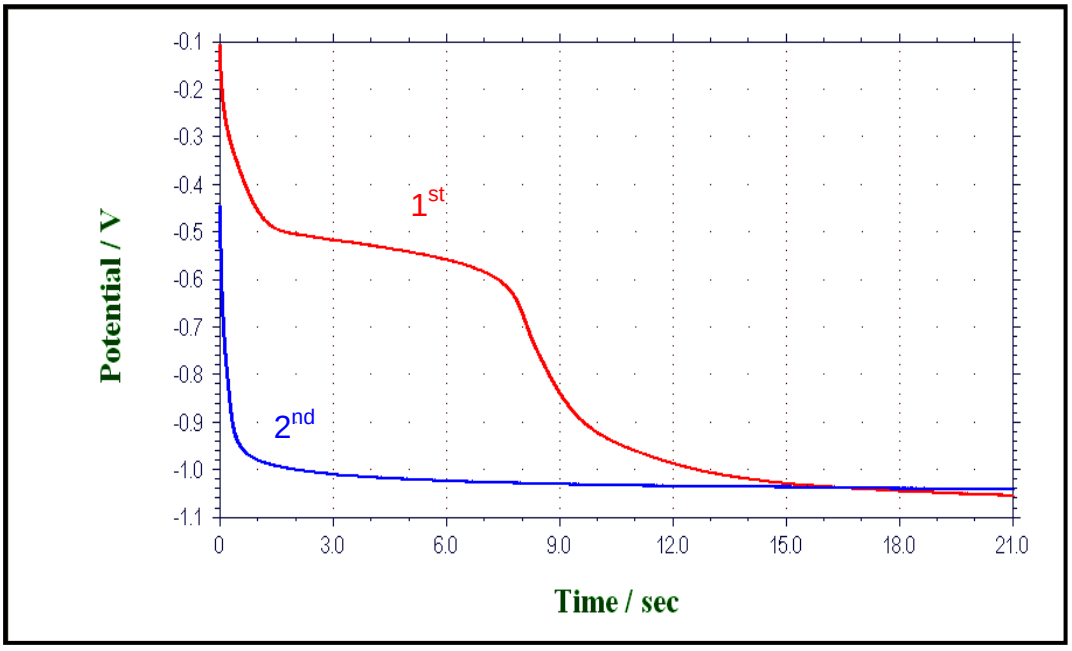

Figure 3-2 Chronopotentiogram of Cu reduction in 0.1 M $NaHCO_3$ solution. Red line (1^{st}) for freshly copper-coated Ru electrode and blue line (2^{nd}) for reduced copper-coated Ru electrode.

In order to verify that the surface of copper-coated ruthenium (Cu/Ru) electrode has the same behavior as copper electrode surface, the Figure 3-3, shows the overlapped cyclic voltammograms (CVs) of copper and Cu/Ru electrode in 0.1 M $NaHCO_3$ solution. It was observed that both anodic and cathodic peaks were similar to each other in copper and Cu/Ru electrode. The only difference between copper and Cu/Ru is in first cycle of voltammogram because the electrodeposited copper layer formed a thin oxide film on the top of Cu surface in acidic plating solution. Therefore, the cathodic peak C(II) at -0.6V (vs. Ag/AgCl) was pronounced at the first cycle (red line) rather than -0.5V (vs. Ag/AgCl) at the second cycle. The oxide layer was also seen in the chronopotentiogram (red line) in Figure 3-2.

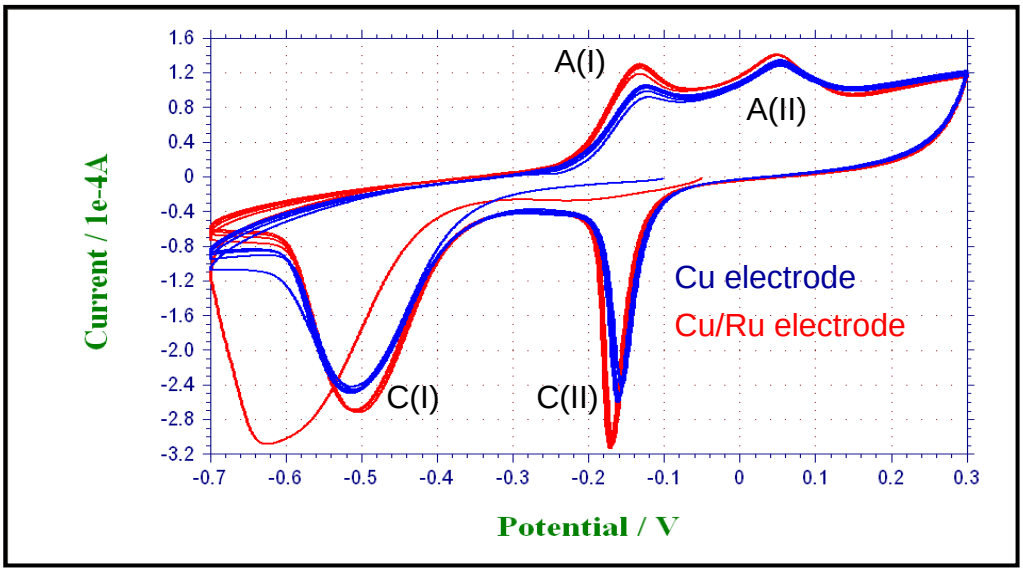

Figure 3-3 Cyclic voltammetry of Cu electrode (blue line) and Cu/Ru electrode (red line) in 0.1 M $NaHCO_3$ solution.

3.4 Electrochemical Characterization of Copper Native Oxide

The growth rate of native copper oxide under air exposure was studied by chronopotentiometry. The air-formed Cu oxide was reduced by applying a constant current density (-0.3mA/cm^2) in 0.1 M $NaHCO_3$ solution. This technique is called cathodic chronopotentiometry from which the layers of plateau indicate the different reduction potential of different oxide layers as shown in Figure 3-4 [11-13]. The reduction of cupric oxide takes place at -0.6V (vs. Ag/AgCl) and that of cuprous oxide at -0.8V (vs. Ag/AgCl). From the chronopotentiogram, the duration of each plateau demonstrates the amount of charge consumed for Cu oxide reduction reaction, from which the oxide layer that was formed upon air exposure can be quantified.

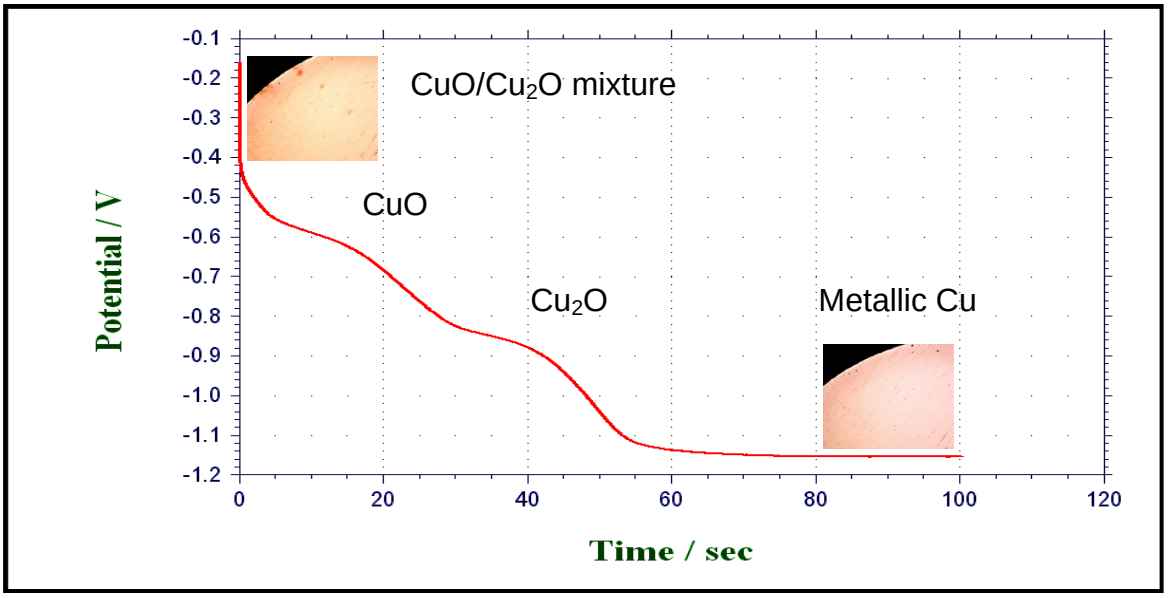

Figure 3-4 Cathodic chronopotentiogram of reducing Cu oxides in 0.1 M $NaHCO_3$ solution with constant cathodic current density (-0.3mA/cm^2).

In Figure 3-5, the chronopotentiogram shows reduction of the copper native oxide that was formed by exposing to air for different period of time such as 10 minutes, 90 minutes, 180 minutes and 24 hours. The native copper oxide formation reaches saturation after exposure to air for two hours. Figure 3-6 shows that the copper oxide layer can reach saturation after 15 minutes immersion in 0.1 M $NaHCO_3$ solution. Comparing the air-formed oxide with the oxide formed by immersion in 0.1 M $NaHCO_3$, the time required to reach oxide saturation is much faster in liquid than exposure to air. Also, the same reduction charge was observed for both type of Cu oxide since the same reducing time of 12 seconds needed when applying the constant cathodic current density (-0.3mA/cm^2).

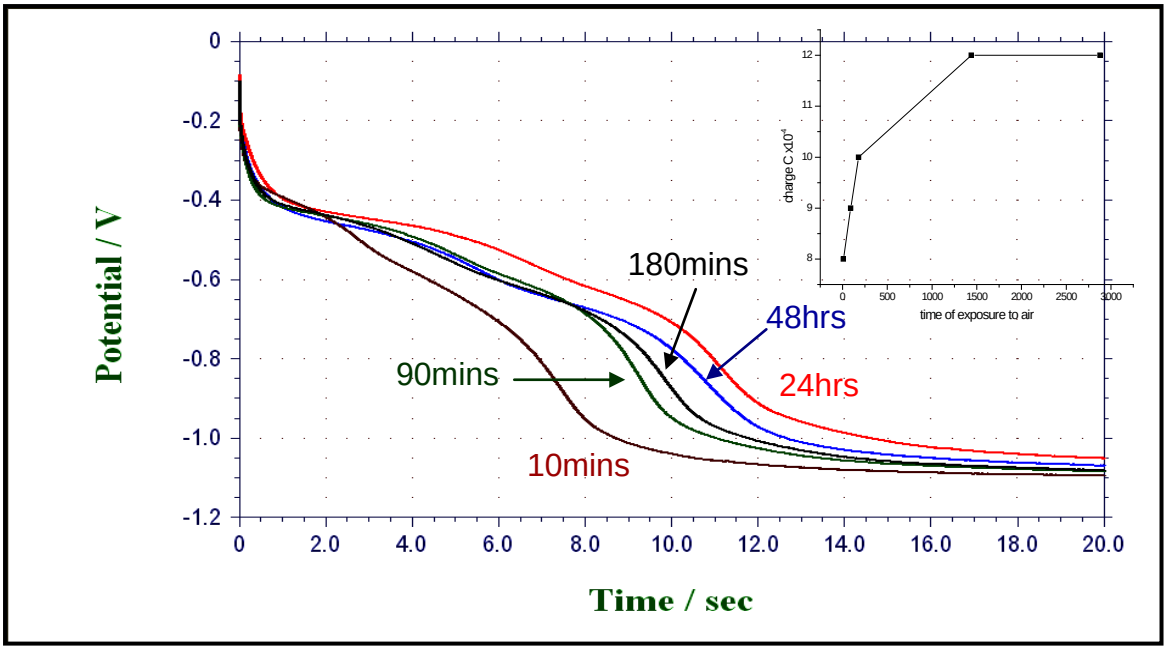

Figure 3-5 Cathodic chronopotentiogram of reducing Cu/Ru electrode in 0.1 M $NaHCO_3$ solution and after varying periods of air-exposed time (*Insert*: exposure time vs. relative charge).

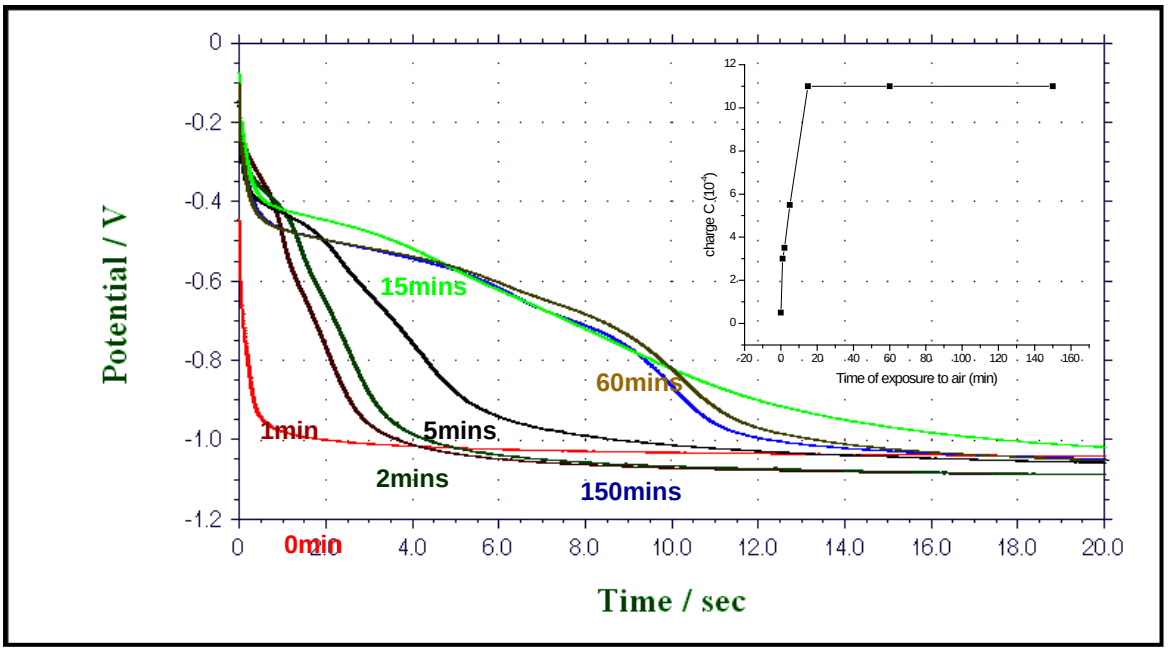

Figure 3-6 Cathodic chronopotentiogram of reducing Cu/Ru electrode in 0.1 M $NaHCO_3$ solution and after varying immersed time in 0.1 M $NaHCO_3$ solution (*Insert*: immersed time vs. relative charge).

The top passivation layer of Cu oxide formed rapidly to prevent from the further oxidation into Cu bulk. Therefore, the cathodic chronopotentiograms can provide the valuable reducing charge of Cu oxides to estimate the formation of each Cu oxide. For instance, the 0 to 6 second is the reduction of CuO and the 6 to 12 second is the reduction of Cu_2O. By calculating reducing charge into the ML of Cu oxides, the passivation film was covered with 1.4 ML of CuO and 2.8 ML of Cu_2O.

3.5 Electrochemical Deposition of Cu(I) Oxide

With the aim of forming only cuprous oxide (Cu_2O) layer, it is difficult to find a

specific potential for constant potential deposition of Cu_2O layer in Cu_2O plating solution (0.6 M $CuSO_4$ within lactate pH 9). Therefore, constant current density deposition was applied to deposit cuprous oxide with a current density value of -0.03mA/cm^2. The interesting phenomenon was shown in Figure 3-7 (blue line), that the potential started to oscillate after 15 seconds and the oscillation lasted for 40 seconds and disappeared when the plating solution was stirred as shown in Figure 3-7 (red line). The oscillating phenomenon was lasting for hours with higher deposition current density (-0.15mA/cm^2) as shown in Figure 3-8. Golden, Switzer and coworkers first discovered this oscillating phenomenon in 1996 [6]. The constant current deposition in Figure 3-8 shows that the potential oscillations were lasting for 100 seconds during Cu_2O/Cu deposition, and the oscillation period is a function of the solution pH, temperature, mass transport and solution concentration and each of spikes in the curve of chronopotentiogram represents the Cu_2O deposition. Switzer et al confirmed the self-assembly Cu_2O/Cu layered nanostructure [6]. The phenomenon of potential oscillation occurred due to the change of local pH. Cu metal deposition was thermodynamically favored at low pH condition and more negative potential (Eq. 3-1). Opposing to Cu, the Cu_2O deposition was favored at higher pH condition and more positive potential (Eq. 3-2). Due to the layered nanocomposites of Cu_2O/Cu in oscillation potential deposition, the layers of Cu inhibited the reduction reaction into inner or deeper layers of Cu_2O. Hence, the underneath of Cu_2O can not be reduced to metallic copper.

$Cu^{2+} + 2e^- \rightarrow Cu$ (Eq. 3-1)

$2Cu^{2+} + 2e^- + 2OH^- \rightarrow Cu_2O + H_2O$ (Eq. 3-2)

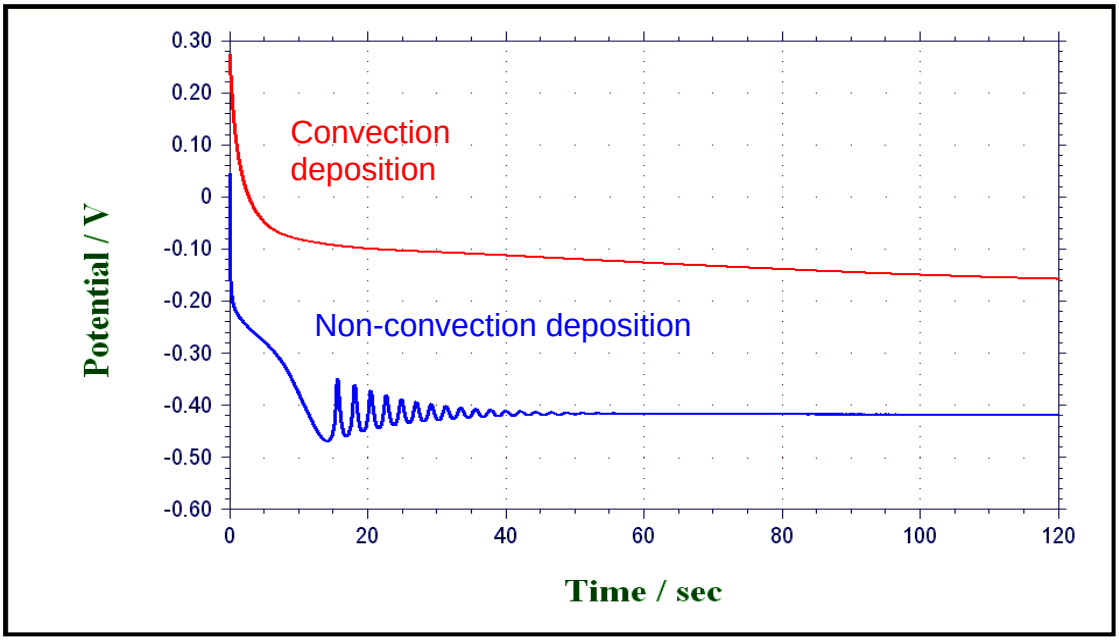

Figure 3-7 Electrodeposition of Cu_2O on Ru electrode by applying current density (-0.03mA/cm^2). The Cu_2O was deposited under stirring convection (red line) and deposited without stirring convection (blue line).

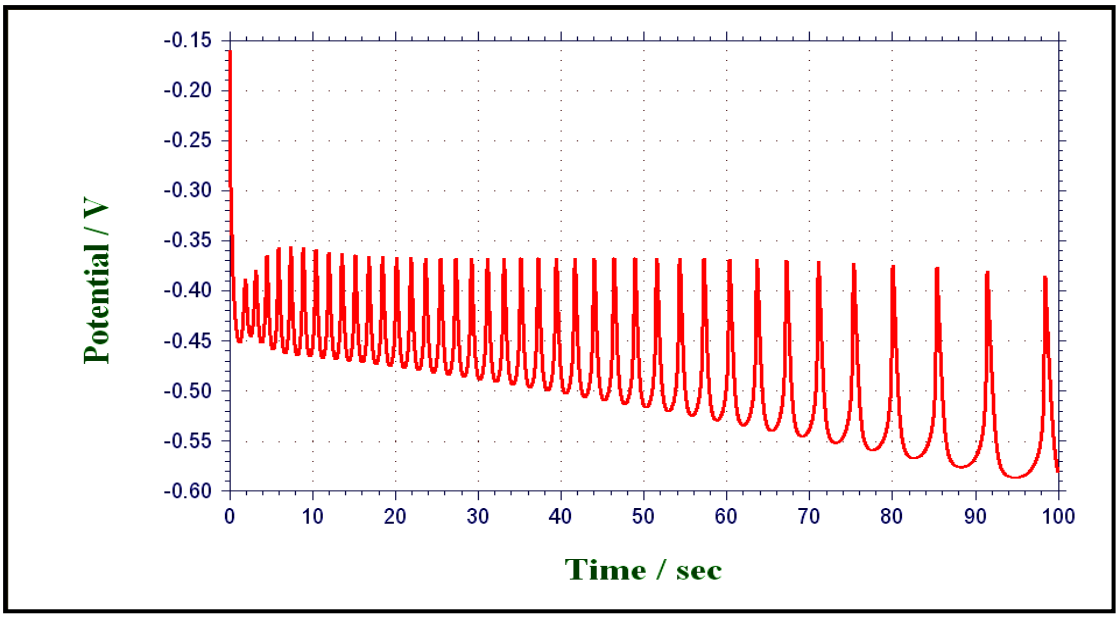

Figure 3-8 Electrodeposition of Cu/Cu_2O in 0.6 M $CuSO_4$ within lactate pH 9 solution with constant current density (-0.15mA/cm^2) on Ru electrode.

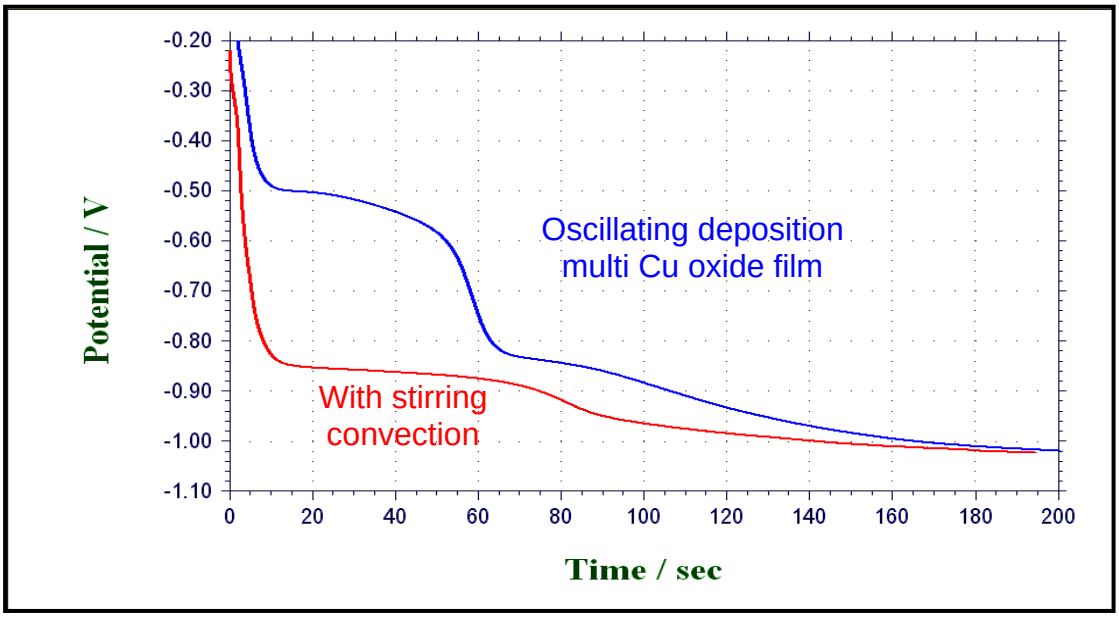

Figure 3-9 Cathodic chronopotentiogram of Cu reduction with constant current density (-0.3 mA/cm2).

In order to deposit uniform Cu_2O layer, the change of local pH on the Ru

electrode surface during the Cu_2O deposition needs to be carefully controlled. With the purpose of having a constant local pH, magnetic stirrer bar was used to create the continue convection in the Cu_2O plating solution. As a result, the oscillation potential phenomenon was removed as shown in Figure 3-7 (red line), which indicates only Cu_2O layer was deposited on the surface. In addition, cathodic chronopotentiometry showed (red line in Figure 3-9) only one reduction plateau with a reduction potential exactly at t he Cu_2O reduction potential around -0.8V, which provided strong evidence of Cu_2O layer deposition.

3.6 Removable of Cu_2O in Glacial Acetic Acid

The research group of K. L. Chavez et al reported that copper oxide layer can be removed without attacking or oxidizing the copper surface by using glacial acetic acid [4]. Copper has good resistance to corrosion in acetic acid [14]. However, acetic acid will react with Cu oxides to form cupric acetate as in the following reaction equations.

$$CuO + 2CH_3COOH \rightarrow Cu(CH_3COO)_2 + H_2O \qquad \text{(Eq. 3-3)}$$

$$Cu_2O + 4CH_3COOH \rightarrow 2Cu(CH_3COO)_2 + H_2O + H_2 \qquad \text{(Eq. 3-4)}$$

This method of etching copper oxide in acetic acid can be applied to verify the Cu_2O as deposited on Ru electrode. The experiment of constant current deposition of Cu_2O was repeated again under convection condition. The Cu_2O layer was deposited followed by removing oxide layer in glacial acetic acid. The Ru electrode surface after dissolving the Cu oxide layer, shows no residual Cu

metal, which was observed under microscope and also the OCP measurement of Ru electrode in 0.5 M H_2SO_4 is *ca.* 0.5V vs. Ag/AgCl suggesting that no Cu metal layer was present. In a separate experiment, the nanocomposites Cu/Cu_2O were deposited without any solution convection. With acetic acid etching, the multilayer of Cu/Cu_2O can not be removed because the Cu layer has higher corrosion resistance in acetic acid. Therefore, the Cu top layer inhibits the etching of Cu_2O underneath of Cu. The multilayer of Cu/Cu_2O remains as a visible brownish layer on the top of Ru electrode after acetic acid etching and the OCP measurement represents the OCP of Cu *ca.* 0.2V vs. Ag/AgCl on the Ru electrode. Based on the cathodic chronopotentiogram and glacial acetic acid etching results, only the Cu_2O layer was deposited on the Ru surface by constant current deposition in convection Cu_2O plating solution.

3.7 Electro-capillarity Deposition of Cu and Cu_2O

New methods of preparing single micro-particles or micro-pattern has been developed by physical vapor deposition or electrochemical deposition [15-18]. The technique of electro-capillary deposition was developed by capillary-based tools filled with the plating electrolyte. Cu or Cu_2O micro-pattern can be made by capillary electrodeposition by making the electrolyte droplet contacting the substrate as shown in Figure 3-10. One example of different thickness of Cu electro-capillary deposition is shown in Figure 3-11.

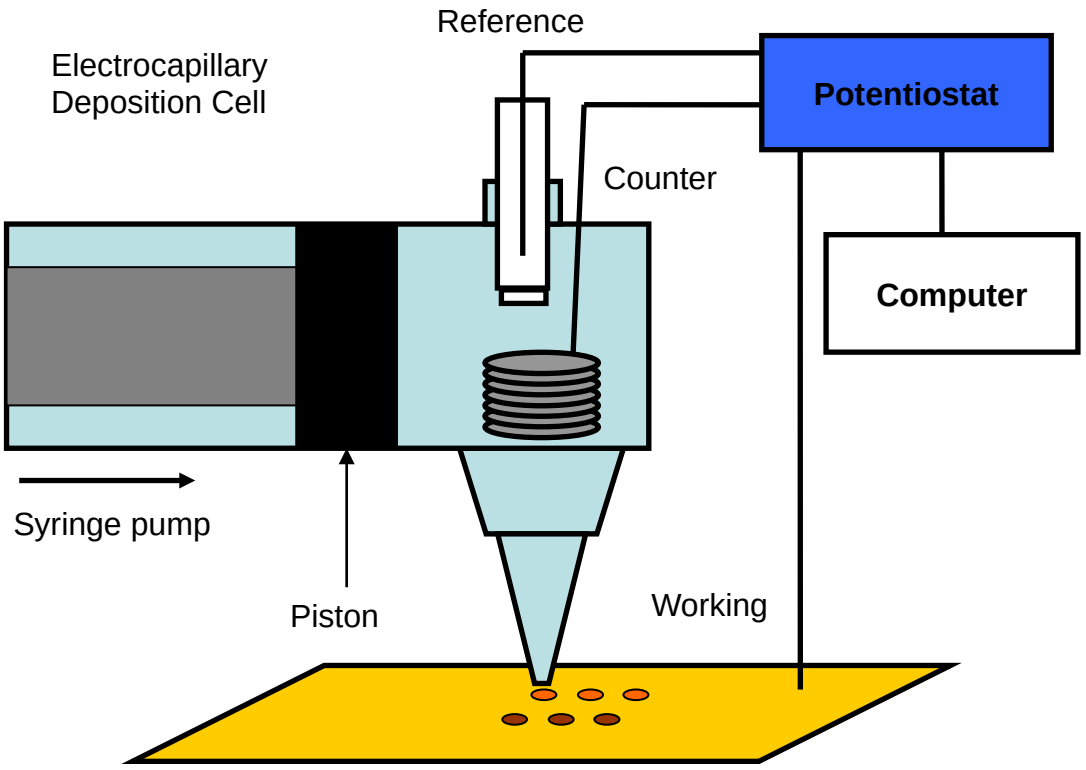

Figure 3-10 Electrocapillarity deposition of Cu and Cu_2O pattern on Au substrate.

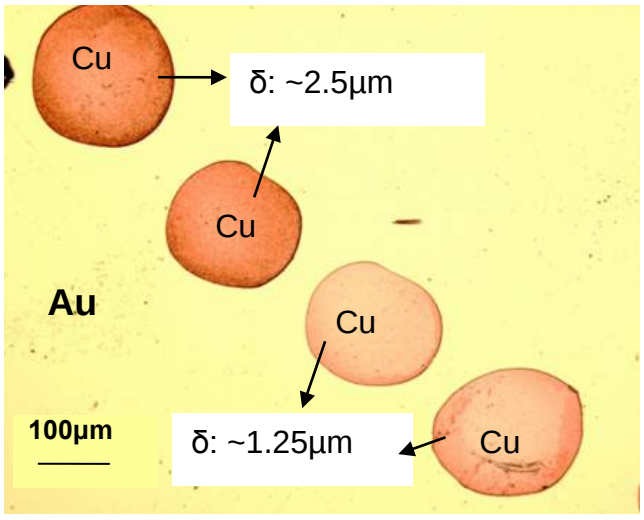

Figure 3-11 Electrocapillarity deposition of different thickness of Cu dots on Au substrate.

The electro-capillary technique was used to deposit Cu dots. Also, by quantifying the charge of Cu deposition on each dots and deposition area, the approximate thickness of Cu dots can be obtained. Whether or not it's Cu_2O dot, was verified by acetic acid etching and constant reduction in 0.1 M $NaHCO_3$ as shown in Figure 3-12(a,b). Utilizing the methodology of Cu_2O deposition with the electro-capillary technique, the corrosion rate of Cu and Cu_2O can be studied in the same environment in the same time. In Figure 3-13, the corrosion rate of Cu_2O was observed to be much faster than that of Cu in 5 mM gallic acid, the detailed mechanism of Cu corrosion in gallic acid will be discussed in chapter 5.

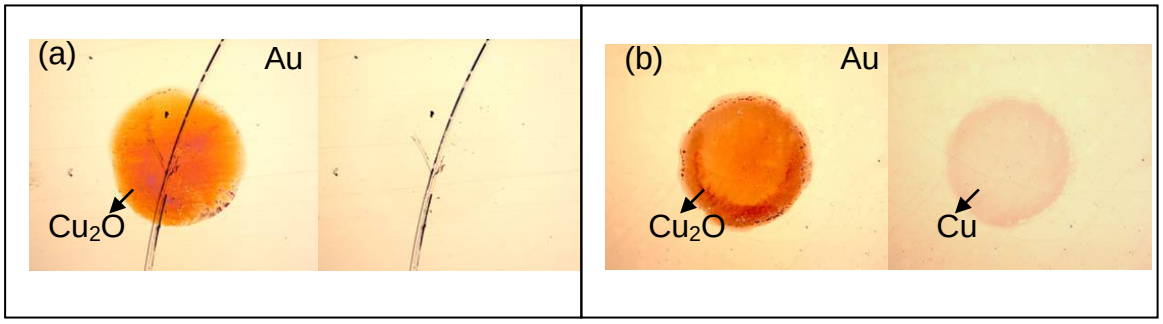

Figure 3-12(a) Corrosion screening of Cu_2O dot in acetic acid.
Figure 3-12(b) Reduction of Cu_2O dot in 0.1 M $NaHCO_3$.

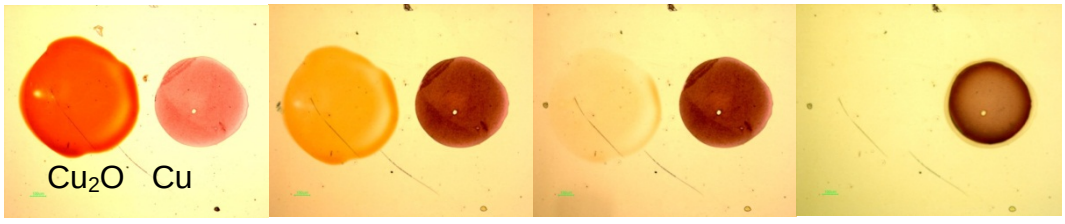

Figure 3-13 Corrosion screening of Cu and Cu_2O dots in 5 mM gallic acid at pH 9.

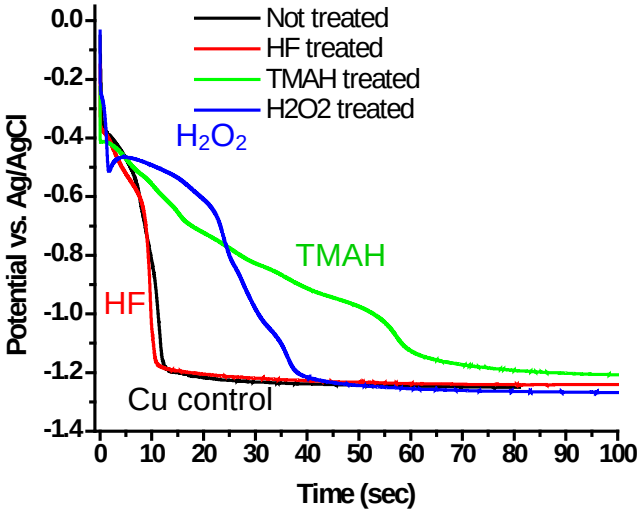

Figure 3-14 Cathodic chronopotentiograms in 0.1 M $NaHCO_3$: Cu wafer treated with different cleaning solutions for (10 min).

3.8 Cu Oxide Composition After Cleaning Process

It is important to characterize Cu oxide composition of Cu surface after different chemical cleaning treatments commonly used in IC fabrication. By looking into the different potential plateaus obtained from cathodic chronopotentiometry and their time duration, it allows us to selectively quantify the Cu(II) and Cu(I) composition. Figure 3-14 shows Cu wafer samples treated with cleaning solutions for 10 minutes. The cleaning solutions can be separated into three categories as shown in table 3-1. (i) Acidic Solution: 100 ml DIW + 1 ml 49% HF (0.49% HF, pH ≈ 1.5) (ii) Alkaline solution: 10 ml 10% KOH + 20 ml 25% TMAH + 70 ml DIW (pH ≈ 14) (iii) Oxidizing solution: 1 ml 10% KOH + 50 ml 30% H_2O_2 + 50 ml DIW (pH ≈ 7.8). The Cu(I) oxide was dominated in TMAH treatment and Cu(II) oxide was dominated in H_2O_2 treatment. The curve of HF is similar to the Cu control without treatment. It was expected that HF will remove Cu oxides

layers.

Generic Cleaning Solutions (recipe from Intel)	
HF	100 ml DIW + 1 ml 49% HF (0.49% HF, pH ≈ 1.5)
TMAH	10 ml 10% KOH + 20 ml 25% TMAH + 70 ml DIW (pH ≈ 14)
H_2O_2	1 ml 10% KOH + 50 ml 30% H_2O_2 + 50 ml DIW (pH ≈ 7.8)

Table 3-1 Three types of generic cleaning solutions

Our collaborator from Intel provides us with three different inhibitor-treated Cu wafers. It is interesting to find out the Cu oxide composition after different chemical cleaning treatments, Table 3-1.

Slot	Short Wafer ID	Treatment
1	70	A100, Alkaline inhibitor A (Cu-A)
2	891	B100, Alkaline inhibitor B (Cu-B)
3	100	C100, Alkaline inhibitor C (Cu-C)
4	218	Control, No treatment (Cu control)

Table 3-2 inhibitor-coated Cu wafers from Intel co.

Figure 3-15 demonstrates the cathodic chronopotentiograms of Cu control and Cu-inhibitors treated after each solution cleaning process. Based on the reduction potential in cathodic chronopotentiogram, the quantity of copper oxides such as $Cu(OH)_2$, CuO and Cu_2O can be separated by its duration of reduction plateau. Figure 3-16 summarizes the data of chronopotentiograms for all of the treatments by normalizing charge scale on the Y axis. Overall, there are more Cu (II) oxide after peroxide treatment, more Cu(I) oxide formation after TMAH treatment except Cu-B, and the inhibitor and oxide layer were removed by HF treatment. The Cu-A sample generated thicker Cu(I) oxide and Cu(II) oxide after TMAH treatment and H_2O_2 treatment, respectively. Therefore, the A inhibitor had

less inhibiting ability that can be removed easily by these cleaning treatments. That is consistent with the Intel's experimental result.

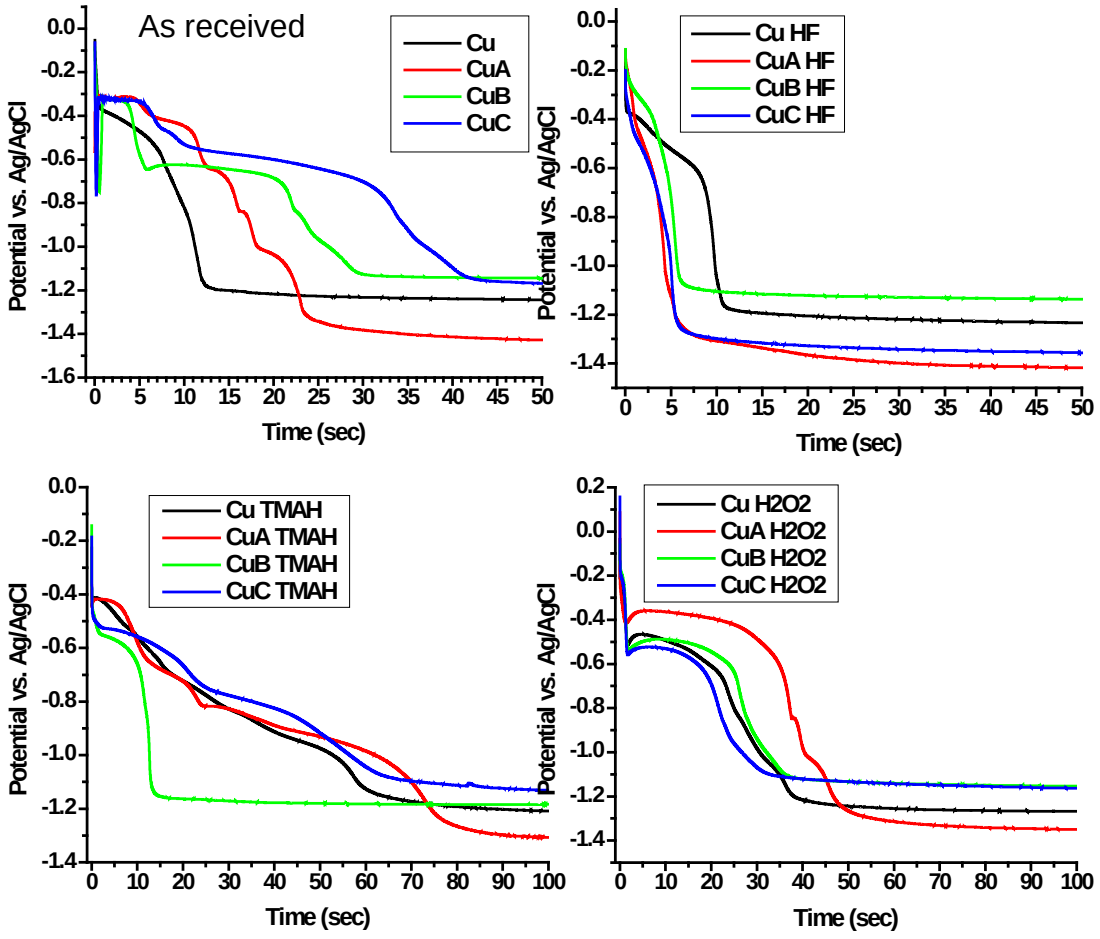

Figure 3-15 Cathodic chronopotentiogram in 0.1M $NaHCO_3$: Cu Control and Cu-inhibitors Treated Wafers (a) as received, (b) after HF treatment (c) after TMAH treatment (d) after H_2O_2 treatment.

Within TMAH treatment, most of the samples cumulated the Cu(I) oxide on Cu surface that is expected to in high alkaline condition. But the Cu-B sample has higher corrosion resistance in TMAH treatment than other samples. Hence, only thin layer of Cu(I) oxide was formed after TMAH treatment.

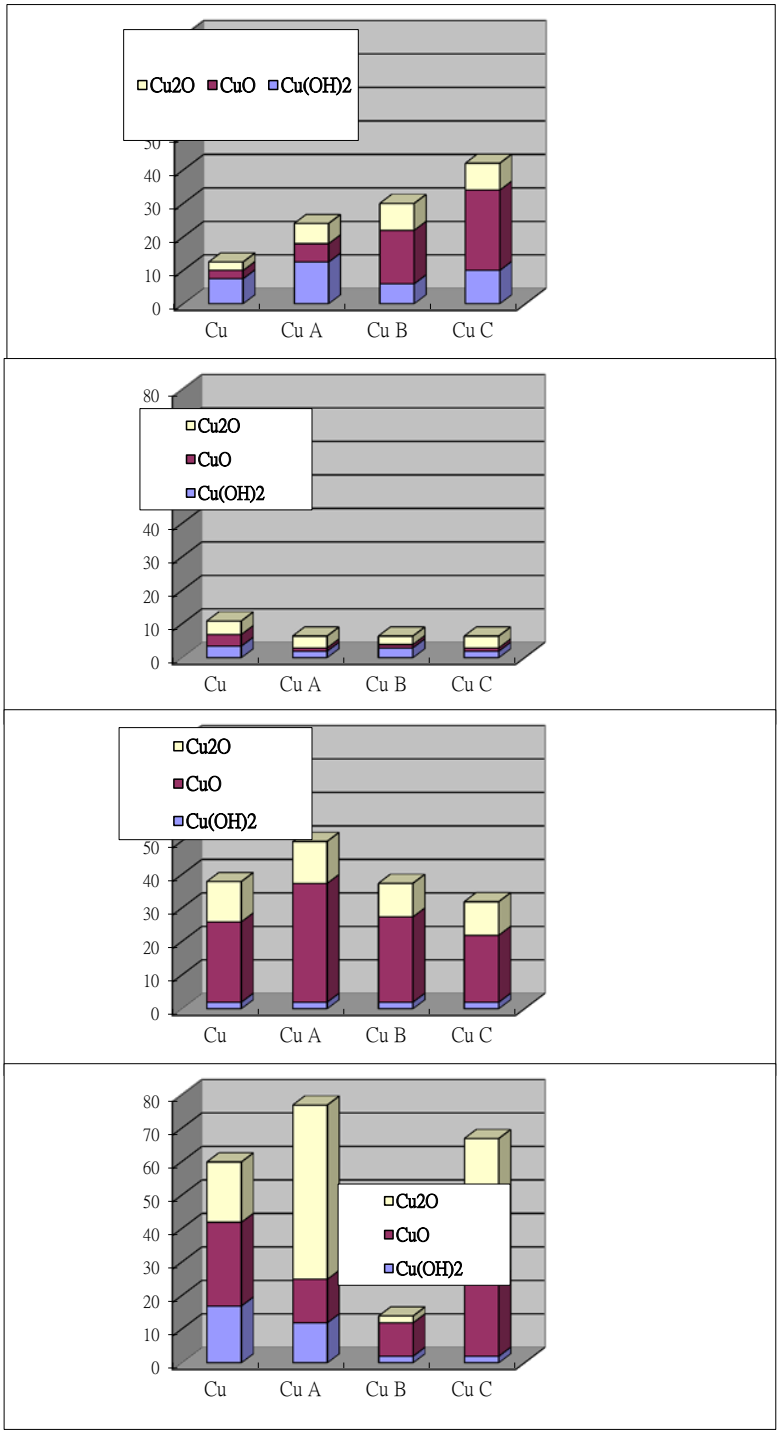

Figure 3-16 Cu oxides Composition after Treated with HF, TMAH and H_2O_2 solution.

3.9 Characterization of Cu Oxides by X-ray Photoelectron Spectroscopy (XPS)

XPS is a powerful tool to characterize the surface chemistry and its oxidation state. In this section, the XPS is used to characterize the Cu oxides. According to national institution of science technology (NIST) data base as shown in Figure 3-17, the binding energy of Cu(0) and Cu(I) at Cu 2p range are closely similar to each other. However, owing to the Cu $3d^9 \rightarrow$ Cu $3d^8 4s^1$ transition, the shake-up satellite peaks of Cu(II) $3d^9$ at Cu 2p range allows the distinction between metallic Cu(0) or Cu(I) and Cu (II).[19] For example, the XPS result of aged Cu powder in Figure 3-18(a) shows the Cu(0) and Cu(I) at Cu 2p are closely similar to each other. However, the XPS result of the mixture CuO and Cu powder is shown in Figure 3-18(b). The shake-up satellite peaks can indicate the present of Cu(II) at Cu 2p range.

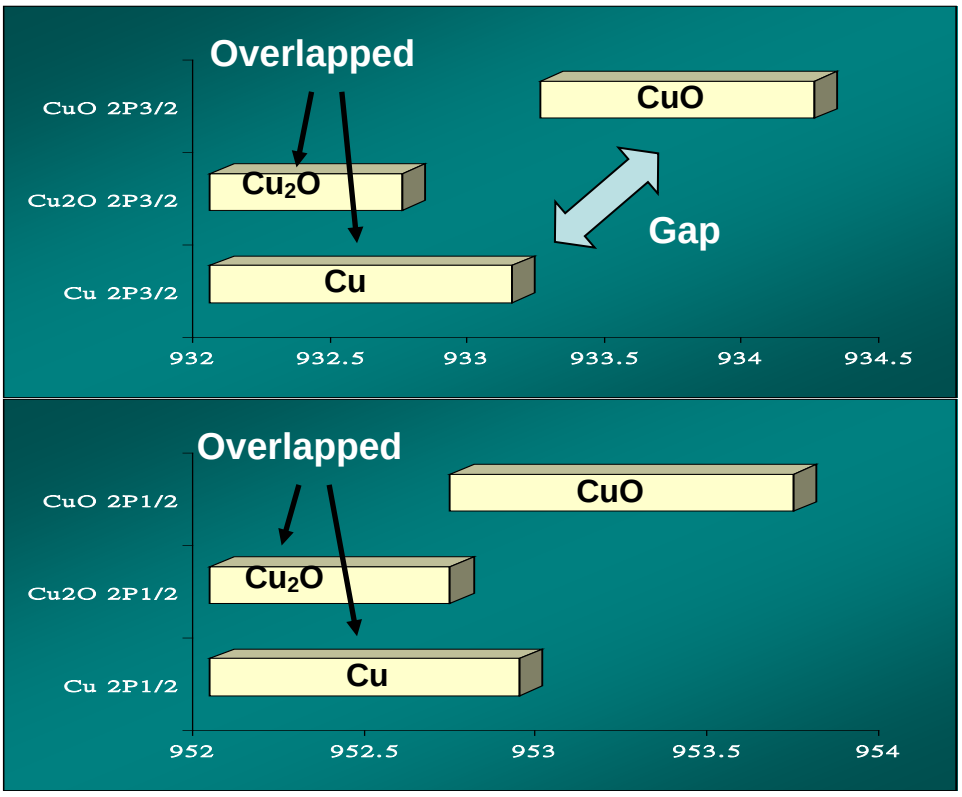

Figure 3-17 Cu and Cu_2O are hard to distinguish at Cu 2p XPS peak range, but CuO can be separated from Cu_2O and Cu at Cu 2p XPS peak range due to the satellite peak (peak range was collected from NIST data base).

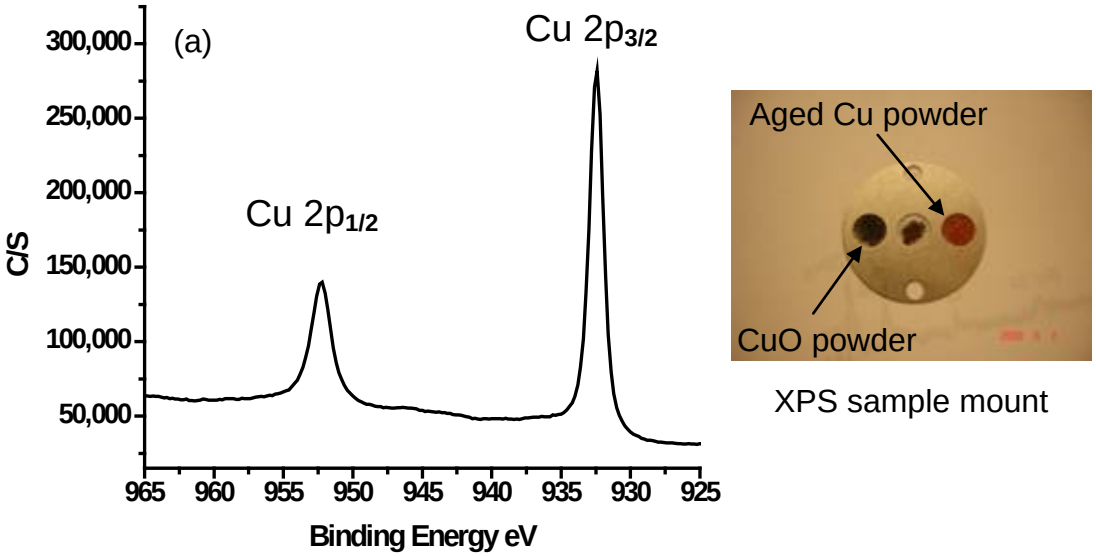

XPS sample mount

Figure 3-18(a) Example of XPS Cu 2p: Cu(0) and Cu(I) mixture from aged Cu powder.

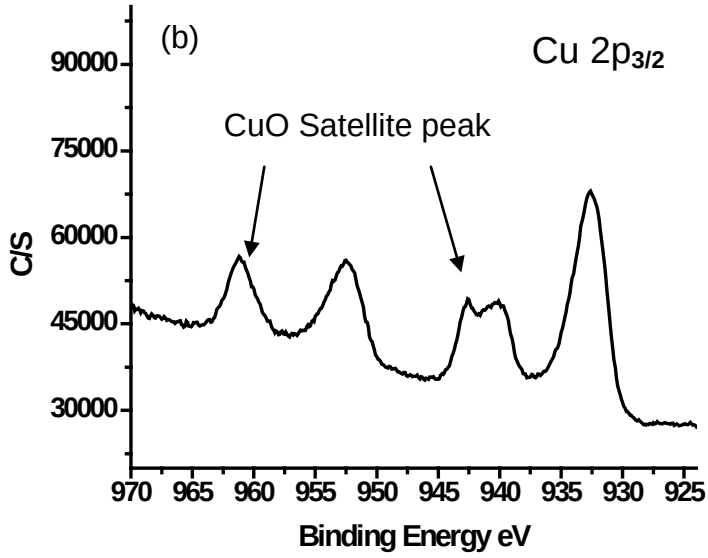

Figure 3-18(b) Example of XPS Cu 2p: Cu(II) from CuO power.

To overcome the problem of characterizing Cu(0) and Cu(I), the X-ray induced Auger Cu peak $L_3M_{4,5}M_{4,5}$ can be used to distinguish metallic Cu(0) and Cu(I), due to the differences in electron relaxation energies in these species

[20,21]. From the NIST data base as shown in Figure 3-19, the electron relaxation energies at LMM show more than 1 eV gap between Cu_2O and metallic Cu, which can help to characterize the Cu(I) and C(0).

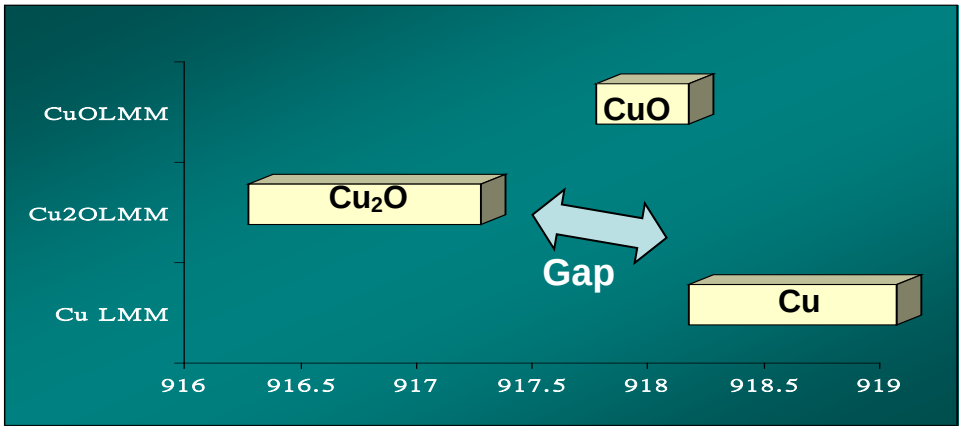

Figure 3-19 Cu_2O and Cu can be distinguished in Auger $L_3M_{45}M_{45}$ peak range.

The Cu rod with 99.995% purity was freshly polished and aged by exposure to air for two weeks. The air-aged Cu rod was attached on XPS sample mount with carbon tape. The small piece of Au film was attached on the top of Cu rod as reference. From the XPS of Cu 2p range, the surface of Cu rod doesn't present the layer of Cu(II) oxide after two weeks of air exposure, confirmed by the absence of satellite peaks in Cu 2p range as shown in Figure 3-20(c). After removing the oxide layer by Ar^+ ion sputter cleaning for *ca.* 75Å, the peak of O1s became leveled as shown in Figure 3-20(a) which illustrates the 75Å of Cu_2O layer was removed. In summary, oxygen diffused into Cu 75Å deep and mainly formed Cu_2O for two weeks of air exposure under room temperature.

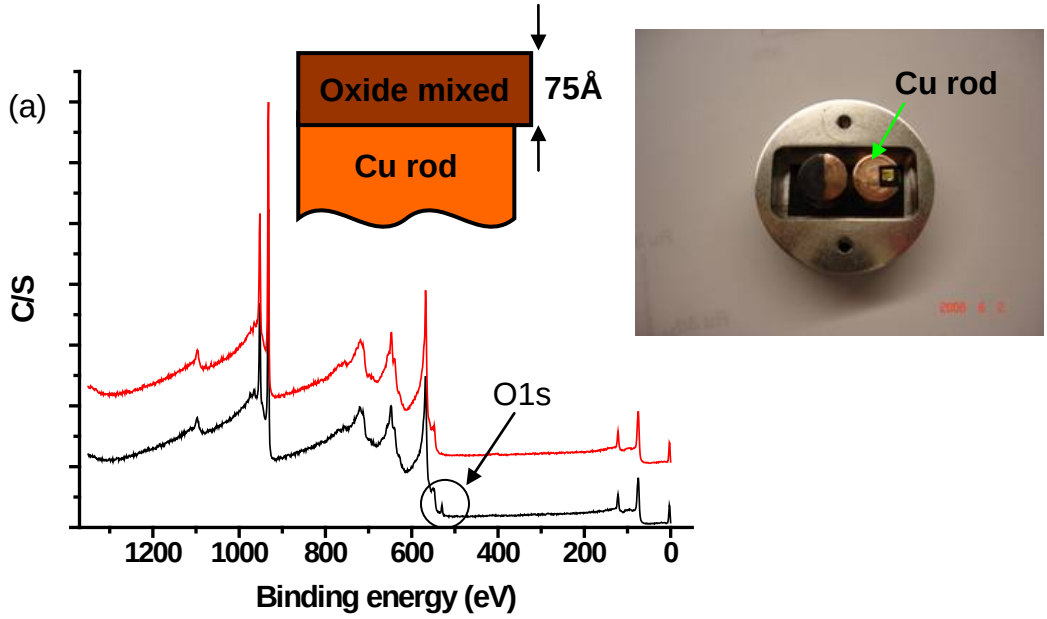

Figure 3-20(a) XPS survey scan of Cu rod before and after Ar^+ ion sputtering for 75Å.

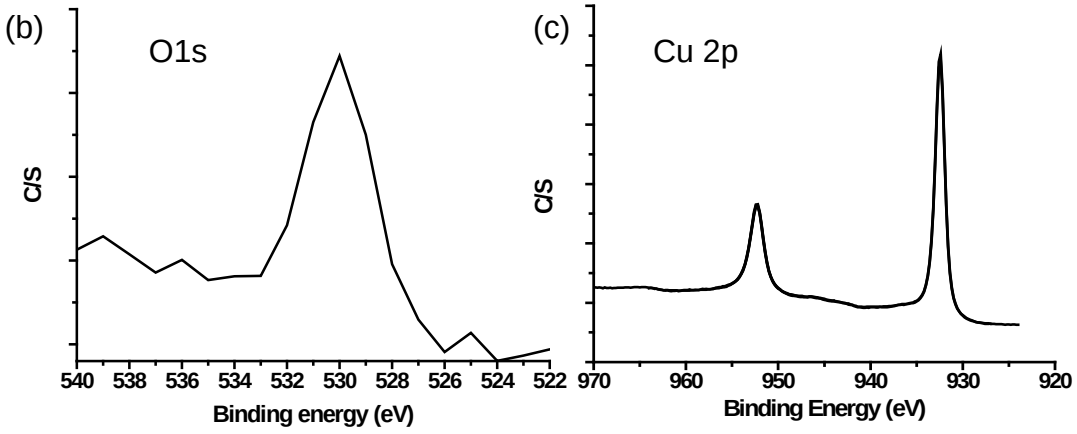

Figure 3-20(b) XPS of O1s enlarged from survey scan of (a) black line, (c) XPS of Cu rod on 2p range after Ar^+ sputtering 75 Å.

Also, the XPS was used for characterizing the growth of Cu_2O in different pH condition. In Figure 3-21, it was shown that the Cu pattern present on Ru substrate can grow the Cu_2O passivation layer after immersing in 0.1 M K_2SO_4 at pH 5 for 90 minutes. The Cu_2O layer also grew in high alkaline condition (0.5 M KOH) for 90 minutes as shown in Figure 3-22. From the depth profiling data, the thickness of the Cu_2O layer was about 20 nm. However, the Cu_2O grew slowly when the pH was *ca.* 6-12 at room temperature.

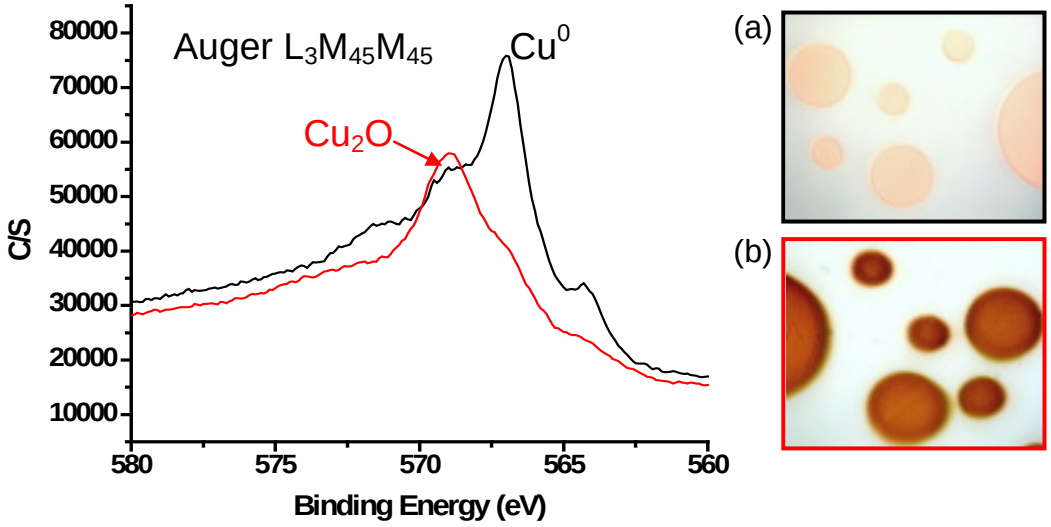

Figure 3-21 XPS auger $L_3M_{45}M_{45}$ peaks of (a) Cu pattern as deposited black line (b) Cu(I) oxide dominated dots after treated in 0.1 M K_2SO_4 at pH 5 (red line).

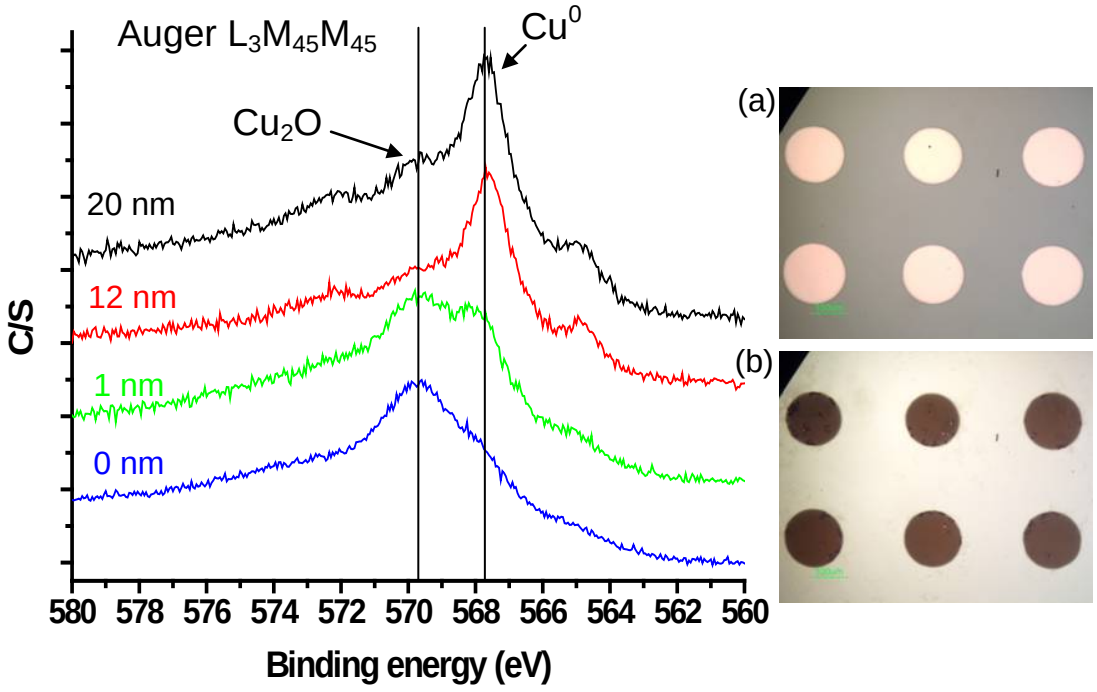

Figure 3-22: XPS auger $L_3M_{45}M_{45}$ peaks of progressing Ar^+ sputtering (0, 1, 12, and 20 nm) on Cu(I) oxide microdots. (a) freshly prepared Cu pattern (b) Cu(I) oxide dominated dots after treated in 0.5 M KOH.

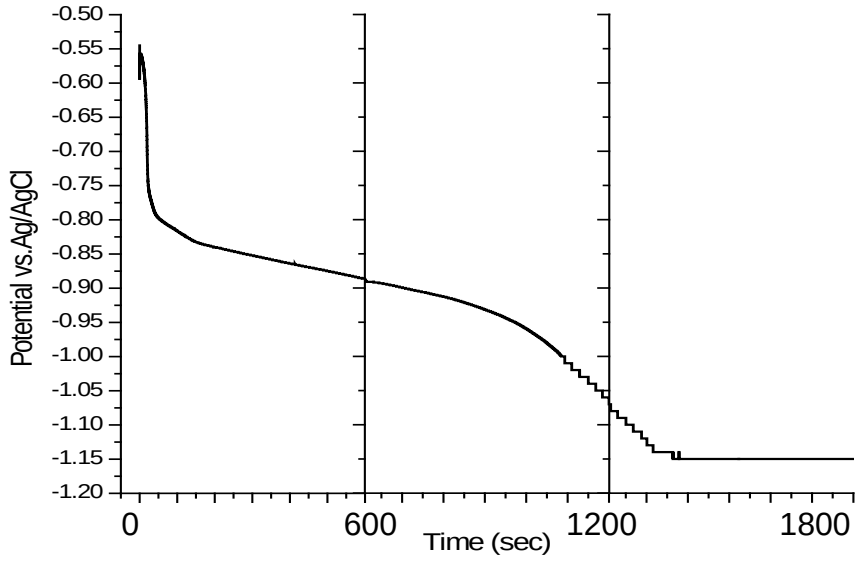

Figure 3-23: Cathodic chronopotentiogram of reducing Cu_2O film that was made by immersing in 0.5 M KOH for 36 hours

The electrochemical characterization of the Cu_2O film prepared by immersing in 0.5 M KOH was shown in Figure 3-23. The cathodic chronopotentiogram illustrates that the Cu_2O film was dominated in high alkaline condition (0.5 M KOH). Therefore, the XPS and electrochemical characterization results are consistent in identifying Cu_2O formation.

3.10 Electrochemical Characterization of Cu Corrosion Inhibitor (BTA)

3.10.1 Tafel Plots and Cyclic Polarization Curves of Cu

By the cross extrapolation of cathodic and anodic current branches from Tafel plot curve, the corrosion current (I_{corr}) and corrosion potential (E_{corr}) can be estimated. The anodic branch refers to the oxidation polarization; the cathodic branch refers to the reduction polarization. Moreover, the cyclic polarization curve

as shown in Figure 3-24(b) is plotted by potentiodynamic scan (X-axis) vs. the log value of absolute current density (Y axis) obtained from CV in Figure 3-24(a). In other words, the cyclic polarization is the Tafel plot with reverse scan or log function of absolute current in cyclic voltammegram. By utilizing the cyclic polarization scan, the corrosion behavior can be understood. Also, the cyclic polarization diagram can study the effect of corrosion inhibitor on protecting substrate from corrosion in the environment that is concerned.

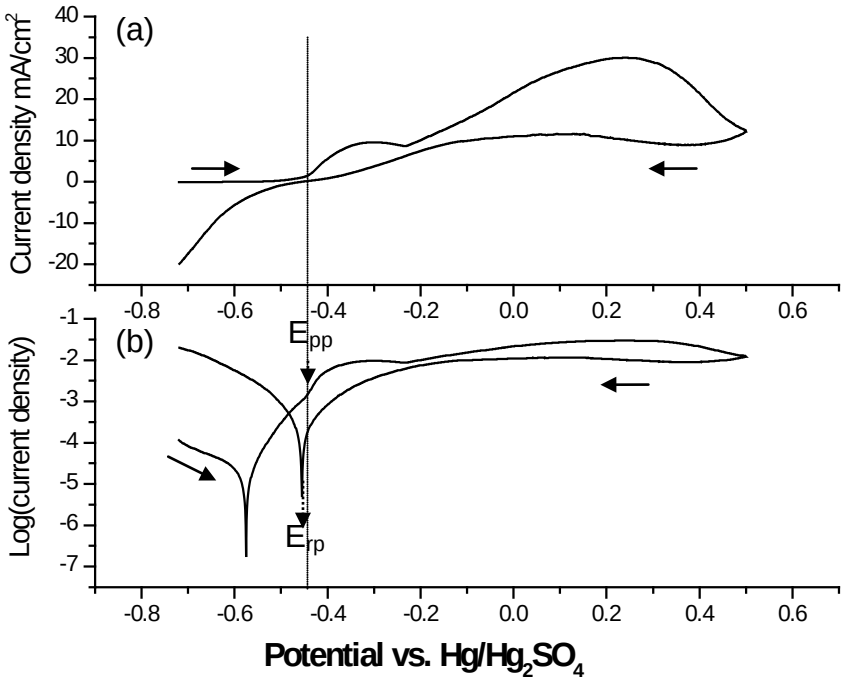

Figure 3-24 (a) LSV of Cu electrode in 0.1 M HCl (b) Tafel plots of Cu electrode in 0.1 M HCl.

Figure 3-24 (a) shows the cyclic voltammegram of Cu electrode in 0.1 M HCl and its corresponding cyclic polarization scan as shown in Figure 3-24 (b). There are several additional quantities appear in cyclic polarization [22] scan such as

the primary passivation potential (E_{pp}) and repassivation potential (E_{rp}) as shown in Figure 3-24 (b). In general, the corrosion will keep going when the OCP is greater than E_{rp}, and will stop when OCP is less than E_{rp} [23]. In Figure 3-24, the Cu electrode was started to dissolve in HCl solution from -0.57V to -0.45V (vs. Hg/Hg_2SO_4) and then electrochemically oxidized to Cu(I) oxide and Cu(II) oxide after more positive potentials of -0.45V and -0.2V, respectively. Thus, the corrosion rate slowed down because the E_{rp} of Cu(II) was greater than OCP of Cu (-0.55V vs. Hg/Hg_2SO_4).

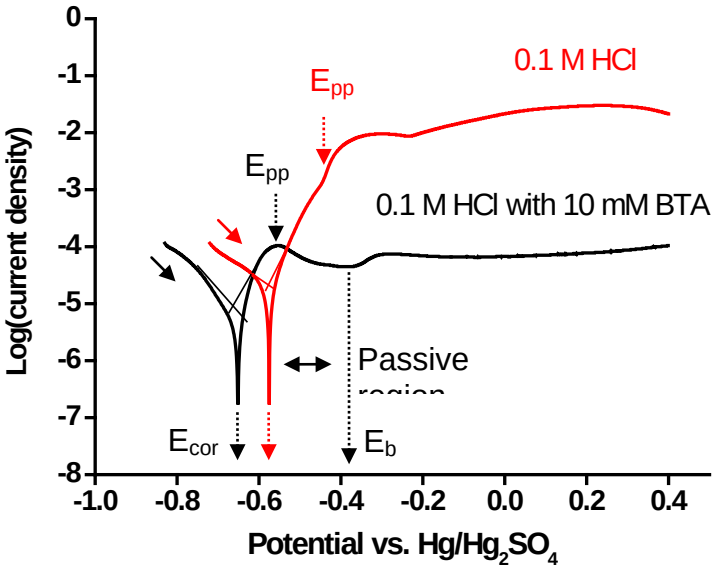

Figure 3-25 Tafel plots of Cu electrode in 0.1 M HCl (red)/10 mM BTA (black).

In Figure 3-25, the anodic branches of Tafel plots illustrates the effect of corrosion inhibitor (BTA, benzotriazole) on Cu corrosion in 0.1 M HCl. Without adding BTA, the anodic branch is much higher than cathodic branch, which demonstrates the corrosion occurred spontaneously. The reference of electrode

satd. Hg/Hg_2SO_4 is at 0.64V corresponding to the SHE. Also, from the point view of Pourbaix diagram in Figure 3-25, there is no passivation layer in 0.1 M HCl (pH = 1) between Cu and dissolved Cu^{2+} comparing with alkaline condition. With additional 10 mM BTA, the corrosion current, I_{corr}: 21.72μAmp/cm^2 decreased to I_{corr}: 9.77μAmp/cm^2. The E_{pp} and E_b are well defined in the anodic branch as shown in Figure 3-25 (black line). The E_b is a breakdown potential which is defined as the potential where the first corrosion current increase after E_{pp}. E_b represents the breakdown potential of the passivation film. The passive region is the portion of the curve between E_{pp} and E_b. The passive region depicts that a thin protective film forms on the top surface to prevent from further corrosion or slow down the corrosion rate. Hence, the passive region on Cu was observed for BTA solution. A thin layer of absorbed BTA on Cu electrode behaves as a protective film to inhibit the corrosion of Cu.

Cu electroplating is usually carried out in acidic electrolyte. For example, the Cu interconnects was electrodeposited in HCl solutions. However, the CMP and post CMP processes is usually performed under alkaline condition where the corrosion inhibitors are added to protect the Cu interconnects. Therefore, it is important to understand the corrosion behavior of Cu in alkaline conditions.

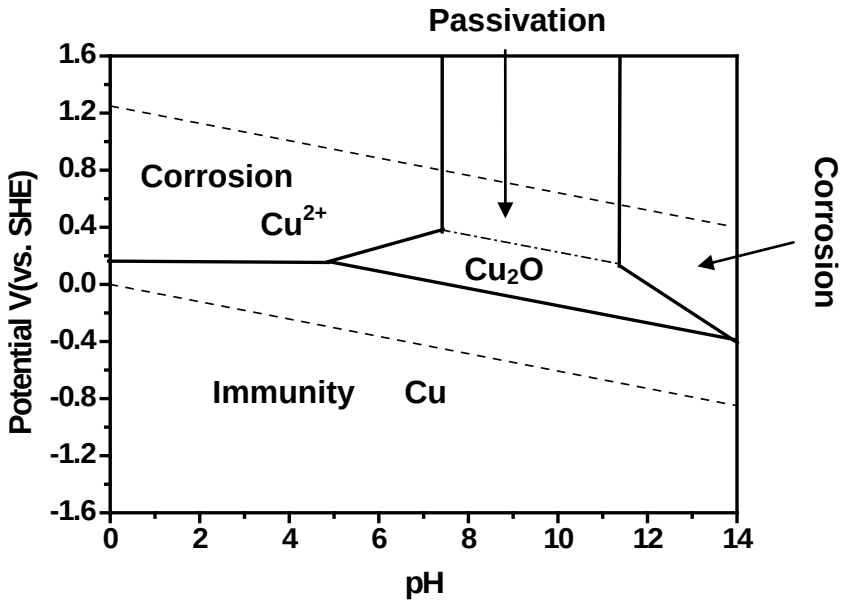

Figure 3-26 Pourbaix diagram of Cu – Domains of corrosion, immunity and passivation for copper.

Figure 3-27 shows the LSVs and Tafel plots of Cu electrode in alkaline solution. The pH value of 0.1 M KOH and 0.1 M NH_4OH is pH 13 and pH 11.4, respectively. The Cu surface formed protective thin film at alkaline condition base on the pourbaix diagram (Figure 3-26). Therefore, without adding any inhibitor, the passive region between E_{pp} and E_b can be found on anodic branch in both KOH (red line) and NH_4OH (black line) solution. The width of passive region as shown in 3-27(b) is used to identify protective film, which means the longer in 0.1M KOH (-0.58V to -0.45V) is better than in 0.1M NH_4OH (-0.6V to -0.57V). Also, base on Pourbaix diagram, the higher alkalinity of 0.1M KOH (pH 13) should form passive film at lower potential than 0.1M NH_4OH (pH 11.4). However, the potential of passive region of Cu in NH_4OH is lower than in KOH because the protective film with Cu(I) formed will be dissolved by forming complex with

ammonia ligands.

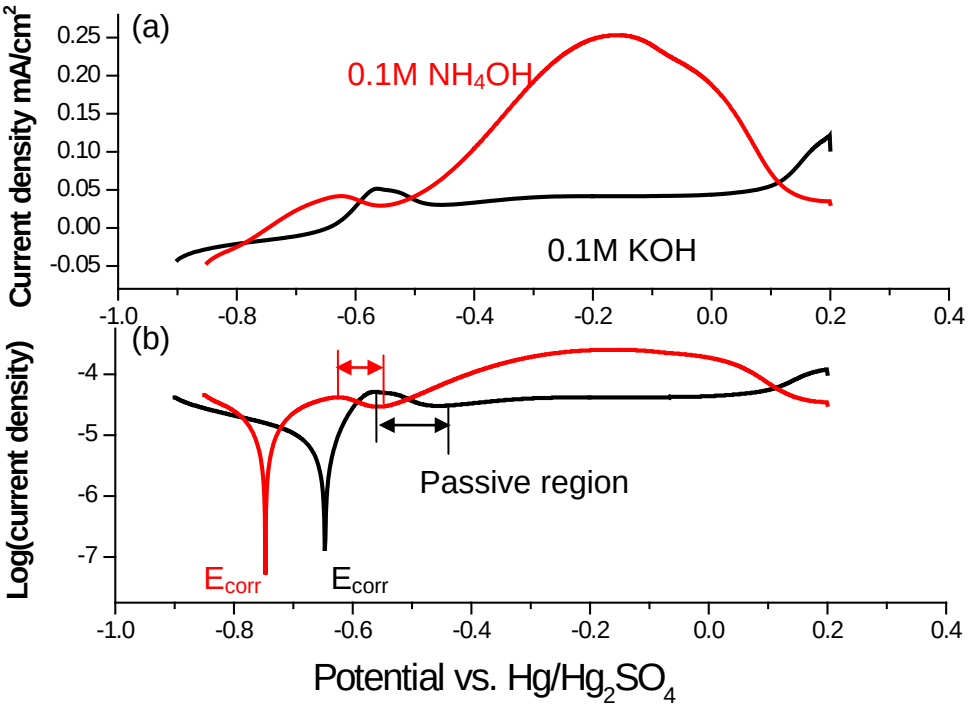

Figure 3-27 (a) LSVs of Cu electrode in 0.1 M KOH (black) and 0.1 M NH_4OH (red). (b) Tafel plots of Cu electrode in 0.1 M KOH (black) 0.1 M NH_4OH (red).

The effect of BTA on inhibition of Cu corrosion in 0.1 M NH_4OH is shown in Figure 3-28. The corrosion current of Cu, I_{corr} was decreased *ca.* 20 times with containing 10 mM of BTA. Also, the corrosion potential of Cu E_{corr} was shifted to higher range even higher than 0.1 M KOH as shown in Figure 3-27 (b), which is supposed to be base on Pourbaiz diagram. Therefore, the BTA absorbed Cu surface as a protective film makes Cu less active in NH_4OH ambient.

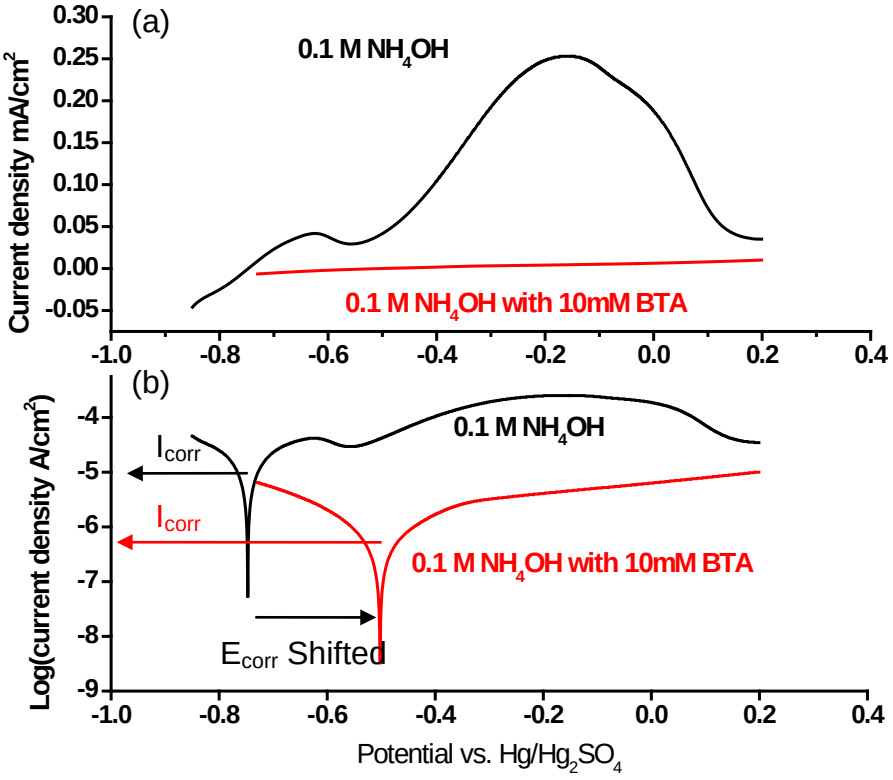

Figure 3-28 (a) LSVs of Cu electrode in 0.1 M NH_4OH (black)/10 mM BTA (red) (b) Tafel plots of Cu electrode in 0.1 M NH_4OH (black)/10 mM BTA (red).

3.10.2 Cyclic Voltammegrams of Cu

Besides Tafel plots and cyclic polarization curves, the cyclic voltammograms was also used to characterize the BTA inhibition. Figure 3-29 demonstrates the effect of BTA on Cu surface. As mentioned before (Figure 3-3) oxidation peak of Cu/Cu(I) on anodic curve at -0.15V. With 10 mM BTA, the both oxidation peaks of Cu/Cu(I) and Cu(I)/Cu(II) were decreased. Especially the oxidation peak of Cu/Cu(I) was leveled in the portion of anodic curve.

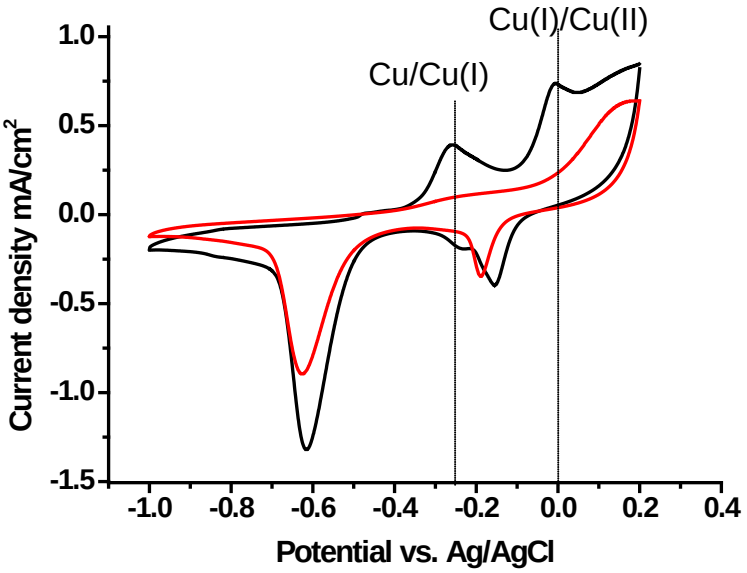

Figure 3-29 CVs of Cu electrode in 0.1 M KOH (black line)/ 20 ppm BTA (red line).

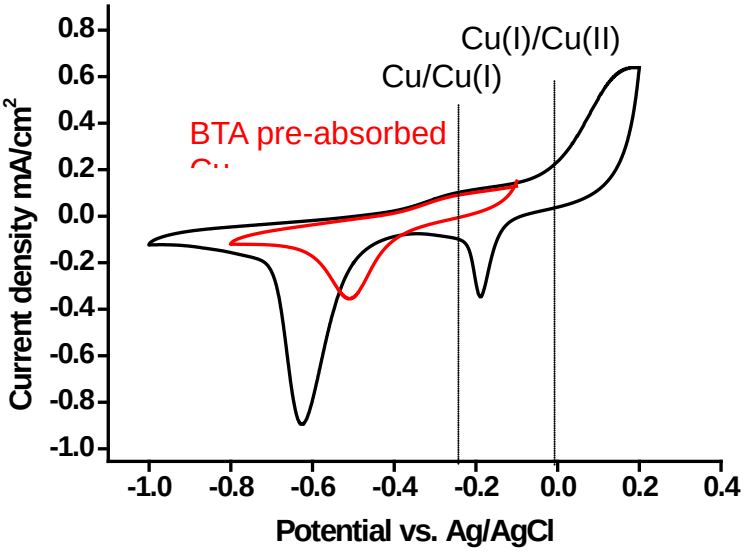

Figure 3-30 CVs of Cu electrode in 0.1 M KOH/20 ppm BTA (black line) and in BTA pre-absorbed Cu in 0.1 M KOH without BTA (red line).

The BTA pre-absorbed Cu electrode (BTA-Cu) was prepared by dipping in 20 ppm BTA/0.1 M KOH for 100 seconds and then rinsed by DI wafer. The CV of BTA-Cu in 0.1M KOH was shown in Figure 3-30 (red line). The black line is the CV of Cu electrode in 20 ppm BTA/0.1M KOH. The absent of oxidation peak of Cu/Cu(I) remained on BTA-Cu electrode even after continue 10 cyclic scans from -0.1V to -0.8V. But, the BTA protective film was removed after scanning toward more positive potential at 0.2V as shown in Figure 3-31 (CV with blue line) and then the second CV shows the oxidation peak of Cu(I)/Cu(II). Sequentially, the CV with green line shows the oxidation peaks of Cu/Cu(I). Hence, the breakdown potential (E_b) of BTA-Cu passivation film should be lower than 0.2V.

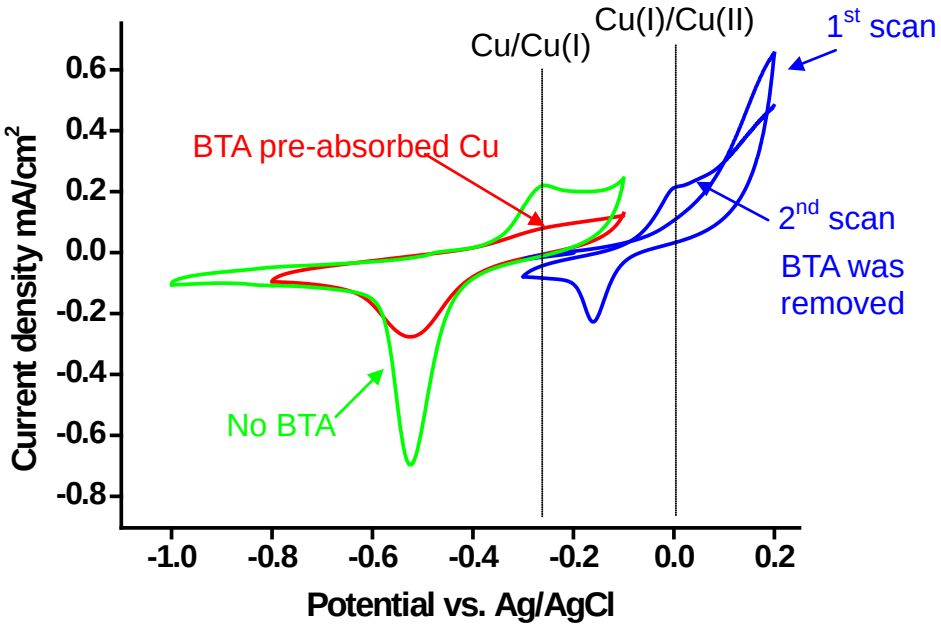

Figure 3-31 CV of pre-absorbed in 20 ppm BTA/0.1 M KOH Cu electrode in 0.1 M KOH without BTA.

In Figure 3-31, comparing the CV of BTA-Cu (red) with the CV of Cu (green), the reduction peak of Cu(I)/Cu is more pronounced on Cu than BTA-Cu surface. Hence, there is a limited protection of pre-absorbed BTA especially on high end of oxidizing potential which means the that BTA can protect Cu by absorbing on Cu or forming protective film with Cu(I) but not with Cu(II). Therefore, the reduction of Cu surface can not get rid of the BTA-Cu protective film.

3.11 Summary

In this chapter, the Cu oxides were characterized by XPS and chronopotentiometry. Moreover, this chapter represents two methodologies of making the cuprous oxide film. One is electrochemical deposition, the other one is treated in high alkaline condition. Both of the methods can make cuprous oxide pattern, which creates a useful platform for further study of corrosion rate in IC fabrication during CMP environments or photovoltaic properties in solar cell design. In addition, the cyclic voltammetry and cyclic polarization scan can characterize the corrosion behavior of metals. This chapter provides the example of Cu metal and corrosion inhibitor, BTA. Further corrosion inhibition study will be covered in part II.

3.12 References

1 L. O. Gronadhl, *Science* **1926,** 36, 306; *J. Am. Inst. Elect. Ingrs*. **1927,** 46, 215; *Rev. Mod. Phys*. **1933,** 5, 141.

2 B. Lange, *Photoelements and Their Applications*, Reinhold: New York, 1939.

3 P. Singer, *Semicond. Int.*, **1997,** 36 (Dec).

4 K. L. Chavez and D. W. Hess, *J. of Electrochemical Society*, **2001,** 148 (11) G64-G643

5 K.K. Yu, K. S.M. Pillai, P. R. Nalla, O. Chyan, *J. Appl Electrochem.*, **2010,** 40

6 Teresa D. Golden, Mark G. Shumsky, Yanchun Zhou, Rachel A. Vander Werf, Robert A. Van Leeuwen, and Jay A. Switzer, *Chem. Mater*. **1996,** 8. 2499-2504

7 Jay A. Switzer, Eric W. Bohanna, Teresa D. Golden, Chen-Jen Hung, Ling-Yuang Huang, and Mark Shumsky. *Mat. Res. Soc. Symp. Proc.* **1997,** 451, 283-288,

8 Jay A. Switzer, Chen-Jen Hung, , Ling-Yuang Huang, F. Scott Miller, Yanchun Zhou, Eric R. Ruab, Mark G. Shumsky, and Eric W. Bohanna, *J of Mat. Res*, **1998,** 13 (4) 909-916

9 Y.C. Zhou · Jay A. Switzer, *Mat Res Innovat,* **1998,** 2:22–27

10 Chyan, O. M. R. Ponnuswamy, T. U.S. Patent No. 7247554

11 Nandini V., Ashok K. M., and Srini R.*, Materials Research Society,* **2007**, 990, 0990-B08-25

12 Jian-Bo He, Dao-Yong Lu, Guan-Ping Jin, *Applied Surface Science*, **2006,** 253, 689-697

13 Shigeyoshi Nakayama, Tokiko Kaji, Masahiro Shibata, Takenori Notoya, Toshiyuki Osakai. *J. of The Electrochemical Society*. **2007,** 154 (1), C1-C6.

14 *Metal handbook*, 2nd ed., J. R. Davis, Editor, p. 554, ASM International, Materials Park, OH, 1998.

15 T. Hamelmann , M.M. Lohrengel, *Electrochemica Acta*, **2001,** 47, 117-120

16 T. Fjiwara, T. Nakaue, M. Yoshimura, *Solid State Ionics*, **2004,** 175, 541-544

17 L. Staemmler, T. Suter, and H. Bohni, *Electrochemical and Solid-State Letters*, **2002,** 5(6), C61-63.

18 K.K. Yu, K. S.M. Pillai, P. R. Nalla, O. Chyan, *J. Appl Electrochem.*, **2010,** 40 L. Yin, I. Adler, T. Tsang, L. J. Matienzo, and S. O. Grim, *Chem. Phys. Lett*., **1974,** 24, 81.

19 I. Milošev and H.-H. Strehblow, *J. Electrochem. Soc.*, **2003,** 150, B517.

20 Matjaž Finšgar, Janez Kovač, Ingrid Milošev, *J. of Electrochemical Society*, **2010,** 157 (2) C52-C60.

21 A. J. Sedricks, *Corrosion of Stainless Steels*, , J. Wiley & Sons: NY, 1979. pp. 54-57

22 Z. Szklarska-Smialowska, *Op. Cit*., P. 4, 39, 44-45

PART II

INVESTIGATION OF BIMETALLIC CORROSION OF COPPER IN CMP RELATED ENVIRONMENTS

CHAPTER 4

STUDY OF BIMETALLIC CORROSION RELATED COPPER INTERCONTECTS USING MICROPATTERN CORROSION SCREENING METHOD AND TAFEL PLOTS[1,2]

4.1 Introduction

In modern microelectronic applications, copper has replaced aluminum as the metal of choice for interconnects because of its higher electrical conductivity [1,2]. Due to the lack of volatile byproducts in the reactive ion etching of Cu, the Cu interconnects are fabricated by a damascene patterning process shown in Figure 4-1. The process involves etching a trench/via pattern into a dielectric, the blanket deposition of a diffusion barrier followed by Cu electroplating, and finally removal of Cu overburden by chemical-mechanical planarization (CMP) [3-6]. Since the CMP process exposes the Cu interconnect and metal barrier to the continual presence of corrosive chemicals, the resulting bimetallic corrosion can

[1]Results presented in this chapter have been published in J. of Appl. Electrochem. Kyle et al., 2010. 40: 143-149. Used with permission from the Springer Science+Business Media B.V.
[2]Results presented in this chapter have been published in ECS Transactions. Kyle et al., 2010. 35(8): 173. Used with permission from the Electrochemical Society.

be detrimental to the overall production yields of integrated circuit devices.

As microelectronic circuits move toward sub 45 nm domains, continued shrinkage of device dimensions makes corrosion related reliability threats even more acute. In addition, ruthenium (Ru) and other noble metals have been actively investigated for use as new diffusion barrier materials for Cu interconnects [7-11]. The increased noble character of diffusion barriers like Ru can further intensify the Cu galvanic corrosion in CMP chemical environments. Therefore, there is a need for an effective methodology to evaluate bimetallic corrosion of Cu interconnects when exposed to CMP and post CMP cleaning conditions.

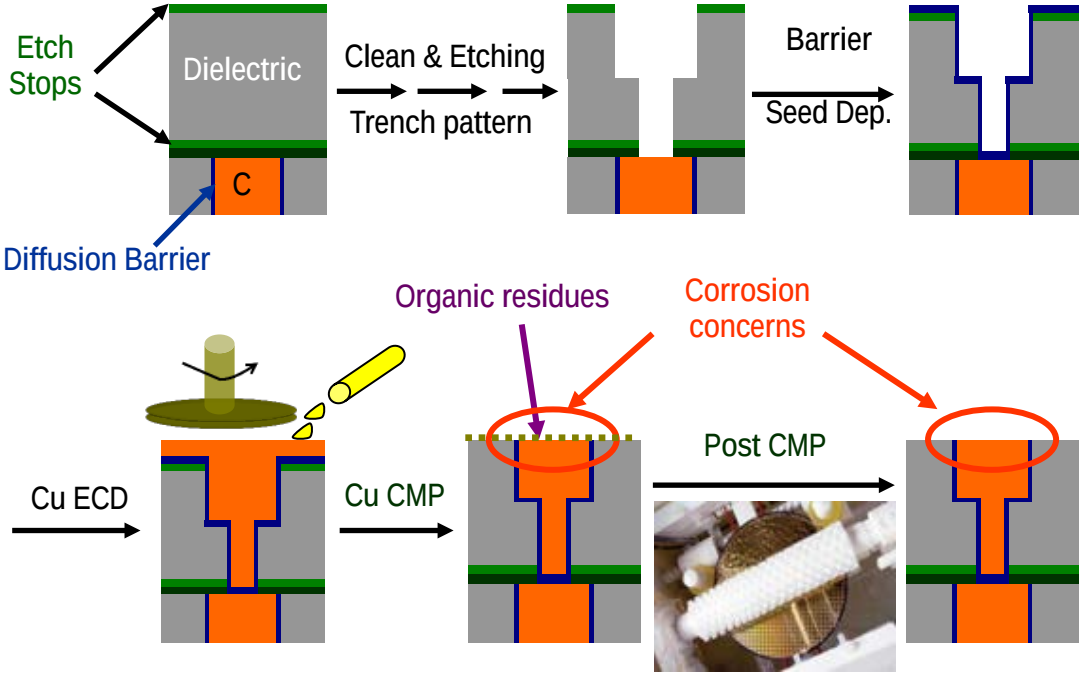

Figure 4-1 Damascene patterning process.

In this chapter, we report a novel Micropattern Corrosion Testing technique

combined with electrochemistry to allow rapid bimetallic Cu corrosion screening in various chemical environments. Two bimetallic interfaces were investigated using a Cu micro dots pattern (d = 130 μm) sputter-deposited on Ta and Ru metal substrates. The Cu/Ta and Cu/Ru micropatterns were immersed in CMP relevant acid and base solutions (H_2SO_4, tartaric, lactic, NH_4OH and KOH) and their corrosion behaviors were studied in situ under continuous optical microscopic imaging. Corrosion potentials and currents measured by Tafel plots technique complement well with micropattern corrosion testing results to demonstrate an enhanced Cu corrosion in Cu/Ru bimetallic contacts when comparing to Cu/Ta.

4.2 Experimental

4.2.1 Micropattern Corrosion Screening

Micropattern Corrosion Study- Circular micropatterns of Cu (ca. 50, and 80 nm thick, 130 μm in diameter) were deposited on selected substrates through a contact mask using a standard DC magnetron sputter (Desktop Pro, Denton Vacuum). Figure 4-2 depicts the fabrication sequence of the corrosion screening micropattern. The Ru (90nm) and Ta (180 nm) barrier metal substrates were sputter-deposited on a silicon substrate pre-cleaned by standard organic clean and HF etch [12]. The visual investigation of in-situ corrosion processes was carried out using a metallurgical microscope (Nikon, Eclipse ME600) by immersing Cu micropattern structures in testing solutions. This visual inspection approach requires an optical clear solution being used. The solutions of K_2SO_4,

tartaric acid, lactic acid, NH_4OH (0.10 M, Aldrich) were prepared with 18.2 MΩ purified water and pH of the solutions was adjusted from 2 to 11.4 with H_2SO_4 and KOH. After submerging in testing solution, the time-lapsed images of the Cu micropattern were recorded by a computer-controlled digital camera connected to microscope.

4.2.2 Tafel Plots, Galvanic Current Measurement and XPS

Tafel plots – A potentiostat (CH Instruments, USA) was employed to acquire the open circuit potentials and Tafel plots. Both sputtered Cu, Ta, Ru metal substrates and solid metal shots were used as electrodes for all electrochemical data. The metal electrodes (d = 5mm) were polished down to 0.5 micron mirror polishing and sonicated in 18.2 MΩ de-ionized water. Three-electrode system with Pt counter and Hg/Hg_2SO_4 reference electrodes were employed in a glass cell to obtain Tafel plots data (IV curves) in corresponding solutions used in micropattern corrosion screening. The galvanic current flow is measured using the source meter (Keithley, 2400 source meter). Electrolytes include 0.1 M ammonium hydroxide, potassium sulfate, and others as mentioned. The x-ray photoelectron spectroscopy (XPS) (Phi 5000 VersaProbe, with an Al K_α 58.7 eV excitation source) provided surface chemical composition information.

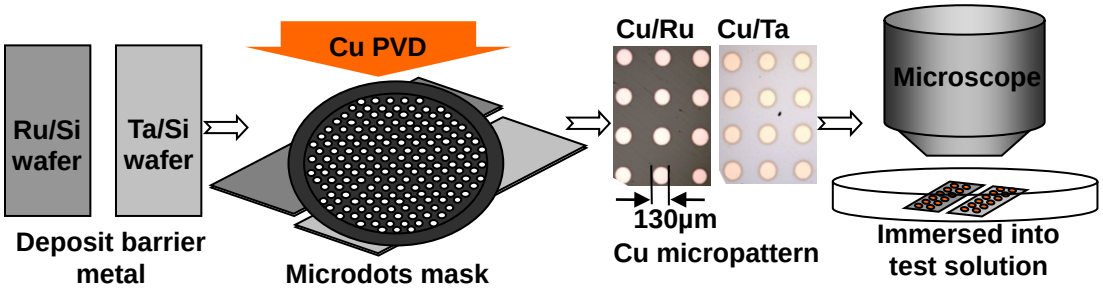

Figure 4-2 Micropattern corrosion screening structure.

4.2.3 High Resolution 3-D Optical Scanning

Optical profilometry allows rapid and accurate three dimensional measurements of microscopic features. Following chemical exposure and galvanic etching, the exact volume change of the metal dots is analyzed using a Zygo NewView 7000 series optical profiler. Wafer coupons are imaged with a 2.5x objective using a 2x zoom as well as with the 10x objective. The resulting images are then processed to exclude the background and partial dots allowing for a volume per dot measurement. Volume changes that were not visible via standard optical microscope become evident, which allows for collection of precise etch rate data. By applying this technique to determine bimetallic corrosion, large numbers of formulation components in varied combinations may be screened quickly for development of cutting edge wet cleans products.

4.3 Chemical Speciation and Effect of Bimetallic Contact

The specific chemical speciation in the solution has a direct impact on the bimetallic Cu corrosion process. Figure 4-3 shows the time lapsed image of Cu

micropatterns deposited on Ru substrate (denoted as Cu/Ru) immersed in four different testing solutions at pH=11.4. The Cu/Ru micropattern screening results indicate that the alkaline NH_4OH induced the fastest Cu corrosion compared with the other three solutions. The time required to completely erode 130 μm Cu microdots can be used as a useful gauge for the relative corrosion trend. Thus, the corrosion rate can be estimated as inversely proportional to the measured corrosion time (t_{corr}) from micropattern corrosion screening. The typical measured corrosion time has *ca.* 7 % error possibly caused by the slight variation of stress and size of sputtered deposited micropatterns. The relative Cu corrosion rate of Cu/Ru micropattern in four testing solutions follows NH_4OH (33 min) > lactate (113 min) > tartrate (249 min) > KOH/ K_2SO_4 (passivated) at pH=11.4. The initial oxidation of Cu metal tends to form different oxidized surface films, Cu_2O/CuO /$Cu(OH)_2$ (hydrous oxide) at neutral to high pH [13, 14]. The surface oxide film will act as a barrier between Cu and the corrosive medium to slow further corrosion of underlying Cu. The Cu/Ru micropattern screening confirms the passivation of Cu/Ru microdots immersed in K_2SO_4/KOH of pH=11.4, ref. Figure 4-3. Ammonium hydroxide (NH_4OH) is commonly used as a basic buffer and complexing agent in the Cu CMP solution. When exposed to a strong complexing ligand like NH_3, the Cu surface oxide barrier dissolves readily by forming $Cu(NH_3)_2^+$ (formation constant $K_f = 7.24 \times 10^{10}$) and the Cu microdots eroded in 33 min [15]. Accordingly, Cu microdots were found to corrode more slowly in solutions containing lactate and tartrate ions with weaker Cu complexing ability

(K_f ~ 10^{5-6}) [15].

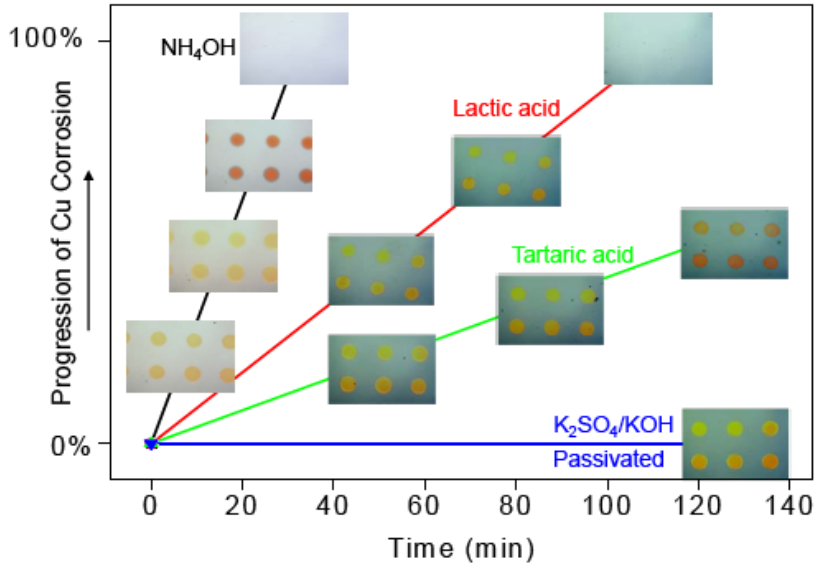

Figure 4-3 Time-lapsed optical images of Cu corrosion screening micropatterns submerged in NH_4OH, lactic acid, tartaric acid and K_2SO_4/KOH solutions at pH 11.4. Cu micropatterns were deposited on Ru substrate.

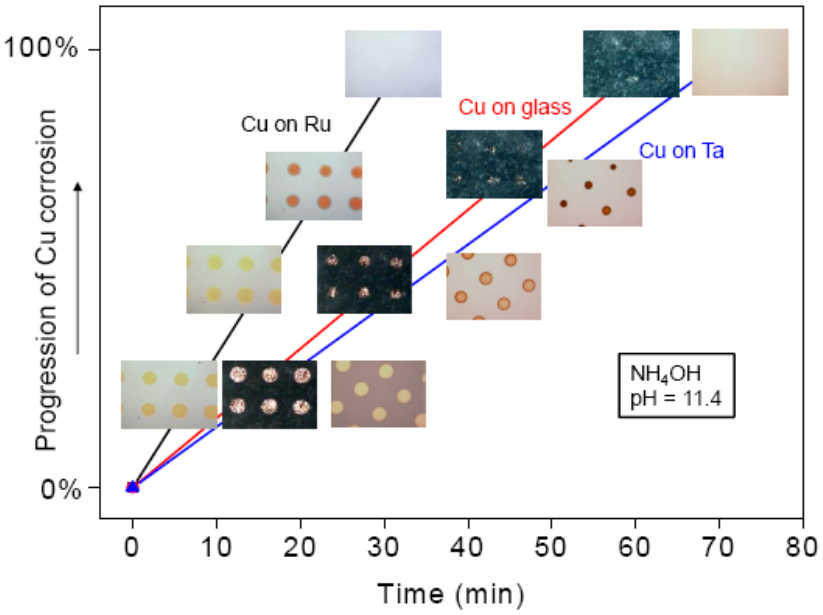

Figure 4-4 Time-lapsed optical images of Cu micropatterns deposited on Ru, Ta and glass substrates, the micropattern corrosion screening was done in NH_4OH solution, pH 11.4.

In addition to solution environment, the nature of bimetallic contact can also affect the rate of Cu corrosion. Figure 4-4 shows the time-lapsed images of Cu micropatterns on three different substrates including Ta, Ru and glass submerged in the alkaline NH_4OH (0.10 M, pH=11.4). Ta is currently used as part of the liner/diffusion barrier for Cu interconnects in integrated circuit devices [16, 17]. Ru is a new promising liner/barrier metal candidate that allows direct Cu plating to streamline the fabrication process [8,9]. Glass was chosen as a non-conductive dielectric substrate. As shown in Figure 4-4, Cu microdots on Ta substrate require nearly double the amount of time as compared to Cu/Ru to corrode completely in NH_4OH pH=11.4 solution. Based on the micropattern screening, the Cu corrosion trend follows Cu/Ru (33 min) > Cu/Glass (63 min) > Cu/Ta (72 min). Similarly, the Cu corrosion rate obtained from Cu/Ru micropattern was found to increase by 4-5 times compared to Cu/Ta in lactate and tartrate pH=11.4 solutions.

Tantalum has a strong tendency to be oxidized and form tantalum oxide (Ta_2O_5) especially when exposed to aqueous medium, Eq. 4-1.

$$2Ta + 5H_2O = Ta_2O_5 + 10H^+ + 10e^- \quad \text{(Eq. 4-1)}$$

The thermodynamically favorable Ta oxidation reaction donates electrons through the Cu/Ta bimetallic contact placing Cu microdots under cathodic protection. In contrast, Ru is nobler than Cu. This inherent nobility of Ru facilitates more Cu oxidation via the galvanic Cu/Ru contact. For all the chemical systems studied in this work, micropattern screening consistently shows enhanced Cu corrosion with

Ru contact. It is interesting to note that Cu microdots deposited on a glass substrate, meant to represent a Cu-only corrosion case, exhibits a corrosion rate between Cu/Ru and Cu/Ta as expected, Figure 4-4.

4.4 Tafel plots

To explore the trend of galvanic corrosion by electrochemistry, Tafel plots were recorded for all four solutions from pH 2 to pH 11.4. Figure 4-5 depicts typical Tafel plots of Cu, Ta, and Ru metal in NH_4OH pH 9 solution. As shown in Figure 4-5, the corrosion potentials mostly follow a general trend of $E_{corr, Ru} > E_{corr, Cu} > E_{corr, Ta}$ which correlates well with the expected metal nobility trend.

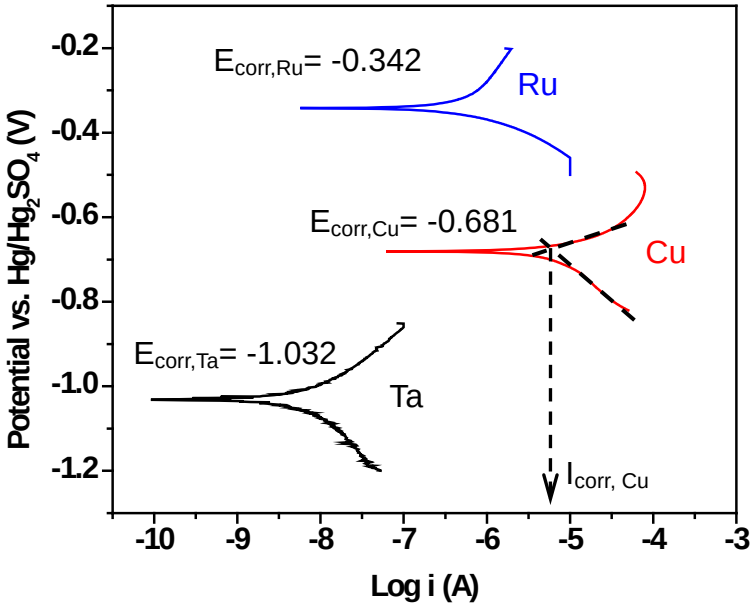

Figure 4-5 Tafel plots of Ru, Cu and Ta measured in NH_4OH solution at pH 9. Corrosion potential (E_{corr}) and corrosion current (I_{corr}) can be obtained from each Tafel plot.

Several approaches are commonly employed to provide quantitative measurements of metal corrosion rates [18]. The methods of recording weight-loss and thickness-loss over time are regarded by corrosion engineers to be the “real” corrosion testing. However, this method is a long-term process not suitable for rapid corrosion screening. Tafel plots provide an alternative electrochemical approach that has the advantage of speed and relative simplicity. The rate of corrosion can theoretically be calculated from the corrosion current which obtained from the intersection of two slopes of cathodic and anodic Tafel plots, as illustrated in Figure 4-5. The disadvantage is that corrosion rate by Tafel plots is acquired from a fresh electrode/solution and the corrosion studied is limited to the short-term only. Actual corrosion situations are often more complex and with time the metal surface may become partly covered with oxide or other coatings that affect the corrosion rate. Furthermore, Tafel plots based on a single metal electrode cannot be directly applied to study specific bimetallic corrosion that simultaneously involves two overlaying metals.

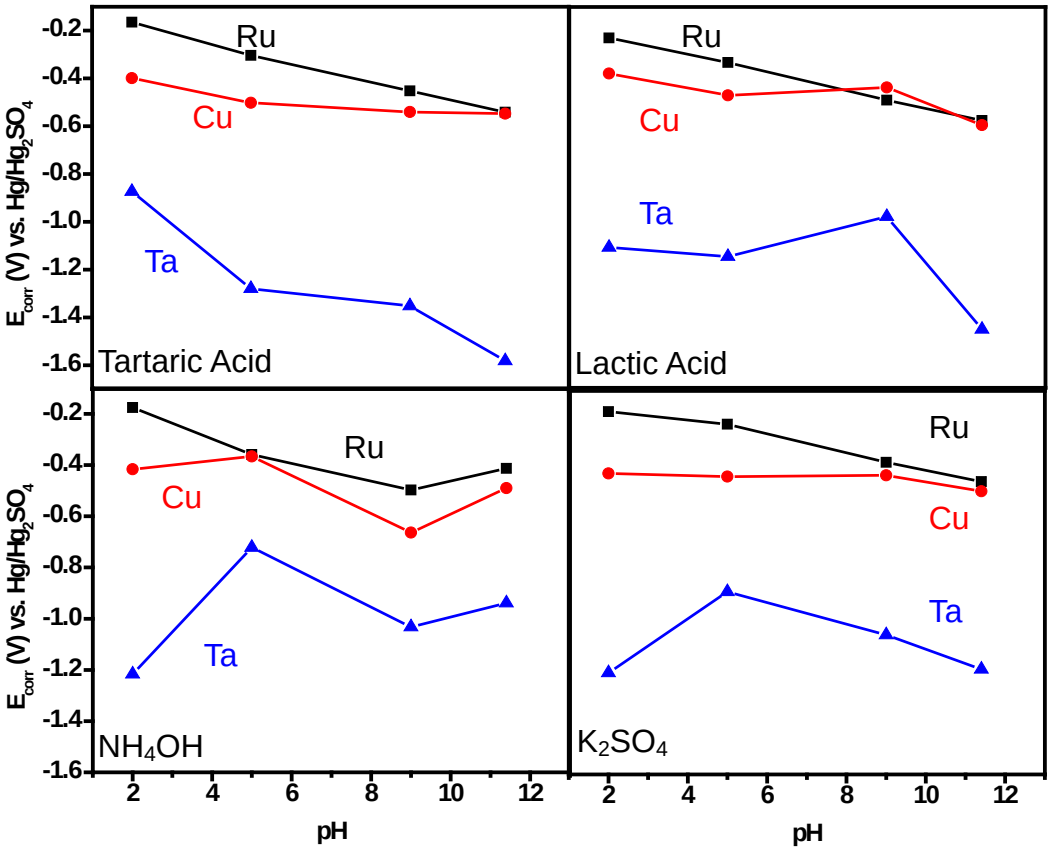

Figure 4-6 Corrosion potentials (E_{corr}) obtained from Tafel plots of Ru, Cu and Ta were plotted vs. solution pH.

4.5 Advantages of Micropattern Screening Method

As demonstrated above, the new micropattern corrosion screening method is better suited for the study of bimetallic corrosion. Different combinations of metals can easily be fabricated into corrosion screening micropatterns as shown in Figure 4-2. The micrometer dimension of micropatterns was designed for optical microscope observation. In addition, the thickness of Cu microdots can be adjusted to study a wide dynamic range of corrosion rates within a reasonable experimental time frame, Figure 4-7. The micropattern screening not only

provides semi-quantitative trend of relative corrosion rate, but also affords a direct visual inspection of actual corrosion processes in real time. The direct imaging of the micropattern is useful in identifying different metastable surface transformations involved in the corrosion process. For instance, Figure 4-8 shows that Cu corrosion on Cu/Ru micropatterns can exhibit distinctly different surface transformations in K_2SO_4 as compared to tartaric acid at the same pH = 5. The visual identification serves as an effective pointer to different metastable surface states that await further surface characterization to gain more insight into the corrosion process. Figure 4-9 shows that the subsequent XPS surface analysis reveals the dark brown/blue coating on Cu microdots after being immersed in K_2SO_4 is mainly Cu(I) oxide. According to Yin et al.[19] shake-up satellites in the Cu(II) $3d^9$ species arise owing to the Cu $3d^9 \rightarrow$ Cu $3d^8 4s^1$ transition. Therefore, the analysis of the Cu 2p peak by XPS allows the distinction between Cu(0) or Cu(I) and Cu(II) species to be made. The Cu 2p spectrum of Cu(I) compounds is closely similar to that from metallic copper Cu(0) in terms of binding energy (BE), line width, and absence of satellites. To overcome the problem of characterization, the X-ray induced Auger Cu peak $L_3M_{4,5}M_{4,5}$ can be used to distinguish lines for metallic Cu(0) and Cu(I), due to the differences in electron relaxation energies in these species. [20,21] In comparison, Cu microdots maintain their metallic color and XPS confirms a relatively thin Cu(I) oxide surface layer on Cu microdots after being immersed in tartaric acid at pH=5.

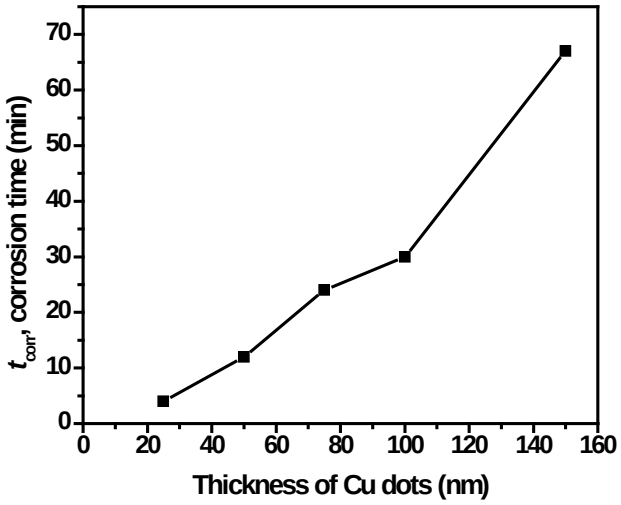

Figure 4-7 Corrosion time (t_{corr}) vs. the thickness of Cu microdot obtained from Cu/Ru micropattern corrosion screening in NH_4OH solution, pH 11.4.

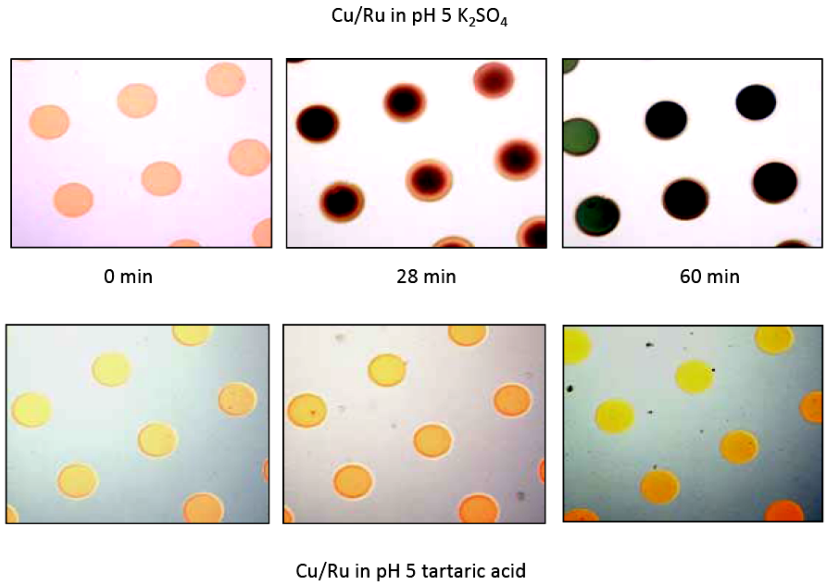

Figure 4-8 Micropattern corrosion screening reveals specific chemicals can cause distinctly different surface layers on Cu microdot

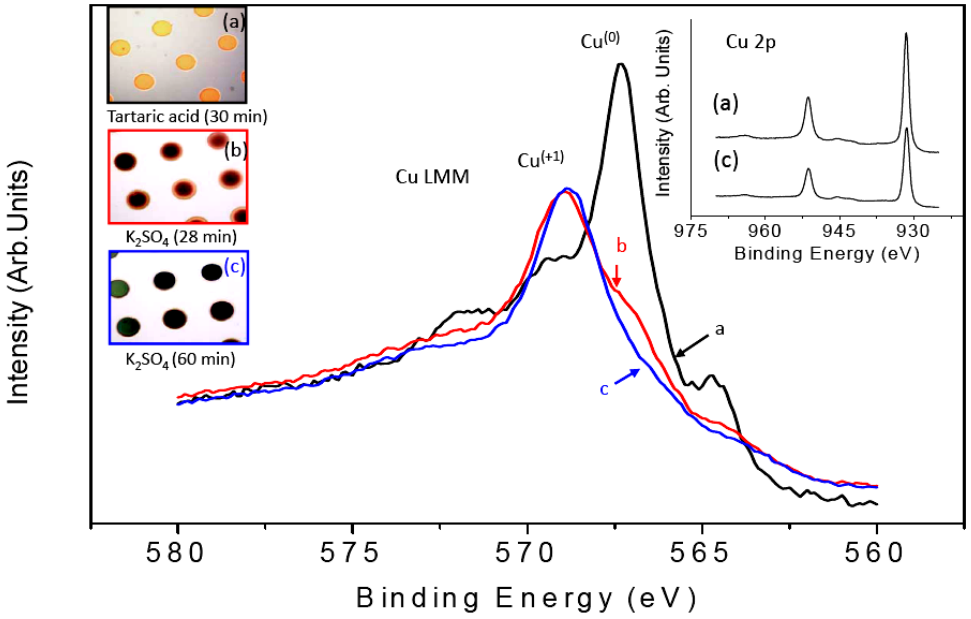

Figure 4-9 The Cu LMM auger spectroscopic analyses show Cu surface layers after immersed in K_2SO_4 (pH 5) are mainly Cu^{+1}, but remain Cu^0 in tartaric acid (pH 5). XPS Cu 2p (inset) can't differentiate Cu^{+1} and Cu^0.

4.6 Micropattern Screening Method Versus Tafel Plots

To compare electrochemical and micropattern approaches, the $I_{corr,\ Cu}$ obtained from Tafel plots and corresponding t_{corr} from Cu/Ru micropattern screening were plotted in the pH ranging from 2 to 11.4 for three testing solutions. As shown in Figure 4-10, both approaches consistently indicate that the Cu corrosion rate decreases when solution pH increases from 2 to 5. In this acidic region, proton reduction (Eq. 4-2) will be the main cathodic reaction to sustain the continual Cu oxidation.

$$2\ H^+ + 2\ e^- = H_2 \qquad \text{(Eq. 4-2)}$$

Increasing alkalinity slows the proton reduction half reaction and the overall Cu

corrosion rate as well. Thus, the observed decreases in $I_{corr,\ Cu}$ correlate well with increasing t_{corr} obtained from Cu/Ru micropattern screening when the solution alkalinity is raised to pH = 5. It is important to note that separate Cu/Ta micropattern screening experiments reveal all Cu microdots on Ta substrate remain intact even after 10 hours submersion in tartaric acid and K_2SO_4 solutions in all pH tested. The results demonstrated that the new micropattern screening is more capable of detecting the effective cathodic protection of Cu microdots by Cu/Ta bimetallic contact. In comparison, $I_{corr,\ Cu}$ measured by Tafel plots is based solely on one Cu metal electrode and does not account for the bimetallic factor of Cu/Ru vs. Cu/Ta.

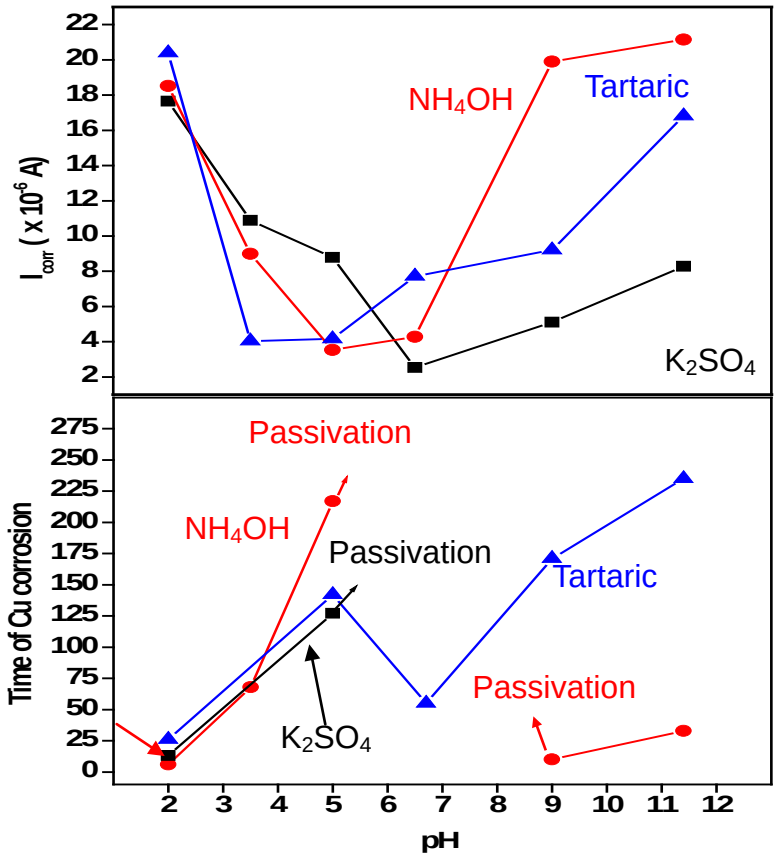

Figure 4-10 (a) Corrosion current ($I_{corr, Cu}$) obtained from Cu Tafel plots and (b) corresponding corrosion time (t_{corr}) from Cu/Ru micropattern corrosion screening were plotted in the pH ranging from 2 to 11.4 for NH_4OH, tartaric acid and K_2SO_4 solutions.

For solutions tested in neutral and alkaline conditions (7 < pH ≤ 11.4), Tafel plots (Figure 4-10a) show a general trend of a low corrosion current plateau near neutral pH and high corrosion activities at higher pH of 9 to 11.4. In NH_4OH solution, the Cu/Ru micropattern results (t_{corr}) reflect the similar corrosion trend measured by Cu Tafel plots except the micropattern screening further reveals that a passivation region exists for Cu microdots at the neutral pH, Figure 4-10b. In neutral pH aqueous medium, Cu favors the formation of stable surface oxides,

mainly Cu_2O. The Cu passivation is easily observable by the Cu/Ru micropattern corrosion study. As the solution alkalinity increases to pH > 9, more NH_3 is available to form soluble complexes with Cu ions and the erosion rate of Cu microdots increased. The micropattern screening results is consistent with the common pH ranges (9-12) utilized in the basic CMP formulation for Cu interconnect [22].

However, the Cu corrosion trend measured by Tafel plots significantly differs from the Cu/Ru micropattern screening result in two other solutions, Figure 4-10a&b. For example, in the K_2SO_4 solution of pH >5, the Cu/Ru micropattern screening indicates Cu microdots were passivated while Tafel plot data shows $I_{corr,\ Cu}$ is varying between 3-8 μA/cm^2 . For tartaric acid solution of pH > 5, Tafel plot data predict a gradual increase of Cu corrosion rate with solution alkalinity. But, the actual Cu corrosion process observed by Cu/Ru micropattern screening reveals a decreasing Cu corrosion rate with increasing solution pH in tartaric acid solution. The diversion could be the result of dynamic chemical balance between the surface oxide formation (Eq. 4-3) and oxide dissolution by complex formation (Eq. 4-4).

$$2Cu + 2OH^- = Cu_2O + H_2O + 2e^- \quad \text{(Eq. 4-3)}$$

$$Cu_2O + 4\ tartrate^{2-} + ½\ O_2 + 2H_2O = 2\ Cu(tartrate)_2^{2-} + 4OH^- \quad \text{(Eq. 4-4)}$$

Unlike NH_3 which is a strong Cu complexing ligand, tartrate ions form weaker complexes with Cu ions [$Cu(tartrate)_2^{2-}$ $K_f = 3.23 \times 10^6$] and are less effective in

removing the oxidized surface layer from Cu microdots. The Cu/Ru micropattern screening shows that observed t_{corr} increases with increasing alkalinity (7 < pH ≤11.4) of tartaric acid solution, Figure 4-10b. The trend could be accounted for as the increasing stability of Cu_2O gradually retards the oxide removal process by complex formation with tartrate ions. For the same reason, SO_4^{2-} ions have no complexing ability with Cu ions and Cu microdots were found to be passivated as expected with surface oxides when immersed in K_2SO_4 solutions of pH > 5.

4.7 Cu corrosion inhibitor-benzotriazole

Benzotriazole ($C_6H_5N_3$, BTA) is a Cu corrosion inhibitor most commonly used in Cu CMP solution formulations [23,24]. During CMP, BTA protects the recessed Cu lines from chemical erosion while the mechanical polishing removes Cu overburden to achieve the overall planarization across the whole wafer. The desirable Cu corrosion inhibition was made possible by a strong chemical reaction of BTA to Cu(+1) surface layer on Cu interconnects [25,26]. However, it is highly desirable that BTA addition be kept as low as possible because the strongly surface bonded Cu-BTA layer often becomes the source of organic contamination that can affect the conductivity and interlayer adhesion of subsequent Cu interconnects. The micropattern screening method can be used to identify the minimum BTA inhibitor concentration required for a particular chemical environment. For example, Figure 4-11 shows the effect of [BTA] concentration on the Cu corrosion time based on Cu/Ru micropattern screening

in NH_4OH solution pH = 11.4. With addition of 2.5 ppm BTA, the Cu corrosion rate of Cu/Ru micropattern was decreased by nearly 10 times. The Cu corrosion rate can be slowed down further over 50 times if 7.5 ppm BTA was added into NH_4OH solution (pH = 11.4). As depicted in the Figure 4-11 inset, more BTA (~ 30 ppm) is need to achieve the same Cu corrosion inhibition on Cu/Ru micropattern if submerged in a more corrosive NH_4OH solution at pH 10. This example demonstrates how micropattern screening is helpful to identify the minimum threshold concentration of Cu inhibitor BTA needed in specific solution environments and bimetallic contacts.

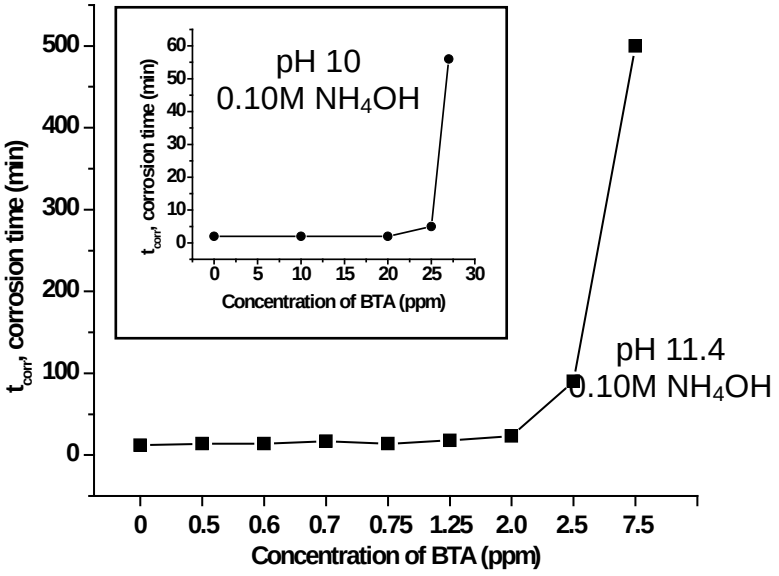

Figure 4-11 Effect of corrosion inhibitor, benzotriazole (BTA), on the corrosion time (t_{corr}). measured by Cu/Ru micropattern in NH_4OH solution, pH 10 and 11.4.

4.8 Discover New Cu Corrosion Inhibitors Using Micropattern Screening

The micropattern corrosion screening method is well suited for discovering new potential Cu corrosion inhibitors in post CMP cleaning formulations. The bimetallic contacts (Cu/Ta, Cu/TaN, Cu/Ru, Cu/W, etc) are fabricated using through-mask sputtering deposition. More importantly, the rapid micropattern screening capability permits efficient investigation of Cu corrosion under different chemical influences including pH, corrosion inhibitors, solvent, complexing agents, ambient conditions etc. to enable rapid development and verification of new cleaning solution formulation.

Figure 4-12 show the corrosion rates (Å/min) of Cu microdots deposited on Ru and Ta substrates submerged in a post CMP cleaning solution without a Cu corrosion inhibitor. The results indicate that higher solution alkalinity tends to promote Cu corrosion and enhanced galvanic for Cu/Ru contacts in all solutions tested. As device structures scale down to sub 22 nm, the Cu loss due to post-CMP cleaning is required to be less than ~1 Å/min to minimize Cu lost and undesirable critical dimension change. As shown in Figure 4-12, there is a clear need to use a corrosion inhibitor to minimize the Cu corrosion rate.

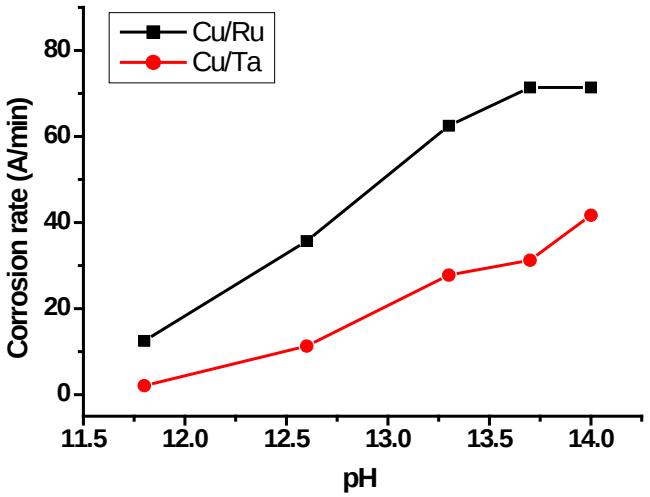

Figure 4-12 Corrosion rate of Cu/Ru and Cu/Ta system in Post-CMP cleaning solution baseline (no inhibitor) with varied pH (diluted by DI water).

To date 15 potential corrosion inhibitor candidates at 10 mM concentration in post CMP cleaner base solution (pH = 11.8) have been screened using the Cu/Ru bimetallic system. This base solution has a background Cu corrosion rate is 12.5 Å/min. As shown in Figure 4-13, micropattern screening successfully identified 9 compounds that can reduce the Cu corrosion rate below the background corrosion rate. In particular, five compounds (*A*-*E*) exhibit excellent Cu corrosion inhibition with overall corrosion rate < 1 Å/min as estimated via top down optical microscopy. The set up of direct galvanic current measurement showed in Figure 4-14. The direct galvanic current measurement of inhibitor *A* showed Cu corrosion current was reduced from an initial 6 Å /cm^2 to nearly zero after 10 minutes. No significant Cu corrosion was observed, based on micropattern images, even after three days submersion in the post CMP solution with 10 mM inhibitor *A*, insert Figure 4-15.

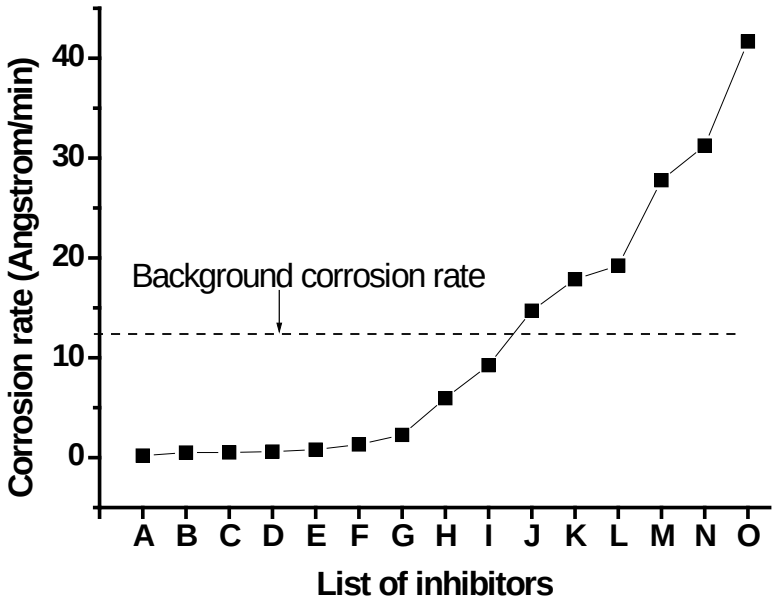

Figure 4-13 Cu corrosion rate on Ru substrate in cleaning solution at pH 11.8 with 15 inhibition candidates from A to O.

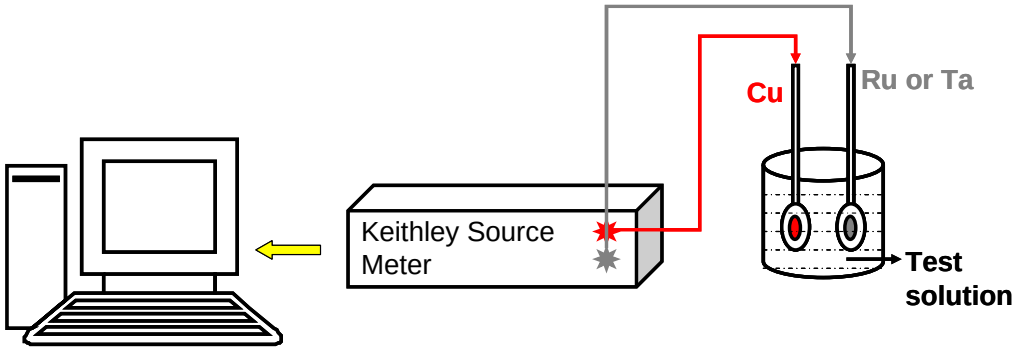

Figure 4-14 The direct galvanic current measurement

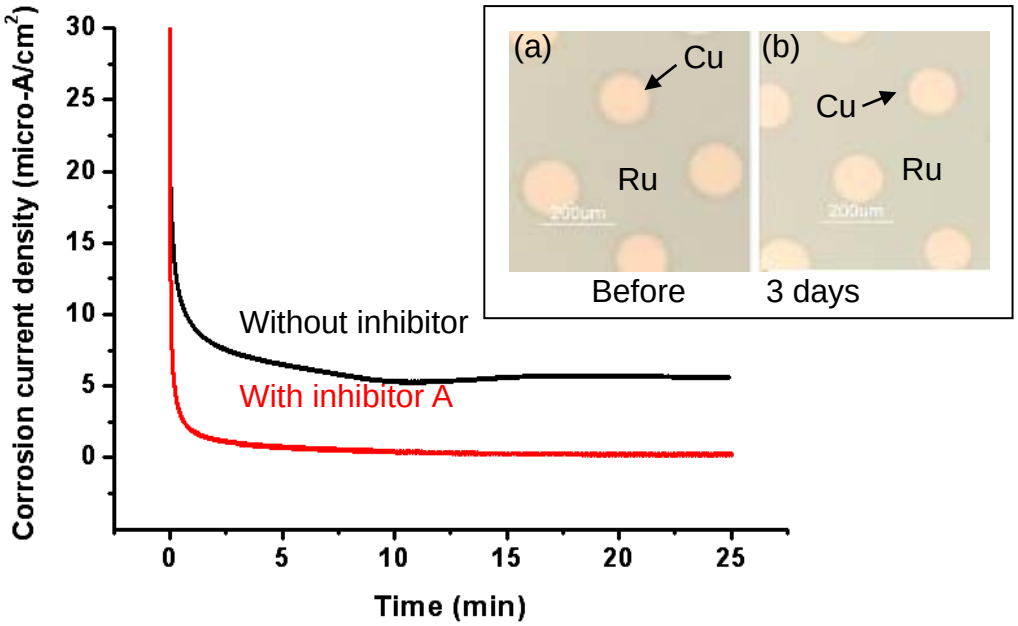

Figure 4-15 Direct galvanic current measurement of Cu/Ru galvanic contact in cleaning solution with and without inhibitor A (10 mM) *Insert*: Cu micropattern on Ru (a) before and (b) after soaked in post-cleaning solution with inhibitor A for 3 days.

In the advanced microelectronic fabrication, the single-wafer processing has gradually replaced the batch-wafer operation. However, single-wafer operation requires significant decrease in allowable process time in order to achieve the overall production rate. Therefore, it is important to determine the early activation process of Cu corrosion inhibition within a few minutes timeline. As shown in Figure 4-16, the optical profiler was utilized to scan high resolution 3D images of Cu microdots that provide thickness and volume information at the early inhibition period. For instance, the optical profiles for Cu microdots soaked with various duration in post CMP solution with 10 mM inhibitor *A* were measured. The optical profiling help to reveal a Cu inhibition delay by inhibitor *A* at the first one minute

period that results in a higher Cu corrosion lost at ca. 8% volume lost per minute shown in Figure 4-17. The initial inhibition activation process can be affected by chemical structure and concentration of the inhibitors, and the chemical solution environments as well. We anticipate more in-depth understanding of corrosion inhibition activation can be achieved by the combination of new optical profiling metrology and other electrochemical and surface characterization tools.

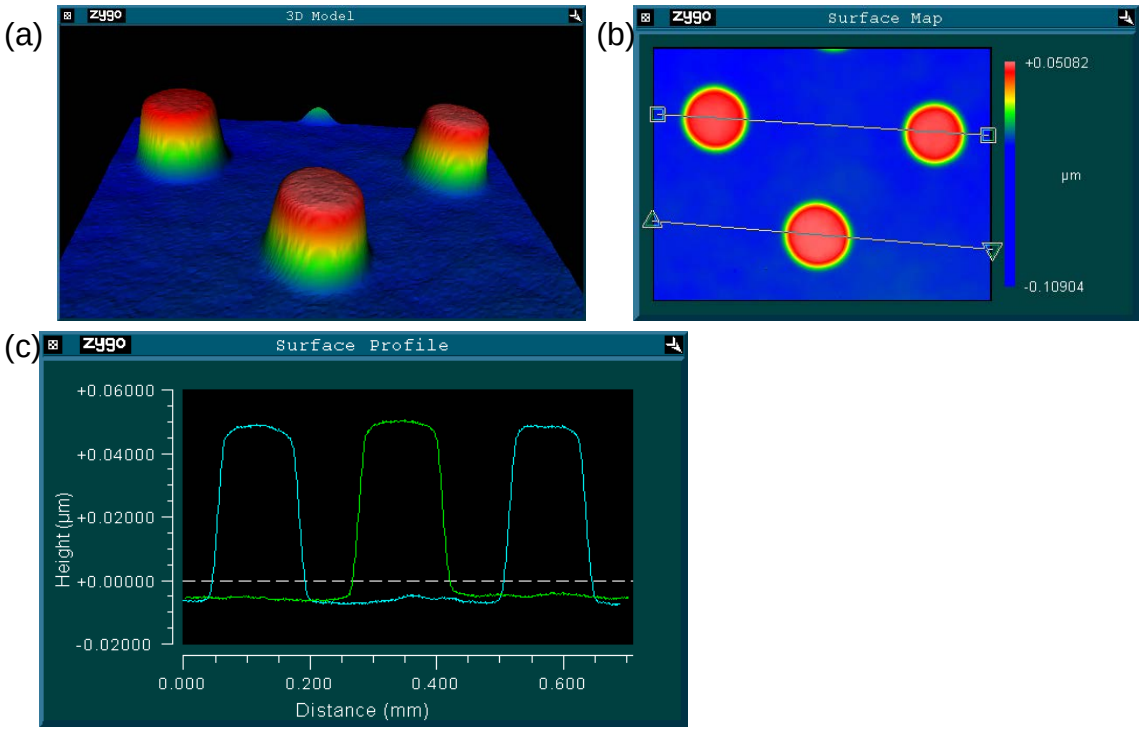

Figure 4-16 One example of optical profiler result: the volume for all three Cu microdots = 2280 $[\mu m]^3$.(a) 3D mode (b) surface map (c) surface profile

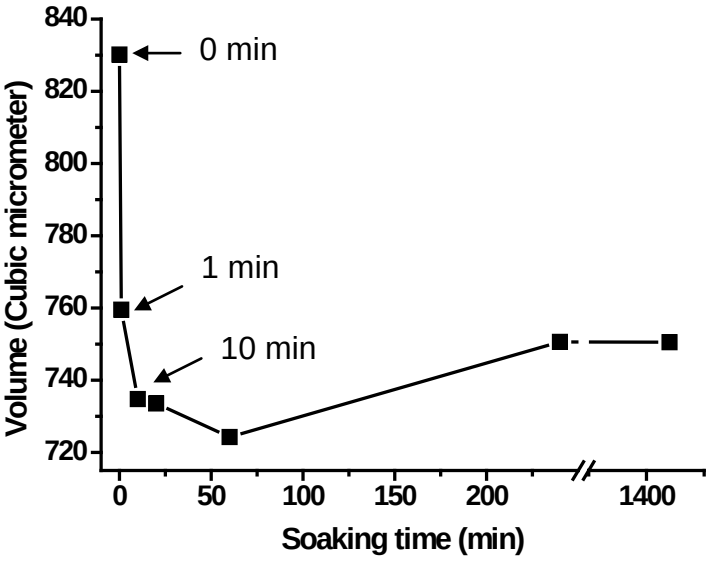

Figure 4-17 Activation study of initial loss of Cu micropattern on Ru substrate soaked in cleaning solution with inhibitor A (10 mM)

4.9 Summary

In summary, a new rapid corrosion screening metrology was developed and demonstrated for effective characterization Cu bimetallic corrosion in CMP relevant environments. Enhanced Cu corrosion induced by the Cu/Ru bimetallic contact was confirmed with all four solutions studied. The balance between oxide formation and complex reaction can affect the extent of Cu bimetallic corrosion. The alkaline NH_4OH solutions with strong complexing ammonia ligands will result in faster Cu corrosion. For tartaric acid and K_2SO_4 solutions, a slower Cu corrosion process that could lead to Cu passivation was observed based on micropattern screening results. The micropattern corrosion screen method also proves to be useful in identifying the metastable surface states during corrosion and determining threshold BTA concentration for Cu corrosion inhibition. New Cu

corrosion inhibitors were discovered using micropattern screening. The high resolution 3-D optical profilometry was found to be useful in evaluating the early activation process of corrosion inhibition.

4.10 References

1. Spencer, TJ.; Osborn, T; Kohl, PA ,*Science,* **2008,** 320:756.
2. Osborn, T; He, A; Galiba, N; Kohl, PA .,*J. Electrochem. Soc.* **2008,** 155, 308.
3. Banerjee, G; Rhoades, RL., *ECS Transactions,* **2008,** 13, 1.
4. Armini, S.; Whelan, CM.; Moinpour, M.; Maex, K., *J. Electrochem. Soc.* **2009,** 156, 18.
5. Li, Yuzhuo *Microelectronic Applications of Chemical Mechanical Planarization,*; John Wiley and Sons: Hoboken, NJ, 2008, pp. 467.
6. Doi, TK (2007) Manufacturing Engineering and Materials Processing 73, 341
7. Kim, IK; Cho, BG; Park, JG; Park, JY; Park, HS., *J. Electrochem. Soc.* **2009,** 156, 188.
8. Chyan O, Arunagiri TN, Ponnuswamy,T., *J. Electrochem. Soc.* **2003,** 150, 347.
9. Chan R, Arunagiri TN, Zhang Y, Chyan O, Wallace RM, Kim, MJ, Hurd, T, *Electrochem. Solid-State Lett.* 2004, 7,154.
10. Lane MW, Murray CE.; McFeely FR, Vereecken PM, Rosenberg, R., *Appl. Phys. Lett.* **2003,** 83, 2330.

11. Kim, IK; Kang, YJ; Kwon, TY; Cho, BG; Park, JG; Park, JY; Park, HS *Electrochem. Solid-State Let.* **2008,** 11, 150.
12. Chyan O. Chen JJ, Xu F, Wu, *J. Anal. Chem.* **1997,** 69, 2434.
13. Pourbaix M. (1975) Atlas of Electrochemical Equilibria Aqueous Solutions, HACE, Houston
14. Gorantla VR, Goia D; Matijevic E, Babu, SV (2005), *J. Electrochem. Soc.*152:912
15. Dean JA Ed., *Lange's Handbook of Chemistry*, p-571, 13th ed, McGraw Hill, New York, 1985.
16. Chen CW, Chen JS, Jeng JS, *J. Electrochem. Soc*. **2008,** 155, 1003
17. Tsao JC, Liu, CP, Wang, YL, Chen, KW, *Journal of Nanoscience and Nanotechnology,* **2008,** 8, 2582
18. Review RW ed. Uhilig's Corrosion Handbook, 2nd ed. Wiley-Intersciecne: New York, 2000.
19. L. Yin, I. Adler, T. Tsang, L. J. Matienzo, and S. O. Grim, *Chem. Phys. Lett*., **1974,** 24, 81.
20. I. Milošev and H.-H. Strehblow, *J. Electrochem. Soc.*, **2003,** 150, B517.
21. Matjaž Finšgar, Janez Kovač, Ingrid Milošev, *Journal of The Electrochemical Society*, **2010,** 157 (2) C52-C60.
22. Naghshineh S, Barnes J, Hashemi, Y, Oldak, EB U.S. Patent 6194366, 2001
23. Kim IK, Kang YJ, Hong YK, Park JG, *Materials Research Society* Symposium Proceedings **2005,** 3-7

24. Deshpande S, Kuiry SC, Klimov M, Seal S, *Electrochem. Solid-State Let.*, **2005,** 8, 98.

25. Poling GW, *Corros. Sci.* **1970,** 10, 359.

26. Thomas D, *J. Electrochem. Soc.*, **1998,** 145, 42.

CHAPTER 5

INVESTIGATION OF COPPER/RUTHENIUM BIMETALLIC CORROSION: EFFECT OF ANTIOXIDANTS IN POST-CMP CLEANING PROCESSES[1]

5.1 Introduction

Antioxidants are common constituents in post chemical mechanical planarization (CMP) cleaning solution used to prevent the oxidation of Cu during the process [1,2]. Usually post CMP is carried out at high pH condition between 9 and 11. By the auto-oxidation mechanism, antioxidants scavenge oxygen present in the solution thereby reducing the availability of oxygen to attack the Cu surface. Figure 5-1 shows different polyphenols with bi- or tri- hydroxyl substituted benzenes used as antioxidants in CMP slurries. Polyphenol antioxidants undergo self-oxidation on exposure to air or oxygen. The first step of oxidation involves the abstraction of hydrogen from hydroxyl group forming semiquinone radical and further oxidation occurs to form stable oxidized species in quinonic form [3]. Therefore, auto-oxidation of polyphenols can be enhanced by increasing pH of the solution [4]. Besides the antioxidant activity, polyphenols can also act as chelating agent for different transition metal ions [5-9].

[1]Results presented in this chapter have been published in ECS Transactions. Kyle et al., 2010. 35(8): 173. Used with permission from the Electrochemical Society.

5.2 Micropattern Corrosion Screening of Gallic Acid

Gallic acid (3,4,5-hydroxybenzoicacid) is one of the polyphenols used as Cu antioxidant in post CMP cleaning formulations [10]. We first investigated the influence of gallic acid on the corrosion of Cu when in contact with different substrates like Ru and Ta. Our micropattern corrosion screening data indicate that Cu receives no protection from corrosion instead actively corrodes in gallic acid under alkaline conditions similar to that of the post CMP clean.

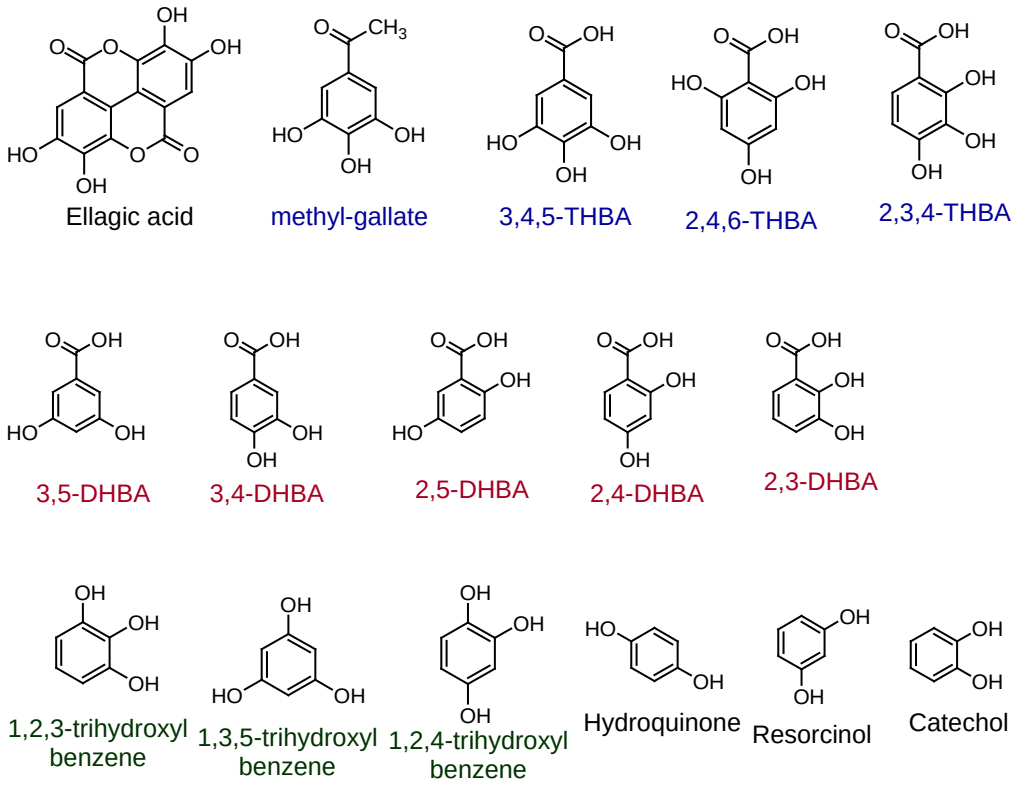

Figure 5-1 Relevant polyphenol antioxidants.

Optical images of Cu micropatterns deposited on Ru and Ta submerged in 5 mM gallic acid at different pH are shown in Figure 5-2(a). At pH 7 Cu microdots

on Ru are corroded in 60 min. In contrast, Cu microdots deposited on Ta are passivated and visually darkened. In more alkaline conditions, two different Cu corrosion behaviors were observed in gallic acid. In less alkaline condition around pH 9, complete erosion of Cu microdots is seen within 22 mins on Ru substrate and 41 mins on Ta substrate. The estimated corrosion rate of Cu on Ru and Ta is 3.2 nm/min and 1.7 nm/min, respectively. It is worth noting that gallic acid at pH 9 offers no corrosion protection but instead accelerates the corrosion of Cu microdots deposited on both Ru and Ta. However, in the more alkaline condition (pH ≥12), Cu corrosion ceased completely in gallic acid on both Ru and Ta substrates.

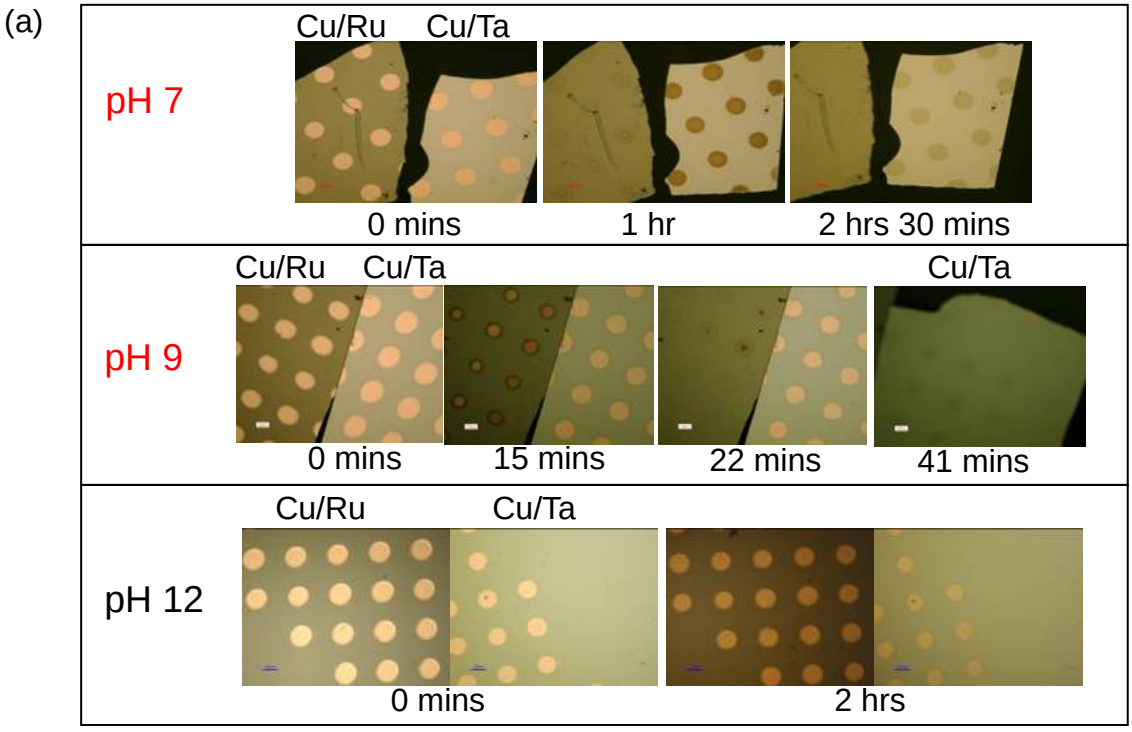

Figure 5-2(a) Micropattern corrosion screening results of Cu/Ru and Cu/Ta in 5 mM gallic acid solution at pH 7, 9, and 12 adjusted by KOH.

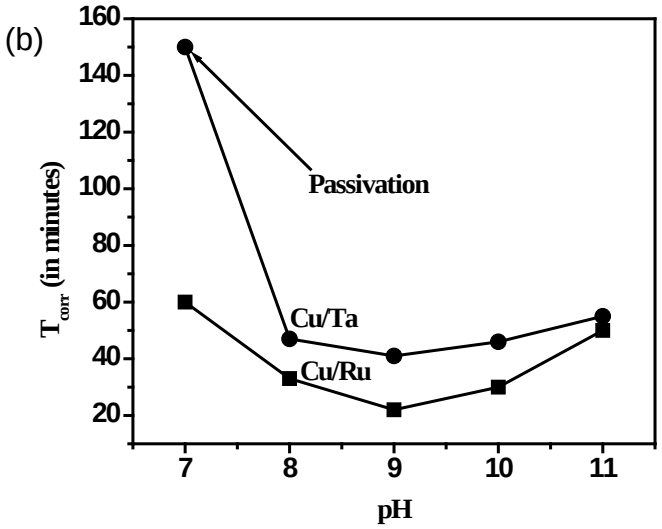

Figure 5-2(b) Micropattern corrosion screening results of Cu/Ru and Cu/Ta in 5 mM gallic acid solution with different pH value adjusted by KOH.

5.3 UV Vis Spectroscopy of Gallic Acid

Gallic acid autoxidation at different pH conditions was characterized by UV Vis spectroscopy (Figure 5-3). Gallic acid remains stable in acidic conditions Figure 5-3(a), pH 5, but the oxidation reaction gradually sets in at pH > 7. Based on UV-Vis spectra, rapid autoxidation of gallic acid takes place in alkaline conditions. Semi-quinone radical exhibits absorption ca. 380-450 nm [11,12]. Figure 5-3 also shows the rate of oxidation of gallic acid since the spectra were recorded at different time intervals in increasing pH conditions. At pH 5 (Figure 5-3a), gallic acid solution remained clear and no absorption peak was observed at 380-450 nm, which demonstrates no formation of semi-quinone radical from oxidation of gallic acid. At pH 7(Figure 5-3b), the radical formation was observed after 3 hours of exposure to atmosphere. Also, the color of solution started to

change from clear to pale green, see insert Figure 5-3b. At pH 9 (Figure 5-3c), the color of the solution turned to dark green within 2 hours and the spectra data illustrates that the radical formation was more pronounced in alkaline condition. Moreover, at pH 12(Figure 5-3d), the color of solution changed to dark green within 15 minutes and further turned to brownish orange which is different from pH 9. The spectra in Figures 5-3c and 5-3d show the absorption wavelength at pH 12 was higher than at pH 7 and pH 9. The extent of oxidation of gallic acid at pH 12 could be higher than at pH 9. The different oxidation progression of gallic acid with solution acidity observed by UV-Vis spectra provides important insights that suggests different species of gallic acid formed could resulted in the pH-dependent corrosion behavior as shown in Figure 5-2.

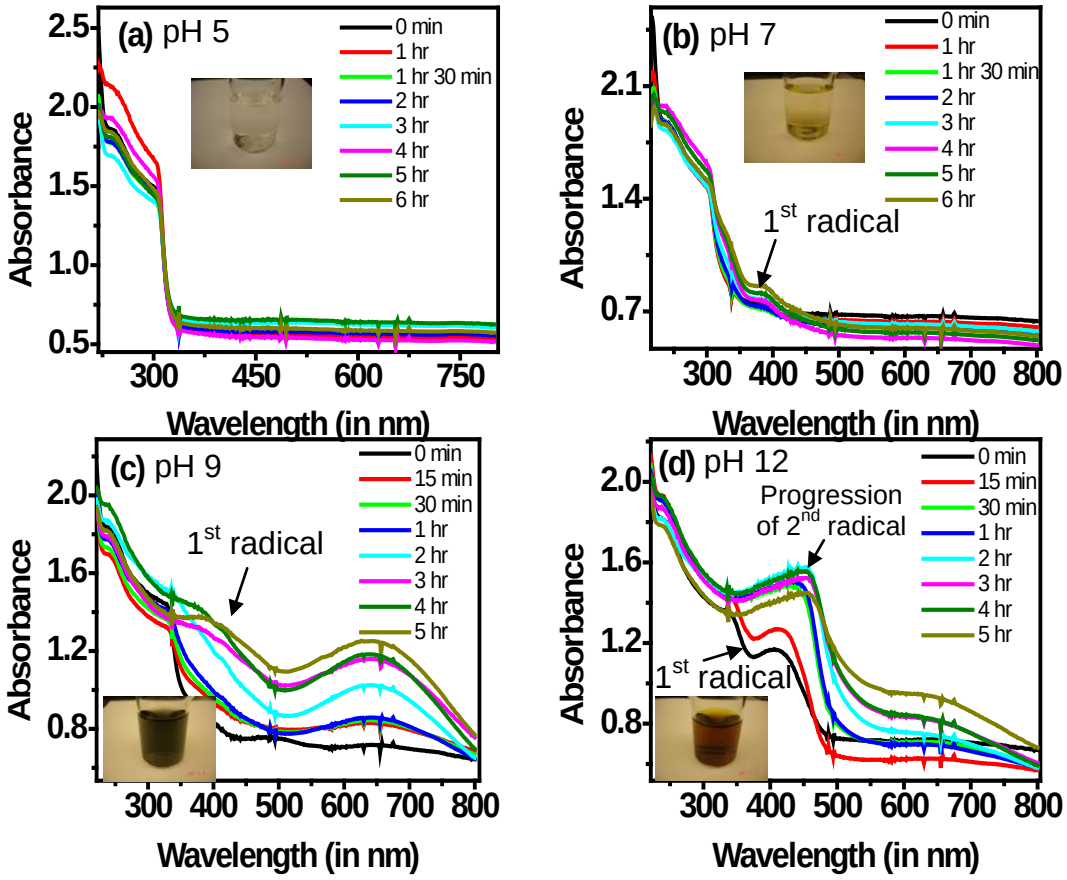

Figure 5-3 UV-Vis spectra's of 5 mM Gallic acid taken at different time intervals to study the rate of semi-quinone formation.

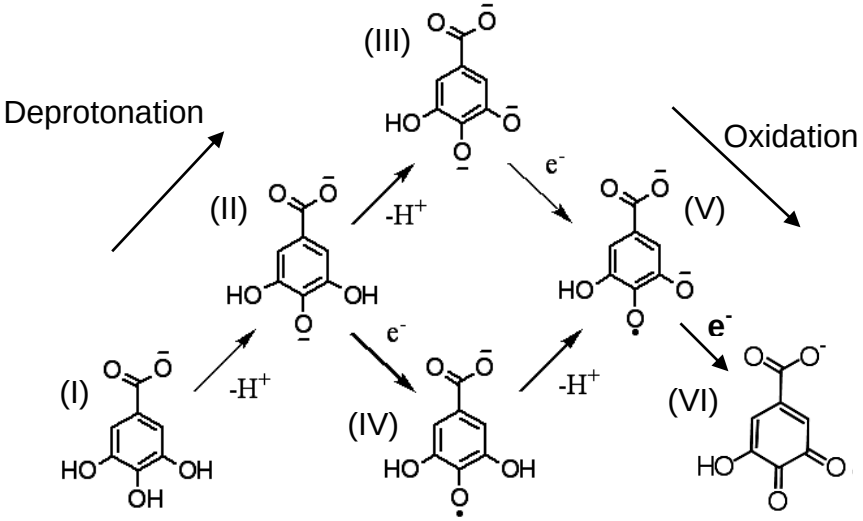

Figure 5-4 pathway deprotonation and oxidation of gallic acid at pH 9.

5.4 Proton Dissociation and Oxidation

The UV-Vis results point out the various oxidation behavior of gallic acid under different pH condition. Therefore, it is important to find out which oxidation state(s) of gallic acid is responsible of Cu corrosion at pH 9 condition. According to the possible oxidation pathway of gallic acid in Figure 5-4, the deprotonation of hydroxyl group in gallic acid is a key intermediate state followed by the oxidation reaction to form radical species. In Figure 5-5, the pK_as of gallic acid and titration curve (5 mM 20ml of gallic acid was titrated by 5 mM KOH) illustrate the proton dissociation process of gallic acid. Stoichiomeitrically, titration curve shows that most of the proton is dissociated from carboxylic acid group at the 1^{st} end point pH~6 after adding 20 ml of KOH ($M_1V_1 = M_2V_2$). With more KOH added to reach pH=9, around 86.3% of $GaAc^-$(I) will be neutralized to form $GaAc^{2-}$(II) through the deprotonation of hydroxyl group at the para-position based on the Eq. (1) (gallic acid pK_{a2} =8.2) [13]. Also, only <2% of species (III) was formed by deprotonation of hydroxyl group at meta-position (pk_{a3} =10.7) at ca. pH 9. It will have even less amount of deprotonation from the second meta-position at pH 9. Titration curve corroborates well with the UV-Vis spectra, Figure 5-3, to explain the process of gallic acid oxidation starting with deprotonation, then followed by radical formation by oxidation. Gallic acid, the oxygen scavenger, can be triggered to react with oxygen rapidly only when the hydroxyl (-OH) group is deprotonated to ($-O^-$), especially in alkaline pH, then oxidized to semi-quinone radical ($-O^{\cdot}$). In order to have structural identification of oxidized gallic acid under different

alkaline conditions, ^{13}C nuclear magnetic resonance (NMR) was used to characterize the solution under high alkaline condition.

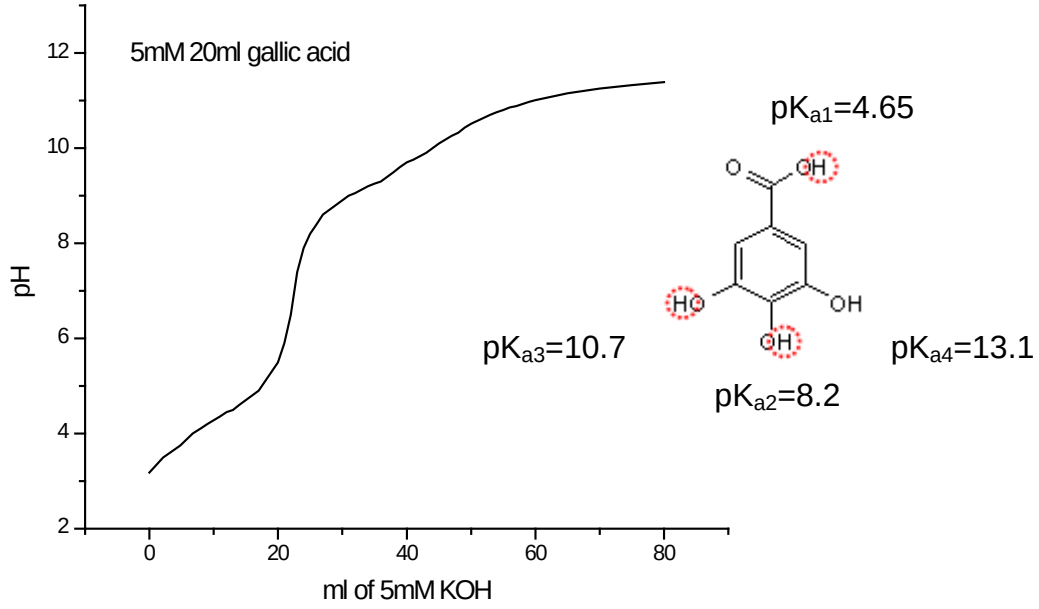

Figure 5-5 Titration curve of gallic acid.

$$pH = pka + log\ \frac{[GaAc^{2-}]}{[GaAc^{-}]} \qquad \text{Buffer Eq. (5-1)}$$

5.5 Identification of Gallic Acid Structure by NMR

Figure 5-6 shows the ^{13}C NMR of gallic acid under different pH condition. The initial pH of the aqueous saturated gallic acid (~35 mM) is pH 3.2 at room temperature. The gallic acid was prepared by using deuterium oxide (D_2O) as solvent and methanol-D was used as reference in acquiring NMR spectra. The pH of gallic acid was adjusted by adding concentrated NaOD. In Figure 5-6, there are 5 different C peaks in ^{13}C NMR spectra. The C peak labeled # 1 belongs to C

carboxylic acid group. The rest of four C peaks labeled # 2-5 belong to the C on benzene ring. The C #2 and C #5 have higher intensity than C #3 and C #4 due to the symmetric structure of gallic acid. The ^{13}C NMR spectra confirm that there is no additional carbonyl group at region between 150 and 180 ppm even at pH 13.5. Thus, no quinone is produced under autoxidation at pH 13.5. Additionally, the shifting of C peaks can give the information of deprotonation. For instance, when pH is increased from 3.2 to 9 the C peak of #1 and #4 are shifted toward down field (high ppm range) due to the increase in electron density after deprotonation of acidic group and hydroxyl group on C #1 and C #4, respectively. Comparing the fresh prepared gallic acid at pH 9 with after 8 hours air exposure, the C NMR spectra didn't change even though the color of solution has changed from green to dark brownish orange. At pH 13.5, the C #2 shifted obviously because the pKa3,4 values of hydroxyl group at meta-positions are 10.1 and 13.1. The C #5 with no hydroxyl group remained at the same position in the C NMR spectra at all pH range. Even though the NMR is unable to detect the radical formation, the information of gallic acid structure and deprotonation of hydroxyl group already offered very helpful evidence of no quinone formation.

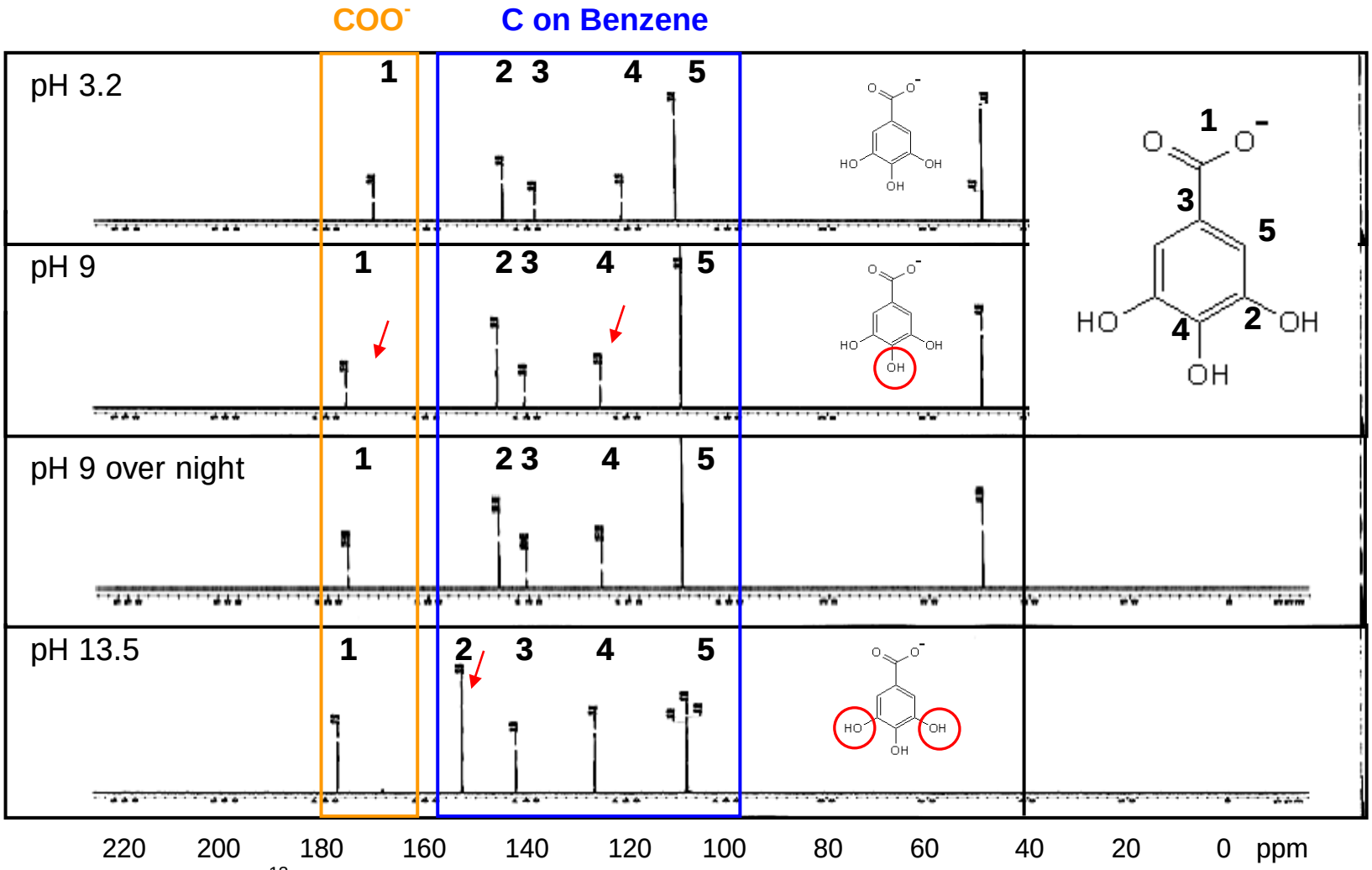

Figure 5-6 shows the ^{13}C NMR of gallic acid under different pH condition.

5.6 Oxygen Effect

A purging nitrogen environment is used to minimize the oxygen content in the solution. At pH 9, limited corrosion of Cu on both Ru and Ta is observed with N_2 purging for at least 3 hour. The result suggests that the oxygen plays a key role of the Cu corrosion in gallic acid as observed in Figure 5-7.

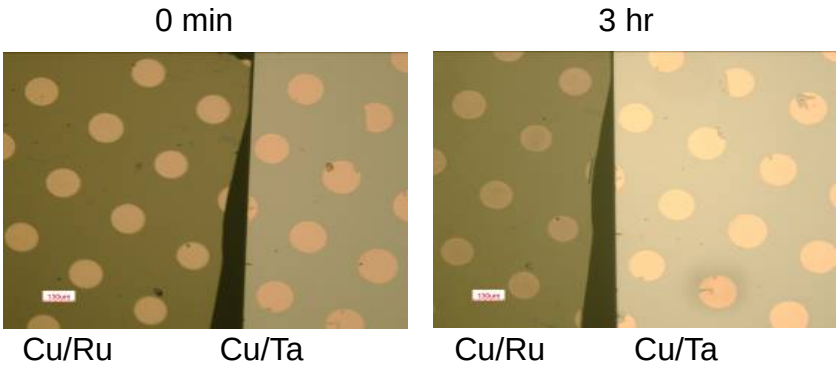

Figure 5-7 Result of micropattern corrosion screening method in N_2 ambient gallic acid at pH 9.

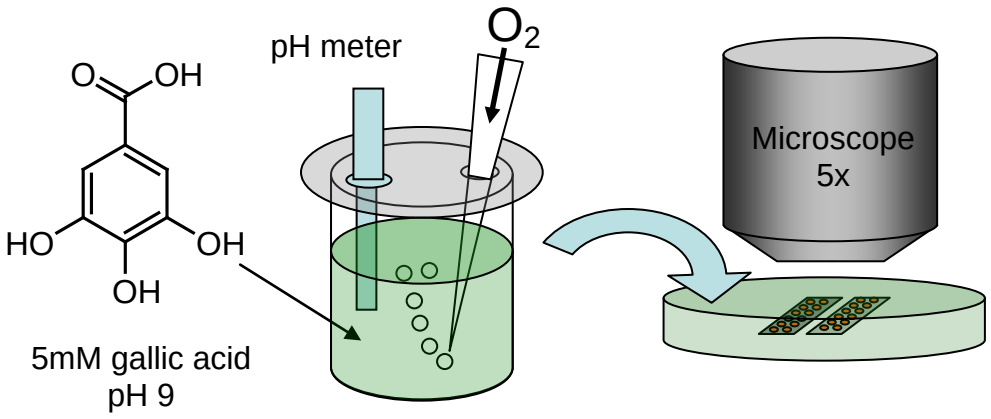

Figure 5-8 Oxygen pre-purged 5 mM gallic acid at pH 9 for corrosion screening.

In order to investigate the role of oxygen in Cu corrosion in gallic acid at pH 9, the result of corrosion screening study with different period of time in O_2 pre-purged gallic acid solution was shown in Figure 5-8. Expectedly, Cu corrosion rate increased after 15 minutes of oxygen purging as shown in Figure 5-9. The corrosion rate of Cu reached to the maximum after 30 minutes of oxygen purged condition and maintained the same corrosion rate for 2 hours. However, the corrosion rate dropped after 6 hours of continuous oxygen pre-purging which illustrates that the corrosive radical/semiquinone that was generated at the beginning by reacting with oxygen, would also be consumed by further reacting with oxygen. In Figure 5-10, linear sweep voltammetry was used to quantify how much reactant was left after autoxidation with oxygen, by scanning the oxidation potential in gallic acid at pH 9. The oxidation plateau from 0.4V to 1.3V reached to the maximum after 15 minutes of oxygen purging and was leveled after 6 hours of oxygen purging, which demonstrates that a lot of corrosive radicals/semiquinone were consumed by on going scavenging oxygen.

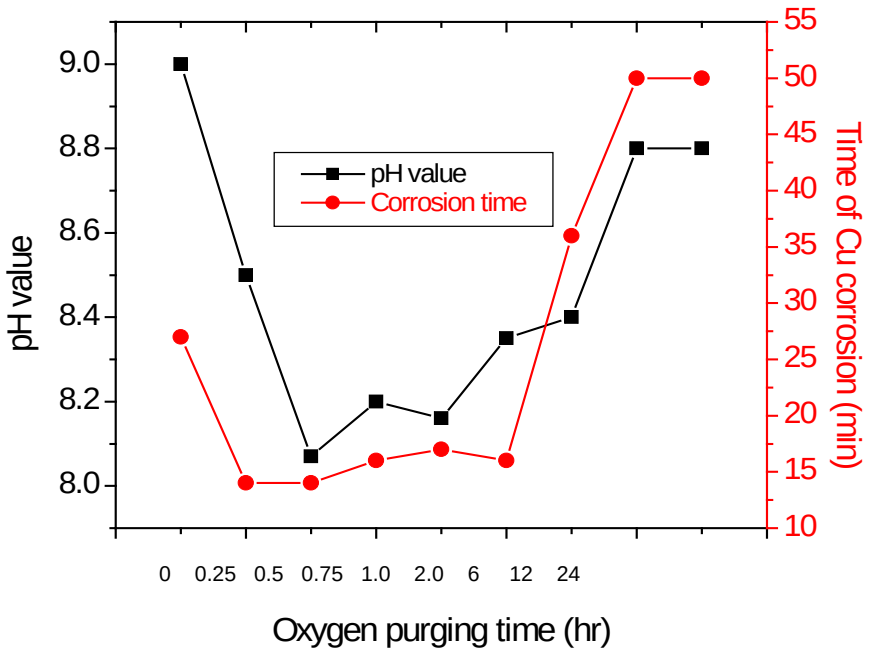

Figure 5-9 Corrosion screening result of oxygen pre-purged gallic acid and monitoring the solution pH by pH meter.

Figure 5-9 also shows, the pH value was changed with different period of oxygen purging time. The pH value was dropped at the beginning, and started to rise back after 30 minutes of oxygen purging. The pH value was dropped from 9 to 8 which means the concentration of proton was increased from 10^{-9} M to 10^{-8} M. The small amount of proton could be contributed by dissociation of hydroxyl group at para-position on gallic acid. However, the pH was increased again after 2 hours due to the fact that the oxygen reduction reaction (ORR) produced hydroxyl ions by reacting with oxygen scavenger, gallic acid at semiquinone form.

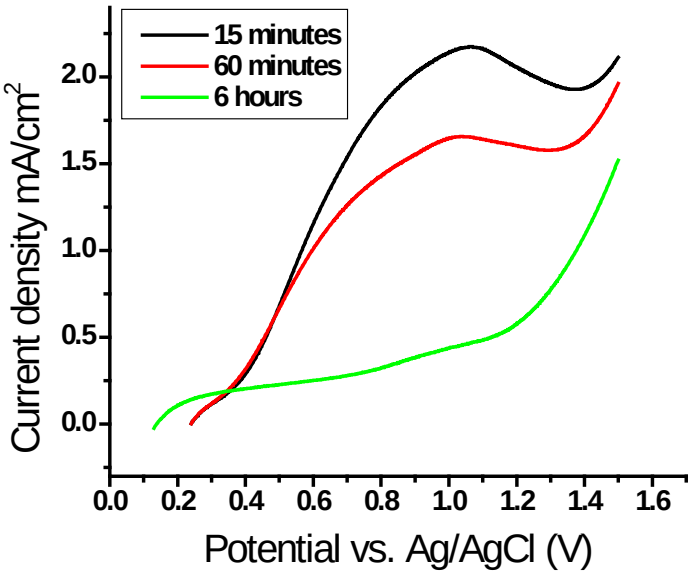

Figure 5-10 Linear sweep voltammetry of 5 mM gallic acid at pH 9 pre-purged with oxygen for various times.

Also, the experiment of air exposure was set up to study the effect of oxygen in air on Cu corrosion shown in Figure 5-11. Comparing air exposure with oxygen purging condition, both air exposed or O_2 pre-purged gallic acid corrodes Cu effectively at the beginning. Exposing gallic acid in lab atmosphere leads to autoxidation forming phenoxyl radical/semiquinone in the solution. However, the Cu corrosion rate decreases in the solution after 11 days of air exposure or 12 hours of O_2 purging. Therefore, O_2 not only leads to form corrosive radical/semiquinone but also consumes the corrosive radical/semiquinone to form higher oxidation state radical/semiquinone species, similar to pH 12 condition, which doesn't cause the corrosion. The pH value of gallic acid changes dramatically in O_2 or air ambient. The pH value keeps decreasing in air exposed condition could be down to the dissolution of CO_2 from air.

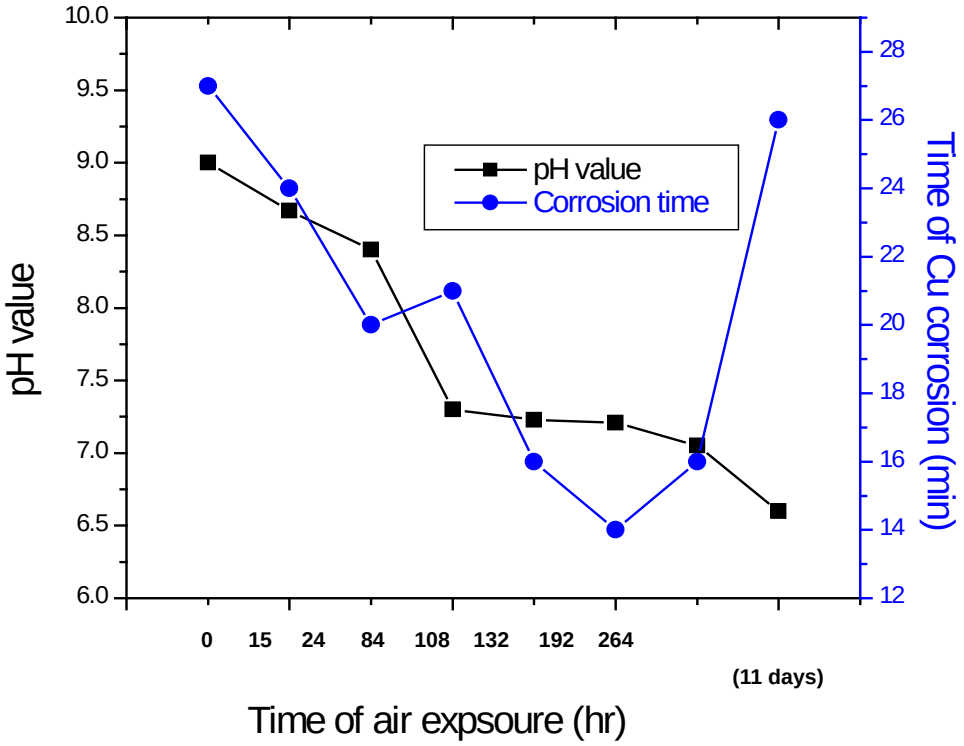

Figure 5-11 Corrosion screening result of air exposed gallic acid and monitoring the solution pH by pH meter.

5.7 Structural Effect

The micropattern corrosion screening method was applied on probing the relevant antioxidants in post-CMP environment as shown in Figure 5-1. The results of corrosion screening suggested that Cu corrosion was enhanced only when the polyphenol contains endiol structure with existence of two adjacent hydroxyl groups on benzene ring such as catechol and gallic acid as shown in Figure 5-12. Also, each polyphenols with endiol structure, like gallic acid, has Cu different corrosion rate under different pH range.

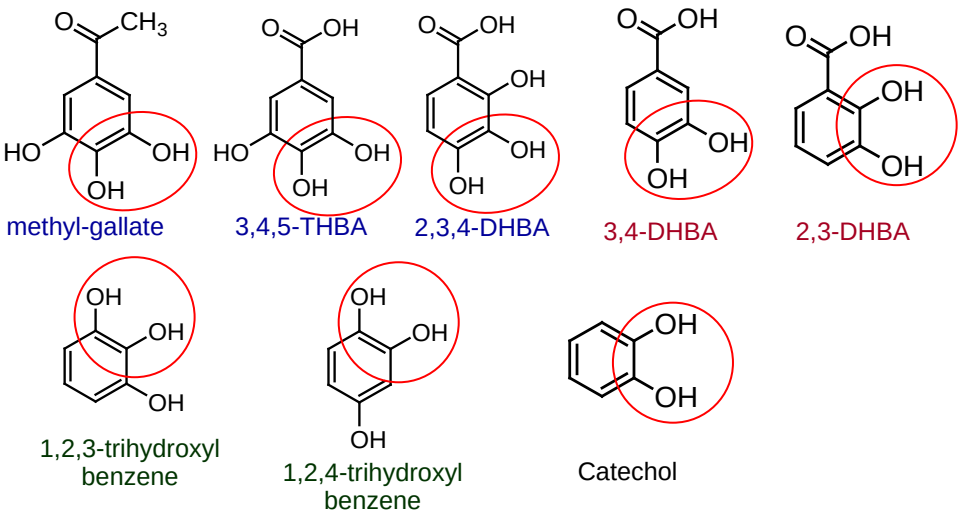

Figure 5-12 Relevant polyphenol antioxidants contain endiol structure.

5.8 Corrosion Mechanism

The Pourbaix (potential-pH) diagram (Figure 5-13) indicates that alkaline solution condition could facilitate Cu oxidation more readily. However, micropattern corrosion testing of Cu/Ru and Cu/Ta carried out in pH 9 DI H_2O shows no sustained Cu corrosion. In general, gallic acid is an effective scavenger for oxygen and hydroxyl radicals and so it minimizes their availability to oxidize copper. In contrast, active Cu corrosion is observed in alkaline gallic acid solution. Therefore, Cu active erosion in Cu/Ru and Cu/Ta bimetallic contacts submerged in alkaline gallic acid cannot be attributed to the Cu oxidation alone. Active Cu corrosion requires both thermodynamically favorable conditions for initial Cu oxidation and proper chemistry that can readily remove oxidized Cu species cumulated on surface to sustain the active Cu erosion. In chapter 4, our

micropattern screening demonstrated that the surface oxidation on Cu in alkaline solution (like K_2SO_4 pH>6) formed stable Cu oxides or Cu hydroxides that lead to passivation. In contrast, ammonia (NH_3) effectively forms complexes with Cu^{2+} to facilitate the active bimetallic corrosion of Cu/Ru in alkaline ammonium hydroxide solution. Furthermore, the effects of Cu bimetallic contacts to Ru and Ta need to be considered in order to establish Cu corrosion mechanism in gallic acid. Based on the electromotive force (emf) series, the nobility of these three metals is in order Ru >Cu and Cu >Ta. Hence positive current flows from Cu to Ru by the oxidation of Cu due to large bimetallic potential difference established between Cu and Ru. Our electrochemical analyses (Tafel plot and direct galvanic current measurement) corroborate the enhanced Cu corrosion on Ru substrate observed by micropattern screen shown in Figure 5-14 and Figure 5-15.

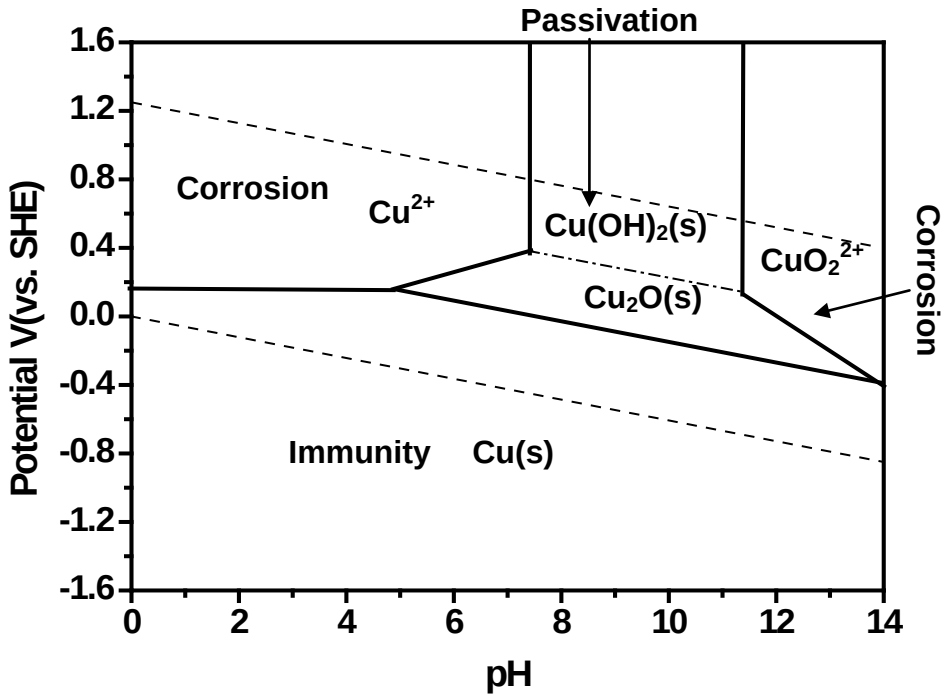

Figure 5-13 Pourbaix diagram of Cu – domains of corrosion, immunity and passivation for copper.

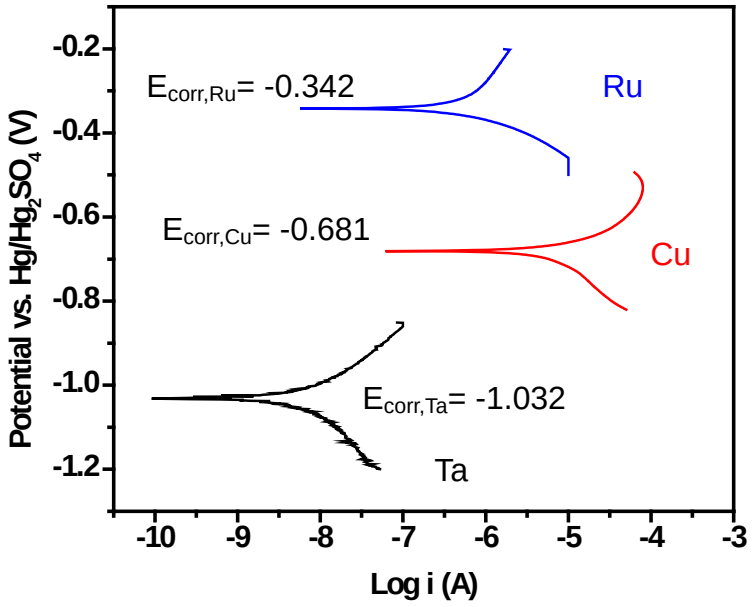

Figure 5-14 Tafel plots of Ru, Cu and Ta electrode in 5 mM gallic acid solution at pH 9.

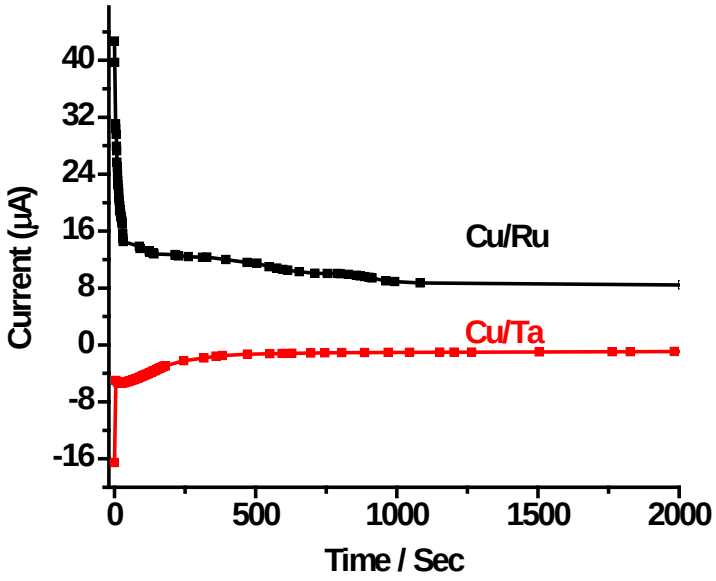

Figure 5-15 Direct galvanic current measurements of Cu/Ru and Cu/Ta in 5 mM gallic acid solution at pH 9.

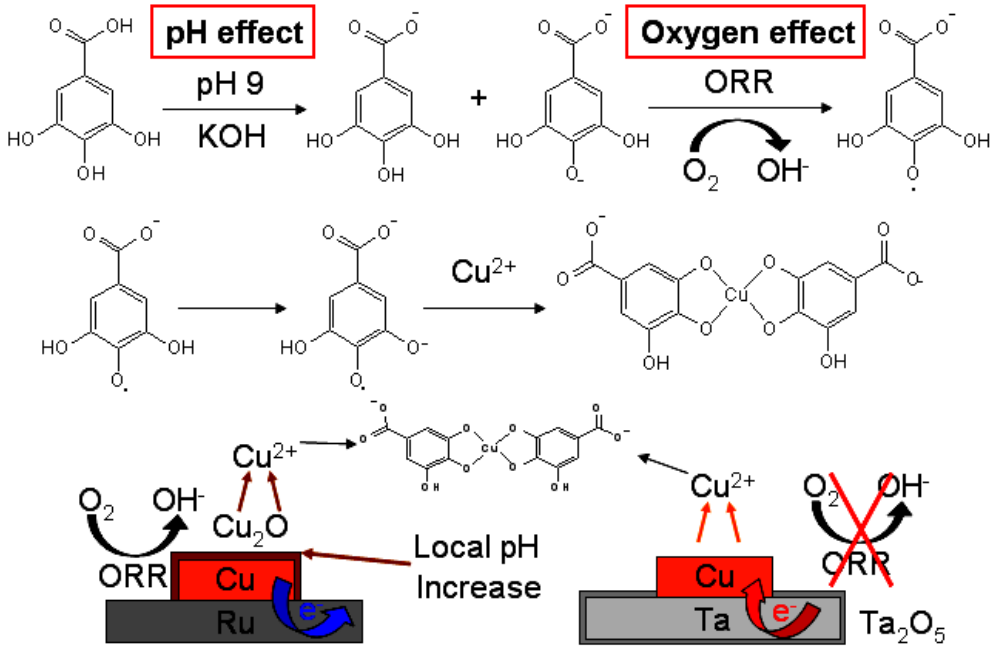

Figure 5-16 Gallic acid corrosion mechanism demonstrates pH, oxygen, substrate and structure effects on Cu corrosion.

Figure 5-16 depicts a framework to develop a plausible Cu corrosion mechanism under alkaline gallic acid solution. At pH 9, the gallic acid will be de-protonated at carboxylic acid and para-hydroxyl positions [14]. Our ambient control corrosion study established that oxygen can greatly accelerate the corrosion of Cu microdots. Ru is well known electrocatalyst for the oxygen reduction reaction (ORR), the common rate determination step for the fuel cell operation. Therefore, ORR reaction on Ru could oxidize the de-protonated gallic acid to anion radicals and readily form Cu complexes by chelating Cu ion with both adjacent hydroxyl sites (chelation of phenolate) [15]. These Cu complexes are highly soluble and provide efficient pathway to remove oxidized Cu and accelerate the Cu corrosion. In addition, with Cu/Ru bimetallic contact, Ru substrate could promote the ORR reaction to raise local pH from 9 to ~12. This increase local surface alkalinity combined with favorable galvanic contact to a Ru further accelerates Cu corrosion. In contrast, the Ta substrate readily forms surface oxide based on the XPS surface analyses. In fact, Ta oxidation provides the cathodic protection to slow down Cu corrosion in Cu/Ta system, Figure 5-15. The Ta oxide surface is not capable of promoting ORR and consequently a lower Cu corrosion rate is observed.

At pH 12, the Cu micropattern formed passivation layer on both Ru and Ta substrates as shown in Figure 5-2a. According to the ^{13}C NMR and UV-Vis spectra data, the different semiquinone/radical structure of gallic acid in high alkalinity resulted in absorbing on Cu surface rather than chelation with Cu to

form dissolved Cu-gallic acid complexes. The ^{13}C NMR spectra data also demonstrates the result of no dimmer formation and quinone formation.

5.9 Summary

A new rapid corrosion screening metrology was developed and demonstrated for effective characterization Cu bimetallic corrosion in post CMP solution environment. Our data suggested that balance between oxide formation and complex reaction can affect the final outcome of Cu bimetallic corrosion. The efficient micropattern corrosion screening helped to reveal the hidden pH dependent corrosive property of gallic acid that was previously perceived as Cu anti-oxidant.

5.10 References

1 W. J. Lee, H. S. Park, S. I. Lee, H. C. Sohn, *J. of Applied Electrochem.* **2004,** 34.

2 T. D. Chandrakant, G. Eur. Banerjee, Patent Appl. (2005) EP 1577934 20050315

3 S. Naghshineh, J. Barnes, E. Oldak, US. Pat. Appl. Publ. 20010004633 (2001)

4 M. Mochizuki, S. Yamazaki, K. Kano, T. Ikeda, *Biocheim. Biophys. Acta*, 2002

5 F. Cariati, S. Deiana, L. Erre, G. Micera, P. Piu, *Inorganica Chimica Acta*, **1982,** 64.

6 K.Gerega, H. Kozlowski, T. Kiss, G. Micera, S. L. Erre, F. Cariati, *Inorganica Chimica Acta,* **1987,** 138.

7 A. Oess, M. V. Cheshire, L. Spack, Vedy, *J. C. Analysis,* **1999,** 27.

8 M. McDonald, I. Mila, A. Scalbert, *J. Agric. Food Chem,* **1996,** 44.

9 B. Beverskog, I. Puigdomenech, *J. Electrochem. Soc.*, **1997,** 144.

10 S. Naghshineh, J. Barnes, Y. Hashemi, E. B. Oldak; U.S. Patent 6194366

11 Schuchmann, M. N.; Bothe, E.; Sonntag, J. Von.; Sonnatag, C. Von. *J. Chem. Soc. Perkins Trans. 2*, **1998,** 791-796;

12 Fink, W. D.; Stong, J. D.; *Spectrochimica Acta* **1982,** 38A, 1295-1298.

13 K.K. Yu, K. S.M. Pillai, P. R. Nalla, O. Chyan, *J. Appl Electrochem.*, **2010,** 40.

14 Oess et al., *The Science of the Total Environment*, **1999,** 228.

15 Kiss, T.; Kozlowski, H.; Micera, G.; and Erre, L. S.; *Polyhedron 8*, **1989,** 647-651.

PART III

ELECTROCHEMICAL CHARACTERIZATION OF ORR CATALYSTS

CHAPTER 6

ELECTROCHEMICAL CHARACTERIZATION OF OXYGEN REDUCTION REACTION (ORR)

6.1 Introduction of ORR in Fuel Cell

Due to the fact that fossil fuels will be used up after several decades, it is necessary to find out alternative energy sources that do not exhaust natural resources or emit the green house gases to harm the environment. The renewable natural resources such as sunlight, wind, rain, tides and the geothermal heat will not be exhausted. However, those natural resources are not consistent or continuous. Therefore, owing to produce stable and consistent power, the energy extracted from natural resources is generally stored as electricity in the storage devices such as batteries. As opposed to the huge and heavy batteries, the liquid hydrogen has been considered as a portable fuel for generation of electric power. Hence, there has been an increasing interest on studying proton exchange membrane (PEM) fuel cell nowadays.

In 1831, Michael Faraday discovered the phenomenon of electromagnetic induction with which the fundamental principle of the electric power generator is based. The early electric power-generator encountered the limitation of power

transmission and relative insufficiency of power generation. At the end of 19th century, the coal-burning generators were the most used in power plants; achieving fewer than 20% efficiency of energy conversion at the turn of the century. However, the limitation of energy resources and the concern for environmental pollutions propel the need to develop new power generation with lower emissions and higher efficiencies. Therefore, the level of research interest in fuel cell has been increased steadily. As part of that developing trend, Ostwald predicted the 20th century would be the “Age of Electrochemical Combustion” [1].

Owing to the space race, it is necessary to develop a power source with lightweight and high efficiency for space application. In 1963 a proton exchange membrane fuel cell (PEMFC) was invented by William Grubb and Lee Niedrach of General Electric [2, 3]. At that time, the ion-exchange membrane had a limited lifetime in the fuel cell [1]. In 1996, Supramaniam Srinivasan, the winner of the Energy Technology Research Award, has greatly extended the durability of the ion-exchange membrane in PEM technology [1, 4]. Subsequently, many papers have been published and research activities have shown the study of operational effects on fuel cell durability, gas diffusion layer, membrane degradation and electrocatalyst stability. In the electrocatalysis study, the major technical challenge in development of commercial PEM fuel cell is to develop an inexpensive, stable and highly efficient electrocatalyst for oxygen reduction reaction (ORR). Due to the excellent electrochemical catalytic activity of platinum metal, platinum-based catalysts have been widely used in fuel cell for both

hydrogen oxidation reaction (HOR) and oxygen reduction reaction (ORR). However, the scarcity of platinum (only 37 ppb in the Earth's crust) [13] causes the price to increase from a historically constant price of $450/troz to the current price of $1,800/troz (March/2011) (Figure 6-1) [5]. Since the amount of platinum loading is a key parameter for increasing power density in PEM fuel cell, several researchers have been studying on new electrocatalyst without platinum so as to minimize the production cost for large scale commercialization.

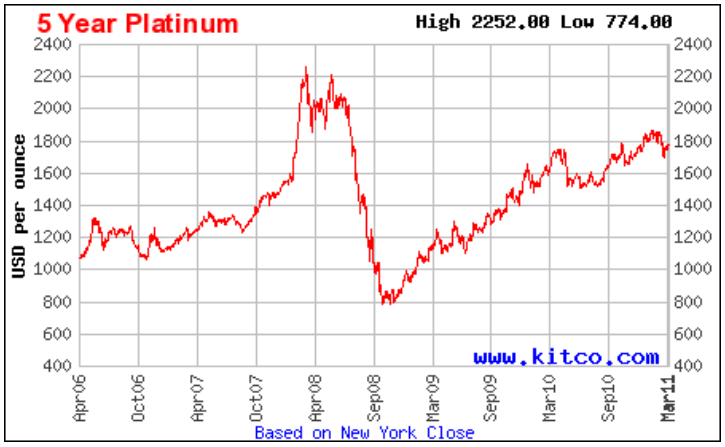

Figure 6-1 History of platinum price (USD per troy ounce)[5].

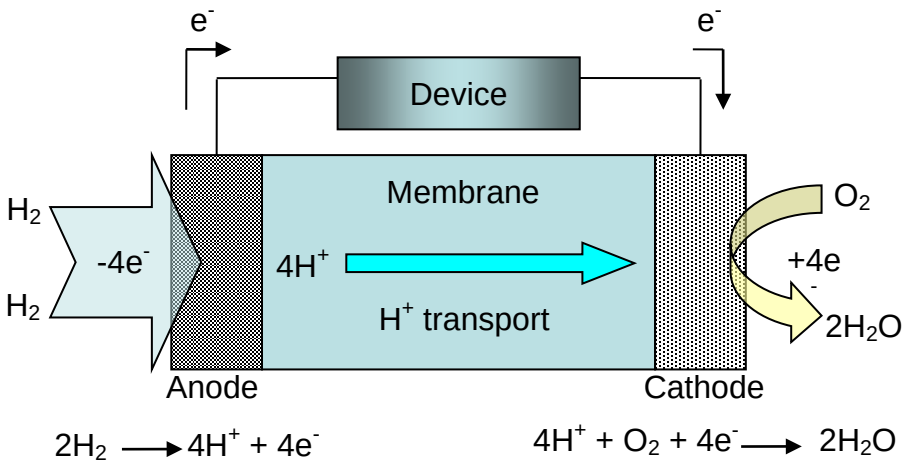

Figure 6-2: Simplified PEM fuel cell reactions.

The PEM technology shown in Figure 6-2 has the best efficiency and power density than other fuel cell technologies that can achieve in air and at low temperature operating condition.

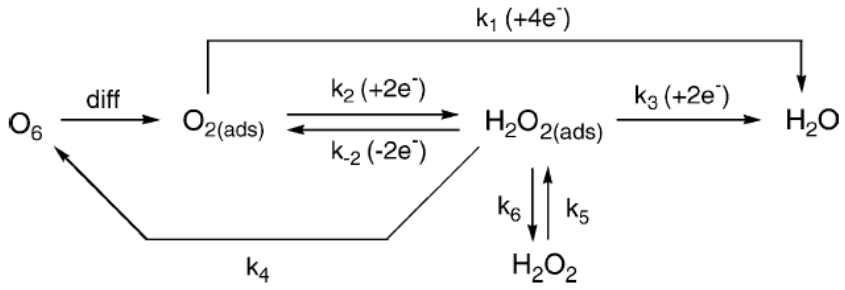

Scheme 6-1 Several individual reactions in ORR pathway[7].

There are several individual reactions proposed in the ORR pathway (Scheme 6-1) [7] that includes the four-electron reduction and two-electron reduction reactions. A four-electron reduction reaction produces the hydroxyl anions directly from the oxygen molecule; the two-electron reduction reaction generates peroxide species which can cause the corrosion of electrocatalyst and chemical degeneration of PEM and decrease the efficiency of energy conversion. Therefore, research groups spent much effort on finding alternative electrocatalysts to minimize the formation of H_2O_2. In PEM fuel cell, the conversion energy of each cell drops, even using Pt-based ORR electrocatalyst, from a theoretical value of 1.229V to 0.7V [8], due to the sluggish kinetic rate of ORR and its high overpotential [9-12]. In order to provide economical catalysts with higher voltage, efficiency, durability, and lower generation rate of peroxide

species, the investigation of new non-platinum cathodic electrocatalyst [13, 14] is considered highly essential.

Owing to the requirement of extended operation life time, the materials of ORR electrocatalyst must have high stability and resistance to corrosion. The noble metals like platinum, palladium, rhodium, ruthenium, osmium, iridium, silver and gold, and their oxides have been widely studied and some were demonstrated to be good electrocatalyst for ORR [15]. Besides that, the recent development of the nano-technique and thin film deposition allow coating of the monolayer of noble metal such as nanoparticles to minimize the loading of precious metals [6]. The non-noble metals were also investigated for electrocatalytic activity especially on higher temperature operation systems [16]. The Pt-based materials are still the best electrocatalysts [16] and commonly used as a comparison standard for the development and discovery of new electrocatalysts on ORR.

6.2 Electrochemical Characterization of ORR

A good ORR catalyst not only has a high reaction rate of four electron transfer oxygen reduction but also has a low rate of two electron transfer as hydrogen peroxide formation. The formation of hydrogen peroxide damages the PEM membrane, which could lead to serious explosive situation when the hydrogen fuel meets the oxygen source through the defected membrane area. Therefore, it is important to analyze and minimize the formation rate of hydrogen

peroxide. Nowadays, the rotating ring-disc electrode (RRDE) and scanning electrochemical microscopy (SECM) systems are used for detecting the rate of hydrogen peroxide formation. In RRDE system, H_2O_2 can be detected at the ring electrode by applying a constant positive potential and can be quantified by oxidizing current from the ring electrode as shown in Figure 6-3 (a). Alternatively, the hydrogen peroxide can be detected by the scanning tip in SECM system as shown in Figure 6-3 (c) [17, 18]. Or the use of fluorescent sensor of hydrogen peroxide [19] in the electrolyte can also optically estimate the formation rate of hydrogen peroxide during the ORR.

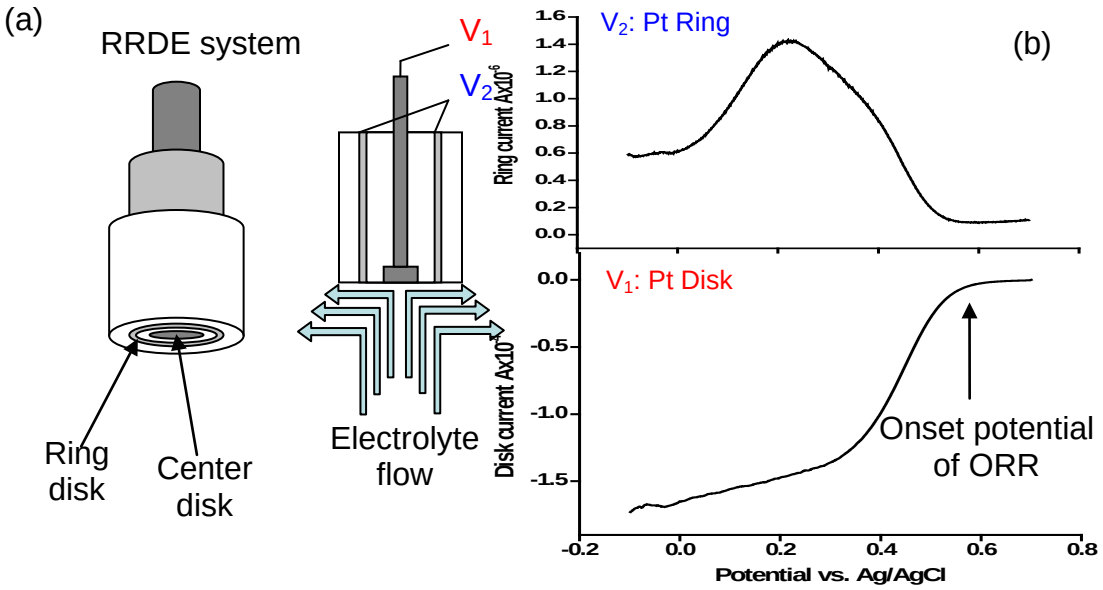

Figure 6-3 (a) RRDE system (b) One example of Pt RRDE in 0.5 M H_2SO_4 with 900 rpm.

(c) SECM system

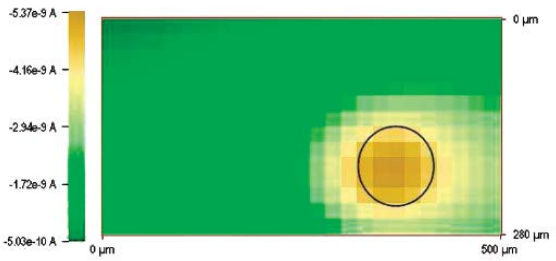

SECM image: mapping current

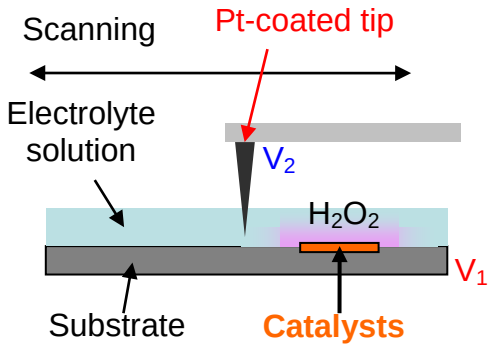

Figure 6-3 (c) Scanning electrochemical microscope (SECM) system [17].

6.2.1 Linear Sweep Voltammetry

Both RRDE and SECM techniques are based on two working electrode system which the second working electrode like ring electrode and scanning tip electrode is useful on detecting hydrogen peroxide. Linear sweep voltammetry (LSV) is one of the electrochemical techniques which is also capable to evaluate the onset reduction potential of ORR catalysts. Though LSV can detect the difference in ORR onset potential between N_2 purged and O_2 purged solutions, it cannot resolve the hydrogen peroxide generation from ORR. However, LSV is a good initial screening technique to quickly probe the new catalysts by evaluating the oxygen reduction onset potential. Subsequently, the formation of hydrogen peroxide can be determined by RRDE at a later time. Usually, the operation temperature of PEM fuel cell is around 80°C. Hence, the thermostat set up as shown in Figure 6-4 is used to raise the operating temperature during the LSV measurements.

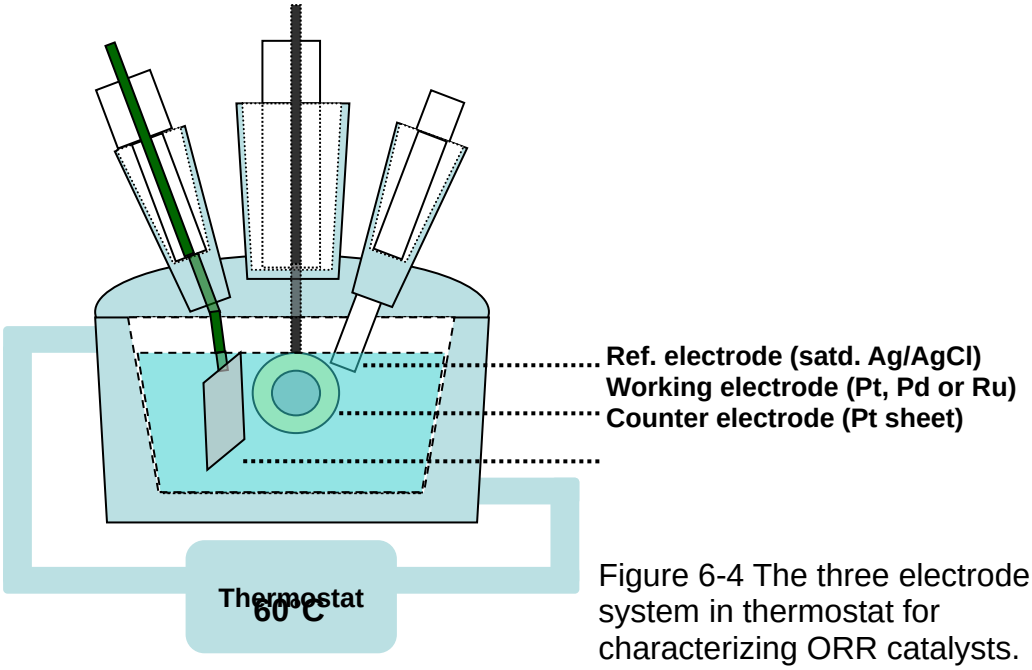

Figure 6-4 The three electrode system in thermostat for characterizing ORR catalysts.

Figure 6-4 (a) shows the Pt CVs in 0.5 M H_2SO_4 under nitrogen ambient (black line) and oxygen ambient (red line) at 60°C. With the increase in dissolved oxygen content in sulfuric acid electrolyte, the reduction charge was observed to be enhanced at cathodic region *ca.* 0.6V (vs. Ag/AgCl) and that is overlapped with the Pt surface oxide reduction peak at *ca.* 0.6V. The reduction of surface oxide imposes some technical difficulty to identify the onset potential of ORR. In order to clarify the onset potential of oxygen reduction reaction, the Pt surface was electrochemically cleaned and reduced before the examination of onset potential of ORR. Figure 6-5 (b) and (c) show the CV and the LSV, respectively. Comparing nitrogen background with oxygen ambient, the CV and LSV can pin point the onset potential of ORR at 0.6V (vs. Ag/AgCl) on Pt catalyst at 60°C.

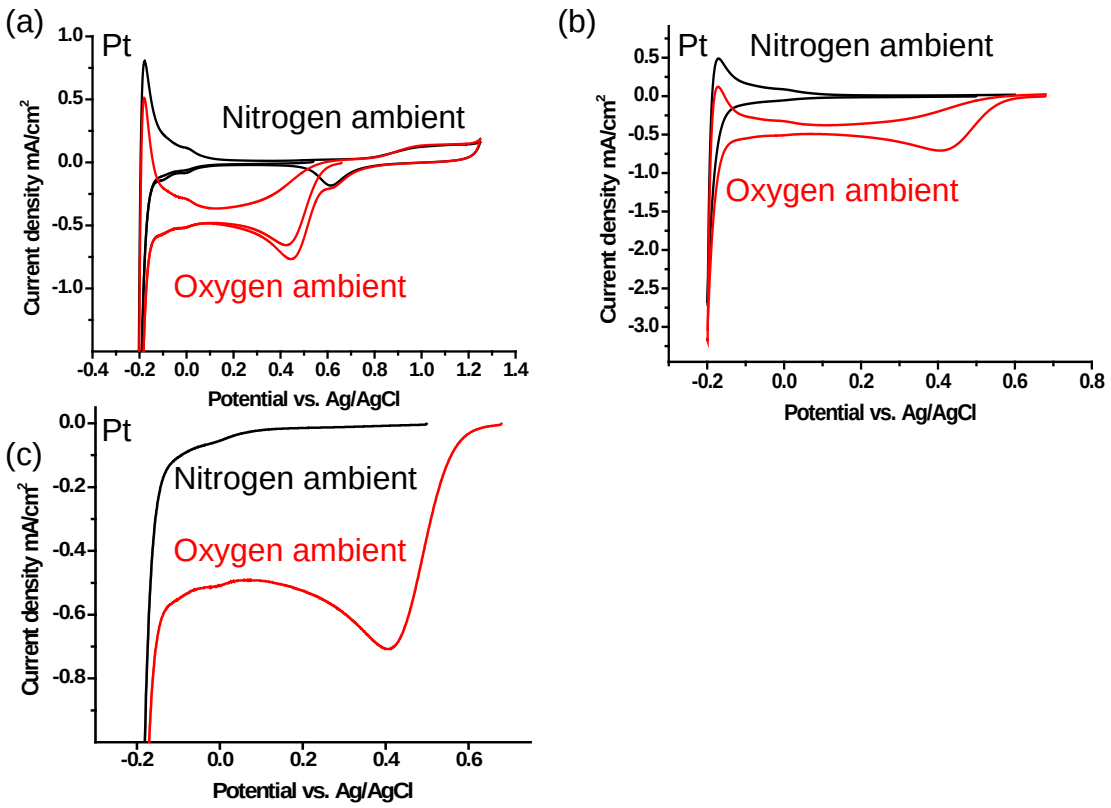

Figure 6-5 (a) and (b) Pt CVs in 0.5 M H_2SO_4 nitrogen ambient (black line) and oxygen ambient (red line). (c) LSVs of Pt in 0.5 M H_2SO_4 nitrogen ambient (black line) and oxygen ambient (red line). Scan rate is 50mV/s for all of LSV and CV.

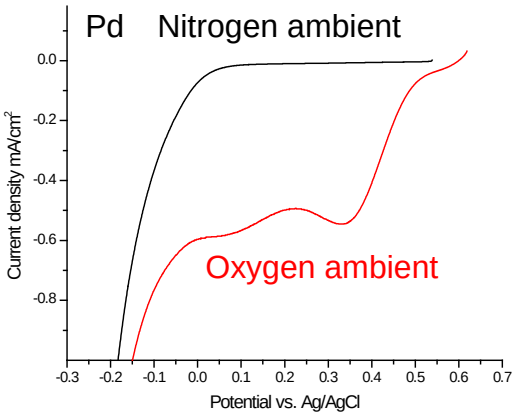

Figure 6-6 LSV of Pd SEC cell in 0.5 M H_2SO_4 nitrogen ambient (black line) and oxygen ambient (red line).

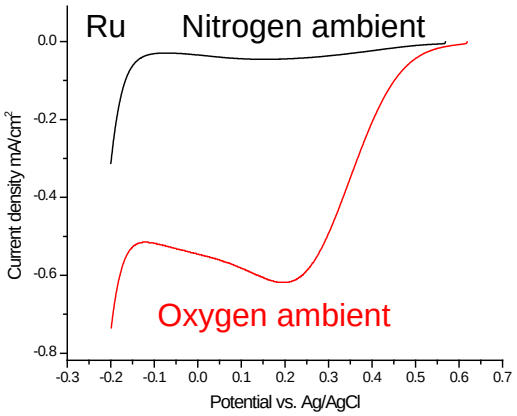

Figure 6-7 LSV of Ru SEC cell in 0.5 M H_2SO_4 nitrogen ambient (black line) and oxygen ambient (red line).

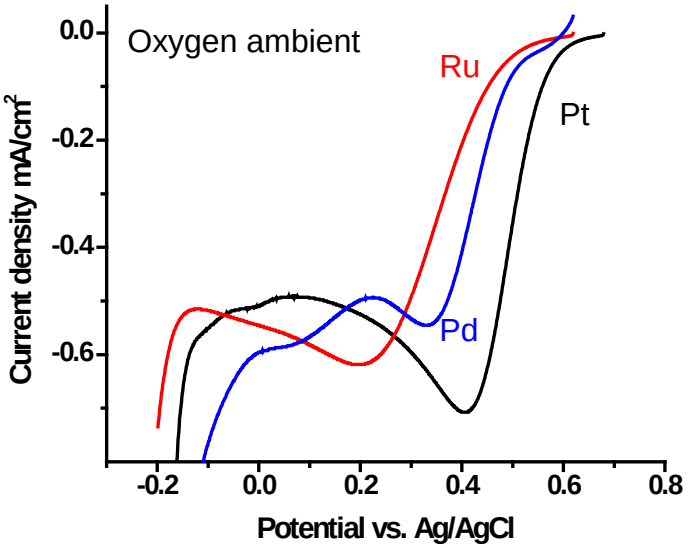

Pt 0.6V
Ru 0.5V
Pd 0.52V

Figure 6-8 Overlapped of LSVs of Pt, Ru, and Pd SEC electrode in 0.5 M H_2SO_4 oxygen ambient at 60°C.

Similar to Pt, the Pd and Ru thin film electrode were also prepared by sputter deposition on glassy carbon electrode. The Pd and Ru LSV results were shown in Figure 6-6 and Figure 6-7, respectively. By comparing oxygen ambient with the nitrogen background, the trend of onset potential was obtained: Pt (0.6V)

> Pd (0.52V) > Ru (0.5V). In Figure 6-8, the overlapped LSV of Pt, Pd and Ru show the different slopes of ORR current versus potential at over-potential region. The initial ORR rate based on current-potential slop is found in the following order: Pt > Pd > Ru. The result of static LSV experiment may not reveal the kinetic limitation of electron transfer process. Therefore, it is important to use RRDE or RDE system for kinetic study.

6.2.2 Rotating Ring-Disc Electrode (RRDE)

Nowadays, majority of ORR catalyst studies have been reported using RRDE system as shown in Figure 6-2. The dynamic potential scanning was applied on center disk and the operation principle is same as LSV. Therefore, the onset reduction potential can be detected at the point where the ORR reduction current increase. The ring electrode in RRDE system was used to detect the formation of hydrogen peroxide and can be done by applying oxidizing potential on ring electrode to oxidize the H_2O_2. The H_2O_2 ($2e^-$) and H_2O ($4e^-$) were generated from center disk during the process of ORR and they were carried by the outward flow pattern toward the surface of ring electrode, Figure 6-2. Hence, H_2O_2 is oxidized to form H_2O when passing through the positively bias ring electrode. The oxidation current was obtained as shown in the top and bottom of Figure 6-2 (b) which is the LSV while the RRDE electrode was rotated at 900 rpm.

The RRDE system not only can reveal the electron transfer number of

ORR catalyst but also can clarify the onset potential of ORR. Besides it can also provide the information on kinetic behavior of ORR catalysts. With increasing rotating speed, the reactants are continuously supplied along flow pattern to the disk electrode surface [20], which allows to verify the kinetic limitation of electron transfer (current) for ORR on different catalysts.

Figure 6-9 (a) and (b) show the result of Pt RRDE in 0.5 M H_2SO_4 at varying rotating speed under lab ambient. And Figure 6-9 (c) and (d) demonstrates the limiting current at different applied potentials. The limiting kinetics depends on the applied potential and it increased when the corresponding overpotential is increased. In Figure 6-9 (c), which shows the square root of rotating speeds versus current density of disk electrode, the non-linear curve (like 0.40V) indicates a kinetic limit situation. In other words, the reaction rate did not change even when the supply of reactant is increased by rotating rate. The kinetic limit region is shown in Figure 6-9 (c) at 0.4V (blue line) which approximates to a current density value of 0.6 mA/cm^2. However, it is hard to find out the rest of applied potential such as 0.2V and -0.1V owing to the limitation of rotating speed, as high rotating speed could generate turbulence flow on electrode surface. Hence, the Koutecky-Levich plots at Figure 6-9 (d) were used to estimate the limiting current. The interception at y axis ($1/I_k$) demonstrates the current limit I_k. The I_k at different applied overpotentials were obtained. For instance, the interception at y axis ($1/I_k$) at 0.4V and -0.1V were 8.0 mA^{-1} and 2.0 mA^{-1}, respectively. By inverse calculating and dividing with

electrode working area (0.196cm^2), the I_k at 0.4V and -0.1V were obtained as 0.63 mA/cm^2 and 2.55 mA/cm^2, respectively. The calculated I_k at 0.4V was 0.63 mA/cm^2 which is close to the value as shown in Figure 6-9 (c). Hence, the higher I_k indicates the lower kinetic limitation of ORR on catalyst surface.

The electron transfer number n can be calculated by following equations

$$N_{eff} = \frac{I_r}{I_d} \qquad \text{Eq. 6-1}$$

$$\text{Electron transfer number } n = \frac{4I_d}{I_d + (I_r/N_{eff})} \qquad \text{Eq. 6-2}$$

$$\text{Mol. \% } H_2O_2 = \frac{I_r}{I_d N_{eff}} \qquad \text{Eq. 6-3}$$

Where N_{eff} is the collection efficiency, I_d is the disk current and I_r is the ring current. The N_{eff} was given as 15 % with rotating speed at 900 rpm. The electron transfer number of Pt is *ca.* 3.62 at 0.2V with limiting current, I_k: 2.23mA and10.4% H_2O_2.

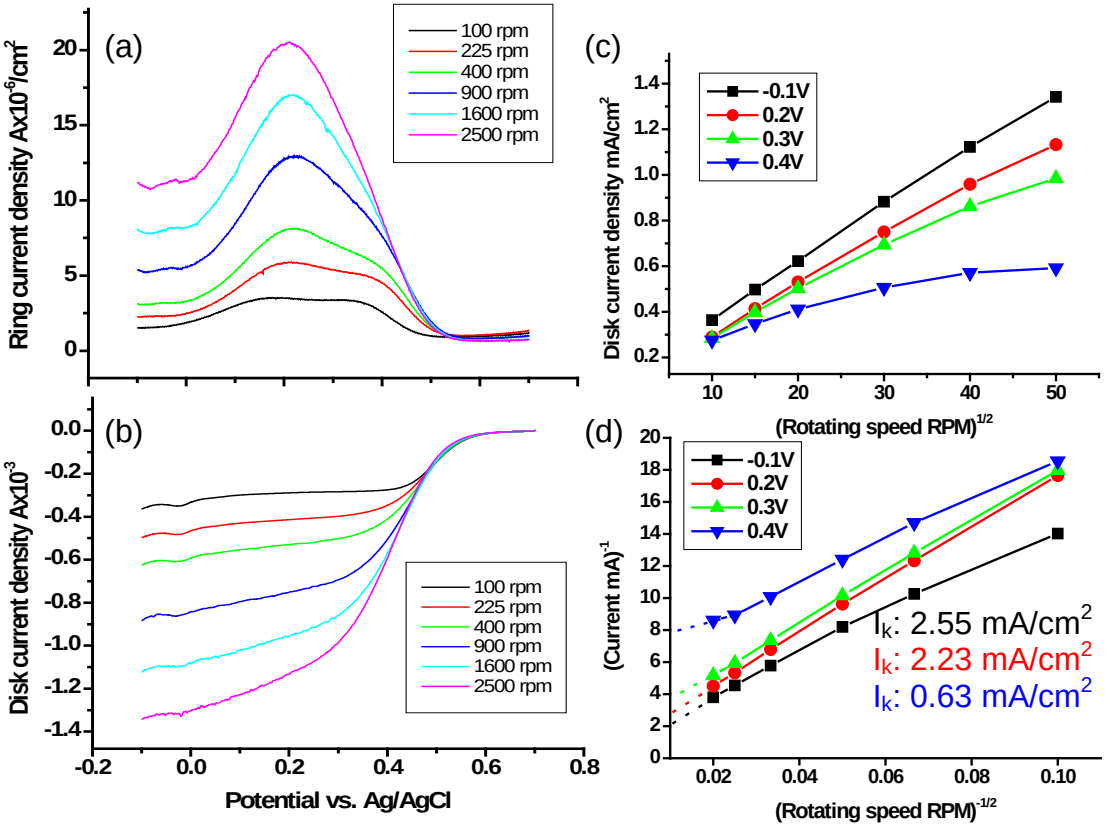

Figure 6-9 the result of Pt RRDE system in 0.5 M H_2SO_4 (lab ambient) with different rotating speed from 100 rpm to 2500 rpm (a)ring current (b)disk current (c)Variation of I with $\omega^{1/2}$ at an RDE (d) Koutecky-Levich plots at varying potentials.

In Figure 6-10, the ORR onset potential on Ru is *ca.* 0.4V, which is 100mV lower than that on Pt. The electron transfer number for Ru is *ca.* 3.36 at 0.1V with I_k: 1.68mA and 19.2 % H_2O_2. In Figure 6-11, RuO_xH_y electrode was made by electrochemically oxidizing Ru electrode. The electron transfer number of RuO_xH_y is *ca.* 3.89 at 0.2V with limiting current, I_k: 1.6mA and 2.9 % H_2O_2. The onset potential of ORR on RuO_xH_y was similar to Pt at 0.5V and the electron transfer number was much better than Pt. The percentage of H_2O_2 generation

was only 2.9% on RuO_xH_y catalyst. But, comparing 6-9(d) with 6-11(d), the current limitation, I_k, on RuO_xH_y at 0.2V was 1.6 mA/cm^2 lower than that on Pt (I_k: 2.23mA/cm^2). Therefore, the kinetic limitation of Pt catalyst is lower than RuO_xH_y catalyst. Even though the ORR electrocatalytic activity on pure Ru electrode was not as good as Pt, the electrochemically oxidized Ru i.e. RuO_xH_y, can be used as a potential catalyst. The electrocatalytic properties of RuO_xH_y catalyst will be discussed at further later section by using spectroelectrochemical method.

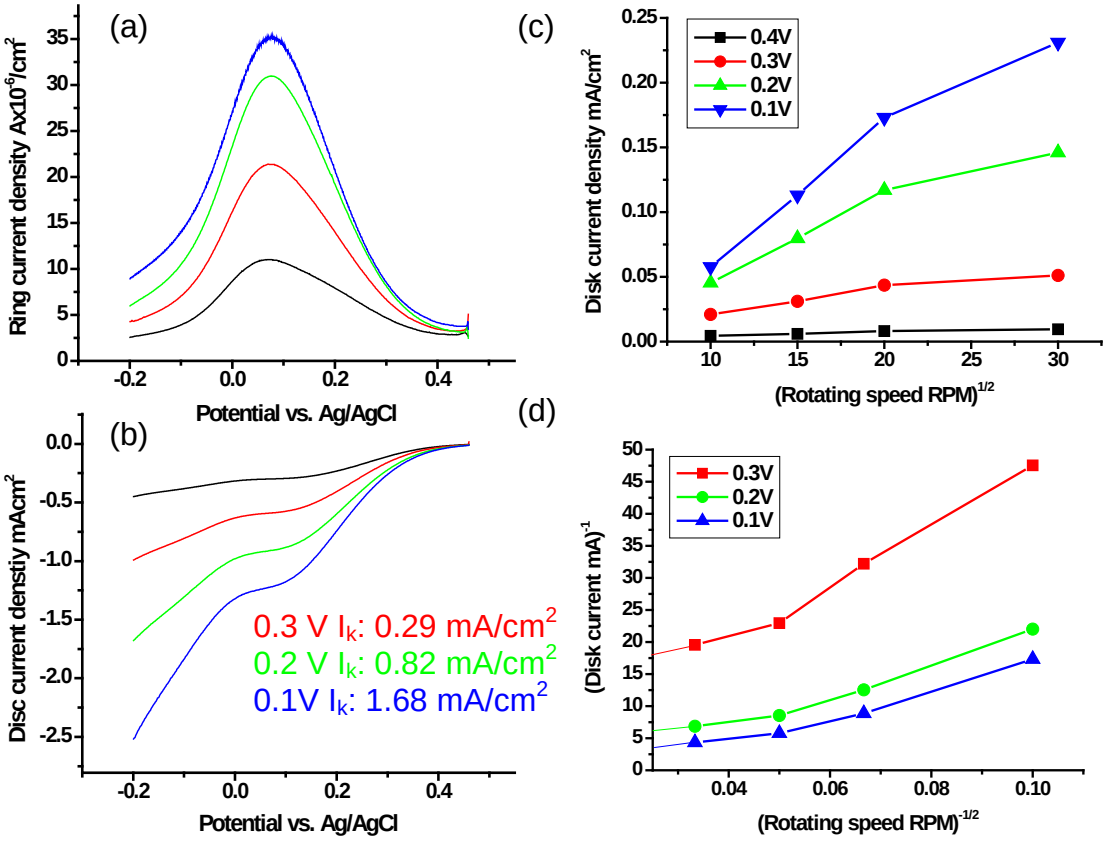

Figure 6-10 the result of Ru RRDE system in 0.5 M H_2SO_4 (lab ambient) with different rotating speed from 100 rpm to 1600 rpm (a)ring current (b)disk current (c)Variation of I with $\omega^{1/2}$ at an RDE (d) Koutecky-Levich plots at varying potentials

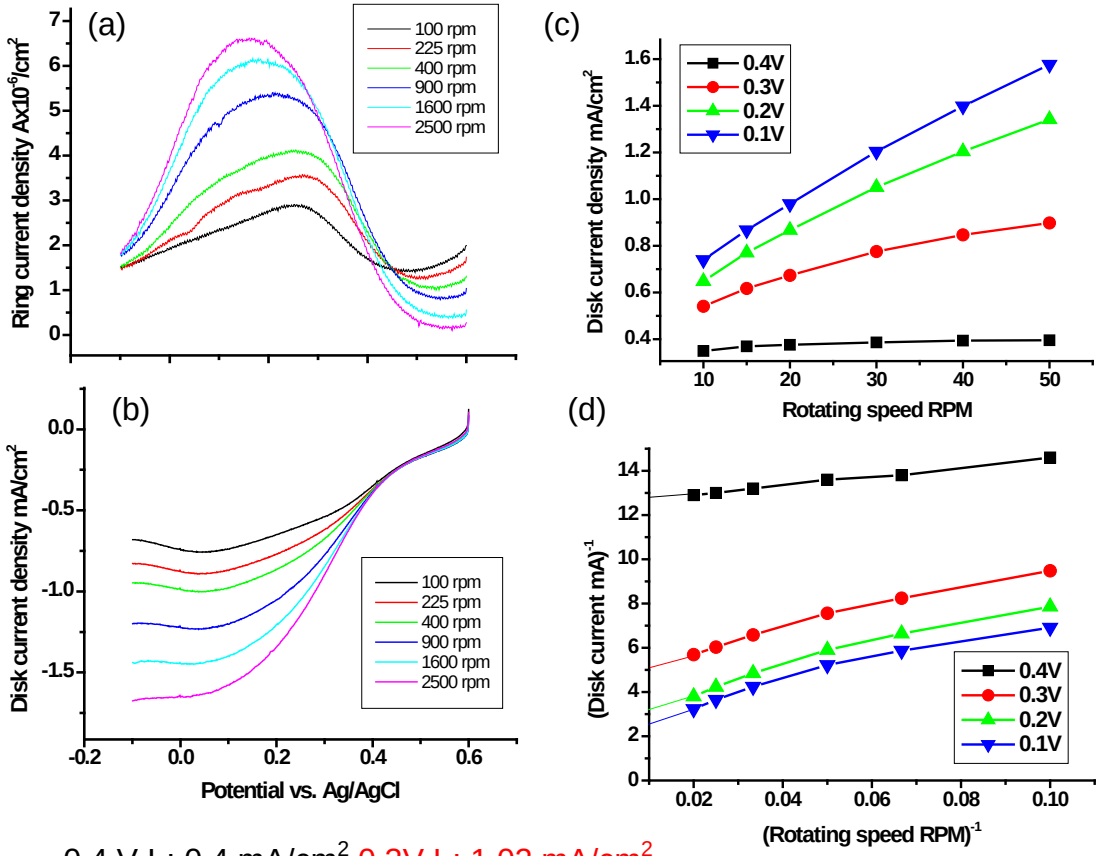

0.4 V I_k: 0.4 mA/cm^2 0.3V I_k: 1.02 mA/cm^2
0.2V I_k: 1.6 mA /cm^2 0.1V I_k: 2.04 mA/cm^2

Figure 6-11 Result of RuO_xH_y RRDE system in 0.5 M H_2SO_4 (lab ambient) with different rotating speed from 100 rpm to 2500 rpm (a)ring current (b)disk current (c)Variation of I with $\omega^{1/2}$ at an RDE (d) Koutecky-Levich plots at varying potentials.

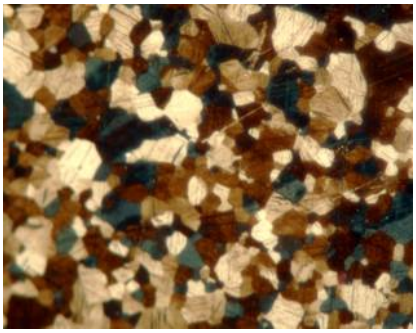

Figure 6-11 (e) microscope image of 500X RuO_xH_y disk.

6.2.3 Spectroelectrochemistry (SEC) Versus RRDE and SECM System

From the view point of catalyst surface, the porosity of electrode surfaces like carbon cloth can be investigated by both SEC and SECM methods which operation conditions are more similar to real fuel cells than using RRDE system. In fact, the operation principle of a RRDE system requires the formation of stable convection solution flow pattern by rotating the disk electrode [20]. In order to have similar flow pattern near electrode surface at the same rotating speed of disk, maintaining a flat electrode surface is crucial to prevent the uncontrollable turbulence flow. However, in a practical fuel cell, thin layer of catalysts are deposited on the porous carbon-substrate to increase the electroactive surface area. As the result, the linear flow pattern and flow speed will be influenced by surface roughness. Hence, the powder-coated catalysts may result in different surface roughness on disk electrode that leads to questionable current density of RRDE, non-suitable as a standard for studying the electrochemical catalysis. Furthermore, the ORR catalysts is fabricated on the proton exchange membrane in a PEM fuel cell (see Scheme 6-2), whereas in the RRDE system the ORR catalysts were fabricated under the coating of PEM material. In contrast, the SEC method directly characterizes ORR catalyst that can provide similar information as RRDE system with less sample preparation.

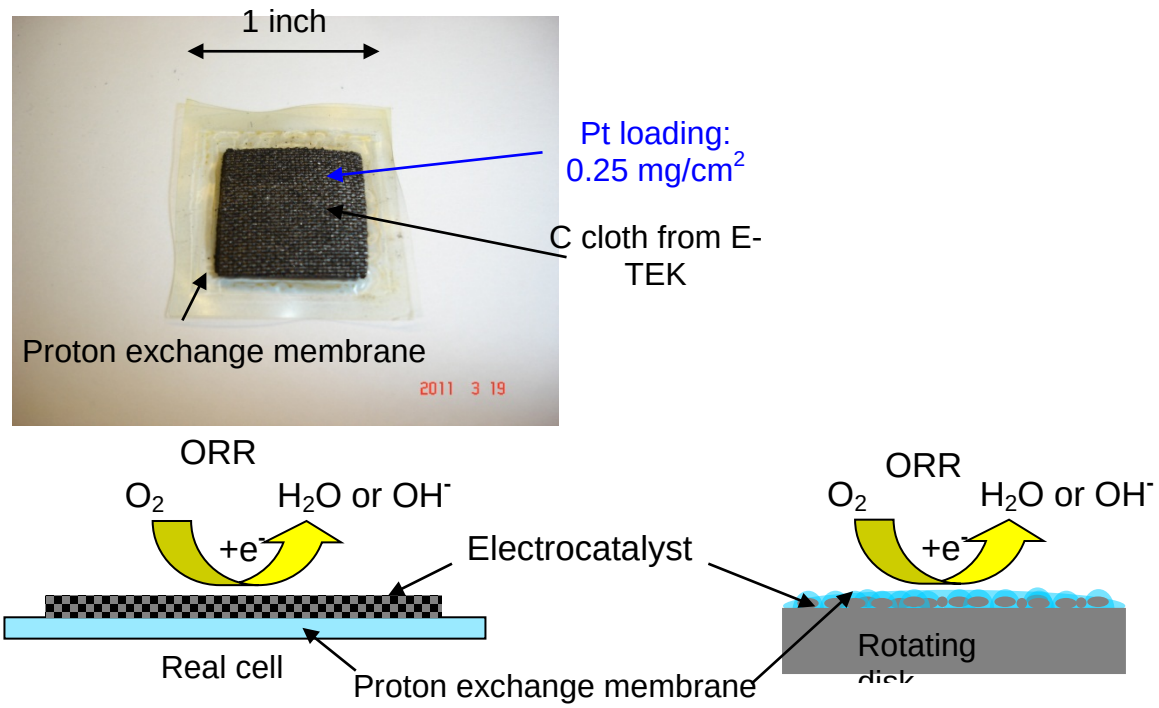

Scheme 6-2 the comparison of the catalyst on practical cell and on RDE.

6.2.4 Spectroelectrochemical Method Set-up

In SEC method, a potentiostat analyzer is used for the electrochemical experiment. All three electrodes i.e. counter electrode (Pt wire), reference electrode (satd. Ag/AgCl), and working electrode shown in Scheme 6-3 will be immersed in a cuvette filled with electrolyte (0.10 M K_2SO_4). Phenolphthalein is added to the electrolyte in order to indicate the change in local pH due to the formation of OH^- ions from ORR. Linear sweep voltammetry is used to scan the potential on the catalyst coated working electrode. During the potential scan the color change near the catalyst surface is recorded by UV-Vis spectrometer (Agilent 8453). The onset potential of ORR can be determined when the

observed absorbance intensity starts to increase. The kinetic rate will be determined by the time dependent intensity of the absorbance operated under the same amount of driving overpotential for ORR.

The pH indicator plays the key role to show the changes in pH occurring at the electrode surface. In other words, the color intensity of the pH indicator reflects the proton concentration near the vicinity of potential ORR catalyst. Also, it is well known that electrochemical system possess heterogeneous distribution of ions in solution/electrode interface. By utilizing this interfacial distribution in electrochemical system, the SEC method can measure the proton concentration variation that can directly relate to the proton consumption or hydroxide generation caused by ORR. As a result, the local pH change can be detected by a miniature pH electrode probe or visually observed by adding a suitable pH indicator. In SEC method, we use the combined effect from pH indicator with the UV-visible spectrometer instead of using a miniature pH electrode. Therefore, the increased absorbance in UV-visible spectra suggests that the pH is changed on local surface area of potential catalyst which can easily correlate to the kinetic rate of ORR activity (in Scheme 6-3). However, sufficient proton concentration gradient at the catalyst/solution interface is necessary for the operation of SEC method; therefore, the buffer solution, strong acid or base could dull or inhibit the color change of indicator.

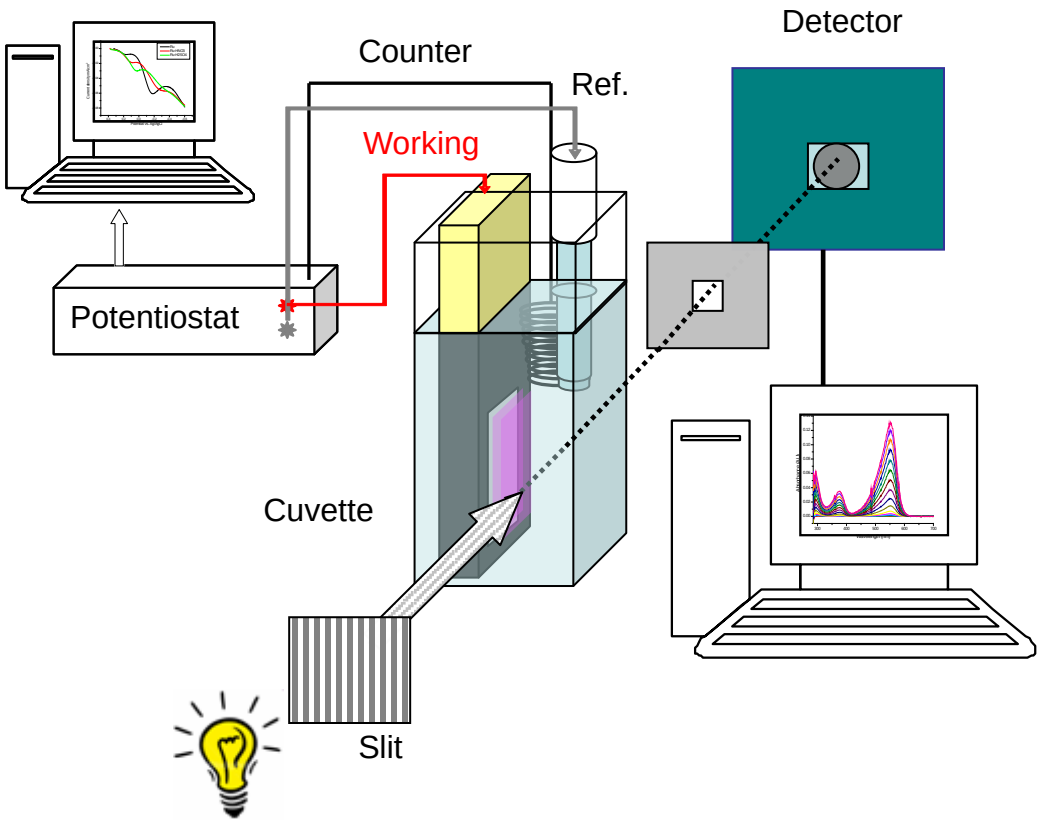

Scheme 6-3 Spectroelectrochemical (SEC) method.

6.2.5 The Study of Catalysts by LSV in 0.1 M K_2SO_4

The perfluorosulfonic acid is commonly used as membrane electrolyte for the proton exchange in fuel cell. The sulfonic acid has similar chemical structure to sulfuric acid. Hence, the sulfuric acid was used as electrolyte for ORR studies. The following study used potassium sulfate (0.1M K_2SO_4 pH~ 5) as an electrolyte for ORR SEC study to prevent rapid neutralization in the typical sulfuric acid solution. Even though some of non-noble metals were investigated to show ORR catalytic responses, the Pt-based materials are still the best electrocatalysts [16]

and commonly used as a comparison standard for the discovery of new electrocatalysts on ORR. Hence, the Pt, Pd, and Ru were selected to be starting materials for ORR study. The thin film electrodes of Pt, Pd, and Ru were prepared by sputtering deposition on Si (100) wafer.

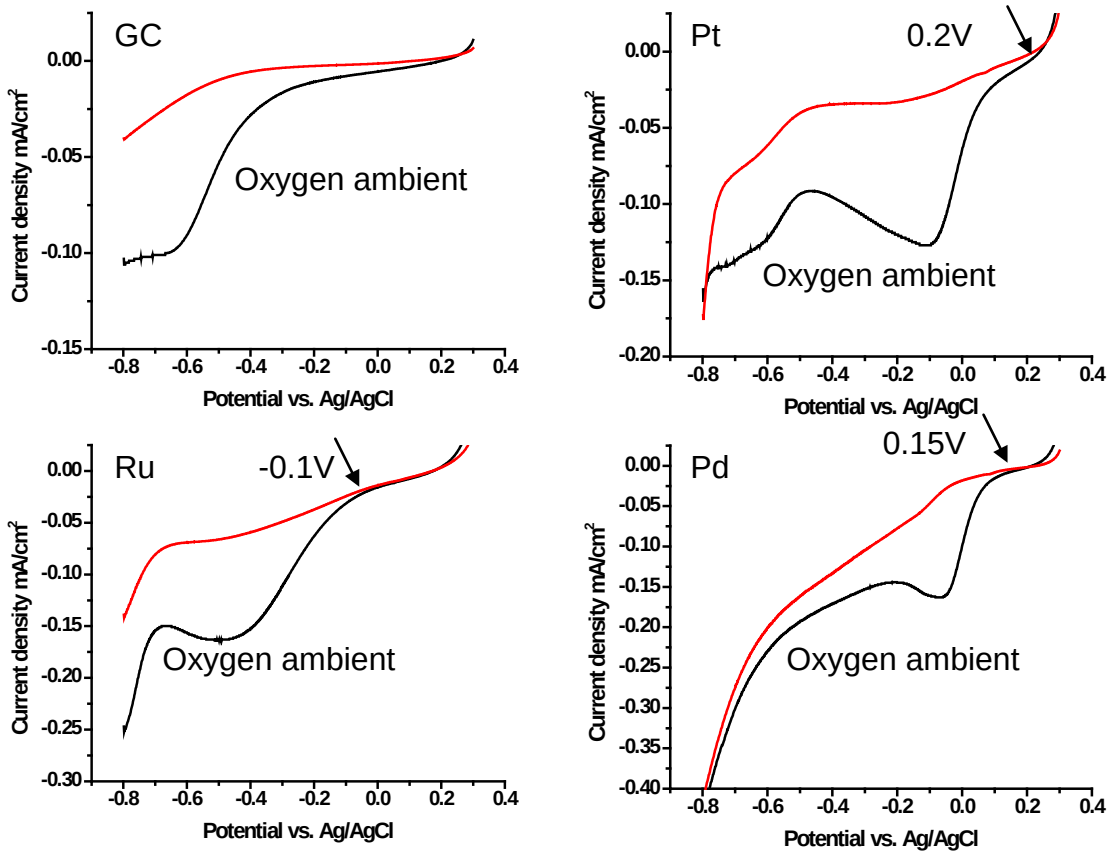

Figure 6-12 LSVs of GC, Pt, Ru, and Pd in 0.1 M K_2SO_4 under lab ambient (red line) and oxygen ambient (black line). Scan rate is 5 mV/s for all LSVs.

Figure 6-12 shows the LSVs of glassy carbon (GC), Pt, Ru and Pd electrodes in 0.1 M K_2SO_4 under oxygen ambient (black line) and lab ambient (red line) conditions. The reduction current of ORR was pronounced with the increasing dissolved oxygen content in 0.1M K_2SO_4, which allows the

identification of the onset potentials of ORR as comparing to nitrogen ambient CV background in 0.5 M H_2SO_4 solution. In Figure 6-12, the ORR can be observed in 0.1 M K_2SO_4 even though the onset potential was shifted toward more negative than the potential in 0.5 M H_2SO_4. The trend of ORR onset potential in 0.1M K_2SO_4 on different catalyst electrodes follows as: Pt (0.2V) > Pd (0.15V) > Ru (-0.1V) in Figure 6-12, which is similar to the trend observed in acidic condition (Figure 6-8). Figure 6-13 shows the LSVs of Pt, Pd and Ru electrodes in 0.1 M K_2SO_4. These electrodes were made by sputter deposition on the top of glassy carbon electrode. The ORR onset potentials were observed to be overlapped with the surface oxide reduction peak at *ca.* 0.2V, which imposes the difficulty for analyzing the accurate ORR onset potential by LSV. In contrast, the spectroelectrochemical method makes it easier to exam the catalysts even with oxide coverage on the catalysts' surface.

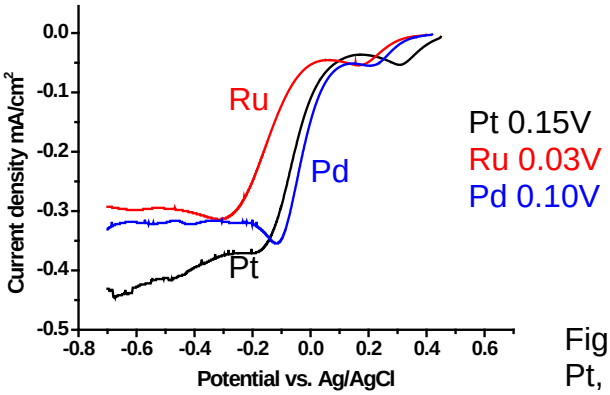

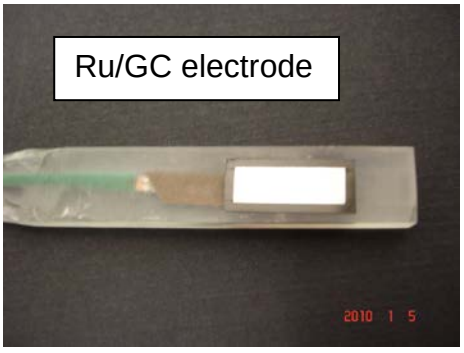

Figure 6-13 Overlapped of LSVs of Pt, Ru, and Pd SEC electrode in 0.1 M K_2SO_4 oxygen ambient at 20°C.

6.2.6 Local pH

Figure 6-14 (a) shows the Pt CV in 0.1 M K_2SO_4 with continuous O_2 purging. The pH value of 0.1 M K_2SO_4 is *ca.* 5. However, the hydrogen evolution reaction (HER) is observed at -0.8V (vs. Ag/AgCl) which is similar to the HER in pH 10 buffer solution (red line) as shown in Figure 6-14 (b). This is caused by the local pH near Pt surface was increased by the formation of hydroxyl ions originating from the ORR from dissolved oxygen. In general, the concentration of dissolved oxygen in aqueous solution is *ca.* 8 ppm, which is equivalent to 0.25 mM [O_2]. Assuming four electron-transfer reactions, the ORR can in principle generate *ca.* 0.5 mM [OH^-] close to the electrode surface that is equivalent to pH 10.7.

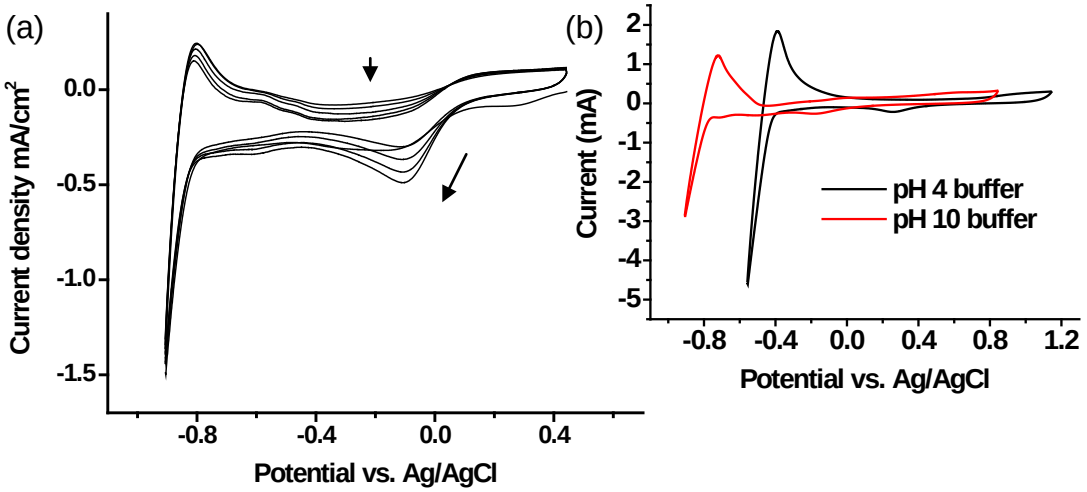

Figure 6-14 (a) CV of Pt electrode in pH 5, 0.1 M K_2SO_4 under the continuous O_2 purging condition (b) the CV of Pt electrode in pH buffer solutions.

The SEC method was applied by introducing the phenolphthalein indicator which can provide the easily detectable color change during ORR from transparent to pink as shown in Figure 6-15. The ORR has occurred on Ru

electrode during potential scan in 0.1 M K_2SO_4 with 20 ppm phenolphthalein.

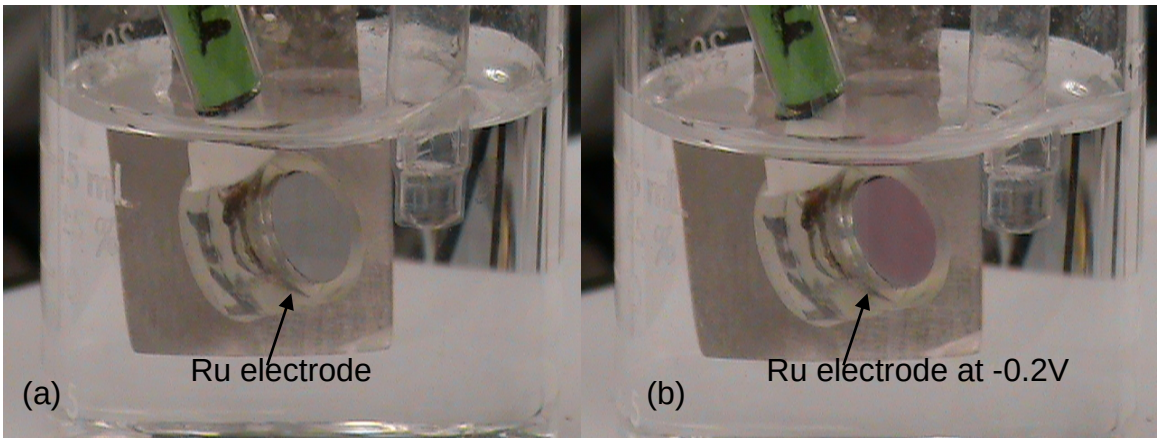

Figure 6-15 Images of Ru electrode during ORR (a) before (b) at reducing potential -0.2V.

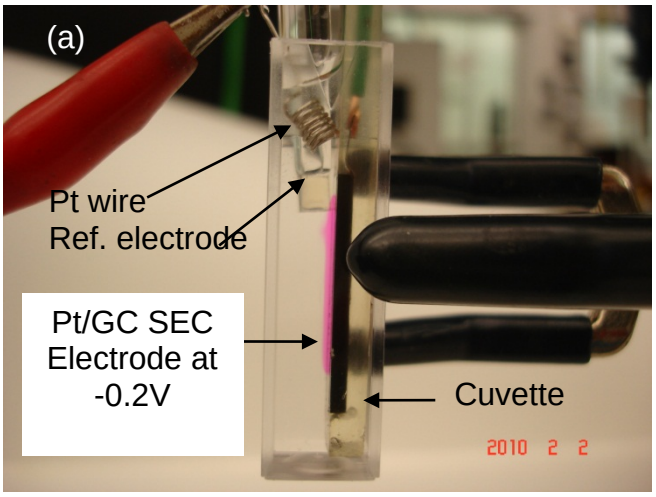

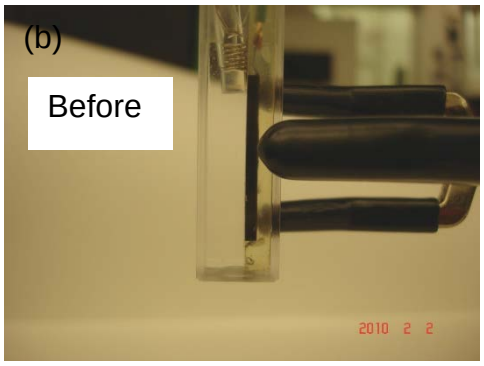

Figure 6-16 (a) Pt SEC cell during ORR at reducing potential at -0.2V. (b) the side view of GC electrode.

In order to utilize the UV-Vis spectrometer, a special GC electrode was built so that it can be placed in cuvette cell for the SEC analysis as shown in Figure 6-16 (b). The catalyst materials were deposited on GC electrode for studying the behavior of ORR. Figure 6-17 shows that the SEC method did work by using the Pt/GC SEC cell. Under different conditions such as oxygen,

atmosphere and nitrogen ambient, the higher absorbance shows the higher concentration of hydroxyl ions that were generated by ORR in more oxygen rich solution. In nitrogen ambient condition, the UV-Vis spectrum was flat, which illustrates that the only factor to cause the increase in absorbance is oxygen reducing process. Also, the LSV results in Figure 6-17 (b) showed the more pronounced ORR reducing current peak at higher oxygen contained ambient that supported the results obtained from UV-Vis spectra.

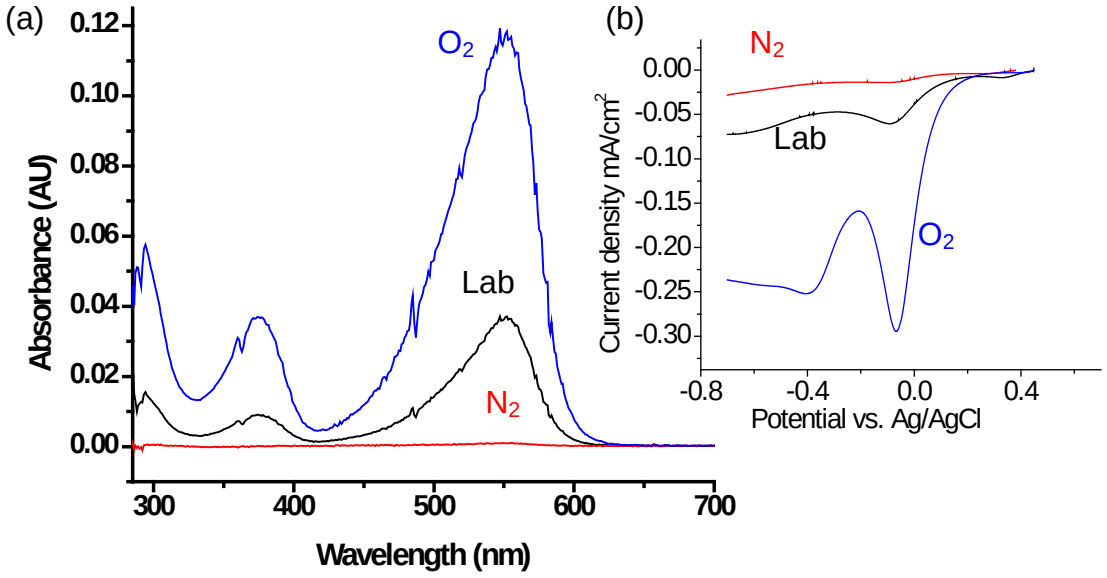

Figure 6-17 (a) the UV-Vis results of Pt electrode under different ambient at reducing potential -0.2V (b) the LSV results during the SEC method. Scan rate is 5 mV/s.

6.2.7 Onset Potential of ORR

Figure 6-18 shows the observed spectra at the different potential control obtained by UV-Vis spectrometer. The spectra were measrued every 50mV steps during the potential scanning (LSV) from OCP to -0.4V. The *insert* spectra in

Figure 6-18 are the expanded view of initial increase in absorbance.

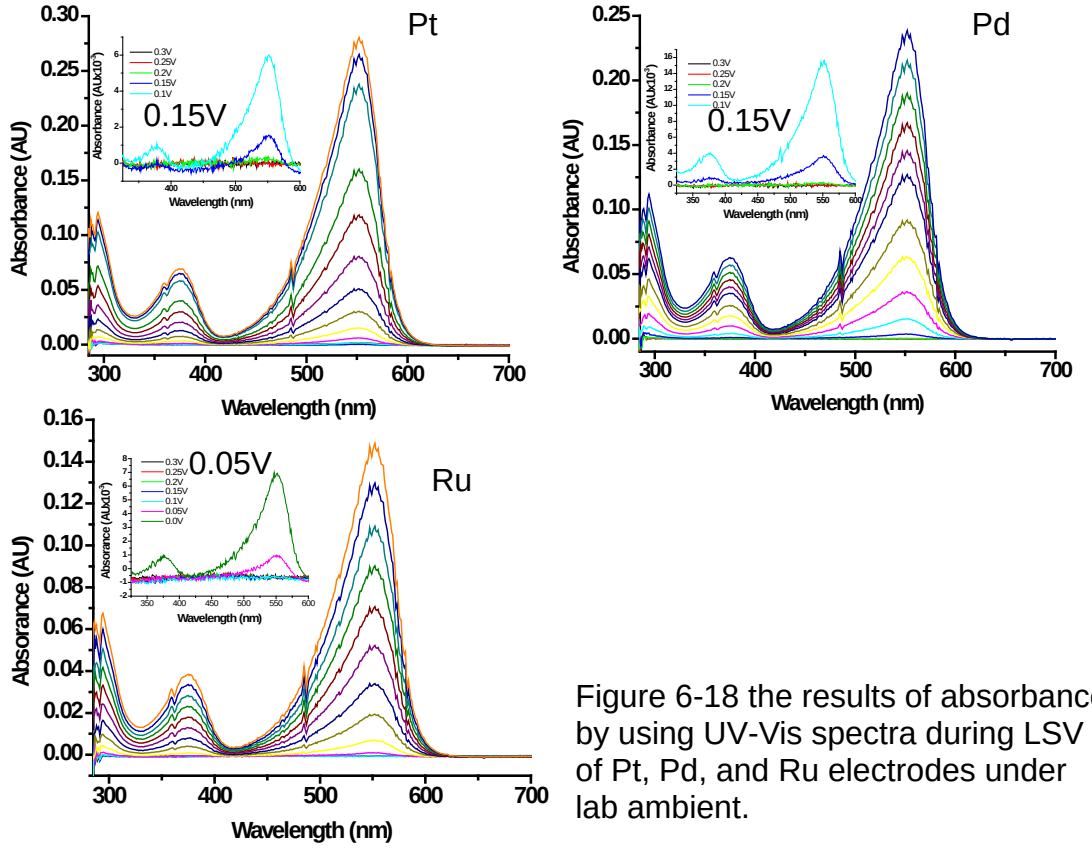

Figure 6-18 the results of absorbance by using UV-Vis spectra during LSV of Pt, Pd, and Ru electrodes under lab ambient.

Figure 6-19 is result of the peak absorbance of 552 nm at specified potential during the LSV. The plot of absorbance versus scanning potential can depict the relative concentration of hydroxyl ions that were generated and cumulated during the LSV. The LSV in the bottom of Figure 6-19 shows that the oxygen reduction peak on Pd was sharper than that on Pt. But, at the same time, the absorbance intensity on Pd was not as high as Pt in Figure 6-19, therefore it would be misleading to judge the performance by LSV alone. The LSV of Pd had larger reducing current than Pt and Ru as shown in Figure 6-12.

However, the large current can be caused by the surface poisoning effect by sulfate ions. The poisoning issue of Pd surface will be discussed at the later section. By using the SEC method, the absorbance can indicate concentration of hydroxyl ions which was only generated by the ORR.

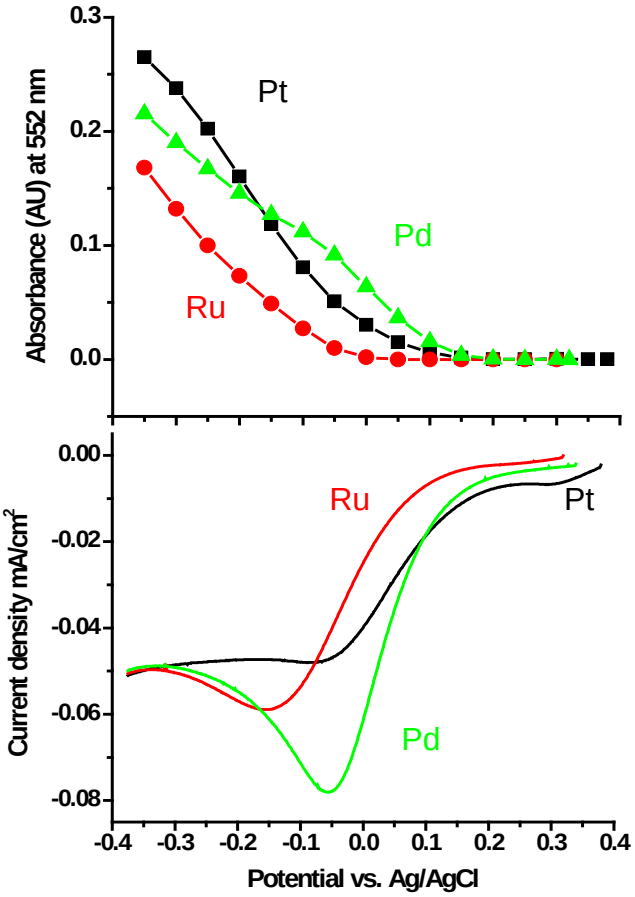

Onset potential of ORR:
Pt: 0.15 V
Pd: 0.15V
Ru: 0.05V

Figure 6-19 the result of figure 6-18 plotted by absorbance versus the potential scan (LSV) scan rate is 5mV/s.

6.3 Durability and Poisoning Issue

The U.S. department of energy reported that the development goal for PEM fuel cell at 2011 is the lifetime within 40,000 hours with less than 10% rated power degradation [21]. The operation lifetime of the fuel cell is a critical issue. The catalysts need to have high tolerance to poisoning contaminants such as

halide ions (Cl-, Br-, I-), methanol, NO_x, CO_x, and SO_x.

Most researches show that sulfur can be a severe poison effect for catalysts in fuel processors for fuel cells. It is well known that very low levels of sulfur can severely deactivate various catalyst systems, by rearrangement of the surface structure through sulfur species [22-26]. The sulfation is the poisoning phenomenon which results in the formation of metal sulfate to cover the catalysts. For example, the sulfation was reported on Pd catalysts to form $PdSO_4$ when exposing to sulfur species [23]. In this section, the SEC method was demonstrated to be useful to reveal the poisoning issue of catalysts like Pt, Pd and Ru. The nitric acid and sulfuric acid containing NO_x and SO_x, respectively, were used as the source of contaminants or poisons to study electrocatalysts.

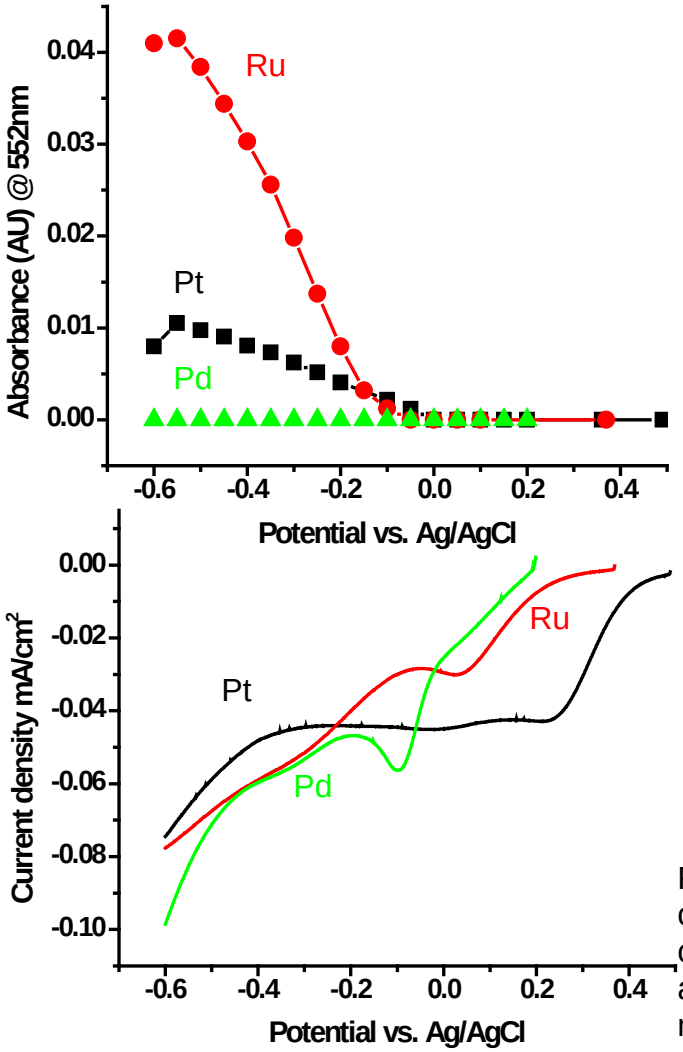

Figure 6-20 Poisoning study of sulfuric acid pre-treated catalysts in 0.1 M K_2SO_4 lab ambient. Scan rate is 5 mV/s.

Figure 6-20 shows the result obtained on the poisoning study of sulfation for the catalysts (Pt, Pd and Ru) by using the SEC method. All of three electrodes (Pt, Pd and Ru) were dipped into 0.5 M H_2SO_4 for 30 minutes and then rinsed with DI water before running SEC experiment. Ruthenium shows higher tolerance in sulfate environment than Pt and Pd. The Pd electrode is found to have severe sulfation resulted in no absorbance in UV-Vis spectra. Based on the

absorbance results in Figure 6-20 at -0.2V, the current degradation on Pt, Pd and Ru in sulfuric acid is 96%, 100% and 82.3% comparing with the data of freshly prepared catalysts. The ORR onset potential on Pt has shifted 200 mV from 0.15V to -0.05V. The onset potential of Ru has shifted 150 mV from 0.05 to -0.1V.

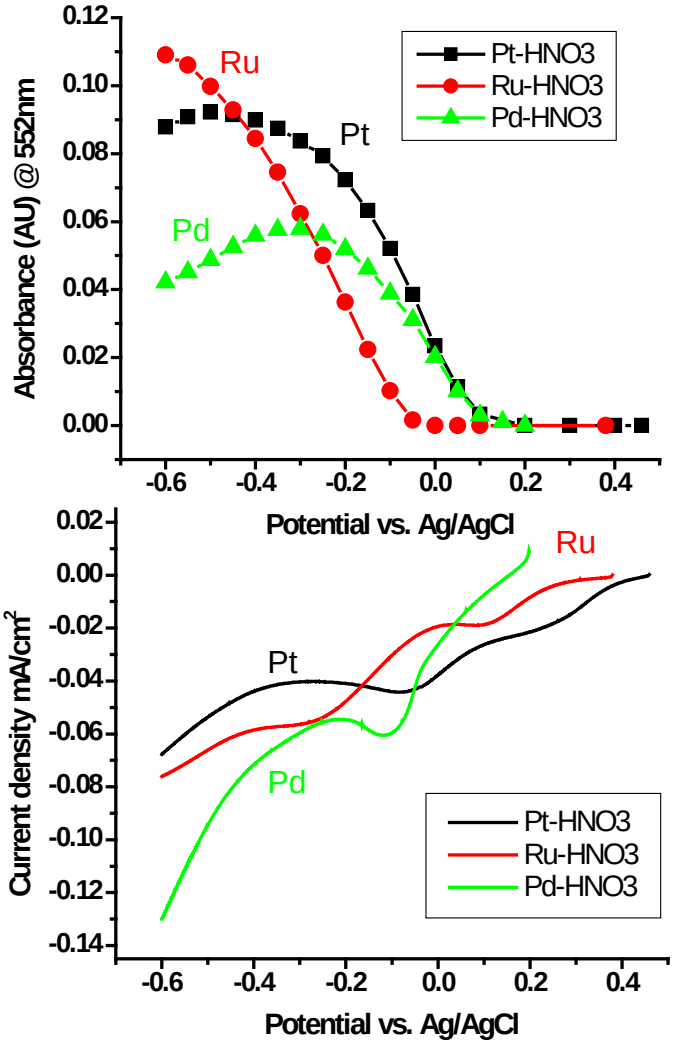

Figure 6-21 Poisoning study of nitric acid. 10% nitric acid lab ambient. Scan rate is 5 mV/s.

The poisoning study of nitric acid was shown in Figure 6-21. The degradation of Pt is 65.4% without potential shift. The degradation of Pd is 77.3%

without potential shift. The degradation of Ru is 44.1% with 100mV potential shift. In Figure 6-22, the SEC and LSV results of sulfuric acid or nitric acid treated Ru surface was shown with non-treatment result. In LSV data, the reduction potential of Ru surface is *ca.* 0.0V to 0.3V. Comparing absorbance and LSV data, the onset potential of Ru occurred only after the Ru surface was reduced. In order to confirm the results obtained by the SEC method, RRDE system was used to verify and compare whether the results from both techniques have the same agreement for catalyst study with poisoning issues.

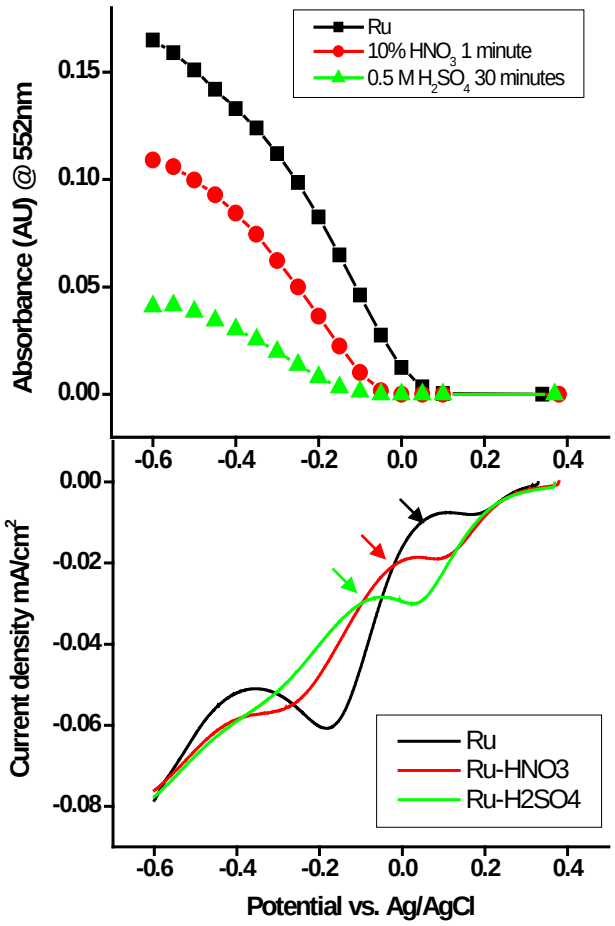

Figure 6-22 Poisoning study of Ru catalyst in sulfuric acid or nitric acid in 0.1 M K_2SO_4 lab ambient. Scan rate is 5 mV/s.

6.3.1 Ring Potential at The RRDE System in 0.1 M K_2SO_4

RRDE system is often used to characterize the ORR catalysts under acidic condition for PEM fuel cell or under alkaline condition for alkaline fuel cell and direct methanol fuel cell. Therefore, it is important to apply the suitable potential in different pH conditions at the ring electrode in order to oxidize and detect hydrogen peroxide. It is reported that the ring electrode was set at 1.0V vs. Ag/AgCl for H_2O_2 detection in acidic electrolyte. However, there is no published data on the required potential to oxidize H_2O_2 in near neutral aqueous electrolyte, like 0.1 M K_2SO_4, related to RRDE system. Hence, this section is going to discuss how to find a suitable applied potential for ring electrode on the ORR study in 0.1 M K_2SO_4 solution.

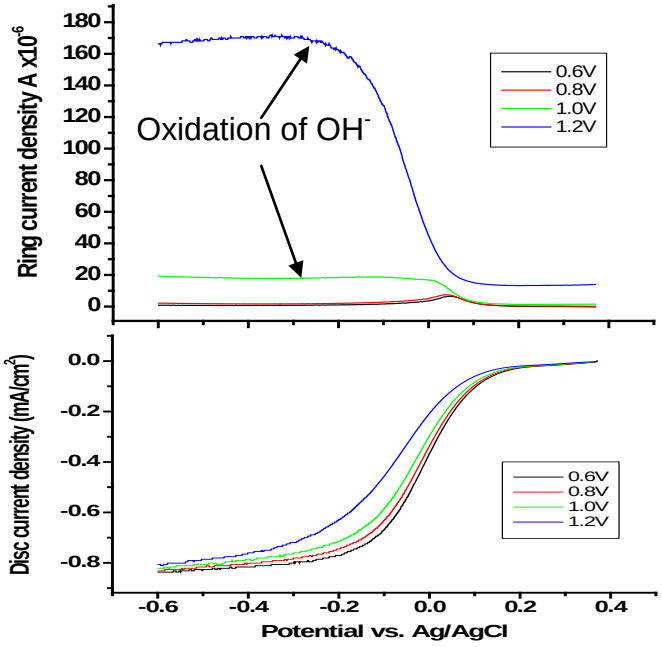

Applied different ring potential

Figure 6-23 Pt Ring potential check in 0.1 M K_2SO_4 pH 5 scan rate 50mV/s 900 rpm Pt LSV.

Figure 6-23 demonstrates RRDE results of the different applied ring

potential with the same rotating speed (900 rpm) in 0.1 M K_2SO_4 solution. The potential at 0.8V (vs. Ag/AgCl) seems to be the suitable potential to oxidize hydrogen peroxide in 0.1M K_2SO_4. The oxygen evolution reaction (OER) by oxidizing water or hydroxyl ion starts to interfere with H_2O_2 detection when the applied potential on ring electrode is higher than 0.8V like 1.0V and 1.2V, Figure 6-23. Therefore, the limit of high end potential for oxidizing hydrogen peroxide can be either 0.8V or 0.6V. So, we checked check whether the ring potential at 0.6V is efficient for oxidizing hydrogen peroxide. Figure 6-24 shows the RRDE result of the different applied ring potential with the same rotating speed (100 rpm). This time a drop of 30% H_2O_2 was added in 0.1 M K_2SO_4 solution.

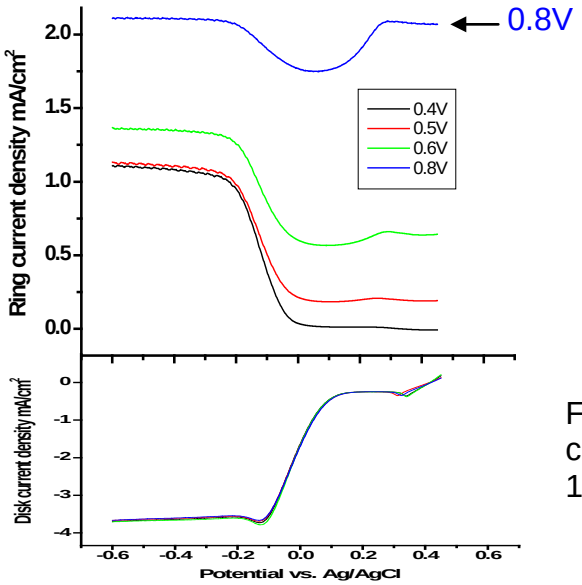

0.8V is the suitable potential to oxidized H_2O_2

Figure 6-24 Pt ring-disk potential check in 0.1 M K_2SO_4 + H_2O_2 with 100 rpm 50mV/s.

By adding hydrogen peroxide in 0.1 M K_2SO_4 solution, the low end oxidizing potential for hydrogen peroxide at ring electrode can be determined by analyzing Figure 6-24. With applying 0.8V at ring electrode, the oxidizing current

of hydrogen peroxide maintains the same (0.22 mA/cm^2) before 0.3V and after -0.2V. The oxidizing current at the ring electrode decreased at region between 0.3V and -0.2V due to reduction of hydrogen peroxide from the center disk. In Figure 6-24, the other applied potentials lower than 0.8V did not keep the same level of oxidizing current indicating the overpotential is not high enough for oxidizing H_2O_2. Therefore, the limiting current was low when overpotential was lower. Also, the oxidizing current shows different levels before 0.0Vand after -0.2V especially at (0.4V, 0.5V and 0.6V) owing to the increasing alkalinity by ORR on center disk. With higher pH condition, the onset potential of oxidizing H_2O_2 should be lower. That's why the oxidizing current on ring went higher after the potential scanned through the onset potential of ORR on center disk.

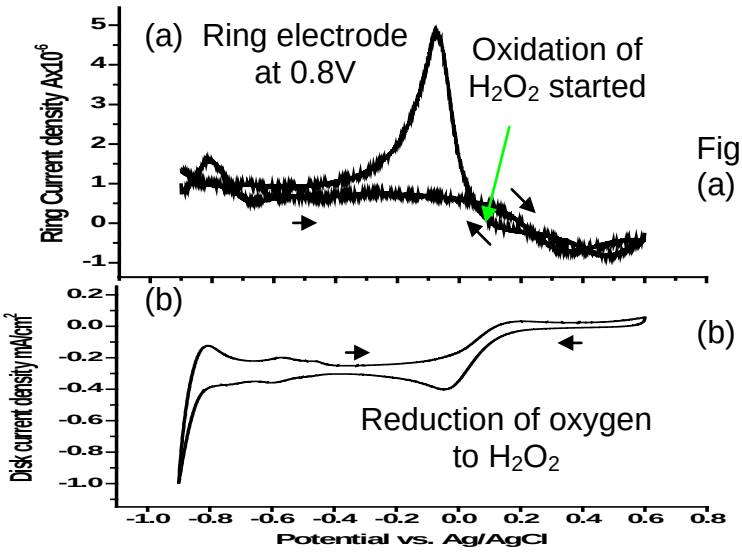

Figure 6-25
(a) The current response on Pt ring-disk with holding potential at 0.8V.
(b) CV of Pt center-disk in 0.1 M K_2SO_4 with 100 rpm 50mV/s

The applied potential at ring electrode was also confirmed by CV for 0.1 M K_2SO_4. Figure 6-25 shows the CV of electrochemically cleaned Pt RRDE in 0.1 M K_2SO_4 solution under the rotating speed (100 rpm). The potential of ring

electrode was set at 0.8V while running CV on disk electrode. When the disk electrode was reaching 0.1V at forward scan (Figure6-25b) in CV, we observed increase oxygen reduction disk current accompanying with an increase of ring current (I_r) that demonstrates successful H_2O_2 detection. The H_2O_2 oxidizing current at the ring electrode (I_r) is increased while oxygen was reduced on center disk electrode. The I_r decreased when the disk potential was scanned to more negative than -0.1V. The increase overpotential of ORR minimized the generation rate of two electron transfer product hydrogen peroxide. And the I_r became stable once the scanning potential reached to -0.4V. When potential scan reversed to positive potential at 0.2V, the I_r decreased again because the ORR stopped. The I_r response shows differently between forward scan and reverse scan because the Pt disk surface was reduced during the reverse scan under higher alkalinity due to the ORR comparing with the Pt oxide during the forward scan.

Since the applied potential on ring electrode was confirmed, the poisoning study can be studied in 0.1 M K_2SO_4 by using the RRDE system. Figure 6-26 shows the RRDE result of Pt disk in 0.1 M K_2SO_4 solution at 900 rpm. The clean Pt disk shows with black line and sulfate aged Pt shows the red line. The onset potential of Pt electrode is *ca.* 0.0V and sulfate-aged Pt is *ca.* -0.2V. The electron transfer number, ‘n’ for cleaned Pt and aged Pt are 3.83 and 3.63, respectively. Figure 6-27 shows the RRDE result from Ru disk in 0.1 M K_2SO_4 solution at 900 rpm. The black line is from clean Ru disk shows and the red line is from sulfate

aged Ru. The onset potential for Ru electrode is *ca.* -0.1V and sulfate-aged Ru is *ca.* -0.15V. The electron transfer number, 'n' for cleaned Ru and aged Ru are the same as 3.8.

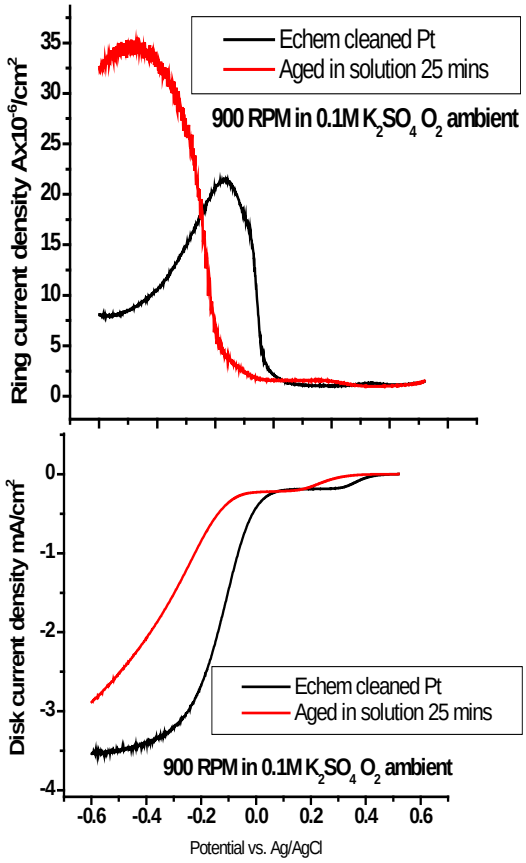

Cleaned Pt surface
Electron transfer number, (n) = 3.83 and H_2O_2 formation *ca.* 4.2%
Aged Pt surface n = 3.66 and H_2O_2 formation ca. 7.8%

Figure 6-26 the clean Pt (black) and sulfate-aged Pt (red) in 0.1 M K_2SO_4 solution at 900 rpm in oxygen ambient.

The ORR onset potential on Pt and Ru thin films observed using SEC method are 0.15V and 0.05V, respectively. The onset potential for Pt and Ru disks in RRDE system are 0.0V and -0.1V, respectively. The onset potential for sulfated Pt and Ru in SEC method is -0.05V and -0.1V. The onset potential of sulfated Pt and Ru in RRDE system is -0.2V and -0.15V. The results were summarized in table 6-1.

Onset potential Vs. Ag/AgCl	Pt	Aged Pt	Ru	Aged Ru
SEC method	0.15V	-0.05V	0.05V	-0.1V
RRDE	0.0V	-0.2V	-0.1V	-0.15V

Table 6-1 the SEC method vs. the RRDE system.

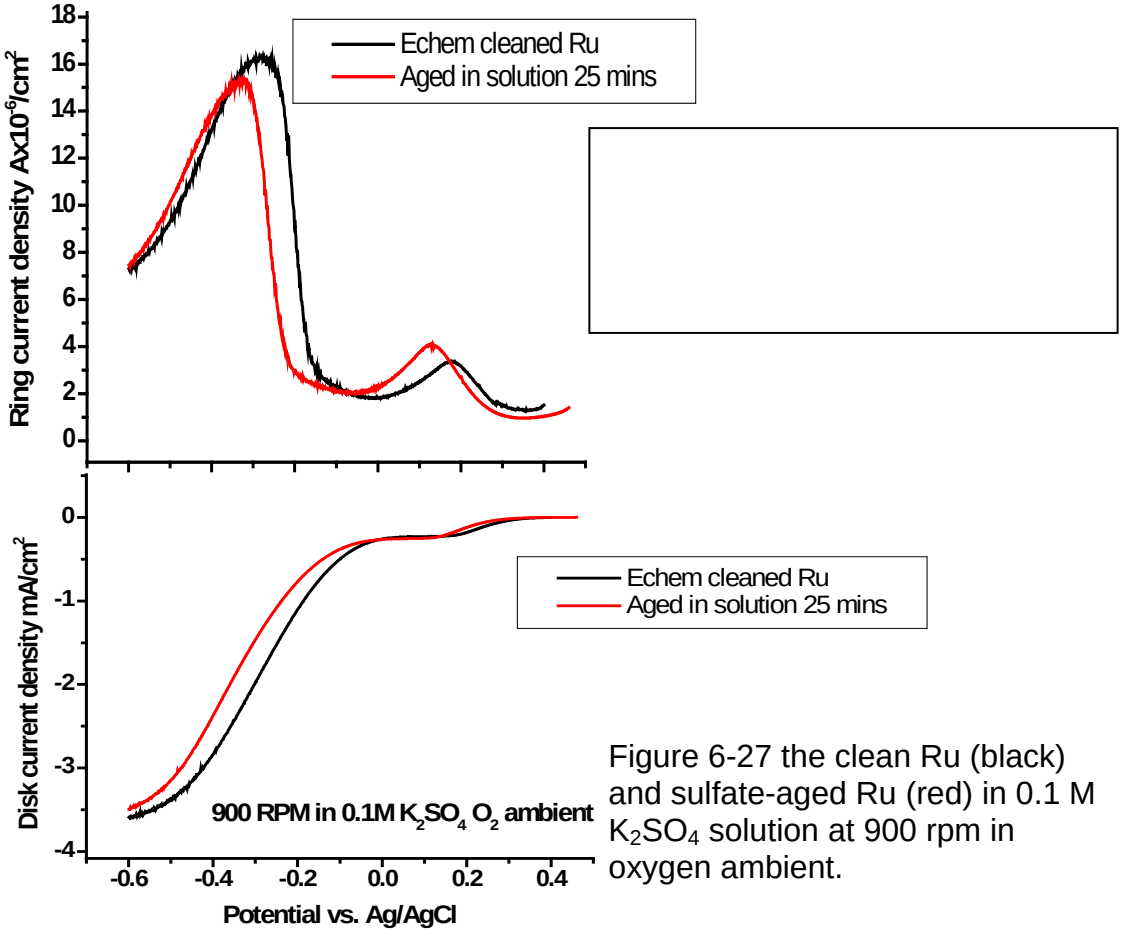

Figure 6-27 the clean Ru (black) and sulfate-aged Ru (red) in 0.1 M K_2SO_4 solution at 900 rpm in oxygen ambient.

Comparing the SEC method with the RRDE system, the SEC method seems to have higher sensitivity for detecting the ORR onset potential. Both

methods show the same trend in case of poisoning issue with sulfate contamination. Ru has higher tolerance for sulfate contamination than Pt surface.

6.4 Surface treatment and recovery from poisoning environment

Since the poisoning issue of sulfation was mentioned before, this section discusses about the way to recover the surface by using hydrogen plasma as shown in Figure 6-28. The hydrogen plasma modified Pd surface becomes active in the SEC method. The absorbance results in Figure 6-28 shows that the recovered Pd surface started ORR even without applying potential. Therefore, the hydrogen plasma can be a way to reclaim the spent catalysts.

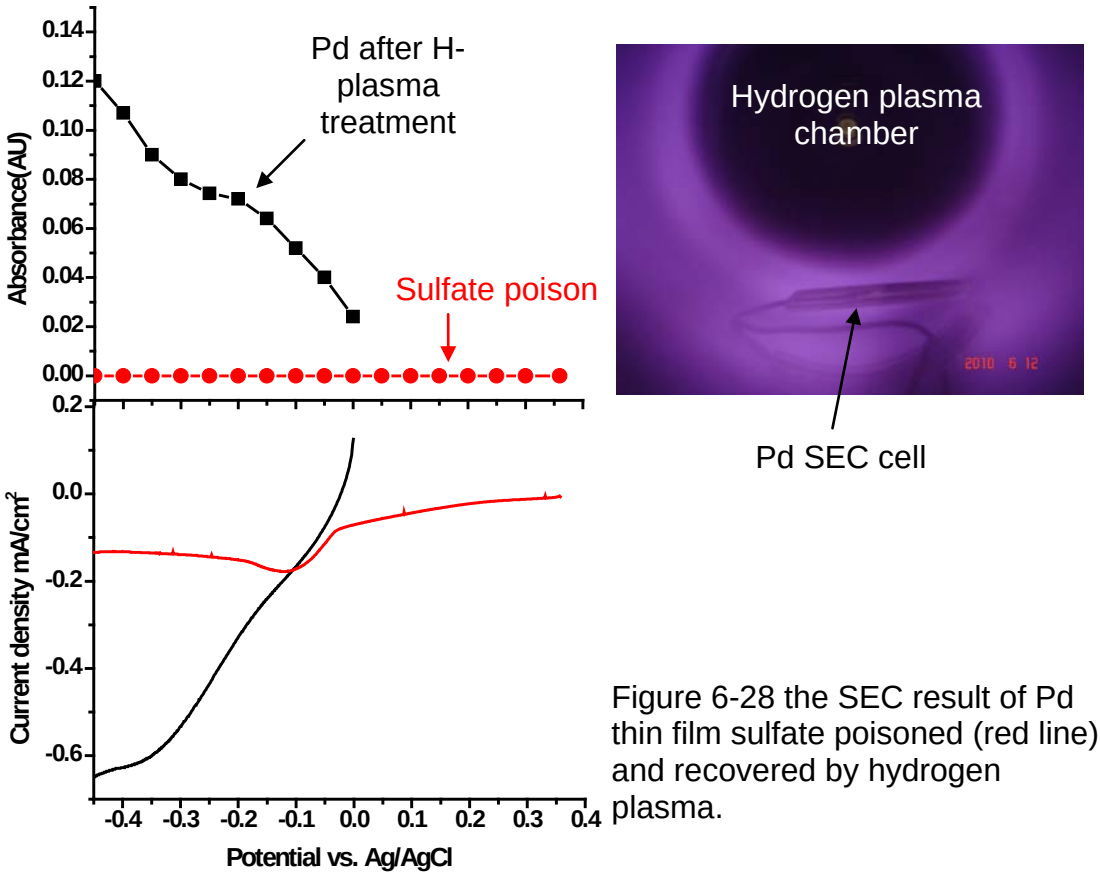

Figure 6-28 the SEC result of Pd thin film sulfate poisoned (red line) and recovered by hydrogen plasma.

6.5 Characterization of RuO_xH_y on ORR

Based on previous catalyst studies Figure 6-11, the RRDE system shows that the RuO_xH_y has promising onset potential and high kinetic current limitation similar to the Pt catalyst. Thus, a thin film Ru wafer was prepared by sputter deposition on Si (100) wafer. The Ru-coated wafer electrode was made into three different regions of Ru oxides by electroxidation, Figure 2-29(b). And then the Ru and RuO_x wafer electrode was immersed into the electrolyte which was used for the SEC method and the potential was applied. As shown in Figure 6-29(a), an intense pinkish color was observed on RuO_xH_y (prepared at +1.3V) surface than

on Ru surface which illustrates the onset potential for RuO_xH_y is higher than Ru surface.

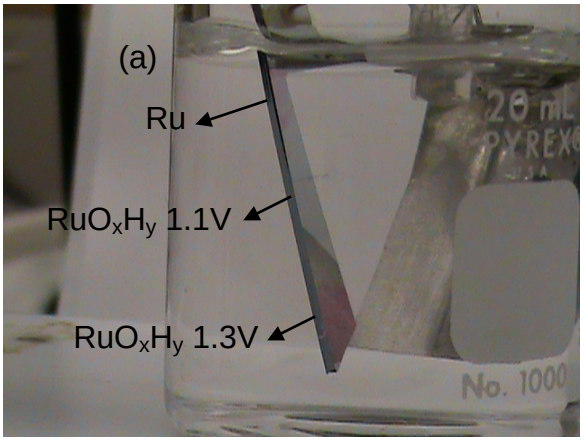

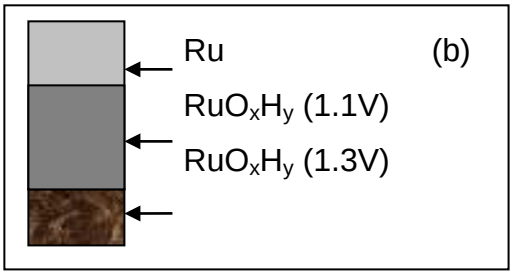

Figure 6-29 Ru wafer with different oxidation states. Applied at -0.1V vs. Ag/AgCl.

Also, the LSV data shows the result that is in agreement that the RuO_xH_y has better onset potential than Ru as shown in Figure 6-30. The onset potentials of RuO_xH_y and Ru are 0.52V and 0.45V, respectively.

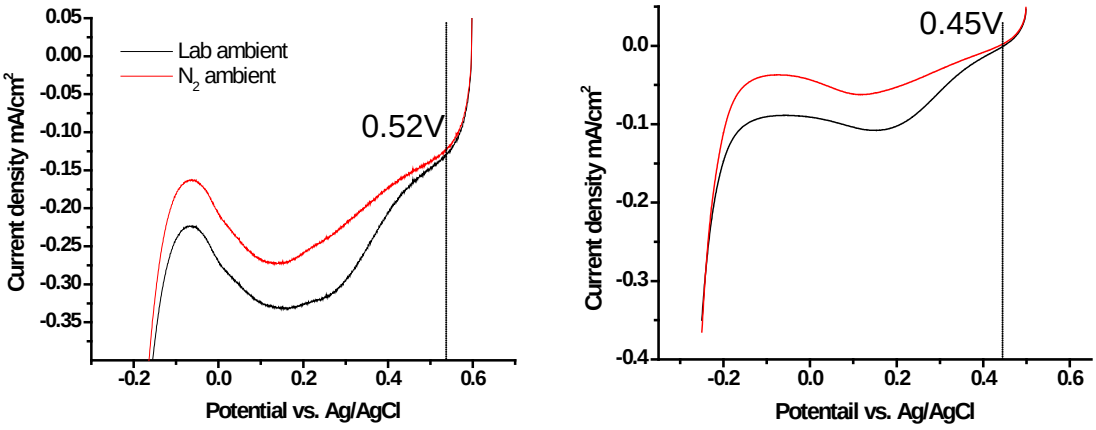

Figure 6-30 (a) RuO_xH_y SEC cell in 0.5 M H_2SO_4 (b)Ru SEC cell in 0.5 M H_2SO_4.

6.5.1 Adhesion on Glassy Carbon (GC)

In order to complete the RuO_xH_y study for the SEC method, it is necessary to have good adhesion for Ru thin film on GC electrode; otherwise the thin film of Ru will peel off under high positive oxidizing potential as Figure 6-31(a) and (b). The GC electrode was treated by oxygen plasma to minimize the organic coverage and to ensure the adhesion of the Ti primary layer on the GC electrode surface. Hence, the film of RuO_xH_y can be modified on the surface of Ru/Ti/GC as shown in Figure 6-31 (c) and (d).

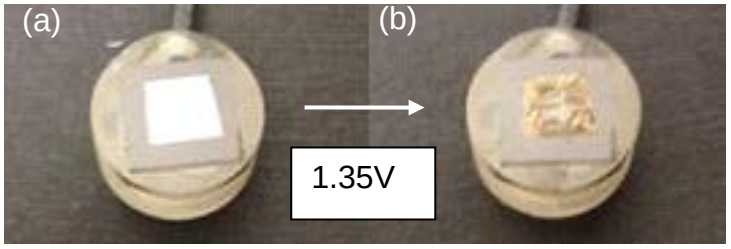

Ru/Ti/GC

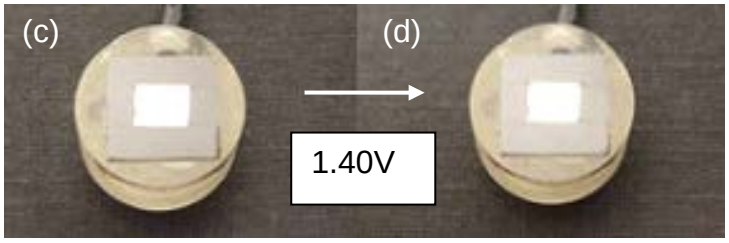

Ru/Ti/ (GC with O-plasma treated)

Figure 6-31 (a) Ru/Ti/GC electrode (b) electrochemically oxidized at 1.35V on Ru/Ti/GC in 0.5 MH_2SO_4 (poor adhesion).
(c) Ru/Ti/ (GC with O-plasma treatment) (d) electrochemically oxidized at 1.40V on Ru/Ti/GC with O-plasma treatment in 0.5 MH_2SO_4 (good adhesion).

6.6 Summary

In this chapter, our result demonstrated that the SEC is a useful new characterization technique to study the oxygen reduction reaction catalysts. The

SEC technique can offer a cheap and rapid optical screening tool to develop a better ORR catalyst. In SEC method, the onset potential for ORR on the catalyst surface can be determined during the potential scan by using the UV-visible spectrometer. It is done by observing the onset of absorbance intensity in the UV-Vis spectra due to the change in the solution color caused by local alkalinity increase of ORR. SEC method is also capable for investigating catalyst poisoning studies. Moreover, the RuO_xH_y was found to be a potential ORR catalyst which shows several outstanding properties such as high tolerance of sulfation, high kinetic current limitation and low percentage of hydrogen peroxide formation.

6.7 References

1. M. L. Perry and T. F. Fuller, *J. of the Electrochemical Society*, **2002,** 149, S59.
2. W. T. Grubb, U.S. Pat. 2913511, 1959.
3. W. T. Grubb and L. W. Niedracn, *J. Electrochem. Soc.*, **1960,** 107, 131.
4. E. A. Ticianelli, C. R. Derouin, A. Redondo, and S. Srinivasan, *J. Electrochem. Soc.*, **1988,** 135, 2209.
5. The bullion desk.com http://www.thebulliondesk.com/ (accessed Nov. 10, 2009)
6. Bin Wang, *J. of Power Source*s, **2005,** 152, 1.

7. H.S. Wroblowa, Y.D. Pan, G. Razumney, *J. Electroanal. Chem.* **1976,** 60, 195
8. U.S. Department of Energy, (2009). *Technology Installation Review* [online]. Available: http://www.eere.energy.gov/femp/ [accessed Nov. 10, 2009]
9. Hui Xu, Uing Song, H. Russell Kunz and James M. Fenton, *J. Electrochemical Soc.* **2005,** 152, A1828.
10. E. P. Ambrosio, C. Francia, M. Manzoli, N. Penazzi, P. Spinelli, *INTERNATIONAL JOURNAL OF HYDROGEN ENERGY*, **2008,** 33, 3142.
11. Y.-X. Chen, M.-F. Li, L.-W. Liao, Jie Xu, Shen Ye, *Electrochemistry Communications*, **2009,** 11, 1434.
12. Ch. Venkatewara Rao and B. Viswanathan, *J. Phys. Chem.C,* **2009,** 113, 18907.
13. Rajesh Bashyam & Piotr Zelenay, *NATURE*, **2006,** 443, 7
14. Thomas E. Wood, Zhongshu Tan, Alison K. Schmoeckel, David O'Neill, Radoslav Atanasoski, *Journal of Power Source*, **2008,** 178, 510.
15. C.-C. Hu, and T.-C. Wen, *Electrochimica Acta*, **1996,** 41, 1505.
16. B. Viswanathan, Ch. Venkateswara Rao1 and U. V. Varadaraju, *Photo/Electrochemistry & Photobiology in the Environment, Energy and Fuel*, 2006, 43.
17. Jose L. Fernandez, Allen J. Bard, *Anal. Chem*. **2003,** 75, 2967-2974
18. Jose L. Fernandez, Darren A. Walsh, Allen J. Bard, *J. AM. CHEM. SOC.* **2005,** 127, 357-365

19. Evan W. Miller, Shelly X. Bian, Christopher J. Chang, *J. AM. CHEM. SOC.*, **2007,** 129, 3459.
20. J. Nikolic, E. Exposito, J. Iniesta, J. Gonzalez-Garcia, and V. Montiel, *Journal of Chemical Education,* **2000,** 77, 1191.
21. J. M. Gran, C. R. Vera, J. M. Parera, *Applied Catalysis A. Gerneral* **2002,** 227, 217-230.
22. Borup et al. *Chem. Rev*. **2007,** 107, 3904-3951
23. D.L. Mowery, R.L. McCormick, *Applied Catalysis B: Environmental,* **2001,** 34 287–297
24. S. Guerin, B. E. Hayden, C. E. Lee, C. Mormiche, J. R. Owen, A. E. Ruessell, *J. Comb. Chem.*,. **2004,** 6, 149-158.
25. P.K. Cheekatamarla, A.M. Lane, *Journal of Power Sources,* **2005,** 152, 256–263
26. R. Bellows, *Am. Chem. Soc.* **2001,** 46, 650–651.

CHAPTER 7

CONCLUSION AND FUTURE PLAN

7.1 Conclusion

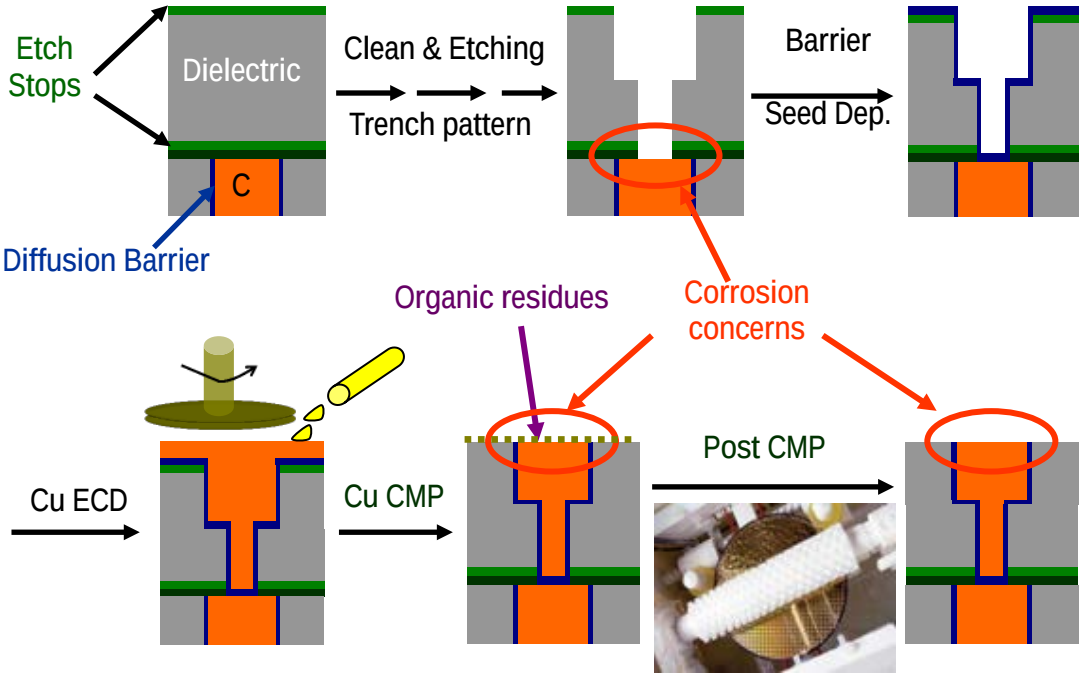

Figure 7-1 Damascene patterning process.

Figure 7-1, the scheme of damascene patterning process can provide a clear frame work of each individual studies reported in this dissertation. The part I of this dissertation dedicates on the fundamental understanding of Cu electroplating on Ru-based substrates as direct plateable liner material which is shown in bottom left of the Figure 7-1. The growth of Ru native oxide does diminish the efficiency of Cu UPD, and bulk plating on Ru surface. However, the

electrochemical formed irreversible Ru hydrate dioxide (RuO_xH_y) shows better coverage of Cu UPD especially formed in sulfuric acid. Both Ru hydrate dioxide and Ru dioxide (RuO_2) are conductive oxides which are directly plateable liner materials as potential diffusion barriers for the IC fabrication.

The part II of this dissertation demonstrates the development of a new rapid corrosion screening methodology for effective characterization Cu bimetallic corrosion in CMP and post-CMP environments as shown in the bottom part of Figure 7-1. In addition, the Echem techniques such as direct galvanic current measurements and Tafel plots were used to determine of corrosion mechanism. By utilizing micropattern corrosion screening method and Echem techniques, the corrosion inhibitors and antioxidants were studied in this dissertation. In the study of corrosion inhibition, the effectiveness of corrosion inhibitor is estimated by the extending duration time of Cu corrosion in the environments. Combining micropattern with the high resolution 3-D optical profilometry, the initial loss of Cu in early activation was able to be predicted for real time cleaning process.

Besides inhibitors, the antioxidants also used as additives in post CMP cleaning solution for protecting Cu from oxidation. However, some antioxidants have endiol structure which caused the corrosion of Cu in alkaline condition. Therefore, the micropattern corrosion screening method provides convenient platform for industrial examination of new compounds. The XPS and electro-characterization of Cu and its oxides composition were studied after air exposure, inhibitor absorption or genetic cleaning processes, which can illustrate

the trend of the growth of each Cu oxide or the left over oxide layers on the top of Cu surface after the process of treatments.

In part III, a new SEC methodology was developed to study the ORR catalysts. This novel SEC cell can offer cheap, rapid optical screening results, which helps the efficient development of a better ORR catalyst. In this method, the onset potential of ORR catalyst can be obtained during the potential scan by using the UV-visible spectrometer. The kinetic rate of the catalyst reaction can be obtained from the intensity of the observed absorbance change. Also, the SEC method is capable for identifying the poisoning of electrocatalysts. Our data show that the RuO_xH_y processes several outstanding properties of ORR such as high tolerance of sulfation, high kinetic current limitation and low percentage of hydrogen peroxide.

7.2 Future Plan

Since the interests of using Ru as directly plateable liner material, better fundamental understanding of various Ru oxides is important. However, the oxidation states of Ru Echem oxides were not investigated in chapter 2, the composition of Ru oxides needs to be verified after electrochemically oxidizing process or reducing process. Hence, thin film analysis of XPS can provide us the composition of each Ru oxide under different oxidizing potential with different oxidizing duration. Also, by comparing dry reducing process such as hydrogen plasma and forming gas annealing, or wet reducing process like electrochemical

reducing process, the reducible or irreducible Ru oxide can be characterized by XPS analysis. Moreover, the penetrated depth of irreducible Ru oxide can be measured by depth profiling XPS.

In chapter 2, the RuO_xH_y which was electrochemically formed in sulfuric acid showed extending coverage of Cu UPD *ca.* 2.38 ML. It will be helpful to use RuO_xH_y EQCM to verify the UPD coverage again. Besides EQCM, the RDE system can also be applied into Cu electroplating system for kinetic study on both UPD region and bulk plating region. Even though the coverage of UPD is surface limited, the UPD and bulk plating should also be affected by substrate physical properties such as capacitance, and resistance or conductivity. By using Koutecky-Levich plots, the kinetic limitation at each applied potential can be found. Therefore, it is interesting to find out the effect of capacitance on Cu electrodeposition, especially on RuO_xH_y surface. The crystallinity of RuO_xH_y still needs more data to confirm whether it is amorphous or crystalline.

The corrosion study in Part II of Cu corrosion inhibitors can be also combined with EQCM and Tafel plot Echem techniques, which can provide the rich information of Cu-inhibitor interface corresponding to polarization potentials such as primary corrosion potential (E_{pp}) and breakdown potential (E_b). Also, the micropattern corrosion screening method can be prepared on EQCM for bimetallic corrosion.

Owing to the fact that the cleaning process is convectional rather than static, the RDE system can be applied on corrosion study with polarization

potential. With varying rotating speed, the interfacial of Cu and inhibitor can be studied. The corrosion rate versus rotating speed under passive region potential between E_{pp} and E_b can study the resistance of the Cu-inhibitor under different rotating speed.

In part III of this dissertation, the SEC method is capable to screen electrocatalyst rapidly by visible observation. Hence, by combining with charged-coupled device (CCD) devices, the enhanced spatial resolution detector can be used to analyze the binary or trinary alloys for new catalysts. Moreover, this method can be applied not only on PEM fuel cell but also on alkaline fuel cell (AFC) and direct methanol fuel cell (DMFC). Furthermore, the SEC method can also be used on (oxygen evolution reaction) OER catalysts for the study of electrochemical water splitting or any surface reaction related to the variation of local pH.

The study of catalyst durability can use the EQCM and electrochemical impedance spectroscopy (EIS). The EQCM can show the mass spectra to detect the mass loss of electro-catalyst. The EIS can yield the information of the performance loss by measuring surface resistance. The x-ray photoelectron spectroscopy (XPS) can be used for checking the stability of oxidation state on electro-catalyst surface.